

Conductive Cellulose Nanocrystals for Electrochemical Applications

by

Xinyun Wu

A thesis
presented to the University of Waterloo
in fulfillment of the
thesis requirement for the degree of
Doctor of Philosophy
in
Chemical Engineering (Nanotechnology)

Waterloo, Ontario, Canada, 2016

© Xinyun Wu 2016

AUTHOR'S DECLARATION

I hereby declare that I am the sole author of this thesis. This is a true copy of the thesis, including any required final revisions, as accepted by my examiners.

I understand that my thesis may be made electronically available to the public.

Abstract

Recognized as the ‘nature’s latest wonder material’, cellulose nanocrystals (CNCs), can be extracted from cellulose, the most abundant biopolymer on earth. This nanomaterial is inherently renewable, nontoxic, sustainable, biodegradable, and has recently been realized at an industrial-scale production at a competitive cost (targeted at \$10/kg). Unlike typical nanomaterials, CNC possesses several attractive properties, such as its remarkable colloidal stability in water, which makes facile solution processing possible. It also has outstanding mechanical properties, high aspect ratio, high surface area, and surface chemical reactivity. The material is extremely versatile such that it can be either used as a reinforcing agent, or be chemically/physically modified to produce the desired functionalities needed for different applications.

In this work, an innovative transformation of CNCs from an intrinsically insulating material into highly conductive materials was achieved. This was made possible by two different approaches: (1) introducing CNCs with another conductive polymer - polypyrrole (PPy) to form hybrid composites; and (2) carbonizing CNCs into carbon nanorods (CNRs). The prepared conductive CNC was further applied to various electrochemical applications, such as supercapacitor (SP), supported metal catalyst, metal-free catalyst, and electrochemical sensor.

In the first approach, two generations of conductive CNCs were developed. Both PPy/CNCs have a core-shell structure with PPy polymerizing *in situ* on the surface of CNCs forming the coating. CNC served as an ideal nanotemplate to promote an ordered growth of PPy on individual CNC rather than in the bulk solution. CNC also provided significantly improved dispersion stability in water for PPy/CNC composites compared to PPy polymerized under similar condition in the absence of CNCs. Gen 1 PPy/CNC synthesis was conducted by first performing simple chemistry to introduce more negatively charged functional group (i.e. carboxylic groups) to the surface of CNCs. These carboxylic groups provided stronger interaction with PPy layer through hydrogen bonding and dopant effect. In Gen 2, surface property of CNCs was tuned by coating a thin layer of an amphiphilic polymer before PPy polymerization. This coating provided a more favorable

substrate for PPy growth compared with Gen 1. Improved synthesis of PPy/CNCs also exhibited an enhanced supercapacitive behavior and more robust cycling stability.

In the second approach, conductive CNCs were fabricated through a calcination process up to 1000 °C, where organic polymers of CNCs were decomposed into carbonaceous materials. In this strategy, CNCs were used as carbon precursor and non-sacrificing template for controlling the carbonized nanostructure. To further improve the electrochemical properties of the synthesized carbon nanorods (CNRs), nitrogen (N)-doping was achieved using melamine-formaldehyde resin (MF) as N precursor that was pre-coated on individual CNC nanorods. The highly-crosslinked porous network of MF resin not only introduced the desired N-doping to the carbon framework, but also generated ordered mesoporous structure during pyrolysis. Moreover, it served as a pivotal role in protecting and stabilizing the structural integrity of the rod-shaped CNCs and preserved the fibrous morphology at high enough temperatures for graphitization. The high surface area, abundant mesopores, and N-functionality make N-doped CNRs (NCNRs) promising candidate as electrode material for supercapacitors and metal-free catalyst.

The conductive NCNRs were further used as conductive carbon substrates for synthesizing supported metal nanoparticle (MNP) catalyst. However, carbon materials are generally unstable in water due to structural hydrophobicity and they also lack surface functionalities for effective stabilization of MNPs. Therefore, a bio-inspired polydopamine (PDA) polymerization on NCNR surface was performed to prepare NCNRs prior to the metal reduction step. PDA modification introduced strong chelation with metal/metal ions and dramatically increased the dispersibility of the supported metal composites, leading to improved reactant accessibility, higher catalytic activity and utilization efficiency of the metal catalysts. Both Pd and Pt nanoparticles as model metal nanoparticles of 1-2 nm were homogeneously reduced on PDA-NCNRs. The supported metal catalysts showed remarkable catalytic activity when used as catalyst for 4-nitrophenol reduction and oxygen reduction reactions. In addition, the electrode modified with prepared Pt/PDA-NCNRs displayed favorable sensing capability towards non-enzymatic glucose detection with very low overpotential in neutral media.

To the best of our knowledge, this work is among the very few pioneering studies that explore the potential of CNCs as highly conductive materials/composites for various electrochemical applications. This thesis unlocks many unexplored applications of CNCs and the findings will provide many sustainable alternatives for the next generation energy storage, electrocatalysts, and electrochemical sensors. It is also expected that this work will contribute to the revival of the forestry industry in Canada by enabling high value-added wood-derived products on the market in the near future.

Acknowledgements

I would like to express my first and foremost gratitude to my supervisor, Professor Michael K.C. Tam, for his guidance, inspiration and encouragement throughout my PhD career. He is always amazingly supportive and he encourages every student to pursue his/her own passionate research topic. At the early stages of my research, I was hesitant in pursuing my proposed research topic since it is somewhat non-conventional to this lab, and I also felt frustrated when things did not go as expected. However, he rebuilt the confidence in me and made me realize the significance of my work. He also spent much effort exploring the resources that I need for my research by reaching out to different labs on- and off-campus. I find him remarkably talented in research and discussing experimental challenges in our weekly one-on-one meetings is always a rewarding experience. He is willing to spend his personal time with his students by organizing various fun group activities, making the lab a wonderful workplace. It has been an incredible journey to be part of his research team and I have enjoyed every minute of it.

I would like to acknowledge Professor Aiping Yu, for generously sharing her lab facilities and knowledge with me to support my research in energy storage field. The achievements in this thesis would not have been realized and facilitated without this precious collaboration.

I would also like to extend my gratitude to my labmates. They are not only knowledgeable and helpful, but also sweet and fun to work with. They have been like a true family to me in Canada.

To my parents, for their unconditional love and support! They are the origin of my endless enthusiasm, motivation and determination.

Dedication

Dedicated to my beloved parents, Xuefei Xu and Xuguang Wu.

Table of Contents

LIST OF FIGURES	xii
LIST OF TABLE	xxii
CHAPTER 1 INTRODUCTION	1
1.1 RESEARCH BACKGROUND AND MOTIVATION	1
1.2 RESEARCH SCOPE AND METHODOLOGY	3
1.3 THESIS OUTLINE	4
CHAPTER 2 LITERATURE REVIEW.....	6
2.1 CELLULOSE NANOCRYSTALS (CNCs)	6
2.1.1 <i>General aspects of CNCs</i>	6
2.1.2 <i>Surface functionalization of CNCs</i>	10
2.1.3 <i>Applications of CNCs</i>	12
2.1.4 <i>Trends and general observations</i>	19
2.2 SUPERCAPACITOR (SP)	21
2.2.1 <i>Fundamentals of SP</i>	22
2.2.2 <i>Intrinsically conductive polymers (ICPs) as SP electrode</i>	26
2.2.3 <i>Carbon-based materials as SP electrode</i>	30
2.3 HETEROGENEOUS CATALYST FOR ELECTROCHEMICAL APPLICATIONS	35
2.3.1 <i>Fundamentals of heterogeneous catalyst</i>	35
2.3.2 <i>Metal nanoparticles/carbon (MNP/C) as supported electrocatalysts</i>	37
2.3.3 <i>Doped-carbon nanomaterials as metal-free electrocatalyst</i>	41
2.3.4 <i>MNPs supported by mesoporous carbon for electrode modification and electrochemical sensing</i>	43
CHAPTER 3 CHARACTERIZATION	47
3.1 MATERIAL CHARACTERIZATION.....	47
3.1.1 <i>Electron microscope (EM) for imaging</i>	47
3.1.2 <i>Spectroscopic techniques</i>	50
3.1.3 <i>CHNS Elemental analysis</i>	55

3.1.4 Zeta potential (ζ -potential)	56
3.1.5 Thermal dynamic analysis (TGA)	57
3.1.6 Brunauer-Emmett-Teller (BET) surface area analysis	58
3.2 ELECTROCHEMICAL CHARACTERIZATION	59
3.2.1 Four-point probe conductivity measurement	59
3.2.2 Half-cell design.....	60
3.2.3 Cyclic voltammetry (CV) and galvanostatic charge-discharge (CD)	62
3.2.4 Electrochemical impedance spectroscopy (EIS).....	63
3.3 CATALYTIC ACTIVITY MEASUREMENTS	63
3.3.1 4-nitrophenol (4-NP) reduction reaction	63
3.3.2 Catalytic oxygen reduction reaction (ORR) tests	65
CHAPTER 4 COST-EFFECTIVE AND SCALABLE CHEMICAL SYNTHESIS OF CONDUCTIVE CELLULOSE NANOCRYSTALS FOR HIGH-PERFORMANCE SUPERCAPACITORS	70
4.1 INTRODUCTION	70
4.2 EXPERIMENTAL SECTION	72
4.2.1 Materials	72
4.2.2 Methods.....	73
4.2.3 Characterization.....	73
4.3 RESULTS AND DISCUSSION	74
4.3.1 Properties of PPy/Tempo-CNC nanocomposite	74
4.3.2 Effect of Py/OH ratio on PPy coating and the electrochemical properties	77
4.3.3 Comparison of specific capacitance (C_s) with other electrode materials.....	83
4.4 CONCLUSION	84
CHAPTER 5 CONDUCTIVE CELLULOSE NANOCRYSTALS WITH HIGH CYCLING STABILITY FOR SUPERCAPACITOR APPLICATIONS.....	85
5.1 INTRODUCTION	85
5.2 EXPERIMENTAL SECTION.....	87
5.2.1 Materials	87

5.2.2 Synthesis of PPy/PVP/CNC hybrid nanostructure	87
5.2.3 Characterization.....	88
5.3 RESULTS AND DISCUSSIONS	89
5.3.1 Effect of surface modification with PVP on PPy growth	89
5.3.2 Effect of PVP modification on electrochemical behaviour of PPy/PVP/CNC	93
5.3.3 Comparison of PPy/PVP/CNC and PPy/TempoCNC.....	95
5.4 CONCLUSION	97

CHAPTER 6 NITROGEN-ENRICHED POROUS CARBON NANORODS TEMPLATED BY CELLULOSE NANOCRYSTALS AS HIGH PERFORMANCE SUPERCAPACITOR ELECTRODE

6.1 INTRODUCTION	98
6.2 EXPERIMENTAL SECTION	100
6.2.1 Materials	100
6.2.2 Synthesis of NCNR.....	100
6.2.3 Characterization.....	101
6.3 RESULTS AND DISCUSSION	102
6.3.1 Characterization of MFCNC composite	102
6.3.2 Effect of pyrolysis temperature on physiochemical properties of NCNRs	105
6.3.3 Effect of pyrolysis temperature on electrochemical behavior of NCNRs.....	107
6.3.4 Comparison of supercapacitive performance of NCNRs with other works.....	111
6.4 CONCLUSION	112

CHAPTER 7 N-ENRICHED MESOPOROUS CARBON DERIVED FROM BIOMASS AS METAL-FREE CATALYST

7.1 INTRODUCTION	113
7.2 EXPERIMENTAL SECTION	115
7.2.1 Materials	115
7.2.2 Synthesis of NCNR.....	115
7.2.3 Characterization.....	116
7.3 RESULTS AND DISCUSSION	117

7.3.1 Material characterization	117
7.3.2 Catalytic activity in 4-NP reduction reaction.....	120
7.3.3 Electrocatalytic activity in ORR	121
7.4 CONCLUSIONS.....	124
CHAPTER 8 POLYDOPAMINE-MODIFIED N-DOPED MESOPOROUS CARBON DERIVED FROM BIOMASS FOR SUPPORTING HIGHLY DISPERSED METAL NANOCATALYSTS	125
8.1 INTRODUCTION	125
8.2 EXPERIMENTAL SECTION.....	127
8.2.1 Materials	127
8.2.2 Synthesis.....	127
8.2.3 Characterization.....	128
8.3 RESULTS AND DISCUSSION	130
8.3.1 Material characterization	130
8.3.2 Catalytic activity of Pd/PDa-NCNR in 4-NP reduction reaction	133
8.3.3 Catalytic activity of Pt/PDa-NCNR in ORR	135
8.4 CONCLUSIONS.....	138
CHAPTER 9 HIGHLY DISPERSED PT SUPPORTED BY N-DOPED MESOPOROUS CARBON FOR ULTRASENSITIVE NON-ENZYMATIC GLUCOSE SENSING	139
9.1 INTRODUCTION	139
9.2 EXPERIMENTAL SECTION.....	141
9.3 RESULTS AND DISCUSSION	142
9.4 CONCLUSION	145
CHAPTER 10 CONCLUSIONS AND RECOMMENDATION FOR FUTURE STUDIES	146
10.1 CONCLUSION AND CONTRIBUTIONS	146
10.2 FUTURE WORK	148
REFERENCES.....	150

List of Figures

Figure 2.1 The hierarchical structure of wood from the tree down to the cellulose molecule. (Moon et al., 2011)	7
Figure 2.2 Schematics showing steps of CNC extraction and illustration of a NFC consisting of ordered crystalline region (i.e. CNC) and disordered amorphous regions. (modified from http://cranstongroup.mcmaster.ca/) (Moon et al., 2011).	7
Figure 2.3 TEM images of cellulose nanocrystals derived from (a) tunicate (b) bacterial (c) ramie and (d) sisal, and (e) Images taken for the 1% wt dispersion of cellulose nanofibers before and after acid hydrolysis (after 3 months), and the illustrate of CNCs showing the negatively charged sulfate groups obtained from sulfuric acid hydrolysis. (Elazzouzi-Hafraoui et al., 2008; Roman & Winter, 2004; Habibi et al., 2008; Garcia de Rodriguez et al., 2006; Li et al., 2015)	8
Figure 2.4 (a) Illustrate of an individual cellulose nanocrystal packed with cellulose chains and (b) structure of repeating anhydroglucoside (AGU) units that constitute the cellulose chains where different positions of carbons are labeled.	10
Figure 2.5 Common chemical modifications of cellulose nanocrystals. [PEG: poly(ethylene glycol); PEO: poly(ethylene oxide); PLA: poly(lactic acid); PAA: poly(acrylic acid); PNIPAAm: poly(N-isopropylacrylamide); PDMAEMA: poly(N,N-dimethylaminoethyl methacrylate)]; PTHF: poly(tetrahydrofuran) and PPGBE: poly(propylene glycol) monobutyl ether]. (Lin et al., 2012).....	11
Figure 2.6 (a) Illustrate of preparing silica iridescent films templated by cellulose nanocrystals, (b) photographs of mesoporous silica films from various initial silica to CNC ratios exhibiting different colors and (c) Transmission spectra representing various colored films shown in (b). (Shopsowitz et al., 2010)	13

Figure 2.7 (a) Procedure of preparing TiO ₂ films using mesoporous silica films templated by chiral nematic cellulose nanocrystals and photograph showing the resultant TiO ₂ films viewed under a left-handed circular polarizing filter (Shopsowitz et al., 2012b); (b) Procedure for preparing porous carbon films using chiral nematic silica-cellulose nanocrystal composite films, the photograph of the resultant carbon films, and the SEM image showing the long-range chiral nematic order formed by rod-like particles in the film. (Asefa, 2012)	14
Figure 2.8 (a) Schematic describing the role of CTAB in the formation of metal nanoparticles on cellulose nanocrystals. TEM images of cellulose nanocrystal supported (b) Ag (c) Cu (d) Au and (e) Pt nanoparticles.....	16
Figure 2.9 Schematic showing of the role of polysaccharide nanocrystals in (a) inhibiting drug diffusion and (b) forming extra physical crosslinking with alginate matrix; SEM images of (c) CNC/alginate bead (d) CHW/alginate bead and (e) SNC/alginate bead. (Lin et al., 2011b)..	18
Figure 2.10 Chart showing the exponential growth of CNC-related publications from 2004 to 2014. (Source: Lux Research, Inc.).....	19
Figure 2.11 Applications of CNCs under investigation industrially (modified from ArboraNano annual report 2014-2015).....	21
Figure 2.12 Schematic of (a) a conventional capacitor and (b) a supercapacitor.	22
Figure 2.13 Ragone plot of energy storage devices. (Kötz & Carlen, 2000).....	23
Figure 2.14 Taxonomy of supercapacitors. (https://commons.wikimedia.org/wiki/File:Supercapacitors-Overview.png)	24
Figure 2.15 Typical conductive polymers and their chemical structures.	27
Figure 2.16 General accepted polymerization scheme for polypyrrole. (Jang, 2006).....	28
Figure 2.17 Oxidation and reduction of PPy	29

Figure 2.18 (a) Strategies for preparing porous carbons of tunable pore sizes using colloidal silica as hard template, and SEM images of mesoporous carbon materials produced with pore sizes of 25 nm (b) and 68 nm (c)) synthesized using silica particles of different sizes (Chai et al., 2004).....	32
Figure 2.19 Five-step synthesis of mesoporous carbon nanostructure templated by tri-block copolymer PEO-PPO-PEO. (Meng et al., 2005).....	33
Figure 2.20 ‘In situ’ heteroatom doping using nanocasting method. (Daems et al., 2014).....	35
Figure 2.21 Illustrate of 4-step heterogeneous catalytic reaction of $C_2H_4 + H_2 \rightarrow C_2H_6$ by nickel (a) Hydrogen is adsorbed on the surface, breaking the H–H bonds and forming Ni–H bonds. (b) Ethylene is adsorbed on the surface, breaking the π -bond and forming Ni–C bonds. (c) Atoms diffuse across the surface and form new C–H bonds when they collide. (d) C_2H_6 molecules escape from the nickel surface, since they are not strongly attracted to nickel. (http://chemwiki.ucdavis.edu/)	36
Figure 2.22 HRTEM images of (a) Pt/CNF and (c) Pt/N-CNF. The corresponding particle size histograms based on the measurement of over 200 Pt NPs are provided in (b) Pt/CNF and (d) Pt/N-CNF.....	40
Figure 2.23 Illustrate for the atomic structure of a N-doped carbon.(Daems et al., 2014).....	42
Figure 2.24 Cyclic voltammetry of (a) bare glassy carbon electrode (GCE) and (b) mesoporous carbon modified GCE in pH 7.4 phosphate buffer solution without (dotted line) and with (solid line) the mixture of 0.25 mM ascorbic acid (AA), 0.25 mM dopamine (DA) and 0.5 mM uric acid (UA) at a scan rate is 100 mV s ⁻¹ . (Zheng et al., 2009)	44
Figure 3.1 Illustrate of the phenomena induced by electron beam-sample interaction. (source: Wikipedia)	47

Figure 3.2 (a) SEM layout and function (b) scheme of topological contrast and (c) example of a typical SEM image reflecting surface topography of the mineral sand. (Source: http://li155-94.members.linode.com/myscope/).....	48
Figure 3.3 Comparison of images for polymer cubosomes using (a) TEM imaging showing the internal structure and where magnified lattice configuration was resolved in (b), and (c) SEM imaging providing a wider view of the samples with inset showing the topography of one cubosome.(La et al., 2014).....	50
Figure 3.4 The electromagnetic spectrum showing the boundaries between different regions and the type of atomic or molecular transition responsible for the change in energy. The colored inset shows the visible spectrum. (www.chemwiki.ucdavis.edu).....	51
Figure 3.5 (a) Four types of possible electronic transitions in molecules and (b) An UV-vis spectrum of tetraphenylcyclopentadienon. (http://plasticphotovoltaics.org)	52
Figure 3.6 (a) Illustrate of the process of photoelectric effect, (b) typical configuration of XPS instrument (source: http://www.tut.fi/en/home) and (c) XPS spectra of an oxidized InAs surface (source: http://biointerface.org/surface/xps/).	55
Figure 3.7 The functional diagram of a typical CHNS elemental analyzer. (Source: Elementar Americas Inc.).....	56
Figure 3.8 Illustration showing (a) zeta potential of a negatively charged particle in a suspension and (b) micro-electrophoresis system is a cell with electrodes. (Source: zetasizer nanoseries user manual).....	57
Figure 3.9 (a) Photos of TGA instrument showing the core units and (b) example of TGA measurement for calcium oxalate monohydrate showing both TG (red) and DTG (blue) curves. (Source: TA instrument user manual and Philips Research bulletin).....	57
Figure 3.10 The IUPAC classification of isotherms. (McCusker et al., 2001).....	59

Figure 3.11 (a) Diagram of four-point probe conductivity measurement and (b) equivalent circuit for four-point probe setup.....	60
Figure 3.12 Illustration of a three-electrode electrochemical cell and the glassy carbon working electrode. (http://chemwiki.ucdavis.edu/ ; Lowinsohn et al. 2014)	61
Figure 3.13 (a) Typical shape of Nyquist plot from EIS test and (b) equivalent circuit from simulation. (Pyun et al., 2012)	63
Figure 3.14 (a) Proposed mechanism for the reduction of 4-NP to 4-AP by Au NP in the presence of NaBH ₄ based on Langmuir-Hinshelwood model, (b) example of typical spectra from UV measurement during 4-NP reduction and (c) Plot obtained from spectra in (b) to calculate the rate constant of the reaction.(Zhao et al., 2015b; Li et al., 2013d).....	64
Figure 3.15 (a) Pine AFMSRX electrode rotator (inset: a rotating ring-disk electrode) and (b) typical electrochemical testing cell for ORR.(source: Pine Instrumentation Inc.)(Hong et al., 2015)	66
Figure 3.16 (a) Typical ORR polarization curves catalyzed by Pt/C solution at the different rotation speeds, and (b) corresponding K-L plots at various disk potentials.(Tiwari et al., 2013)	68
Figure 3.17 Example of cyclic voltammetry in ORR test to calculate electrochemically active surface area.....	69
Figure 4.1 (a) In situ chemical oxidation polymerization for the synthesis of PPy/CNC nanostructures; (b) Color change of the reacting solution during the polymerization process.	74
Figure 4.2 (a) Comparison of a pure PPy suspension with visible flasks (left) and a homogenous PPy/CNC suspension (right); (b) Freeze-dried sample of pure PPy in the form of random flakes(top) and PPy/CNC in the form of powder (bottom); (c) TEM images of TEMPO-CNC and (d) PPy/CNC at Py/OH = 16.	75

Figure 4.3 SEM image for (a) Pure PPy using bulk synthesis without adding CNC (b) PPy/CNC polymerized with Py/OH molar ratio of 16, the insert is the zoom-in HRSEM for a single nanorod of PPy/CNC; (c) PPy/CNC polymerized with Py/OH molar ratio of 50, showing thick PPy coating evolving from rod shape into spherical shape.....	76
Figure 4.4 (a). Dynamic change of zeta potential of PPy/CNC particles during polymerization; (b). TGA curves of TEMPO-CNC (green line) and PPy/CNC (red line) with Py/OH =16 and bulk PPy (black line).	76
Figure 4.5(a) Effect of feeding ratio of Py/OH on the conductivity of PPy/CNC, (b) An illustration of how conductive PPy/CNC (black sheet pressed from PPy/CNC powder prepared at Py/OH =16) can conduct electricity in a circuit to light the bulbs.....	78
Figure 4.6 (a) FT-IR; (b) Raman Scattering; (c) UV-Vis spectra of PPy/CNC system synthesized with various Py/OH ratios of 1:1, 2:1, 4:1, 8:1, 12:1, 16:1, 25:1, and 50:1.....	80
Figure 4.7 (a) CV curves of PPy/CNC prepared with different Py/OH feeding ratios at scan rates of 0.01 V/s, 0.05 V/s and 0.1 V/s. (b) Effect of Py/OH on the capacitance of PPy/CNC; (c) Charge and discharge test at different charge currents of 1A/g, 2A/g, and 5A/g for PPy/CNC where Py/OH = 16.	82
Figure 4.8 Nyquist plots obtained from EIS for different PPy/CNC samples in 0.5 M KCl where Py/OH=4, 8, 16, 25, 32 respectively.....	83
Figure 5.1 Schematic illustrating the formation of proposed core-shell PPy coated CNC. PVP was adsorbed onto the CNC surface prior to the polymerization to promote the homogeneous growth of PPy shell.	88
Figure 5.2 TEM images for (a) pristine CNC; (b) PPy/PVP100/CNC; (c) PPy/PVP40/CNC; (d) PPy/PVP10/CNC; (e) PPy/PVP5/CNC; (f) PPy/PVP0/CNC.....	90

Figure 5.3 TGA curve for Pristine CNC, PPy, PPy/PVP100/CNC, PPy/PVP10/CNC, PPy/PVP0/CNC. All samples were placed in an inert ceramic crucible and heated from 25 to 800 °C at a heating rate of 10°C/min in 20 mL/min in air atmosphere.	90
Figure 5.4 PPy polymerization in the presence of equal amounts of pristine CNCs and PVP/CNCs with cartoon illustrating the two drastically different morphologies of the end products.	91
Figure 5.5 (a) The effect of the degree of surface modification on CNC on the zeta-potential and conductivity of the hybrid material of PPy/PVP/CNC after polymerization, and (b) Kinetic study: the effect of polymerization time on the conductivity and zeta-potential of PPy/PVP10/CNC. TEM image shows the morphology of PPy/PVP10/CNC sample under polymerization time of 24 hours.	92
Figure 5.6 (a) Specific capacitance from CV test for PPy/PVP10/CNC polymerized at different time intervals. The FESEM image shows the porous structure formed by drop casting PPy/PVP10/CNC solution on the working electrode. (b) charge-discharge curves of PPy/PVP10/CNC electrode at different current densities. (c) Cycling performance of the PPy/PVP10/CNC electrode at the current density of 10 A g ⁻¹ . The inset shows the charge-discharge curves of the last 10 cycles.	94
Figure 5.7 (a) CV curve of different cycles for sample PPy/TempoCNC during 1000 cycles at 0.1 V/s scan rate. The TEM image shows the typical morphology of PPy/Tempo-CNC. (b) CV curve of different cycles for sample PPy/PVP/CNC during 1000 cycles at 0.1 V/s scan rate. The TEM image shows the typical morphology of PPy/PVP/CNC. (c) Comparison of Capacitance loss between PPy/PVP10/CNC and PPy/Tempo-CNC (d) Proposed mechanism that PVP layer as a binder releases the stress and provides better accommodation for the conformational change for PPy during cycling.	96
Figure 6.1 Schematic of 2-step synthesis of nitrogen-doped carbon nanorods.	100

Figure 6.2 (a) FTIR characterization for the freeze-dried MFCNC and CNC powder, and (b) TGA measurement for MF resin, MFCNC and CNC under N ₂	103
Figure 6.3 (a) TEM image for pristine CNCs, (b) High resolution TEM for pristine CNCs with uranyl acetate staining, and TEM images for (c) MFCNCs, (d) NCNR800, (e) NCNR 900, and (f) NCNR 1000.....	103
Figure 6.4 (a) XRD and (b) RAMAN spectra characterization for N-MFCNC prepared at various carbonization temperatures	105
Figure 6.5 (a) N ₂ adsorption/desorption isotherms and (b) the corresponding PSDs of samples carbonized at different temperatures.	107
Figure 6.6 (a) Cyclic Voltammetry curves for NCNR800, NCNR900, NCNR1000 with the same scan rate of 0.01 V/s; (b) Capacitance retention profiles with increasing scan rates for NCNR800 NCNR900 and NCNR1000; (c) Cyclic Voltammetry curves for NCNR900 at various scan rates; and (d) Charge/discharge curves for NCNR900 at various current density.	108
Figure 6.7 (a) Stability test for NCNR900 at 20 A/g charge/discharge rate for 2000 cycles, and (b) electrochemical Impedance Spectroscopy for NCNR800 NCNR900, NCNR1000 under 5 mV (AC voltage).	109
Figure 6.8 (a) CV for NCNR900 with the scan rate of 0.01 V s ⁻¹ , 0.05 V s ⁻¹ and 0.1 V s ⁻¹ in 2M KCl; (b) CV for NCNR900 with the scan rate of 0.01 V s ⁻¹ , 0.05 V s ⁻¹ and 0.1 V s ⁻¹ in 6M KOH; (c) CV for NCNR800,NCNR900, and NCNR1000 at the same scan rate of 0.01 V s ⁻¹ in 2M KCl; (d) CV for NCNR800,NCNR900, and NCNR1000 at the same scan rate in 6M KOH; (e) Cycling stability in 2M KCl electrolyte of NCNR900 at 20 A g ⁻¹ current density and (f) Cycling stability test in 6M KOH electrolyte for NCNR900 at a 20 A/g current density.....	111
Figure 7.1 Strategy for preparing mesoporous nitrogen-doped carbon nanorods (NCNR).....	116

Figure 7.2 (a) HRTEM image for pristine CNCs, and TEM images for (b) MFCNCs, (c) NCNRs and (d) cMeCNC	118
Figure 7.3 (a) FTIR spectra for pristine CNC, MFCNC and NCNR sample, and (b) N ₂ adsorption/desorption isotherms for sample NCNR in comparison with and cMeCNC. Inset: the comparison of pore size distribution between NCNR and cMeCNC.	119
Figure 7.4 (a) Time-dependent UV-vis spectra of 4-nitrophenol reduction catalyzed by NCNR and (b) Plot of adsorption intensity A of peak at 400 nm and ln(A/A ₀) against the reaction time t for 4-nitrophenol reduction catalyzed by NCNR.....	121
Figure 7.5 ORR performance of N-CNR: (a) CV curves under both N ₂ and O ₂ saturated 0.1 mol L ⁻¹ KOH; (b) LSV curves under different rotating speeds; (c) Koutechy-Levich plots under different potential vs RHE with transferred number of electrons (insert plot); and (d) Tafel plot.	123
Figure 7.6(a) High resolution XPS spectrum of N 1s and the structure of different nitrogen species; (b) composition of nitrogen species in N-CNR.....	124
Figure 8.1 Schematic of our experimental strategy for preparing Pt and Pd heterogeneous nanocatalysts supported by PDa-NCNR.....	127
Figure 8.2 (a) HRTEM image for pristine CNCs, and TEM images for (b) MFCNC (c) NCNR and (d) PDa-NCNR. Inset of (c) and (d) shows the particle dispersion over 1 hour.	130
Figure 8.3 TEM images of (a) Pt/PDa-NCNR (b) Pt/NCNR (c) Pd/PDa-NCNR (d) Pd/NCNR and comparison of dispersion stability after 3 months undisturbed (e) Pt/Pda-NCNR(left) and Pt/NCNR(right), and (f) Pd/Pda-NCNR (left) and Pd/NCNR(right).....	131
Figure 8.4 (a) XRD and (b)TGA characterization in N ₂ flow of Pt/PDa-NCNR and Pd/PDa-NCNR and the N 1s XPS high resolution spectrum of (c) NCNRs and (d) Pt/PDa-NCNRs	132

Figure 8.5 The plot of $\ln (A_t/A_0)$ against time for the reduction of 4-NP at 298 K catalyzed by Pd/PDa-NCNR. Inset: The time-dependent absorption spectra of the 4-NP reduction reaction catalyzed by Pd/PDa-NCNR.....	134
Figure 8.6 The ORR activity comparison of Pt/PDa-NCNR with commercial Pt/C in (a) cyclic voltammetry, (b) ECSA, (c) polarization curves and (d) potential as functions of different catalytic activities (kinetic current, mass activity and specific activity).....	136
Figure 8.7 Cyclic voltammetry curves (a), ORR polarization curves (b) and the summary of ECSA, mass and specific activities at 0.9 V vs. RHE before and after 3000 cycles in ADT test for Pt/PDa-NCNR with commercial Pt/C.....	138
Figure 9.1 (a) CV of Pt/PDa-NCNR in 1xPBS (pH 7.4) containing glucose in the range of 0-30 mM at 100mV/s scan rate. The arrow shows the increasing of the peak current and the shifting of peak potential with increasing glucose concentration, and (b) Amperometric current response of Pt/PDa-NCNR in 1mM Glucose, 0.02 mM Ascorbic acid (AA), and 0.02 mM Uric Acid (UA) solutions (1x PBS pH 7.4, continuously stirred, N ₂ purged) at varying voltages with inset showing amperometric current measured at +0.28V in response to an addition of 0.02 mM AA, 0.02 mM UA, and 1mM glucose.....	143
Figure 9.2 (a) Amperometric current response of the Pt/PDa-NCNR upon successive addition of glucose at +0.28 V in 1xPBS (7.4 pH). Inset: Glucose response time, and (b) calibration curve displaying 2 linear ranges: 0.01 mM to 2 mM and 2 mM to 30 mM Inset: Lower concentration linear range between 0.01 mM and 1.2 mM glucose.....	144
Figure 10.1 Summary of research topics in this work.....	148

List of Table

Table 2.1 Comparison of CNC and other materials in the key physical parameters. (http://people.forestry.oregonstate.edu/john-simonsen/research-areas).....	9
Table 4.1 Capacitance measured in different studies on Single-walled carbon nanotube (SWCT), Multi-walled carbon nanotube (MWCT) , PPy-coated MWCT, graphene sheet, hybrid nanostructure of PPy/graphene and CNC/PPy fabricated using a) in situ chemical polymerization method in our work b) Electrochemical co-deposition method(An et al., 2001; Frackowiak et al., 2000; Zhang et al., 2011; Li et al., 2011; Han et al., 2010; Liew et al., 2013)	84
Table 5.1 Comparison in synthesis and key characterizations of the improved PPy/PVP/CNC and PPy/TempoCNC system.....	95
Table 6.1 Summary of physicochemical characterization by BET and the composition of various N- MFCNCs by elemental analysis.....	106
Table 6.2 Summary of capacitance performance of MFCNC 800 MFCNC900 MFCNC1000 in neutral, alkaline and acidic electrolytes.....	110
Table 6.3 Comparison of the Cs value of various N-doped Carbon Systems reported in recent years.	112
Table 7.1 Summary of the surface area and pore properties from BET measurement for CNC, MFCNC, cMeCNC and NCNR samples.....	120
Table 8.1 Comparison of the catalytic performance and origins of Pd nanocatalyst supported on various substrates for 4-NP reduction	135
Table 9.1. Comparison of performance of Pt based non-enzymatic glucose sensors in neutral PH.	144

Chapter 1 Introduction

1.1 Research background and motivation

The challenge and conflict between increasing human demands and the depletion of natural resources has become a major global challenge in the 21st century. Nanotechnology has emerged as a promising approach to address the sustainability issue in different fields using nano-sized materials that offer unprecedented efficiency and reactivity. (Diallo et al., 2014) Electrochemistry is one of the areas where nanotechnology has made the most profound impact. Many precisely engineered nanostructures with diverse compositions, properties and functionalities have been developed and they have revolutionized many industrial products: batteries that are lighter yet more powerful, consumer electronics that are more portable and flexible, vehicles that are driven by cleaner energy etc. It is expected that nanotechnology will continue to inspire new innovations in a wide range of electrochemical applications, such as catalysts, energy storage and conversion, sensors, etc.

With science and technology at the nanoscale progressing rapidly, critical new challenges appear that are associated with the toxicity and non-recyclability of nanomaterials, raising both public health and environmental concerns. Time and high energy processing techniques also greatly hinder the industrialization of the products. We will outline some examples of some challenges when applying nanotechnology in electrochemical field, and they constitute the driving force for the research reported in this thesis.

Carbon-based nanomaterials, carbon nanotube (CNT), graphene (G) and active carbon, are the most popular candidates for various electrochemical applications due to their good conductivity, high surface area, mechanical robustness, chemical inertness, and wide availability. However, the high manufacturing cost, low yield and toxicity of CNT and G are widely recognized as serious drawbacks.(Zurutuza & Marinelli, 2014; Liu et al., 2013b) Further problems are associated with poor utilization of the active surface area due to material stacking or agglomeration during processing.(Georgakilas et al., 2012) Active carbons possess many challenges in their fabrication such as the necessities to go through energy-consuming heat treatment up to thousands of degrees, adding corrosive reagent for the activation process (e.g. KOH), using nonrenewable resources as carbon sources. The regeneration of nanosized active carbon is also difficult. (Wang et al., 2009b; Ahmadpour & Do, 1996) In the field of energy storage, many nanostructured carbons with high surface area and interconnected pores are ideal candidates as supercapacitor electrode materials.

However, current strategies to achieve the desired surface area and porosity in carbon structure often involve the use of exotic hard templates, expensive surfactants, high-cost polymeric carbon sources and complicated procedures. (Hou et al., 2005; Fang et al., 2009; Meng et al., 2006). Because of this, their mass production is extremely difficult. In the field of electrocatalyst, three general trends have appeared: (1) to enhance the utilization efficiency of expensive metal catalysts (2) to replace noble metals with non-noble ones, and (3) to replace metal catalyst with metal-free substitutes. Downscaling conventional metals to the nano-size regime is an effective approach to enhance the utilization efficiency of metal catalysts. However, due to the high surface free energy, MNPs have the tendency to grow during synthesis and they further agglomerate during catalytic reaction, resulting in a significant loss of catalytic sites. The small size of MNPs also impose regeneration problem, leading to economic waste and secondary pollution. In this context, supported metal catalyst has emerged as a promising solution and it enables highly dispersed MNPs with smaller sizes to be synthesized on a suitable solid substrate. The ideal substrate material should have sufficient mechanical strength, high surface area, porosity, certain surface interaction with MNPs and conductivity (for electrocatalyst). Carbon nanomaterials have shown great promises in the past for supporting metals. However, these materials have poor stability against precipitation in water, resulting in limited solution accessibility to the active sites. They also lack surface functionalities for efficient impregnation of metal ions, and the stabilization of MNPs. Facing the challenges mentioned above, changes have to be made such as using alternative nanomaterials that leave the minimal environmental footprint, applying more effective ways of tuning the material properties, and exploring simpler techniques for mass production.

As a new class of nanomaterial that comes from renewable biomass, cellulose nanocrystals (CNCs) can be readily extracted from cellulose, the most abundant biopolymer on earth. The growing interest in CNC is mainly due to the many attractive features include, (i) high dispersion stability in water; (ii) superior mechanical strength yet low in weight, (iii) high aspect ratio and large specific surface area, and (iv) enriched surface functional groups. (Peng et al., 2011; Zaman et al., 2012; Moon et al., 2011; Ly et al., 2008; Berry et al., 2010) All the above features make CNC a promising reinforcing nanomaterial, or a versatile substrate for many chemical/physical modifications to achieve the desired functionalities. Current interests in CNCs are mainly focused on applications, such as reinforcing agents in polymer matrix and textiles, anticounterfeiting films, wound dressings, drug delivery, filtration membranes, and personal care formulations. (Peng et al., 2011) The use of CNCs is expected to offer a green alternative to replace CNTs in reinforcing applications. Recently, there are several programs established worldwide to produce CNCs at an industrial scale. Canada

has taken the lead and commissioned the world's first demonstration plant using a continuous process capable of producing 1000 kg per day of CNC. The industrialization of CNCs offers tremendous impetus to the wide application and commercialization.

Thus far, limited attention was paid to applying CNCs in electrochemical applications, which is understandable mainly because CNCs are insulating in nature. However, it should be emphasized that CNC itself has great potential to be made highly functional and CNCs with electrochemical properties (conductivity, capacitance, etc.) would be an appealing alternative to replace conventional conductive materials in many electrochemical applications.

1.2 Research scope and methodology

As discussed above, this thesis focuses on the development of conductive CNC systems for electrochemical applications. The spirit of 'green' nanotechnology (Karn, 2008) was exploited in our experimental design since we believe that it is crucial for both sustainability and industrialization. For instance, harsh chemical modification of CNCs is strictly limited, and they are achieved through either physical interactions or using simple and green chemistry. The following summarize the guidelines for experimental design: 1) using renewable resources wherever possible 2) adopting energy efficient processing 3) avoiding toxic chemicals and 4) incorporating life cycle strategies in product design and engineering.

Herein, the specific research scope is outlined below:

- Synthesis of hybrid material of polypyrrole (PPy) and CNC nanocomposite for supercapacitor applications**

PPy, an intrinsically conductive polymer, was combined with CNCs to introduce the desired electrochemical functionalities. PPy was formed by in-situ polymerization on the surface of individual CNC to form a homogeneous conductive coating. The effect of various experimental parameters on the polymer growth and electrochemical properties was investigated in detail. Further supercapacitive performance was evaluated by comparing with other popular electrode materials.

- Fabrication of nitrogen(N)-doped mesoporous carbon nanorods (NCNRs) for supercapacitor applications**

CNCs served as carbon precursor and non-sacrificing template to control the carbonized nanostructure. Melamine-formaldehyde resin (MF) as N precursor was first polymerized and condensed on the surface of CNC before pyrolysis. The effect of carbonization temperature on the obtained carbon structure as well as its supercapacitive performance were characterized in detail.

- **NCNRs as novel platform for supported metal electrocatalyst and electrochemical sensor**

The prepared NCNCs were used as a substrate to assist in the reduction and immobilization of MNPs for electrocatalytic application. Simple chemical modification was conducted on NCNRs to enhance the interaction with metals and improving the dispersability of the hybrid catalyst composite. Pt and Pd NPs as model metals were reduced onto modified NCNRs to validate the strategy. The catalytic activity of supported Pt or Pd catalysts were evaluated by catalyzing 4-nitrophenol (4-NP) reduction reaction and oxygen reduction reaction (ORR). Moreover, supported Pt/NCNRs modified electrode was used as biosensor for detecting glucose.

- **NCNRs as metal-free catalyst**

The potential of NCNRs as metal-free catalyst was evaluated. NCNCs were used to catalyze both 4-NP reduction reaction and ORR. The results were compared with metal-based catalysts and similar carbon-based catalysts.

1.3 Thesis outline

This thesis consists of ten chapters. Chapter 1 provides an overview of the research background, and also introduces the research motivation and scope. Chapter 2 provides an in-depth literature review on cellulose nanocrystals (CNCs), which is the key material being investigated in this research followed by a literature review on the main research advances in supercapacitor and electrochemical catalysts. Chapter 3 describes the principles of several critical characterization techniques used in this research. Chapter 4 presents the synthesis and performance of conductive PPy/CNC as supercapacitor electrode material, and Chapter 5 summarizes the synthesis and performance of conductive PPy//PVP/CNC as supercapacitor electrode material. Chapter 6 presents the fabrication of N-doped mesoporous carbon nanorods (NCNRs) as supercapacitor electrode material, while Chapters 7 demonstrates the potential of NCNRs as metal-free catalyst, and Chapter

8 reports on the use of NCNRs as novel substrate to deposit and support MNPs as electrocatalysts. Chapter 9 presents the application of supported Pt electrocatalyst in glucose detection, and Chapter 10 concludes the major contributions in this thesis and provides suggestions for future work.

Chapter 2 Literature review

2.1 Cellulose Nanocrystals (CNCs)

2.1.1 General aspects of CNCs

Cellulose is the most abundant biopolymer on earth and, as a part of the biomass, can be renewed continuously through photosynthesis in quantities of the same order as the world reserves of minerals and fossil fuels (Klemm et al., 2004). Being readily available, cellulose-derived materials such as wood, cotton and paper have played an important role in our societies over thousands of years. Naturally occurring materials often develop their functionality, flexibility and mechanical strength by utilizing a hierarchical structure of building blocks, as exemplified for wood in Figure 2.1. At the most basic level of this hierarchy, cellulose in the cell wall provides reinforcement for trees, plants, algae and some sea creatures (e.g. tunicates). (Moon et al., 2011)

Cellulose nanocrystal (CNC) is the most rigid element constituting cellulose. The critical steps during the extraction of CNCs from the forest resources is illustrated in Figure 2.2. To extract cellulose fibers from wood, they must first be separated from other main components of the cell wall: hemicellulose and lignin. This is achieved in a pulping process where wood is chemically and/or mechanically disintegrated into discrete fibers.(Biermann, 1996) The resultant pulp fibers can then be further disintegrated into microfibrils, or microfibrillated cellulose (MFC), using high shear field homogenization.(Turbak et al., 1983) As MFC contains fibrils with nanoscale dimensions (fibril diameter: ~2–40 nm, fibril length: >1 μm), the terms nanofibrillated cellulose (NFC) or nanocellulose are also used. (Moon et al., 2011) These NFCs contain alternating amorphous region and crystalline regions as illustrated at the bottom of Figure 2.2. It is generally believed that the amorphous regions within cellulose fibers originated from chain dislocations on segments along the elementary fibril where microfibrils are distorted, tilted and twisted due to internal strain. (Rowland & Roberts, 1972) The widely adopted approach to isolate cellulose nanocrystals in the past decade are based on acid hydrolysis where the amorphous regions are preferentially hydrolyzed, and crystalline regions with higher resistance to acid remain intact. (Anglès & Dufresne, 2001) The process removes all the defects on the microfibrils, cleaves the cellulose fibers transversely, and produces rod-like CNCs, or elsewhere referred to as ‘cellulose whiskers’ cellulosic nanofibers’, etc. Vivid descriptions on the morphology of NFC and CNC are ‘spaghetti-like’ and ‘rice-like’ respectively, given by Prof. Emily Cranston. (<http://cranstongroup.mcmaster.ca/>)

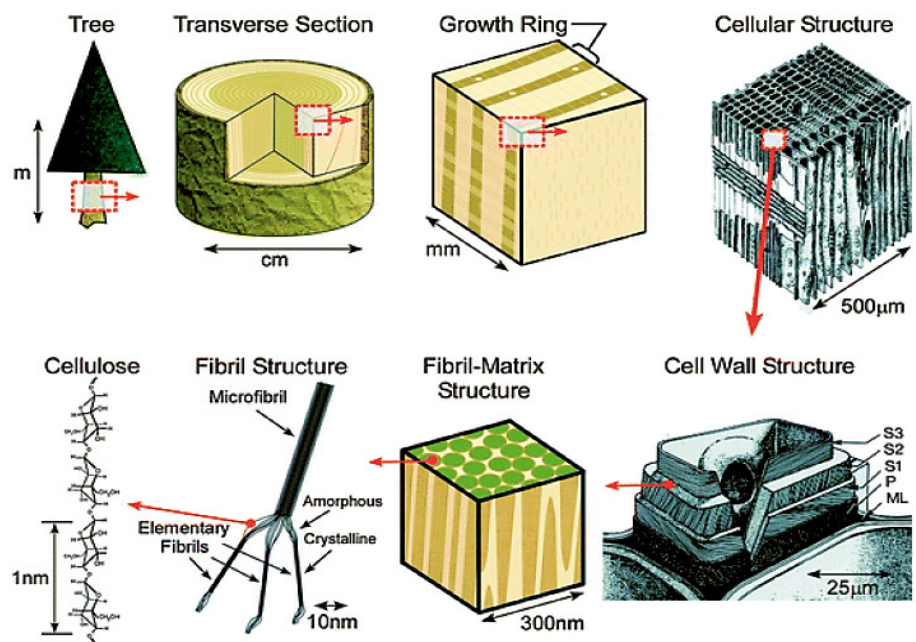


Figure 2.1 The hierarchical structure of wood from the tree down to the cellulose molecule. (Moon et al., 2011)

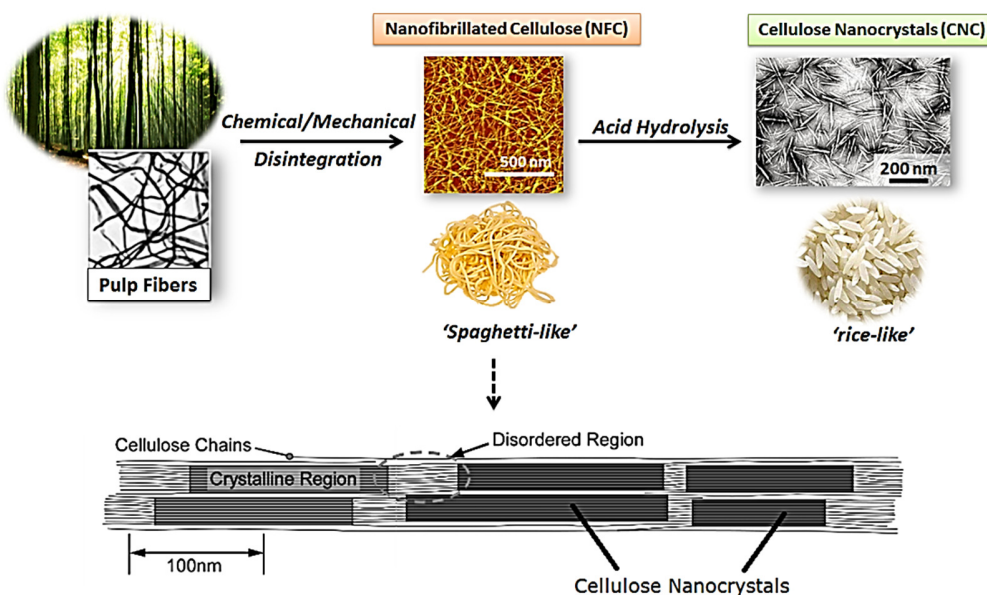


Figure 2.2 Schematics showing steps of CNC extraction and illustration of a NFC consisting of ordered crystalline region (i.e. CNC) and disordered amorphous regions. (modified from <http://cranstongroup.mcmaster.ca/>) (Moon et al., 2011).

CNCs are crystals with a high aspect ratio (L/d). The dimension of CNCs is dependent on diverse origins under different hydrolysis condition. (Habibi et al., 2010b) Figure 2.3(a)-(d) shows the TEM images for CNCs obtained from different sources via acid hydrolysis.

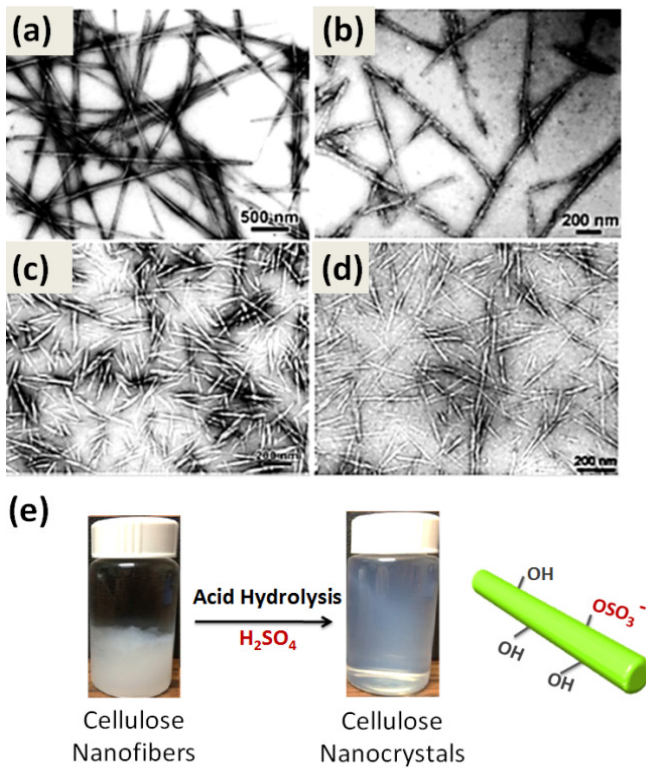


Figure 2.3 TEM images of cellulose nanocrystals derived from (a) tunicate (b) bacterial (c) ramie and (d) sisal, and (e) Images taken for the 1% wt dispersion of cellulose nanofibers before and after acid hydrolysis (after 3 months), and the illustrate of CNCs showing the negatively charged sulfate groups obtained from sulfuric acid hydrolysis. (Elazzouzi-Hafraoui et al., 2008; Roman & Winter, 2004; Habibi et al., 2008; Garcia de Rodriguez et al., 2006; Li et al., 2015)

Though other types of acid such as hydrochloric acid (Araki et al., 1998) have also been proposed, the most common condition today is to use 64 wt% sulfuric acid under hydrolysis temperature of 45 degrees for 25-45 min. (Habibi, 2014) It is also worth noting that when sulfuric acid is used as hydrolyzing agent, a spontaneous dispersion of CNCs in water can be obtained due to the strong negatively charged sulfate acid groups introduced onto the cellulose surface (Figure 2.3(e)). (Ranby, 1951) To clarify, the CNCs in our study are exclusively produced through the sulfuric acid hydrolysis of native pulp fibers, with a diameter of 2-5 nm and average length of 100-200 nm, provided by FPInnovations and Celluforce Inc.

As listed in Table 2.1 , CNC has a greater axial elastic modulus than the synthetic fiber Kevlar, and their mechanical properties are within the same range as those of other reinforcement materials such as carbon fibers, steel wires and carbon nanotubes (CNTs). (Moon et al., 2011)

Table 2.1 Comparison of CNC and other materials in the key physical parameters.

(<http://people.forestry.oregonstate.edu/john-simonsen/research-areas>)

Material	Density (g cm ⁻³)	Strength (GPa)	Longitudinal Modulus (GPa)	Transverse Modulus (GPa)
Kevlar	1.4	3.5	124-130	2.5
Carbon fiber	1.8	1.5-5.5	150-500	-
Steel wire	7.8	4.1	210-369	-
Clay nanoplatelets	-	-	170	-
Carbon nanotubes	-	11-63	270-950	0.8-30
Boron nanowhiskers	-	2-8	250-360	-
Cellulose nanocrystals	1.6	7.5-7.7	110-220	10-50

Besides being incredibly strong yet lightweight, many other attractive features of CNCs include, but are not limited to having: (i) high aspect ratio and specific surface area, (ii) dispersion stability in water, (iii) enriched surface active groups, (iv) low cost and abundance, (v) biodegradability and biocompatibility. Moreover, CNCs with asymmetric rod-like structure exhibit nematic behavior under certain conditions. It was observed that above a critical concentration, CNCs undergo an isotropic-to-anisotropic phase transition and rearrange themselves spontaneously into chiral nematic ordering (i.e. liquid crystalline phase). (Habibi et al., 2010b) The phenomenon can also be controlled in the presence of external stimuli (AC electric field, magnetic field etc.) (Fleming & Gray, 2000) All the above make CNC a promising reinforcing nanomaterial, or a functional nanomaterial for the fabrication of other hybrid nanostructures with enhanced properties. (Peng et al., 2011; Zaman et al., 2012; Moon et al., 2011; Ly et al., 2008) Upon their discovery, these smallest cellulose building blocks, have gained a tremendous level of attention from industry and it is the central focus of a wide array of research efforts for different applications. Canada is the pioneering country in carrying out CNC-related studies and has recently commissioned the world's first demonstration plant that has successfully achieved the production of CNC at 1000 kg per day. The industrialization of the CNCs becomes the key impetus to their wide application.

2.1.2 Surface functionalization of CNCs

A huge advantage of CNCs is the abundant hydroxyl groups (-OH) in their structure, providing enormous possibilities of various modification and functionalization. CNC is formed by cellulose chains stacking into a bundle with the smallest unit consisting of anhydroglucose (AGU) units (Figure 2.4). An understanding of the sequence of OH reactivity at different positions of AGU is helpful for the precise control on the degree of chemical modifications. It has been found that the reactivity of 6-OH on CNC is 10 times that of 2-OH, and 2-OH is twice active than 3-OH. (Lin & Dufresne, 2014) Moreover, due to the highly packed arrangement of cellulose chain forming each polysaccharide nanocrystal, only the OH groups on the surface should be considered active for chemical reaction rather than counting on the number of surface OH over all the cellulosic chains. It was estimated for CNCs that only 1/3 of the calculated -OH are exposed on the surface feasible for chemical modification and the amount is estimated to 0.0037 mol of -OH per gram of CNCs (Habibi et al., 2006, 2010b)

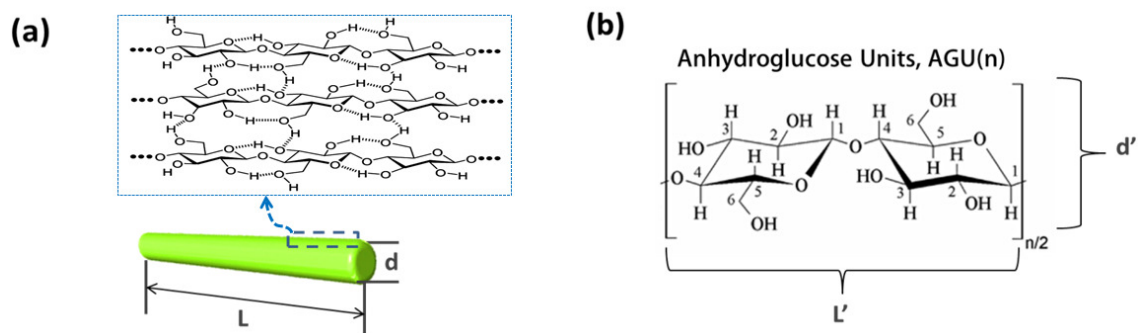


Figure 2.4 (a) Illustrate of an individual cellulose nanocrystal packed with cellulose chains and (b) structure of repeating anhydroglucose (AGU) units that constitute the cellulose chains where different positions of carbons are labeled.

Besides the naturally occurring -OH on CNCs, other types of surface functional groups can be introduced through different extraction methods. When sulfuric acid is used as the hydrolyzing agent, it reacts with the surface -OH groups of cellulose and convert them into negatively charged sulfate esters with an enhanced stabilization effect. (Dong, 1998) However, such conversion yield is rather low, only 0.85%, 0.76% and 0.8% of the sulfur elemental content was detected for dried CNCs extracted from sisal, ramie, and cotton. (Habibi et al., 2010a) It is also reported that when acid hydrolysis is performed with an acid mixture of hydrochloric acid and acetic acid, the CNC surface will be decorated with hydrophobic acetyl groups. (Braun & Dorgan, 2009)

The surface modification of CNCs can be achieved through both non-covalent interactions with various polymers and chemical reactions occurring on the surface –OH groups. Noncovalent approach is often achieved through the adsorption of surfactants or polyelectrolytes based on physical forces include electrostatic interaction, hydrogen bond, or van der walls force. (Habibi, 2014) While this approach is more convenient than chemical modification, it is mostly used for the purpose of improving the dispersion stability of CNCs in organic solvents and the compatibility with the polymer matrix or composite material. For example, CNCs modified with anionic and non-ionic surfactants have been found to better disperse in polylactic acid (PLA) and polystyrene-based composite fibers respectively. (Bondeson & Oksman, 2007; Kim et al., 2009; Rojas et al., 2009)

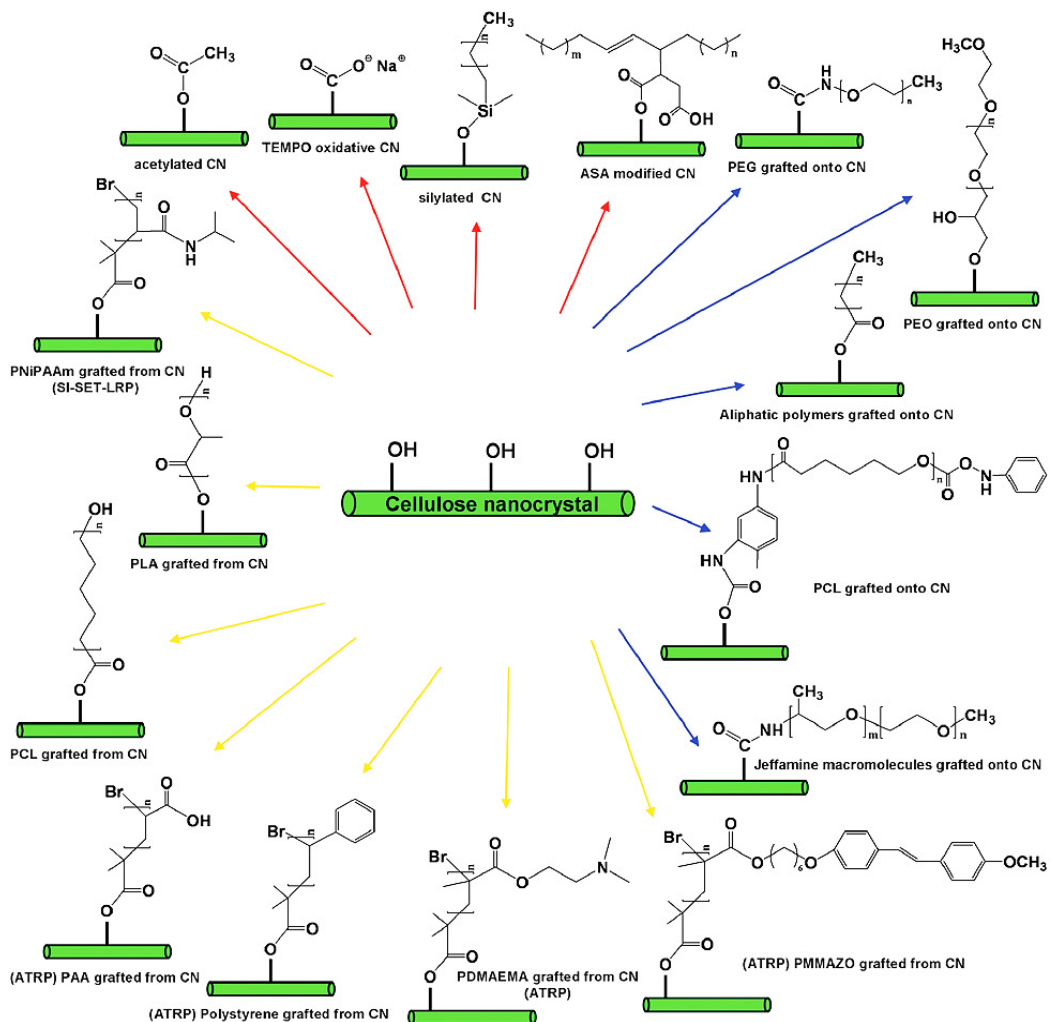


Figure 2.5 Common chemical modifications of cellulose nanocrystals. [PEG: poly(ethylene glycol); PEO: poly(ethylene oxide); PLA: poly(lactic acid); PAA: poly(acrylic acid); PNIPAAm: poly(N-isopropylacrylamide); PDMAEMA: poly(N,N-dimethylaminoethyl methacrylate)]; PTHF: poly(tetrahydrofuran) and PPGBE: poly(propylene glycol) monobutyl ether]. (Lin et al., 2012)

There are many ways for chemical modifications on the surface -OH groups. Figure 2.5 summarizes the common routes for various surface modifications on CNCs published recently (Lin et al., 2012). Their approaches can be categorized into three main categories: (1) substitution of surface -OH groups with small molecules (labelled with red arrows) (Çetin et al., 2009; Lin et al., 2011a; Yuan et al., 2006; Goussé et al., 2002; Pei et al., 2010; Braun & Dorgan, 2009; Habibi et al., 2006); (2) polymer grafting using ‘graft to’ method using various coupling agents (labelled with blue arrows) (Zoppe et al., 2009; Junior de Menezes et al., 2009; Habibi & Dufresne, 2008; Siaueira et al., 2009; Araki et al., 2001; Siqueira et al., 2010; Berlizot et al., 2009); and (3) polymer grafting using ‘graft from’ strategy based on ring opening polymerization (ROP), atom transfer radical polymerization (ATRP), and single-electron transfer living radical polymerization(SET-LP) (labelled with yellow arrows) (Chen et al., 2009; Goffin et al., 2011; Habibi et al., 2008). The significance of chemical modification of CNCs is often to introduce specific functionality that enable many advanced applications including personal care, biomedicine, water treatment, hydrogel etc.

2.1.3 Applications of CNCs

The most convenient and straightforward application of CNCs is to reinforce various matrix materials for improved mechanical properties. Though simple modifications are often needed to further improve the compatibility between the CNCs and the polymer matrix. This can be conveniently achieved by strategies like the addition of surfactants (Habibi, 2014)(Isogai & Kato, 1998), compatibilizer (Petersson et al., 2007), and through loosely adsorbed/chemically graft polymers (De Mesquita et al., 2012; Habibi, 2014; Goussé et al., 2002).

The phenomenon of rod-like species like CNCs to self-assemble into nematic ordering above a critical concentration has been used to render photonic CNC films. (Dujardin et al., 2003; Shopsowitz et al., 2010). The experimental approach is illustrated in Figure 2.6 (a). The film was formed through a sol-gel process using a mixture of tetramethoxysilane (TMOS) and CNCs in alkaline media. While the mixture was allowed to gradually evaporate, self-assembly of CNCs was induced and the arrangement displayed nematic liquid crystalline order serving as templates. After the films were formed, CNCs were removed from the system via calcination. The resulted silica films are the exact replica of the chiral nematic structure of CNCs preserving iridescent colors under various wavelengths across the entire visible spectrum. As shown in Figure 2.6(b) and (c), by varying the concentration of CNC suspension from low to high (S1 to S4), blue, green, yellow, and red colors can be obtained for the prepared films respectively. Interestingly, these colors will disappear once the films are wet but are regained upon drying.

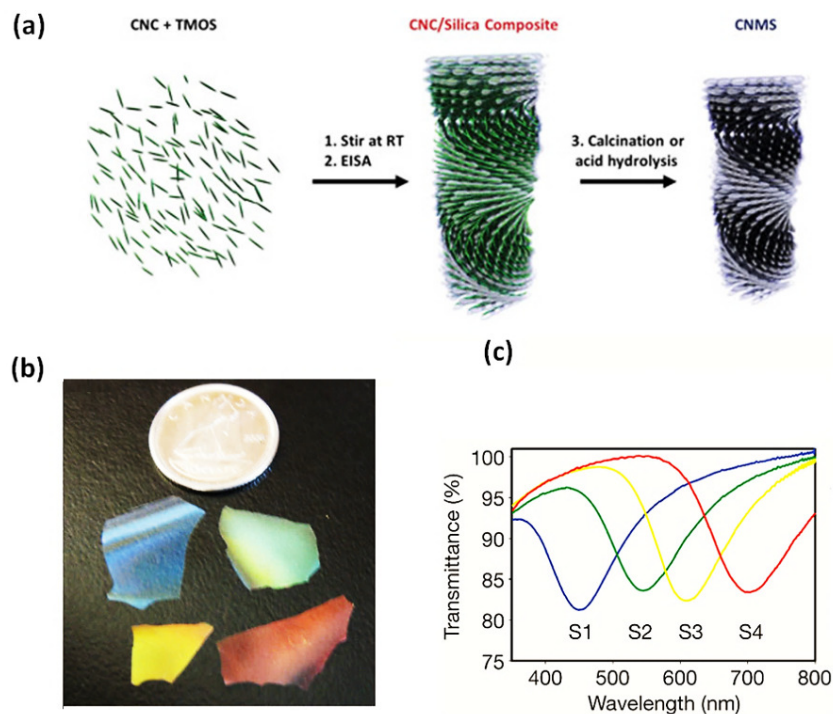


Figure 2.6 (a) Illustrate of preparing silica iridescent films templated by cellulose nanocrystals, (b) photographs of mesoporous silica films from various initial silica to CNC ratios exhibiting different colors and (c) Transmission spectra representing various colored films shown in (b). (Shopsowitz et al., 2010)

Using the same approach, ethylene-bridged mesoporous organosilica flexible films with long-range chirality and photonic property was prepared. In this case, acid hydrolysis was used to remove CNCs. (Shopsowitz et al., 2012a) Moreover, films prepared with this method possess special mesoporosity (aligned cylindrical pores of around 15 nm in diameter) and they are the vacancies left by CNCs. A high pore volume of up to $0.6 \text{ cm}^3 \text{ g}^{-1}$ and Brunauer-Emmett-Teller (BET) surface area of up to $800 \text{ m}^2 \text{ g}^{-1}$ were obtained for CNC templated films. By further introducing titanium precursors into the mesopores of the above silica films followed by silica removal, free standing films of anatase TiO_2 nanocrystals were obtained (Figure 2.7a). (Shopsowitz et al., 2012b). The resultant TiO_2 film exhibits high-surface-area ($150\text{--}230 \text{ m}^2 \text{ g}^{-1}$) and mesoporosity with long-range chiral nematic ordering that selectively reflects left-handed circularly polarized light. Such films can find promises in applications, such as dye-sensitized solar cells, photocatalysts, sensors, and batteries. (Dujardin et al., 2003)

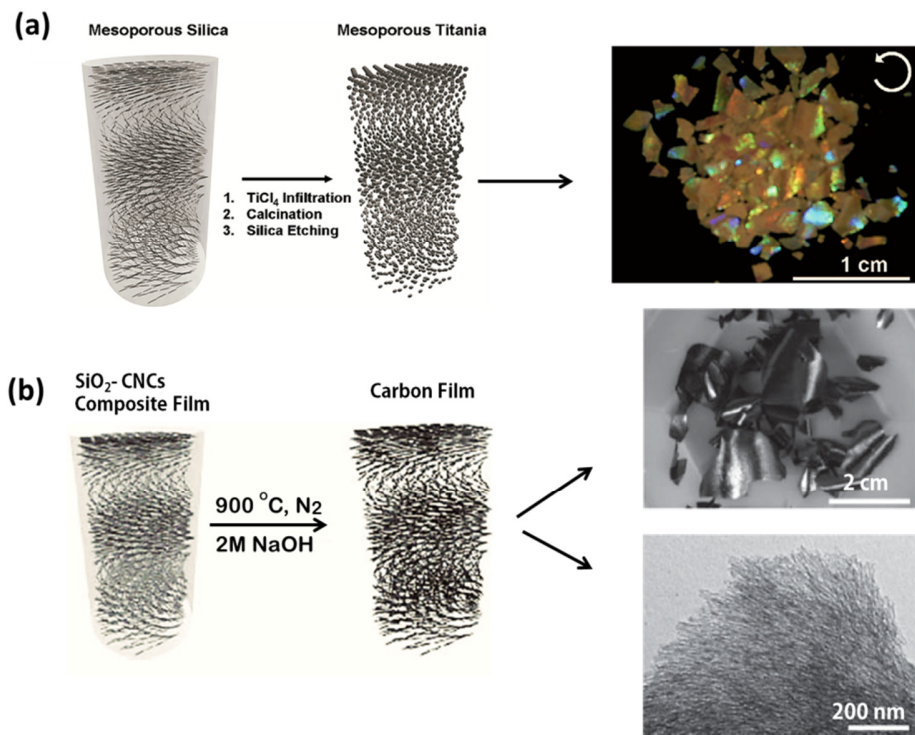


Figure 2.7 (a) Procedure of preparing TiO_2 films using mesoporous silica films templated by chiral nematic cellulose nanocrystals and photograph showing the resultant TiO_2 films viewed under a left-handed circular polarizing filter (Shopsowitz et al., 2012b); (b) Procedure for preparing porous carbon films using chiral nematic silica-cellulose nanocrystal composite films, the photograph of the resultant carbon films, and the SEM image showing the long-range chiral nematic order formed by rod-like particles in the film. (Asefa, 2012)

The strategy of preparing CNC-templated TMOS film can also be used to fabricate mesoporous carbon materials (Asefa, 2012). In this case, CNCs serve as the non-sacrifice template and carbon source and silica is used for stabilizing the nematic ordering of self-assembled CNCs. The conversion of silica-CNC composite film to carbon films can be achieved through carbonization under inert gas at 900 degrees followed by the removal of silica (procedure is illustrated in Figure 2.7(b)). Free-standing carbon films with metallic gloss were obtained and these semiconductive films exhibit very high surface area reaching $1460 \text{ m}^2 \text{ g}^{-1}$ with a pore volume of $1.22 \text{ cm}^3 \text{ g}^{-1}$. SEM image shows a clear long-range chiral nematic structure of the obtained carbon film formed by graphitized CNCs. (Asefa, 2012) Nitrogen(N)-doped carbon films can also be prepared this way by simply pre-coating CNCs with metal amine complex ions before mixing with the silica precursor. (Shopsowitz et al., 2011) These mesoporous carbon films hold promises for macromolecular

adsorption (Han et al., 2000), double layer capacitors (Lee et al., 1999), lithium ion batteries (Pang et al., 2015; Ji et al., 2009), and catalyst carriers (Joo et al., 2001).

CNCs have also been used as ideal templates for supporting inorganic nanoparticles (NPs). The common strategy is to reduce NPs from their precursor in the presence of CNCs by adding reducing agent, NaBH₄ or H₂, or using thermal reduction. Using CNCs as substrates for this purpose was found to efficiently promote the nucleation and dispersion of NPs. Recent research has also suggested multiple roles of CNCs in this process, serving as reducing agent, capping agent, and/or stabilizing agent (Padalkar et al., 2010) Cubic-shaped TiO₂ NPs were synthesized by simply reacting TiCl₄ within CNCs suspensions. CNCs was found to accelerate the crystal growth and promote the cubic formation of the TiO₂. (Zhou et al., 2007) Ag NPs were reduced with NaBH₄ on TEMPO oxidized CNCs. TEMPO-mediated oxidation introduces carboxylic groups on CNC for the purpose of creating strong coordination effect with the metal ions. (Liu et al., 2011b) Direct reduction and immobilization of Ag NPs was also achieved using periodate-oxidized CNCs in mild alkaline environment with aldehyde surface functional groups serving as the reducing functionality. However, the Ag nanoparticles reduced by aldehyde-CNC were relatively large with sizes ranging from 20 to 45 nm. (Drogat et al., 2011) Metal nanoalloys of Au-Ag were also prepared on TEMPO-CNCs through a simultaneous one-pot reduction step in the presence of both metal precursors. (Shin et al., 2008; Liu et al., 2011a) Using hydrothermal treatment, nickel (Ni), selenium (Se) NPs were reduced onto CNCs at an elevated temperature (Shin et al., 2007a, 2007b) Padalkar et al. reported on the synthesis of Ag, Au, Cu, and Pt nanoparticles using the same CNCs as templates with the assistance of a cationic surfactant, cetyltrimethylammonium bromide (CTAB). The proposed strategy was illustrated in Figure 2.8 (a). MNPs are first reduced from AgNO₃ and stabilized by CTAB; The stabilized MNPs, which are decorated with polar cationic quaternary ammonium groups, will interact with and bind to the polar surfaces (-OH) of CNCs. (Padalkar et al., 2010) TEM images of various CNC supported MNPs are shown in Figure 2.8(b)-(e). Following the same strategy, the synthesis of cadmium sulfide (CdS), zinc sulfide (ZnS), and lead sulfide (PbS) NPs were also achieved on CNCs in the presence of CTAB. (Padalkar et al., 2011)

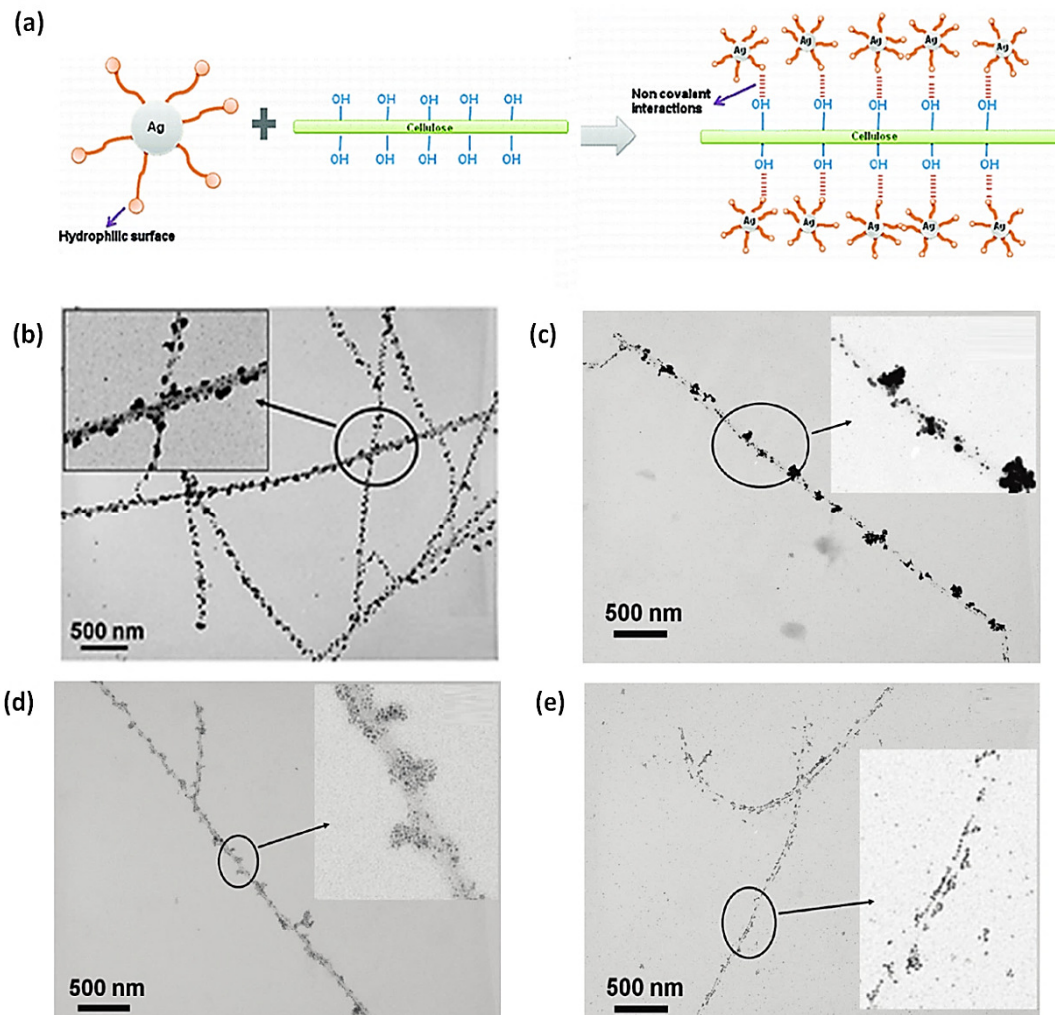


Figure 2.8 (a) Schematic describing the role of CTAB in the formation of metal nanoparticles on cellulose nanocrystals. TEM images of cellulose nanocrystal supported (b) Ag (c) Cu (d) Au and (e) Pt nanoparticles.

Using CNC as a versatile platform to prepare supported functional nanomaterials has the apparent advantages of low cost and simplicity when compared to using other reported templates such as DNAs, and proteins. The optimal reduction of MNPs assisted by CNCs can lead to interesting composite materials that are especially promising for use as heterogeneous catalysts in a variety of reactions. High catalytic efficiency can be expected from highly dispersed MNPs that provide high active sites. In one of such studies, Au NPs were reduced on CNCs using a chemical reduction reaction, and the Au/CNCs composite exhibited 840 times higher the catalytic efficiency in catalyzing the reduction of 4-nitrophenol (4-NP) in comparison with the conventional Au NPs supported by other polymers. (Koga et al., 2010; Lam et al., 2012) Monodispersed Pd NPs with sizes of 0.8-3.6 nm were reduced on CNCs with H₂ and the hybrid catalyst possessed superior

catalytic performance in the hydrogenation of phenol to cyclohexanone and the Heck coupling reaction of styrene. In contrast, much poorer performance was observed for Pd NPs supported by Al₂O₃, carbon, or cellulose as the substrate. (Cirtiu et al., 2011; Rajender Reddy et al., 2006)

Pristine CNCs have low cytotoxicity, bioactivity, biocompatibility, biodegradability, and environmentally benign. (Anon, 2009), providing great impetus for its use in bio-related applications. The surface reactivity of CNCs enables various bioconjugation with special functional groups, resulting in a promising platform for diversified bio-applications. For example, MNP conjugated CNCs can be used as labels to detect DNA hybridization. (Liu et al., 2011b, 2011a) Various fluorophores (Rhodamine B isothiocyanate, fluorescein isothiocyanate etc.) labelled CNCs were synthesized, and the hybrid materials are promising for various imaging technique (spectrofluorometry, fluorescence microscopy, and flow cytometry) to be used for *in vivo* bioimaging. (Dong & Roman, 2007) In another study, a pH-sensitive dual fluorescent labelling on CNCs (one reaction with the isothiocyanates and the other with the thiol–ene) was also developed that has the potential to be used in biosensing. (Nielsen et al., 2010)

CNCs can also be used to reinforce hydrogels as novel drug delivery matrix to achieve the controlled release of drugs. In one study, three types of polysaccharide nanocrystals - CNCs, chitin nanowhiskers (CHWs), and starch nanocrystals (SNCs) were incorporated in three alginate-microsphere hydrogel beads respectively. (Lin et al., 2011b) The rationale behind the strategy is illustrated in Figure 2.9 (a), rigid polysaccharide nanocrystals introduced in the hydrogel matrix can effectively restrict the motion of alginate chains, inhibit the diffusion of drug and slow down the collapse of the beads. At the same time, the reinforcement of microbeads was also achieved through additional physical crosslinking by forming hydrogen bonding between polysaccharide nanocrystals and alginate. Three nanocomposite microspheres produced from the approach exhibited more consistent swelling characteristics, higher encapsulation efficiency, and prominent sustained release profiles. Moreover, beads reinforced with rod-shaped CNCs and CHWs exhibit a higher stability and prolonged drug release than those with platelet-shaped SNCs. This might associate with tendency to agglomeration resulting in poorer dispersion of SNCs in the matrix, as well as the lower aspect ratio of SNCs in providing the inhibition effect.(Lin et al., 2011b)

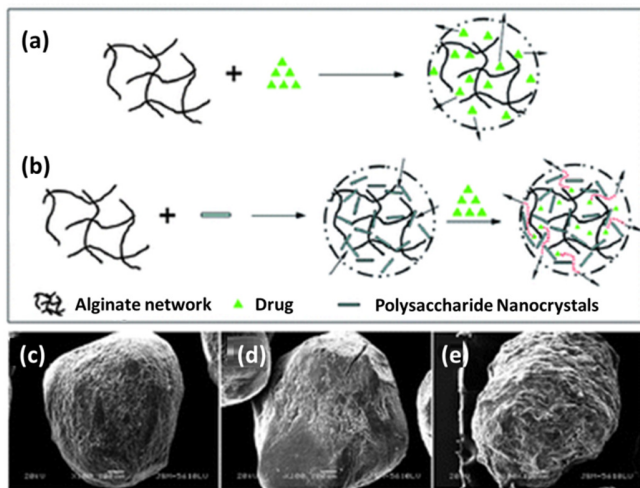


Figure 2.9 Schematic showing of the role of polysaccharide nanocrystals in (a) inhibiting drug diffusion and (b) forming extra physical crosslinking with alginic matrix; SEM images of (c) CNC/alginate bead (d) CHW/alginate bead and (e) SNC/alginate bead. (Lin et al., 2011b)

Instead of adding CNCs as reinforcing agents into the hydrogel, they can also be functionalized to yield hydrogels alone. Both physically crosslinked chitosan-CNC hydrogel (Wang & Roman, 2011) and chemically crosslinked hydrogel formed by composite material of β -cyclodextrins-grafted CNCs/pluronic polymers and α -CD (Lin & Dufresne, 2013) have also been developed. Moreover, CNCs and CTAB-modified CNCs were found to be promising drug excipients capable of binding significant quantities of water-soluble ionisable drugs (tetracycline and doxorubicin) (Jackson et al., 2011) and hydrophobic anticancer drug (docetaxel, paclitaxel, and etoposide) (Jackson et al., 2011) respectively.

In tissue engineering, the development of scaffolds with specific physical, mechanical, and biological properties is an important subject (Place et al., 2009). Ideal scaffold materials need to possess certain mechanical strength and interconnected pores to provide the critical physical support and sites for cell growth and proliferate into targeted functional tissues. In recently years, CNCs were widely explored and used in various forms of nanoscaffold systems: 2D films (Pooyan et al., 2012, 2013; Hossain et al., 2012; George et al., 2012; Santerre et al., 2005), porous scaffold either as nanomats (He et al., 2014b) or aerogels (Wang et al., 2010e; Bulota et al., 2012; Kohnke et al., 2012). The purpose of incorporating CNCs in these structures consisting of biopolymers, such as collagen, starch, gelatine, alginate, PVA, PEG, and PAA, is mainly for reinforcement, added functionalities, or stronger cell adhesion of the scaffold. (Dvir et al., 2011; Dugan et al., 2010)

2.1.4 Trends and general observations

As discussed above, the superior physical and chemical properties of CNCs make it a rather versatile ‘wonder material’. The growing research interest in CNCs is clearly evidenced by an exponential growth in the number of academic publications over the last decade (Figure 2.10). The fruitful research discoveries from various disciplines have promised a wide spectrum of CNC applications with many novel functionalizations. Traditional research areas mostly focused on utilizing the intrinsic properties of CNCs (chiral nematic self-assembly property for templating or film forming, high mechanical strength for reinforcing various matrix, etc.). Increasingly, highly functional and smart nanocomposite systems based on CNCs are under development, such as shape-memory materials (Liu et al., 2015c), self-healing materials (Biyani et al., 2013), stimuli responsive systems (Way et al., 2012; Kan et al., 2013) have been reported.

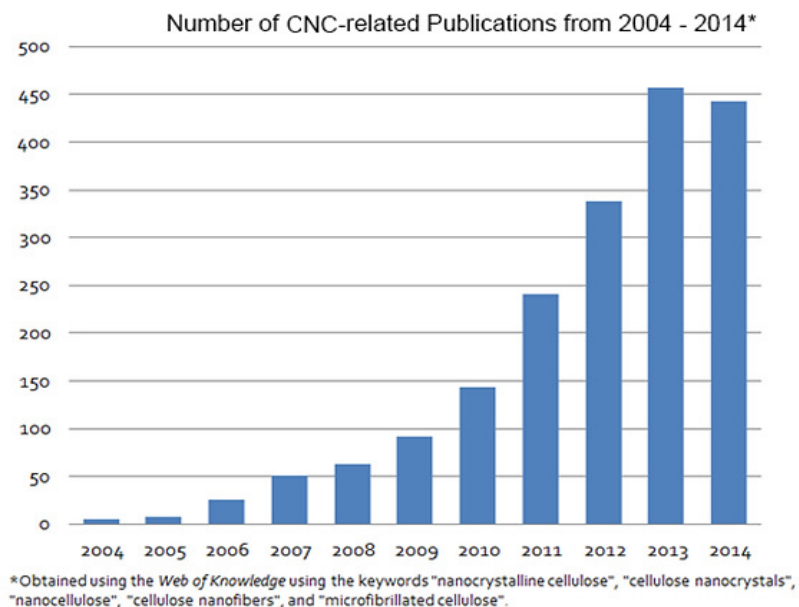


Figure 2.10 Chart showing the exponential growth of CNC-related publications from 2004 to 2014.

(Source: Lux Research, Inc.)

One particular trend that represents the advanced utilization of CNC is in the electrochemical applications. Though CNCs are insulating in nature, conductivity can be readily gained by forming composite materials with another conductive component through either physical/chemical reaction. Some examples of the electrochemical applications of CNCs in recent years are: CNC/Graphene oxide(GO) composite films for paper electronic; (Valentini et al., 2013) tempo-oxidized CNCs/CNTs for ultra-strong, transparent, and printable conductive ink; (Koga et al., 2013)

GO/CNC on lithographic patterns of interdigitated electrodes on polymer substrates as transparent and eco-friendly proximity sensor; (Sadasivuni et al., 2015) PPy/CNC for high capacitive supercapacitor electrode;(Liew et al., 2010, 2013; Yang et al., 2015) PPy/CNC as the substrate for conjugation of glucose oxidase and glucose sensing; (Esmaeili et al., 2015) Optically transparent and conductive G nanoplatelets/CNC films for polymer solar cells.(Valentini et al., 2014) It was demonstrated in the above studies that, by incorporating CNCs in the above systems, much improved electrochemical performance was achieved through the synergy between CNCs and the conductive material. The conductive functionality introduced to CNCs also open a much wider range of advanced applications where high value-added products can be realized.

In the industrial domain, many R&D projects aiming at commercializing CNC-based products are being pursued, however, very limited fields have been explored. Based on the latest annual report released by ArboraNano Network (ArboraNano, 2014), the business opportunities for CNCs being explored are listed in Figure 2.11. A general trend in those applications is that CNCs are used in a most straightforward way (e.g. as additives into their conventional matrix/formulations). These applications mainly take advantage of the inherent properties of CNCs without complicated chemistry involved. For instance, CNCs with antioxidant & antimicrobial effect were added into food packaging for extended shelf life; Stronger textiles/paper were manufactured by adding CNCs as reinforcing agents; CNCs exhibiting liquid crystal self-assembly behavior are used in ink for anti-counterfeiting applications; the ability of CNC to act as a rheological modifier is explored in oil & gas drilling process. The advanced applications using highly functionalized CNCs (those proposed in the research field) have rarely been explored in industry.

Though the advantages of CNC were mostly cited by the industry as being low cost, the importance of cost is secondary if the material itself is not useful. To explore applications within the scope of taking advantage of their intrinsic properties will only end up producing low value-added products. With the production of increasing number of types of nanomaterials at the industrial scale, pristine CNCs will be easily challenged or replaced by many other cost-effective alternatives. Fortunately for CNCs, they are highly functional, and they can be adapted for use in many advanced engineering applications. Therefore, the critical task today is to efficiently translate academic results into high value-added industrial products. The large gap in the activity between academic and industry today is largely due to the heavy dependence on sophisticated apparatus, toxic/expensive reactants, harsh chemical treatment, tedious/complicated and low yield processing in lab-scale fabrication. It is thus highly desirable to use energy-efficient, convenient and sustainable processing to produce highly functionalized CNCs from a practical point of view.

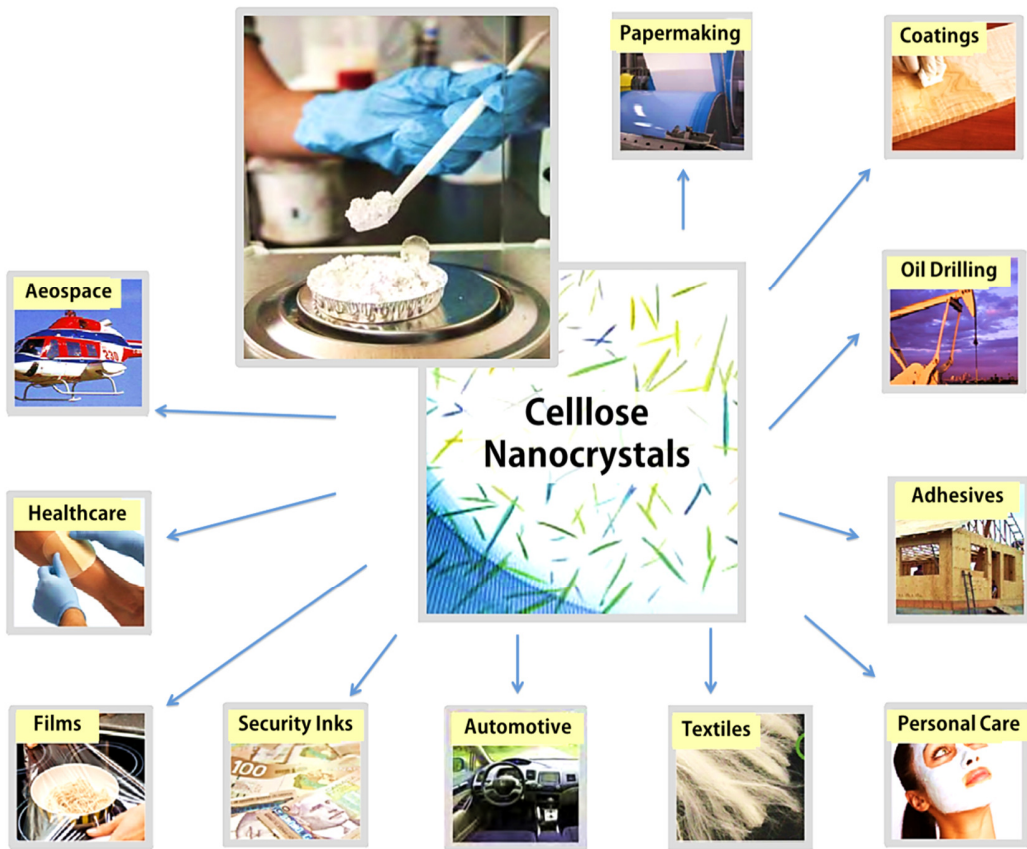


Figure 2.11 Applications of CNCs under investigation industrially (modified from ArboraNano annual report 2014-2015)

2.2 Supercapacitor (SP)

Confronting the energy crisis in the 21st century, the exploration of green energy alternatives to replace fossil energy is critical. Current solutions, such as solar photovoltaics and wind turbines, are capable of generating energy from renewable sources and feed power directly into the grid. However, these energy sources are intermittent in nature and the devices do not have energy storage capability, which lead to fluctuating power supply, preventing them from becoming a primary energy source. Therefore, efficient energy storage technologies are highly needed to store the intermittent energy and use it on demand. Energy storage technologies can also transform our transportation system by replacing the current chemical fuel-based powertrain into an electricity-based one (i.e. electric car) for a more sustainable future. The technologies will also benefit mobile consumer electronics (e.g. cellphones, laptops, cameras) that have become ubiquitous in modern society. Battery is currently the dominant energy storage technology that offers robust power supply for various mobile devices. However, it has to be recharged often, which takes a long time.

Moreover, their energy storage potential diminishes over charge-discharge cycles due to material degradation. Finally, it generates limited power density that fails to meet many peak power demands. The challenges in modern energy storage technologies have led to the intense research interest in supercapacitor (SP). Herein, some basics of SPs will be introduced. The advances and general trend in developing SP electrode materials are also reviewed since the electrode material is the key component that critically determines the performance of energy storage devices.

2.2.1 Fundamentals of SP

Supercapacitor (SP), sometimes also referred to as ultracapacitor, pseudocapacitor, or electrochemical double-layer capacitor, works essentially the same as a capacitor and thus can achieve rapid charge/discharge compared to that of a battery. As illustrated in Figure 2.12(a), capacitor consists of two separated conducting electrode plates, and when a voltage is applied to a capacitor, a charge accumulates on them, and oppositely charged ions from the electrolyte will efficiently produce on the surfaces of each electrode. During discharge, charges on the plates decrease as electrons flow through a circuit, and ions are released from the plates to the electrolyte. The major difference between a capacitor and a SP is that the former uses electrode plate to store charge, while SPs uses highly porous materials for charge storage (Figure 2.12b). In the case of SP, the electrode plate is just the current collector. Since porous materials exhibit much higher surface area that exposed to the electrolyte, SPs display dramatically increased charge storage ability (energy density) compared to capacitors.

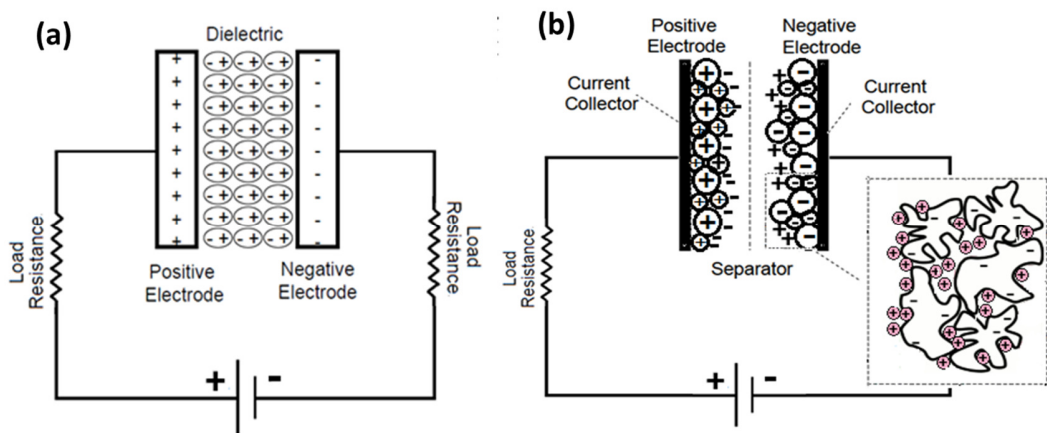


Figure 2.12 Schematic of (a) a conventional capacitor and (b) a supercapacitor.

As an innovative energy storage technology, SPs not only charge faster than batteries, but are also able to offer larger amount of energy within short pulses (power density). Moreover, theoretically

they possess infinite cycle life since they do not suffer from material degradation such as in batteries, that wear down in the process. The long life means that it is more environmentally friendly due to less waste disposal. SPs have been recognized as the next generation energy storage devices that bridge the gap between batteries and capacitors. In Figure 2.13, a graph termed a “Ragone Plot” summarizes the energy and power density of various energy storage devices. As observed from the diagram, SPs overlaps with batteries at high power density & low energy density and with capacitors at low energy density & high power density.

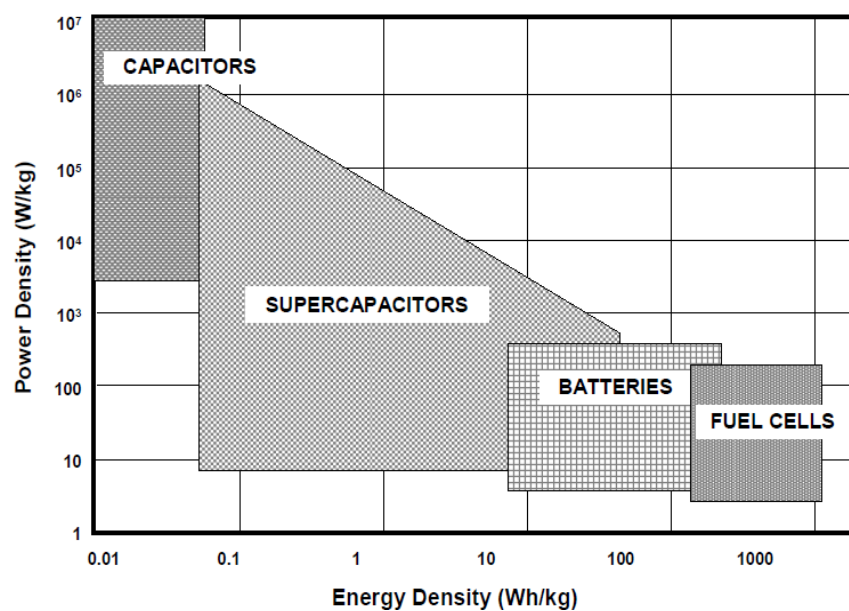


Figure 2.13 Ragone plot of energy storage devices. (Kötz & Carlen, 2000)

Energy can be stored in SPs either through double-layer adsorption (non-faradaic mechanism), electron transfer process (faradaic mechanism), or a combination of both. Based on this, SPs can be classified into three categories: electric double-layer capacitors, pseudocapacitors, and hybrid capacitors respectively. (Burke, 2000) The classification of different supercapacitor devices and their common proposed electrode materials are shown in Figure 2.14.

For electric double-layer capacitors, charges are stored at the interface of the electrode and the electrolyte through electrostatic interaction without any redox reaction. Therefore, the process is highly efficient and reversible. Electric double-layer capacitor generally features in stable performance for extremely long charge-discharge cycles, typically up to 10^6 cycles. In comparison, batteries are limited to about 10^3 cycles. Therefore, electric double-layer capacitors are well suited for applications that involve non-user serviceable locations, such as deep sea or mountainous

regions. Typical electrode materials for electric double-layer capacitors are carbon-based materials, such as activated carbons, carbon aerogels, and carbon nanotube. (Conway, 1999; Kötz & Carlen, 2000)

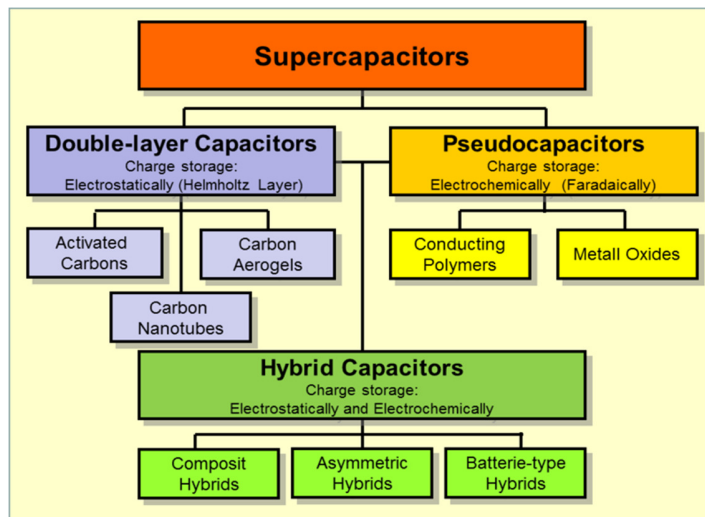


Figure 2.14 Taxonomy of supercapacitors. (<https://commons.wikimedia.org/wiki/File:Supercapacitors-Overview.png>)

Pseudocapacitors store charge as a result of an electron transfer process between electrode and electrolyte. The faradaic process may involve electrosorption, reduction-oxidation reactions, and/or intercalation processes.(Conway et al., 1997) In this case, charges can be stored in the whole volume of the material where redox reaction can take place rather than just on the surface in the case of double-layer mechanism using physical adsorption. Therefore, pseudocapacitors can generally achieve greater capacitances and energy densities than electric double-layer capacitors. However, since there is electron transfer involved, it suffers a shorter cycling longevity (Mastragostino et al., 2001).

Hybrid capacitors combine the relative advantage of both electric double-layer capacitors and pseudocapacitors by storing charges through both Faradaic and non-Faradaic processes. Hybrid capacitors can achieve energy and power densities greater than electric double-layer capacitors without sacrificing the cycling stability. Research has focused on three major types of hybrid capacitors, based on their electrode configuration: composite, asymmetric, and battery-type respectively. Composite electrodes integrate carbon-based materials with either conducting polymer or metal oxide materials in a single electrode to achieve higher capacitances than their individual counterpart. (Frackowiak et al., 2006) Asymmetric hybrids typically couple an activated carbon as the negative electrode with a conducting polymer as the positive electrode.(Laforgue et al., 2003)

Battery-type hybrids couple a supercapacitor electrode with a battery electrode. This configuration attempts to combine the high energy characteristics of batteries with the high power, long cycle life, and fast recharging of supercapacitors. Research has focused primarily on using nickel hydroxide, lead dioxide, and LTO ($\text{Li}_4\text{Ti}_5\text{O}_{12}$) as one electrode and activated carbon as the other. (Li et al., 2005)

SPs are promising for a wide range of applications towards a more sustainable energy future from hybrid/electric cars to various consumer electronics. It can also be used for electric grid, to provide a buffer for power surges. The device is also found in cell phone base station or backup power systems. It should however be noted that the invention of SPs is not to replace the current energy storage technologies as the sole power source. In fact, in many applications, none of the individual energy storage device can perform up to the desired energy and power density. However, when used in conjunction with other energy storage systems, they are able to satisfy a much higher demand. For instance, the battery/SP hybrid (Frenzel et al., 2011), fuel cell/battery/SP hybrid (Pede et al., 2004) have been developed for electric vehicles. In these applications, SPs are used for the efficient storage of regenerative energy (braking energy) and support the high power demand (during acceleration) for their rapid discharge; while batteries and fuel cells are used at constant cruising speed for prolonged drive distance due to their high energy density.

The market of SPs is fast growing and it is expected to generate \$3.5 billion in energy storage revenues, accounting for 5% of the battery market in 2020 (Based on the analysis from *Ultracapacitor Market Forecast 2015-2020*). Despite the great promises, current SPs are also more ‘super’ in size and in cost, hindering their industrial adoption. The low energy density is still the major shortcoming of SPs, far below that of mid-end batteries and fuel cells. Moreover, SP generally exceeds the cost of battery due to the difficulty in fabricating high surface-area electrode material with superior capacitive performance. Therefore, more advances are needed to develop high-performance SP electrode material with low-cost processing for commercialization.

The general criteria for a good SP electrode material are high specific capacitance (C_s) (i.e. capacitance per unit mass), high rate capability (retention of capacitance at high scan rate/current density), and high cycle stability. Since the above supercapacitor performance is determined by the following factors of the electrode material, thus they become the main consideration and requirements in electrode design (Yu et al., 2015) :

- a) **Surface area:** Charges are most efficiently stored on the surface of the electrode material, thus a higher C_s can be obtained for electrode material with a higher surface area. Significant

improvement in the surface area can be achieved from the development of various nanostructured materials.

- b) **Electronic and ionic conductivity:** Both electronic and ionic conductivity play critical roles for Cs and rate capability performance since they are directly related to the efficiency of charge transport. Typical strategies to improve the electronic conductivity are the elimination of binder in electrode material and the proper design of nanostructured current collector with efficient electron pathways. The well-controlled porosity (precise control of pore size, pore distribution etc.) of the electrode material can effectively improve the ionic conductivity (e.g. mesopores have been shown to facilitate the ionic transport).
- c) **Mechanical and chemical stability:** The mechanical and chemical stability critically determine the cycling stability of the electrode. Phase change, dissolution, and side reaction of active materials are the major causes leading to performance loss during cycling. Fine tuning the structure of the electrode within nanoscale regime offers new opportunities to address the above issues.

Other requirements for SP electrode material include low toxicity, low cost, thermal stability, and corrosion resistance. In the following sections, two typical SP materials will be specially reviewed where their properties, advantages and disadvantages, and recent advances as SP electrode material will be discussed.

2.2.2 Intrinsically conductive polymers (ICPs) as SP electrode

Intrinsic conductive polymers (ICPs) are polymers having an alternating carbon double (C=C) and single bond (C-C), forming a π -conjugated backbone. Typical ICPs are listed in Figure 2.15. Such structure facilitates the delocalization of electrons along the polymer chains. (Reynolds et al., 1989) Through a process called doping, a dopant in the form of extra electrons or a ‘hole’ (a position where an electron is deprived) is injected into the structure, leading to electrical conductivity due to the flexibility of the electron flow.

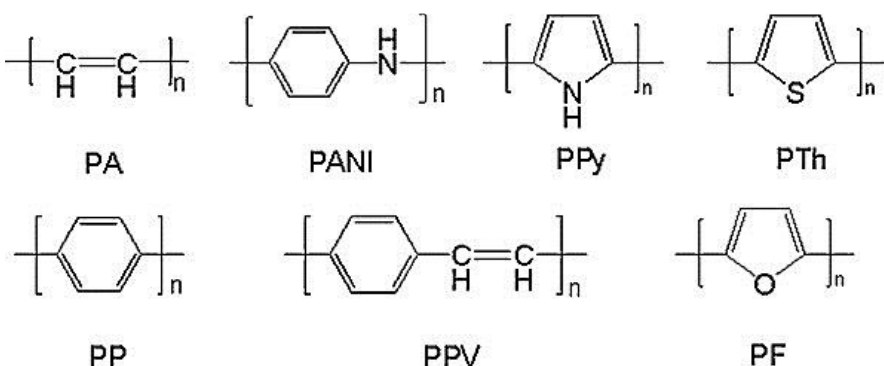


Figure 2.15 Typical conductive polymers and their chemical structures.

ICPs can be synthesized via either chemical or electrochemical polymerization from the respective monomers. The polymerization mechanism of PPy is illustrated as an example in Figure 2.16. In the first step, radical cations of ($C_4H_5^+$) are generated by oxidation. In the second step, radical-radical coupling occurs between two radical cations, resulting in the formation of a dimer, followed by deprotonation. Finally, the dimer labeled as bipyrrole is re-oxidized and coupled with other radical cations consecutively during the chain propagation. In electropolymerization, pyrrole monomers and an electrolyte salt are dissolved in a suitable solvent. As the working electrode is brought to high enough anodic potentials, a conducting PPy film is formed on the electrode; In chemical polymerization, an oxidizing agent such as ammonium persulphate (APS) or $FeCl_3$ is responsible for the oxidation of the monomers, oligomers and longer polymer chains (Jang, 2006). In both methods, the propagation of the polymer chain accompanies the inclusion of counterions, anions, to balance the excess positive charge on the polymer backbone. These counterions come from either the polymerization solution or the oxidizing agent.

The main advantages of chemical over electrochemical polymerization are that the polymers can be deposited on a variety of conductive or nonconductive substrates and bulk quantities of polymer can be produced for practical applications. Generally, the conductivity and yield of chemically synthesized PPy depend on factors as the choice of oxidant and solvent, the monomer to oxidant ratio, and the duration and temperature of the polymerization reaction. The major disadvantages of chemical polymerization are that there is a limited choice of suitable oxidants and few available counterions; impurities are introduced with the oxidant; and complicated side reactions occur during the long reaction period, leading to poor control of the degree of chemical degradation during synthesis (Patil et al., 1987). Moreover, bulk polymerization of conductive PPy results in a polymer that is generally insoluble and infusible, which significantly hinders its further processing and applications.

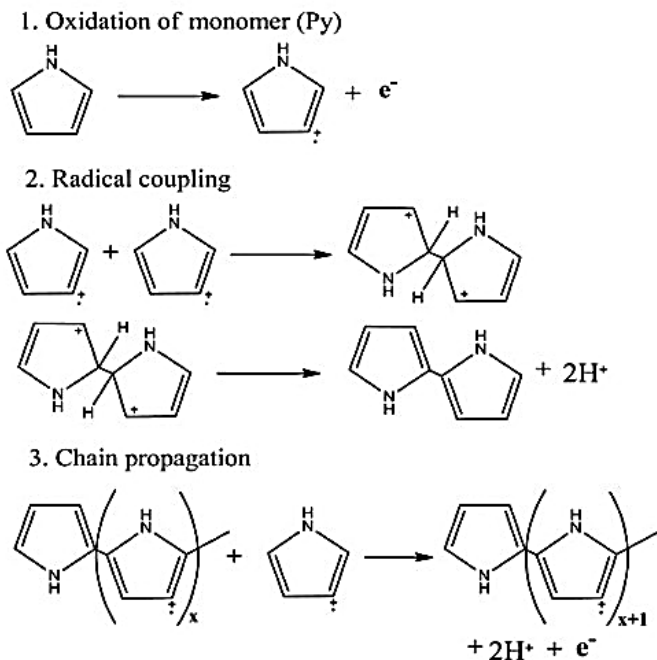


Figure 2.16 General accepted polymerization scheme for polypyrrole. (Jang, 2006)

Three most popular ECPs for supercapacitor applications are polypyrrole (PPy), polyaniline (PANI) and poly(ethylenedioxythiophene) (PEDOT) due to their relatively high conductivity, redox switching property, ease in synthesis, and high Cs. (Peng et al., 2007) Further, their relatively low cost, light weight and environmentally friendliness are also appealing. When ICPs are coated on the electrode, they can be electrochemically oxidized or reduced, where charge storage can occur. The operating voltage window for ICPs is determined by its insulating-conducting switching potential (negative potential limit) and overoxidation potential where ICPs undergoes irreversible structural degradation (positive potential limit). Sometimes, water oxidation potential will affect the positive potential as well.

The fast and simple electrochemistry occurs on ICPs makes them ideal candidates as SP electrode material. As an example, typical redox reaction occur on PPy is illustrated in Figure 2.17. The redox reaction proceeds rather rapidly, allowing efficient charging and discharging as electrode material. The process also accompanied with counter-ion movements, either impregnate in or being expelled from the ICPs, for charge neutralization. It is important for ICPs to have a structure with (1) high surface area that is also accessible by the electrolyte for high Cs; (Sharma & Bhatti, 2010) and (2) high robustness to endure the volume expansion due to constant ion diffusion. (Peng et al., 2007) Today, the foremost hindrances for the development of ICP-based material for SP application is its

poor cycling stability due to its low mechanical strength, low capacities caused by poor degrees of attainable doping, and mass transport limitations due to thick agglomerated structures. One effective strategy to address the above problem is the fabrication of nanostructured CPs since they offer greatly improved specific surface area (i.e. surface area per mass) and mechanical strength due to the many advantages associated with the nanosize effect. (Pan et al., 2010) Nano-sized structure also enables short pathway for efficient ion transfer. Batteries based on nanostructured ICPs can possess higher power densities compared to conventional conducting polymers due to enhanced charge/discharge rates. (Cao & Mallouk, 2008; Liu et al., 2008)

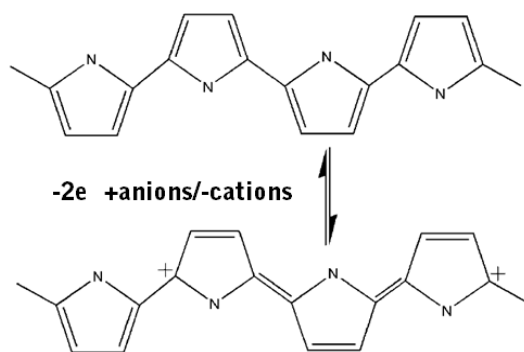


Figure 2.17 Oxidation and reduction of PPy

Among many synthetic strategies proposed, template synthesis has offered a most facile, efficient, and highly controllable route to designing and synthesizing novel conducting polymeric nanostructures and composites. Template synthesis relies on an external template material as scaffold to direct the growth of ICP. This can be achieved either through '*channels inside pores*' route where the polymerization is performed inside a porous membrane with well-defined sizes, such as anodized alumina oxide (AAO) (Martin, 1994); or through '*seeding*' route where pre-existing nanostructured materials serve as seeds to orchestrate the growth of ICPs. These materials can range from inorganic metal oxide (Zhang & Wan, 2003) to various biological templates like DNA.(Ma et al., 2004; Pan et al., 2010) Template synthesis is by far the most straightforward, versatile and widely used fabrication method for well-controlled nanostructured ICPs. This can be readily achieved using both chemical and electrochemical polymerization. A major drawback with template synthesis however, is the post-synthetic purification step required to remove the template in order to liberate the pure polymer. The difficulty can vary greatly depending on the nature of the template used. In some cases, harsh conditions for template dissolution will damage the synthesized nanostructured CP.

In addition to fabricating pure nanostructured ICPs, composite materials of ICPs have also been investigated. In particular, to grow ICP over another robust and anisotropic substrate material to form one dimensional (1D) nanocomposite is a very useful approach to improve and extend the functionality of ICPs.(Lu et al., 2011) Compared to other three dimension nanostructures (0D-nanoparticle, 2D-nanosheet, 3D-entangled network), 1D nanostructure with high aspect ratio could efficiently transport electrical carriers along one controllable direction. Other distinct properties from the synergistic effect of each component may also be observed in the ICP-based nanocomposites, including improved chemical properties or combined multi-functionalized chemical/physical/biological properties (Lu et al., 2011). For example, the addition of carbon nanotubes (CNTs) into conducting polymers was demonstrated by the enhanced electrical properties. The conductivity of CNT/PPy nanocables synthesized by cetyltrimethylammonium bromide (CTAB) directed polymerization approach was one order of magnitude higher than that of PPy synthesized under the same conditions, but without the addition of CNTs.(Zhang et al., 2004) In recent years, there is a growing interest to incorporate wood fiber as the substrate via facile chemical oxidation polymerization (Huang et al., 2005; Sasso et al., 2010) The resulting hybrid nanocomposite inherit the intrinsic properties of high surface area and good dispersibility of cellulose matrix and demonstrate enhanced electrochemical properties and better processability. However, due to the length of those micro-sized cellulose fiber, the polymerization can only be performed over an entangled 3D matrix of cellulose network with the resulting nanocomposite being a film, or hydrogel, limiting their further processability for many applications.

2.2.3 Carbon-based materials as SP electrode

Carbon, of various forms, is the most popular and the only commercialized SP electrode material today due to its good conductivity, high surface area, chemical stability, mechanical strength, and corrosion resistance.(Kötz & Carlen, 2000) Carbon nanotubes (CNTs) and graphene (G) are two very attractive materials for SP applications, both of which have superior electrochemical activity, and exceptional theoretical surface area. (Arico et al., 2005; Du et al., 2011; Zhu et al., 2011b; Liu et al., 2010a) However, the production of good-quality CNTs and graphene is rather costly and achieving the theoretical surface area is often hindered by entanglement, aggregation or stacking during processing due to their hydrophobicity. G sheets prepared from various methods including chemical/thermal exfoliation of graphite followed by different reducing technique (e.g. heat, reducing agent) have been widely investigated as SP electrode material. The Cs of G obtained from those studies is usually below 150 F g^{-1} at a practical scan rate (e.g. 0.1 V s^{-1}). (Ku et al., 2010; Chen et al., 2010; Stoller et al., 2008) The hydrophobicity (i.e. poor electrolyte wettability) and ‘stacked

geometry' (poor utilization of electrochemical surface area) are the main problems that hinder the supercapacitive performance of G. Functionalized G sheets have been developed through approaches like solvo-thermal production, KOH treatment, low-temperature thermal exfoliation in air, etc. Using these techniques, different functional groups (e.g. oxygen) can be introduced to the carbon framework where enhanced Cs can often be obtained from pseudocapacitance and improved wettability of G. (Du et al., 2010; Li et al., 2011; Lin et al., 2011c) Moreover, various G-based nanocomposites, G/conductive polymer (Yan et al., 2010; Gómez et al., 2011; Wang et al., 2009a) and G/metal oxides (Wang et al., 2010a; Zhang et al., 2009b; Wu et al., 2010), have also been synthesized to alleviate the stacking issue of G, and at the same time, imparting extra pseudocapacitance to G with those pseudocapacitive materials. CNT is similar to pristine G in the sense that it generally gives relatively low capacitance due to the hydrophobicity and low surface functionalities. Carboxylic acid and ester functionalized CNTs were thus developed to improve the electrolyte wettability and to enhance Cs. (Zhao et al., 2009) Various composite materials taking advantages of the high surface area CNT and high Cs of another psuedocapacitive material have been developed including CNT/PPy (Wang et al., 2007), CNT/PANI (Zhang et al., 2009a), CNT/PEDOT (Lota et al., 2004), CNT/ZnO (Zhang et al., 2009c), CNT/RuO₂ (Reddy & Ramaprabhu, 2007), and CNT/MnO₂(Kang et al., 2010) have also been developed. One significant advantage of CNT and G-based electrode is the feasibility of developing the next generation flexible SP devices due to their good flexibility. (Davies et al., 2011; Yu et al., 2010; L.Nyholm, G.Nystrom, A. Mihranyan, and M. Stromme, 2011; Wang et al., 2009a)

Besides graphene and CNTs, carbon-based materials can be derived from a wide variety of carbon sources via pyrolysis such as coal (Lozano-Castello et al., 2003), wood (Wei et al., 2011), pitch (Wang et al., 2010c), coconut shells (Hulicova-Jurcakova et al., 2009), seaweed (Bichat et al., 2010), or polymers (Hsieh & Teng, 2002). Since the predominant charge storage mechanism for carbon is through electrostatic adsorption, an ideal carbon structure should possess a high active specific area for enhanced charge storage ability, and a porous structure that facilitates mass transfer and ion diffusion, leading to high power density. It has also been shown that ordered mesoporous structure with pores within 2 to 50 nm in size is particularly advantageous, compared with micropores, and macropores, for efficient shortening the mass transfer and accelerating the reaction kinetics.(Zhu et al., 2016)

Ordered mesoporous carbon nanostructure can be fabricated by both hard and soft templating methods (Wang et al., 2010d). In the former approach, solid materials with defined porous structures such as silica, nickel foam, zeolite etc. are used as templates, and carbon precursors are introduced

to the template by techniques like nano-casting, infiltration, and chemical vapor deposition (CVD). (Hou et al., 2005; Fang et al., 2009) By further extracting the templating material through harsh chemical treatment, the carbon structure replicating the ‘negative’ structure of the templates can be obtained. To illustrate the strategy, a simple example was provided in Figure 2.18. Highly ordered porous carbon with tunable pore sizes in the range of 10-1000 nm was synthesized using silica spheres as hard templates and phenol and formaldehyde as carbon precursor. (Chai et al., 2004) The strategy has the apparent advantage of straightforwardness, fidelity in producing the desired structure, and there is a wide range of template material with different shape and porosity to choose from. However, the fabrication process is relatively tedious, time-consuming and low in yield, which is unsuitable for industrial scale production.

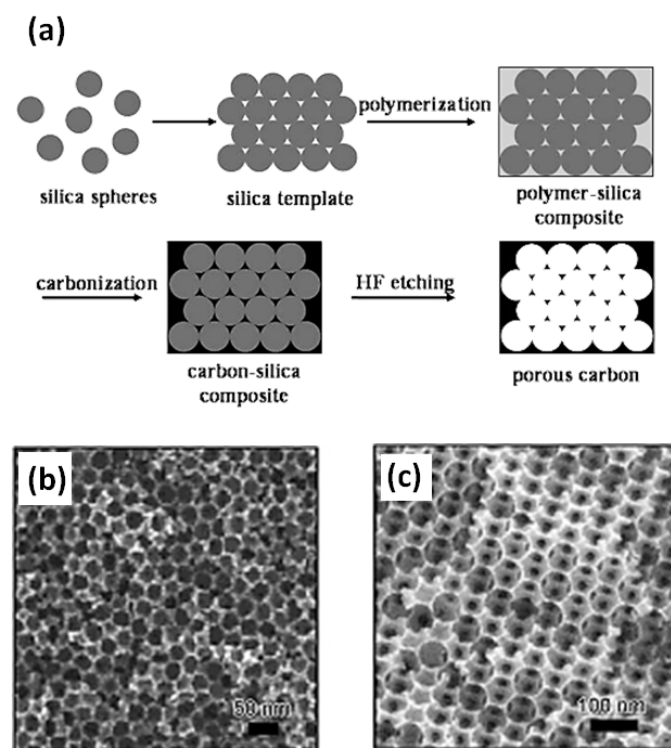


Figure 2.18 (a) Strategies for preparing porous carbons of tunable pore sizes using colloidal silica as hard template, and SEM images of mesoporous carbon materials produced with pore sizes of 25 nm (b) and 68 nm (c)) synthesized using silica particles of different sizes (Chai et al., 2004)

In contrast, soft templating method uses amphiphilic molecules, such as surfactants and block copolymers that self-assemble into nanostructures as templates. The strategy of soft templating is illustrated with an example shown in Figure 2.19 using triblock copolymer PEO-PPO-PEO templates and resol mixtures (F127, F108, and P123) to fabricate mesoporous carbon. The

approach involves 5 steps: (1) resol synthesis from soluble, low molecular weight of phenol and formaldehyde (2) mesoporous polymer structure formation by solvent evaporation induced self-assembly of PEO-PPO-PEO, (3) curing of resol by thermopolymerization and forming rigid zeolite-like hydrocarbon network to stabilize the surfactant template, (4) surfactant template removal by calcination under N₂ (300-500°C), and (5) carbonization (900-1400°C) for transformation of carbon material. By varying the mixing ratios of resols to surfactants, and using surfactants of different ratios of PEO/PPO, highly ordered carbon frameworks of diverse structures can be obtained, including 2-D hexagonal, 3-D bicontinuous, body-centered cubic, and lamellar mesostructures. (Meng et al., 2006)

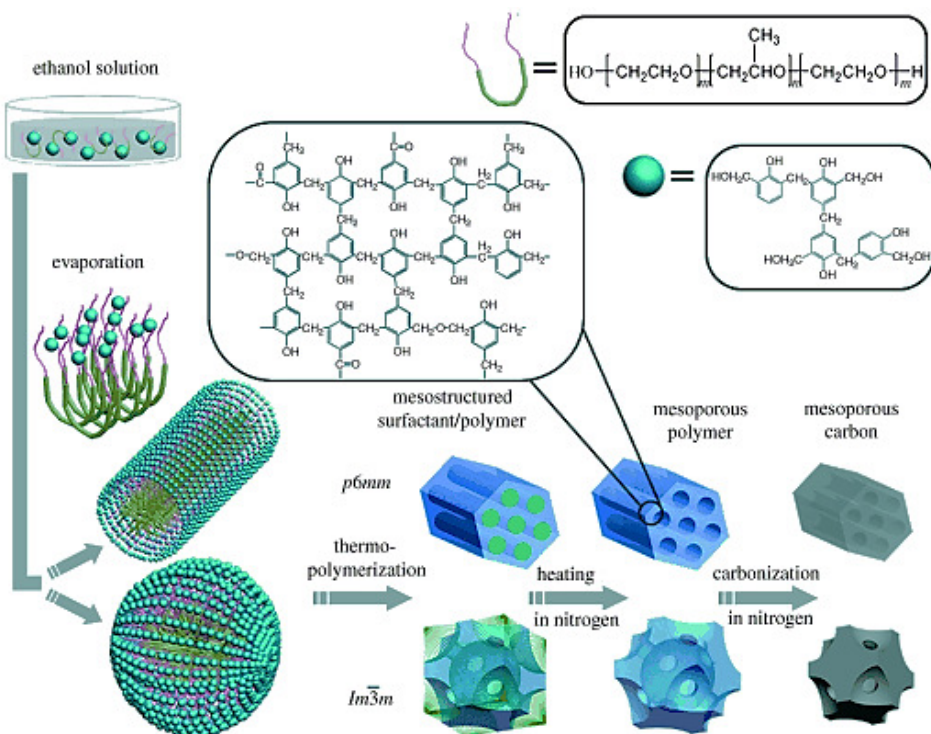


Figure 2.19 Five-step synthesis of mesoporous carbon nanostructure templated by tri-block copolymer PEO-PPO-PEO. (Meng et al., 2005)

While soft templating has the potential of mass production of mesoporous carbon compared to hard-templating, the polymers suitable for such purpose are rare and costly. The strict requirements for polymers used as templating agent are (i) the ability to self-assemble into nanostructure; (ii) the presence of at least one pore-forming and one carbon-yielding component; (iii) the decomposing temperature of the pore-forming component has to be above the curing temperature of carbon-yielding component and below the carbonization temperature; and (iv) the ability of carbon-yielding

component to cross-link into robust nanostructure that can survive the extraction of pore-forming component. (Liang et al., 2008) Therefore, exploring alternative approaches for synthesizing mesoporous carbon nanostructures with low-cost and facile processing remain an important research challenge.

Another way to enhance the capacitive performance with higher energy density for carbon-based materials is possible through heteroatom-doping of the carbon framework. Elements include boron(B) (Kwon et al., 2009; Cermignani et al., 1995; Wang et al., 2008b), phosphorus (P) (Wang et al., 2013a; Paraknowitsch & Thomas, 2013; Paraknowitsch et al., 2013), sulphur (S) (Hasegawa et al., 2011), and nitrogen (N) (Tan et al., 2013; Wen et al., 2012; Chen et al., 2013c, 2012a; Qin et al., 2009; Chen et al., 2013b; Jeon et al., 2014) have been already been investigated. Using the strategy, higher specific capacitance (C_s) can be obtained due to the combined effect of electric double-layer capacitance from the carbon material and the pseudocapacitance from doping-induced reactions. Heterogeneous doping can also contribute to the enhanced electrochemical activity, such as higher conductivity, improved wettability of the electrolytes, which will further be advantageous for SP application.(Lee et al., 2011; Li et al., 2010b; Kim et al., 2007; Paraknowitsch & Thomas, 2013) Nitrogen (N) has been the most heavily studied dopant and N-doped carbon generally exhibit greatly improved C_s while maintaining a superb cycling durability. (Zhao et al., 2015c; Zhu et al., 2015; Cao et al., 2011; Zhao et al., 2015a; Wang et al., 2013a; Jeon et al., 2014) Though still under debate, it is widely accepted that the N species that are responsible for the faradaic reactions are pyridinic and pyrrolic N (Wang et al., 2012a).

Two strategies are commonly used to introduce N into carbon matrices: post-treatment with bases, such as ammonium, amine, urea; and ‘in-situ’ doping with N-rich precursors during carbon fabrication. The first strategy normally results in surface doping with relatively low N content (Jurewicz et al., 2004; Kim et al., 2008; Jurewicz et al., 2008; Cao et al., 2011) while the second one typically results in a more efficient, higher and uniform N doping. An illustrate of how heteroatoms are doped ‘in situ’ during nanostructured carbon synthesis is provided in Figure 2.20. Dopant precursors are first introduced together with the carbon precursor into the pores of the silica template. After further graphitization and the removal of the template, heteroatom-doped carbon material is obtained. N precursor can be introduced through techniques include CVD (*e.g.* acetonitrile, pyrrole) (Xia & Mokaya, 2005; Yang et al., 2005; Hou et al., 2005) or liquid impregnation (*e.g.* *N,N'*-bis(2,6-diisopropylphenyl)-3,4,9,10-perylenetetracarboxylic diimide (PDI), acrylonitrile, pyrrole) (Liu et al., 2010c; Lu et al., 2004; Shrestha & Mustain, 2010). However, it is more challenging to dope when synthesizing carbon structures using soft templating method. One

study has proposed N-doped mesoporous carbon synthesis by replacing phenol or resorcinol with melamine serving also as N-rich precursor during soft templating synthesis. (Liu et al., 2011c)

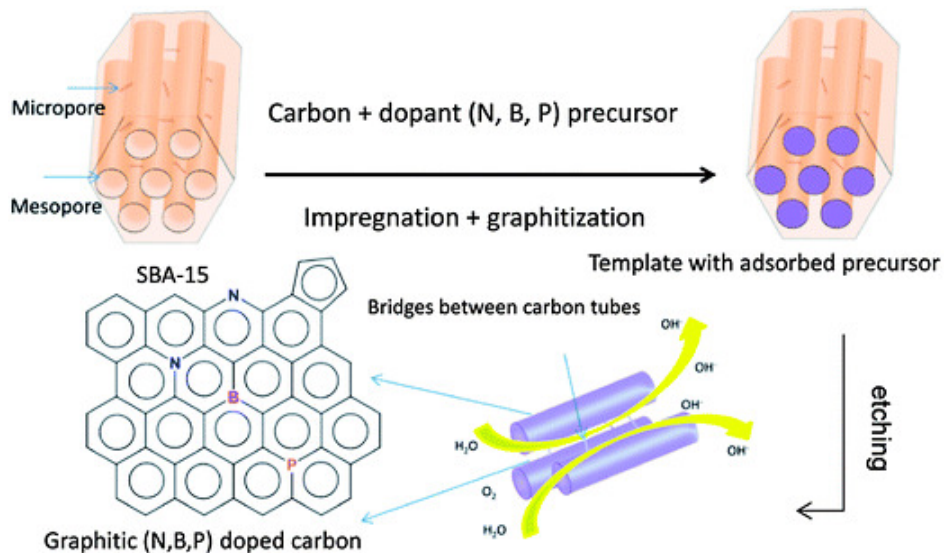


Figure 2.20 ‘In situ’ heteroatom doping using nanocasting method. (Daems et al., 2014)

Recently, the production of nanostructured carbon materials from biomass has attracted much interest.(Raymundo-Piñero et al., 2006; Li et al., 2012b; Wu et al., 2013c; Nguyen et al., 2014; Long et al., 2014; Chen et al., 2013a, 2012a) The approach is fascinating since the material used is renewable, widely available, and cost effective. However, to date, carbon structures produced from biomass typically have low surface area ($< 20 \text{ m}^2 \text{ g}^{-1}$) and are non-porous in the absence of activation or templating. (Zhao et al., 2010) Therefore, the task of developing carbon-based electrode materials with high surface area, porosity, and effective heteroatom doping using simple and cost effective methods still remains.

2.3 Heterogeneous catalyst for electrochemical applications

2.3.1 Fundamentals of heterogeneous catalyst

Catalysts play a pivotal role in 90% of chemical process and the manufacturing of over 60% of the chemical products.(Horváth, 2003) Catalysts can be distinguished based on whether they occupy the same phase as the reaction mixture. Homogeneous catalysts are present in the same phase as their reactants and products (gas or liquid); whereas heterogeneous catalysts exist as a different phase (typically) solid than the phase where reaction occurs. (Davis & Davis, 2003) Heterogeneous catalysis is extremely important in large-scale applications and is at the heart of

modern energy and chemical industries. (Hagen, 2006) The advantage of heterogeneous catalysts is the relative ease in catalyst isolation and regeneration, making continuous chemical process possible. The recyclability also fulfills the requirement for green/sustainable chemistry. (Öhlmann, 1999) Heterogeneous catalyst functions by providing an active surface where a reaction takes place. In this case, gas or liquid phase reactions only happen on the surface of the catalyst (solid) instead of within the gas or liquid phase. An example of heterogeneous catalytic reaction is illustrated in Figure 2.21. As shown, there are generally four stages involved in the heterogeneous catalytic process:

- Adsorption of the reactants on the catalyst surface
- Activation of the adsorbed reactants
- Reaction of the adsorbed reactants
- Desorption of the reaction product from the surface into the initial liquid/gas phase

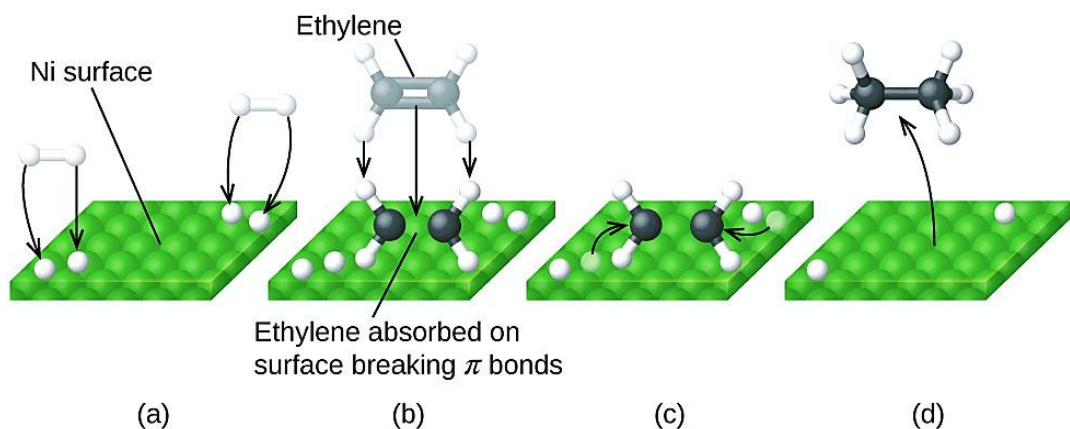


Figure 2.21 Illustrate of 4-step heterogeneous catalytic reaction of $\text{C}_2\text{H}_4 + \text{H}_2 \rightarrow \text{C}_2\text{H}_6$ by nickel (a)

Hydrogen is adsorbed on the surface, breaking the H–H bonds and forming Ni–H bonds. (b) Ethylene is adsorbed on the surface, breaking the π -bond and forming Ni–C bonds. (c) Atoms diffuse across the surface and form new C–H bonds when they collide. (d) C_2H_6 molecules escape from the nickel surface, since they are not strongly attracted to nickel. (<http://chemwiki.ucdavis.edu/>)

The critical limitation, however, is associated with the available active surface area of the heterogeneous catalysts. The adsorption step is typically the rate-limiting one, since it has to wait till the reactant product leaves the saturated active surface of catalyst. The catalytic efficiency of heterogeneous catalyst is thus directly determined by its available active surface area. Moreover, heterogeneous catalysts are generally very expensive (e.g. rare metal like Pt). Since only the surface is effective in catalyzing the reaction, the bulk internal volume is actually wasted. Therefore, to achieve higher catalytic activity and the utilization efficiency of the active catalyst, downscaling the

catalyst size to nanoscale has emerged as a popular approach. Nano-sized catalysts exhibit unprecedented catalytic efficiency due to the dramatically increased surface to volume ratio and open active sites. (Bell, 2003) However, the synthesis of nanocatalysts is challenging since they tend to grow in size to minimize their high surface free energy. The agglomeration may also occur during the catalytic reaction, leading to greatly diminished surface area and deactivation of the catalysts. The recyclability for these nanoparticles is also a problem due to their small size, raising both economics and environmental concerns.

Catalytic activity for heterogeneous catalysts can be expressed in terms of reaction rates (k), preferably normalized to the surface area of the active phase (e.g., metal surface area for supported metal catalysts) that can be characterized by various chemisorption techniques (e.g. Brunauer-Emmett-Teller BET method). Specific rates that are normalized to catalyst weight are also used. However, the best interpretation of catalytic activity is the turnover frequency (TOF), since it is normalized to the number of active sites of the catalysts and represents the rate at which the catalytic cycle turns over. (Deutschmann et al., 2000) TOF is also independent of how much catalyst is used in the reactor and is thus recommended for general comparison between different studies.

Many solid materials are widely used such as metals, metal oxides, or metal sulfides are rather useful heterogeneous catalyst. However, rarely do catalysts of simple compositions used in industry (e.g. pure Ni), and they typically consist of several components. Heterogeneous catalysts can be categorized into several families: unsupported (bulk) catalysts; (2) supported catalysts; (3) hybrid catalysts and several others. The ones that are most relevant to this thesis will be introduced herein.

2.3.2 Metal nanoparticles/carbon (MNP/C) as supported electrocatalysts

A variety of non-noble (Fe, Co etc.) and noble metals (Pt, Pd etc.) are the most effective catalyst used in electrochemical processes. Traditionally, these metals were practiced in their bulk form and their catalytic activity is relatively low. Poor utilization efficiency of the catalysts also leads to economic waste since only the surface of the catalyst contributes to the reaction. Electrochemists have long been working on how to minimize the electrode cost by reducing the catalyst loading without a loss in the catalytic activity, and reducing the amounts of metals is a popular solution. However, metals are high in surface free energy and they have a strong tendency to reduce their surface area by agglomerating during the catalytic reaction. An effective strategy to address the agglomeration of MNPs is to disperse them on a high surface area solid supports that are able to stabilize MNPs during synthesis. Materials as supports need to be mechanically robust, chemically

inert (no inference with the reaction), thermally stable, high in surface area, and possess sufficient porosity. The most commonly used templates for supporting MNPs are inorganic templates like transitional aluminas, SiO_2 , MCM-41, TiO_2 (anatase), ZrO_2 (tetragonal), MgO etc. Other inorganic complexes that are also used include aluminophosphates, mullite, kieselguhr, bauxite, and calcium aluminate.(Deutschmann et al., 2000) In particular for catalyzing electrochemical reactions, MNPs have to be immobilized on a substrate with good conductivity to boost current density during test. Carbon-based materials are promising candidates for this purpose for their mechanical strength, good conductivity, and chemical inertness.(De Volder et al., 2013; Antolini, 2012; Auer et al., 1998) Currently, carbon black is mostly used in industry for supporting various electrocatalysts. Other commercial carbons (graphene, CNTs, active carbon etc.) have also been widely reported for supporting MNPs. (Julkapli & Bagheri, 2015; Li et al., 2003; Joo et al., 2001) For example, Pt-Pd NPs were well dispersed on multi-walled CNTs, and the hybrid catalyst exhibits remarkable electrochemical stability and catalytic activity in ORR. (Golikand et al., 2011)

The preparation for supported metals using carbon support normally requires a combination of the following steps: (i) introduction of the metal precursor on the support (ii) drying and calcination, and (iii) reduction. In the first step, impregnation process is often needed to further enhance the contact between metal precursor and the support. Impregnation promotes the penetration of metal ions into the internal pores of the carbon by homogenizing the mixture of carbon support in the concentrated metal precursor solution. The technique has been widely applied for many carbon substrates (CNTs, carbon spheres, activated carbons, structured carbons etc.) due to its simplicity and good control of the metal loading (Yang et al., 2011). However, problems associated with pore blocking and poor metal dispersion are often described as the main drawback for the technique, especially when the metal loading is high (Wang et al., 2008a). After the impregnation, carbon is filtered, and dried. Post calcination of carbon in oxidizing atmosphere is sometimes needed to further stabilize MNPs by decomposing the metal precursor with the formation of an oxide. The process also removes the gaseous products (water, CO_2) and undesired ions previously introduced. In the final step, MNPs are reduced by either thermal treatment in H_2 flow, or by chemical reducing agent in solution such as hydrazine and NaBH_4 . In H_2 reduction, the purity of the reduction gas has to be high enough to remove water during reaction from the support since vapor can be detrimental for a high dispersion of the metal. (Pinna, 1998)

Current challenge for carbon-supported metal nanocatalysts lies in the poor stabilization of carbon support (Li et al., 2013e) as most of the carbon materials lack functional groups to favorably interact with MNPs. This will lead to low metal-loading, metal agglomeration, and metal catalyst leaching

during reactions. The improvement of surface wettability/solubility of the carbon substrate is also critical for a favorable reduction of MNPs as well as the reactant accessibility of the hybrid catalysts. (Guo et al., 2012)

Mesoporous nanocarboneous materials with high surface area and interconnected pores have been widely used for supported metal catalyst synthesis. This type of substrate was demonstrated to favor highly dispersed metal deposition, and may provide confinement effect for MNP growth (Li et al., 2013e). However, achieving high surface area and porosity often necessitates the use of complicated template synthesis and a tedious activation processes which is either complicated, costly or giving low yield that barely meet the practical demands (Lu & Schüth, 2006; Xu et al., 2008; Banham et al., 2011).

Recently, the strategy of using N-doped carbon as support was shown to remarkably enhance the catalytic activity and durability of the supported metal nanocatalysts compared to their N-free counterparts. (Liang et al., 2013a; He et al., 2013; Lee et al., 2014; Mabena et al., 2011) It was proposed that N-functionality works by reducing the mobility of MNPs and establishing favorable N-metal interaction, resulting in highly dispersed MNPs against aggregation, as well as improved stabilization effect. (Li & Antonietti, 2013; Wong et al., 2013; Mabena et al., 2011; Li et al., 2013e) Prominent examples include the high catalytic performance of Pt/N-carbon catalyzing p-nitrophenol (p-NP) reduction; (Liu et al., 2012b) Pd/N-magnetic carbon catalyzing Heck, Suzuki, and Sonogashira coupling reactions (Yoon et al., 2007); Au/N-graphene catalyzing selective oxidation of benzylic alcohols (Xie et al., 2012). Besides organic reactions, MNP supported by N-doped carbon are more widely investigated in electrochemical processes. Pt/N-carbon composite showed a more superior catalytic activity compared to the commercial Pt/C catalyst, which is attributed to a finer Pt NP size (3.7 nm compared to 4.0 nm). (Li et al., 2010c) Similarly, Jiang et al. prepared N-doped carbon nanofiber (CNF) where N is post-doped using sonochemical process. (Jiang et al., 2011) They further showed that Pt NPs supported on such prepared N-CNF have a lower particle size distribution compared to the N-free counterpart (shown in Figure 2.22), and Pt/N-CNF electrode also display greater electrocatalytic activity towards ORR. Enhanced electrocatalytic activity was also observed on Pt dispersed on N-mesoporous carbon. (Guo et al., 2011) A greater power density was obtained in catalyzing ORR using Pt/N-carbon nanocoil compared to its N-free counterpart, and the synergistic contribution of N-doped carbon substrate was elucidated. (Cao et al., 2011)

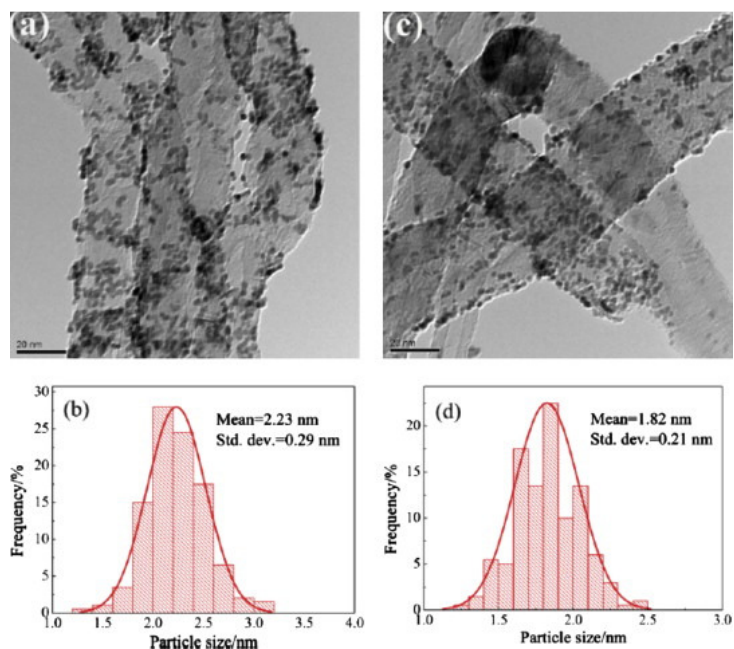


Figure 2.22 HRTEM images of (a) Pt/CNF and (c) Pt/N-CNF. The corresponding particle size histograms based on the measurement of over 200 Pt NPs are provided in (b) Pt/CNF and (d) Pt/N-CNF

Besides noble metals, there is currently growing research interest in replacing Pt-based catalysts with non-noble metal catalysts in many electrochemical derives such as proton exchange membrane cells (PEMFCs), polymer electrolyte membrane fuel cells (DMFCs), and alkaline fuel cell). Non-noble metals are relatively cheap, and have higher tolerance to fuel poisoning (e.g. methanol and ethanol), though their activity has yet to match that of Pt (Bezerra et al., 2008). Within the context, N-doped carbon materials were found to be promising substrate in assisting non-noble metal synthesis due to the strong coordination effect between N and non-noble metals. It was demonstrated in the synthesized Fe/N-C and Co/N-C hybrid catalysts that the presence of heterogeneous phase on carbon support surface was a main requirement for effective catalysis to occur. (Bezerra et al., 2008) A post heat treatment under N₂ (pyrolysis) of the supported metal composite was found to further improve their stability and selectivity towards water. (Wong et al., 2013)

However, as discussed in section 2.2.3, current N-doped carbon materials are usually synthesized using chemical vapor deposition (CVD) (Wang et al., 2010d) or cold plasma treatment (Gong et al., 2009) with N-containing gases, the pyrolysis of N-rich precursors often involving time-consuming activation process (Lota et al., 2007; Shrestha & Mustain, 2010) or the harsh etching of expensive templates (e.g. silica) for the impregnation of Carbon and N precursors after pyrolysis (Ania et al.,

2007; Fuertes & Centeno, 2005). A more cost-effective and facile processing is needed for N-doped mesoporous carbon to be widely used in industry for supporting metal electrocatalysts.

2.3.3 Doped-carbon nanomaterials as metal-free electrocatalyst

Though carbons of various forms (CNT, G, porous carbons) are commonly used as substrate for supported nanocatalysts, they may also be used on their own as heterogeneous catalysts. Actually, activated carbon and glassy carbon have already been used in the past as catalysts in some chemical and electrochemical reactions. (Muñiz et al., 2000; Sarapuu et al., 2003) Research efforts have now moved towards developing high-performance metal-free catalyst with an attempt to replace conventional metal and metal oxide-based catalyst for ORR and oxygen evolution reaction (OER) respectively. The main driving force is in the attractive advantages of carbon-based materials being cheaper, more stable, and widely available.

Most carbon-based metal-free catalyst requires carbon structure to be doped with selected elements (N, B, P, S or Se) for tuning the chemical activities. (Zhang & Dai, 2015) The effect of doping on the carbon properties is associated with the following factors of the doping element: (1) number of electrons in the external shell, (2) electronegativity, and (3) size. The most common doping element is nitrogen (N) and it has a similar size to carbon with one electron more than carbon in the external shell. The atomic structure of a N-doped carbon is illustrated in Figure 2.23, N may exist in four bonding configurations: pyridinic (N1), pyrrolic(N2), graphitic(N3–N4), and oxidized pyridinic. N1 and N2 atoms positioned at the edge or defect sites, which do not increase the number of electrons in the delocalized π -system. In contrast, N3-N4 replace carbon atoms within the graphitic structure to share the same configuration as graphitic carbon atoms, and introduce extra electrons in the delocalized π -system. Pyridinic (N5) in its oxidized form may also exist. (Sharifi et al., 2012) The enhanced electrochemical activity is generally related to the lone electron pair of N1 and an extra electron in the delocalized π -orbitals donated by N3-N4. (Shao et al., 2008) Moreover, N-doping creates defects not only within the carbon structure but also on the edge. Since these edge defects have lower coordination, they can be effectively translated into active sites for catalytic reactions. (Alexeyeva et al., 2010)

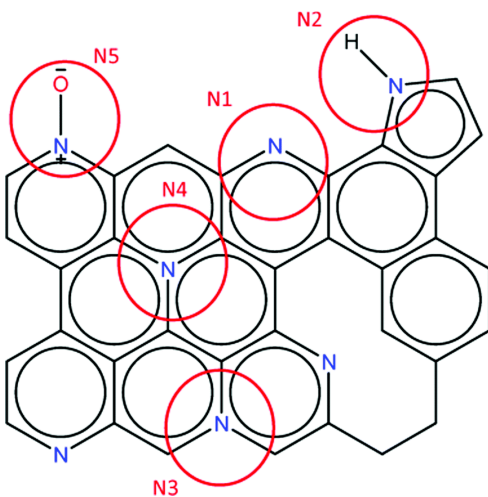


Figure 2.23 Illustrate for the atomic structure of a N-doped carbon.(Daems et al., 2014)

Among various doping elements, N is by far the most popular one for carbon-based metal-free catalyst. N-doped carbons typically exhibit a high conductivity resulting from π -delocalization, as well as a higher catalytic stability and resistance to CO and methanol poisoning than Pt/C. (Liu et al., 2010c) Under careful structural engineering, remarkable catalytic activity can be obtained that is comparable to metal-based catalysts. For example, it was found that vertically aligned N-CNT arrays exhibit a 3-times higher the electrocatalytic activity and durability than that of the commercial Pt/C electrodes in catalyzing ORR process. (Gong et al., 2009) It was further demonstrated by theoretical calculation that the high catalytic activity of doped-carbon catalyst in ORR is attributed to the doping-induced charge redistribution on adjacent carbons, which changed the O₂ chemisorption mode, effectively weaken the O–O bonding and facilitate the ORR process. (Gong et al., 2009) Recent papers have proposed promising applications of various N-doped carbon nanomaterials for catalyzing a wide variety of electrochemical processes that are crucial reactions in fuel cells, metal-air batteries, water splitting for fuel generation, and dye-sensitized solar cells.(Liu et al., 2015a; Zhang et al., 2014b; Ju et al., 2013; Zhang et al., 2015; Zhao et al., 2013b; Kumar et al., 2013)

Several parameters should be carefully considered in the design of N-doped carbon synthesis that critically impact their catalytic performance: the surface area, porosity, degree of graphitization, number of edge sites, and the position of N within the carbon structure. (Su et al., 2013) Carbon materials having high external surface and sufficiently large pores (i.e. mesopores) offer a large amount of active sites that can also be easily accessed. (Gavrilov et al., 2012) A higher graphitization degree offers a higher conductivity, facilitating electron transfer. However, there is a

trade-off when choosing the proper calcination temperature since a higher temperature tends to decrease the surface area of the carbon structure due to sintering but at the same time increases its graphitization degree.(Oh et al., 2011) Proper N-doping (doping content and the type of doping) is also crucial, which can be controlled by different doping methods, the type and amount of N-precursor used, and carbonization parameters.(Zhu et al., 2013; Liu et al., 2010b, 2005)

Much less works have explored the application of doped carbon materials with other element (i.e. B, P, S, Se and I) as metal-free electrocatalysts. In these published studies, similar catalytic activity and stability have also been demonstrated in ORR, however with quite different mechanisms accounting for catalytic activity compared with that of N-doped carbons. For example, elements like B and P exhibits a rather diverse electronegativity (EN) than C, thus the catalytic activity mainly arises from the disruption of the uniformity of the charge distribution in the carbon structure by these dopants. In contrast to N, the EN of B and P is lower than C, which tend to donate electrons to carbon and thus create a partial positive charge on the dopant atoms. In this case, the active sites become the dopant element instead of the neighboring carbon atoms. (von Deak et al., 2010; Wang et al., 2011)

Although the exact catalytic nature of various doped-carbon systems requires more in-depth theoretical study and experimental investigation, the promising results widely observed so far have promised their future contribution in various sustainable energy devices as electrocatalysts. The current challenges that need to be resolved, which limit its commercialization are tedious fabrication, harsh synthesis condition, high processing cost, and relatively low activity compared with metal-based catalyst.

2.3.4 MNPs supported by mesoporous carbon for electrode modification and electrochemical sensing

Electrochemical sensing, is one of the most important and powerful tools in analytical chemistry. The modification of an electrode surface with an intelligently-designed modifying layer is a popular strategy used for electrochemical sensors towards either enhanced sensing sensitivity or added functionality or specificity. (Wang, 1991) The modifying layer can be fabricated by simply drop coating the suspension containing modified particles onto the bare electrode. The modified particles can also be formulated into a carbon paste and coated onto the electrode. In recent years, various mesoporous nanomaterials have been found to be promising as electrode modifier. The advantages of these materials are summarized below: (i) enormous specific surface area (more surface-active

sites, ideal for immobilizing suitable reagents); (ii) easily accessible pores (efficient mass transport); and (iii) mechanical strength. (Walcarius, 2013) Studies have been carried out to investigate the impact of the mesoporous modification of the electrode on the kinetics of mass transfer in the solution. The observation strongly supports the crucial role of mesoporous material as the electrode modifier in effectively enhancing the sensitivity due to more efficient mass transfer induced by the porous structure. (Walcarius, 2008) As shown in Figure 2.24, bare glassy carbon (GCE) electrode showed a very weak redox response in a solution mixture of dopamine(DA), uric acid (UA), and ascorbic acid (AA) and the peak is not distinguishable. In contrast, it is feasible to achieve simultaneous detection for the three with mesoporous carbon modified GCE evidenced by well-resolved peaks, enhanced current response and lower overpotential. (Zheng et al., 2009) The superior electrochemical performance was proposed to be due to the improved mass transfer kinetics related to high surface area and easily accessible pores, as well as catalytic capabilities (edge-plane graphite sites). Due to the same reasons, mesoporous nanostructured carbon is often found to outperform CNT and G, in terms of sensitivity, extended linear range, and lower detection limit in sensing applications. (Zhu et al., 2008; Zhou et al., 2008)

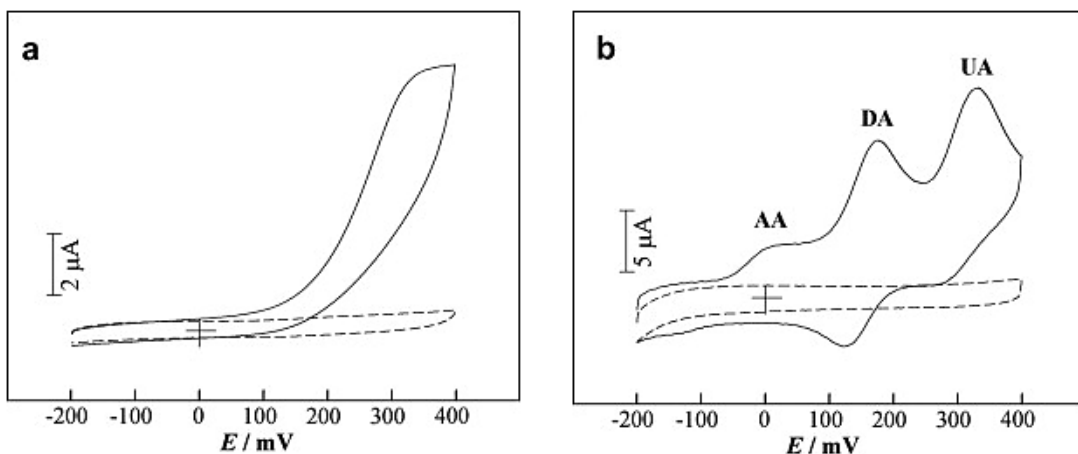


Figure 2.24 Cyclic voltammetry of (a) bare glassy carbon electrode (GCE) and (b) mesoporous carbon modified GCE in pH 7.4 phosphate buffer solution without (dotted line) and with (solid line) the mixture of 0.25 mM ascorbic acid (AA), 0.25 mM dopamine (DA) and 0.5 mM uric acid (UA) at a scan rate is 100 mV s^{-1} . (Zheng et al., 2009)

The surface of mesoporous materials termed as electrode modifier on the electrode may also serve as an ideal support for immobilizing another functional reagent such as metal nanoparticles (MNPs). Such configuration is widely adopted in electrocatalytic sensors where MNPs are immobilized on

the mesoporous support on the electrode surface and serve the important function of catalyzing the electrochemical redox reaction on the surface of the electrode reduce the overpotential of the reaction. (Walcarius, 2015) In such design, mesoporous carbon acts as an intermediate layer between MNPs such as Pt NPs and the electrode material such as glassy carbon. The existence of mesoporous carbon not only assists the highly dispersed reduction and stabilization of MNPs but also reduces the mass transfer pathway and facilitate the electron transfer of the electrochemical reaction. Compared with other mesoporous nanomaterials such as silica, carbon material has the apparent advantage of having good electrical conductivity, which enables facile electrochemical reduction of metal precursor directly onto the mesoporous carbon structure on the electrode. (Su et al., 2010) The conductivity of the modifier also facilitates the efficient electron transfer from the MNPs to the electrode surface, providing synergistic effect of the carbon support and the catalytic nanoparticles.

Electrocatalytic detection of H₂O₂ using Au, Pt, Pd NPs/mesoporous carbon modified electrode have been reported using commercial carbon CMK-3. (Wang et al., 2010b; Bo et al., 2010b, 2010a) Another widely explored area using supported metal electrocatalysis is biosensing, especially non-enzymatic glucose sensing. Although some pure mesoporous materials, metals (Ling et al., 2011), metal alloys (Li et al., 2013a), or carbon (Ndamanisha & Guo, 2009) by themselves have demonstrated their capability of sensing glucose, but the detection is only possible in strong alkaline media. Using mesoporous carbon supported MNPs such as such as Pt (Su et al., 2010) as the electrocatalyst, the glucose detection was readily achieved at low overpotentials in media close to neutral pH. The Pt/mesoporous carbon modified electrode also showed high resistance to poisoning by chloride ions and the stable sensing performance is free from the oxidation interference of other common species. In another study, PtPd alloy (Bo et al., 2011) was reduced onto porous onion-like carbon by microwave irradiation. When PtPd/onion-like carbon modified electrode was used, the direct detection of glucose was also achieved with enhanced current response and good selectivity against AA, UA, and DA.

As reviewed in Chapter 2, nanotechnology has provided many new opportunities to innovative electrochemical applications include supercapacitor (SP) devices, catalysts, and electrochemical sensors. Numerous nanostructured materials with precisely engineered structure and functionalities are keep being reported, and the increasing progress promises transformations of many traditional industries. However, critical challenge associated with the research fields remains in the development of a desired functional nanomaterial using environmentally benign resources and low cost processing, to allow a wide industrial adoption. The nanomaterial of CNC with attractive

physiochemical features provides a rather versatile platform to be engineered into various highly functional systems using simple chemistry. In addition, using biomaterial has the apparent advantages of being cost-effective and sustainable. In this thesis, attempts have been made to transform CNC into various materials of well-controlled morphology, structure, and electrochemical properties for different electrochemical applications.

Chapter 3 Characterization

This chapter is intended to introduce the basic background of the main instruments used for material characterization. Electrochemical techniques for evaluating the capacitive material and the protocol for catalytic test to evaluate the synthesized catalyst materials are introduced. An understanding of these tools and tests can help us better comprehend the interpretation of the results in the subsequent chapters.

3.1 Material characterization

3.1.1 Electron microscope (EM) for imaging

EM consists of many powerful tools for resolving the ultrastructure of various organic or inorganic materials. EM uses high energy electron beam (10^5 smaller than the wavelength of visible light photons) as a source of illumination to achieve resolution much higher than optical microscope down to nanoscale.

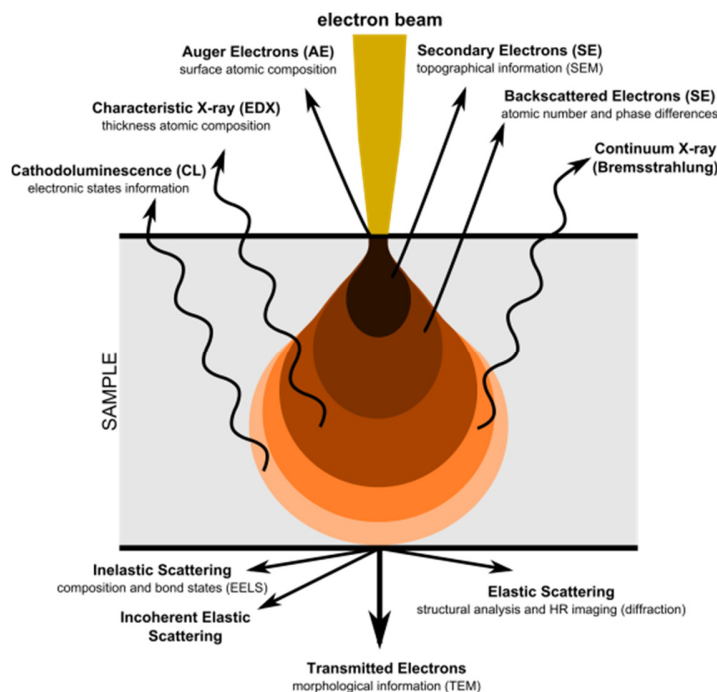


Figure 3.1 Illustrate of the phenomena induced by electron beam-sample interaction. (source: Wikipedia)

When the electron beam is accelerated and reaches the sample, a wide variety of signals are generated as a result of electron beam-sample interactions. An illustration of different signals induced from such interaction is given in Figure 3.1. These signals provide valuable information on the structural or compositional features of the sample.

● Scanning electron microscopy (SEM)

SEM is one of the most commonly used technique in nanotechnology for direct imaging the topographical feature of solid materials. The layout of SEM instrument is shown in Figure 3.2(a). SEM utilizes a focused electron beam under high vacuum to raster on the surface of the specimen line by line. The signals scattered (mostly secondary electrons) from the surface of the sample are captured by electron detectors and the information is transferred to a computer for digitizing the image.(Zhou & Wang, 2007) Since more electrons can escape the sample and be detected at the edge, it will appear brighter on the image. Such ‘edge-effect’ is illustrated in Figure 3.2(b), and it is the dominant factor from which good contrast reflecting the exact surface topography of the sample is obtained on SEM image Figure 3.2(c) Besides providing the surface visualization of the sample, SEM can also unveil the information on sample’s chemical composition, crystalline structure of the sample by collecting other signals (e.g. X-rays).

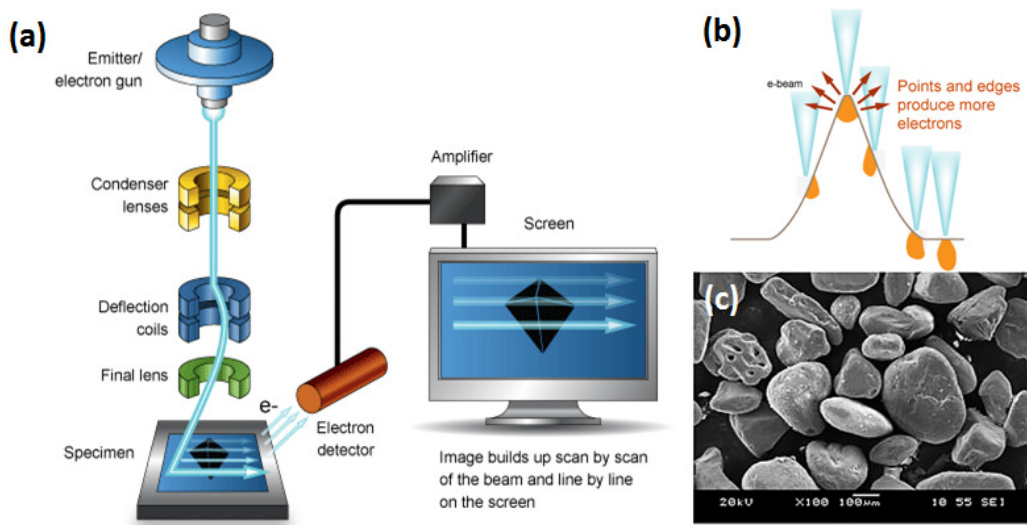


Figure 3.2 (a) SEM layout and function (b) scheme of topological contrast and (c) example of a typical SEM image reflecting surface topography of the mineral sand. (Source: <http://li155-94.members.linode.com/myscope/>)

One limitation of SEM though is that samples have to be conductive to avoid charging where images appear overly bright, drifted or even distorted. Spray with gold is mostly used for non-conductive materials prior to imaging. In this research, since all the materials are conductive, there is no special need for sample preparation. For SEM, a small amount of samples in a dried powder form are loaded onto one side of the double-sided carbon tape with the other side already taped on top of the sample stub. Then the sample stub is mounted onto the sample holder plate and introduced inside the vacuum chamber for further imaging.

● **Transmission Electron Microscopy (TEM)**

Similar to SEM, TEM also uses a focused electron beam to interact with the specimen except that the electron beam passes through a series of electromagnetic lens and illuminates the whole area of the sample. Moreover, as the name implies, it deals with electron signals that pass through the sample instead of being scattered. The signals are thus collected from below the sample, magnified and projected onto a phosphorescent screen, and is captured by a high resolution camera. Therefore, the samples suitable for TEM have to be sufficiently thin (i.e. electron transparent). Denser areas or areas containing heavier elements appear darker on the TEM image since fewer electrons are able to transmit through (Egerton, 2005). Compared to SEM, TEM images elucidate the internal feature of the sample instead of surface, and TEM can achieve much higher resolution than SEM. High resolution TEM can achieve the direct imaging of crystalline lattice with a resolution of 0.5 angstroms. Therefore, TEM can be used to obtain different information on the sample include morphology, crystallography or composition etc. However, SEM has the advantage of providing a broader view for mass sample imaging. Figure 3.3 shows the difference between TEM and SEM technique when imaging the same cubosome sample.

In this research, TEM images are captured with a Philips CM10 electron microscope under 60 keV acceleration voltage. TEM samples were prepared by first dispersing the sample particles in a water/ethanol solution at a low concentration of 0.01-0.05% wt%. Then using a plastic pipette to extract, a small volume of suspension is transferred onto a formvar copper grid (200 mesh coated with carbon) and dried at room temperature.

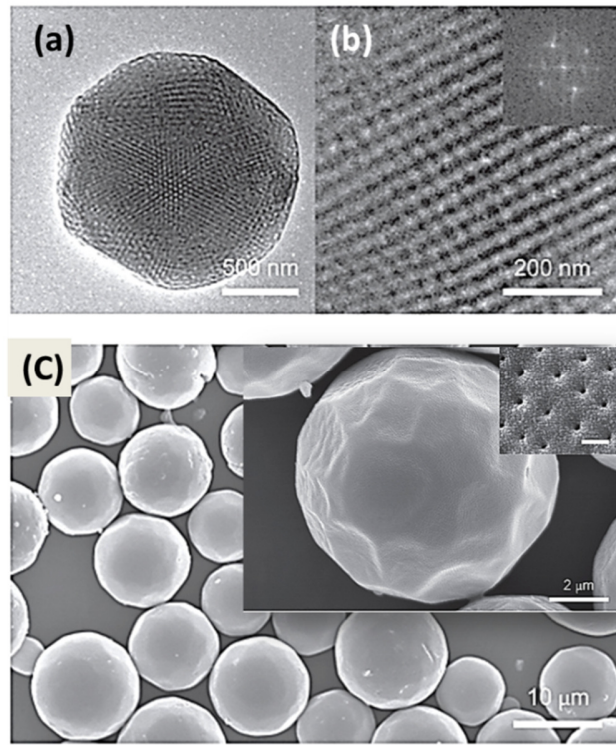


Figure 3.3 Comparison of images for polymer cubosomes using (a) TEM imaging showing the internal structure and where magnified lattice configuration was resolved in (b), and (c) SEM imaging providing a wider view of the samples with inset showing the topography of one cubosome.(La et al., 2014)

3.1.2 Spectroscopic techniques

Spectroscopy is a branch of science that studies various phenomena induced by the interaction of electromagnetic radiation with matter. Electromagnetic radiation can expand over a wide range of frequency and wavelength (Figure 3.4). The electromagnetic spectrum can be divided into many different regions based on diverse types of atomic or molecular transitions that give rise to the absorption or emission of photons. Different spectroscopic techniques are made possible by analyzing either the energy transfer between a photon and the sample, or the change in electromagnetic radiation due to scattering, dispersion, refraction, etc.

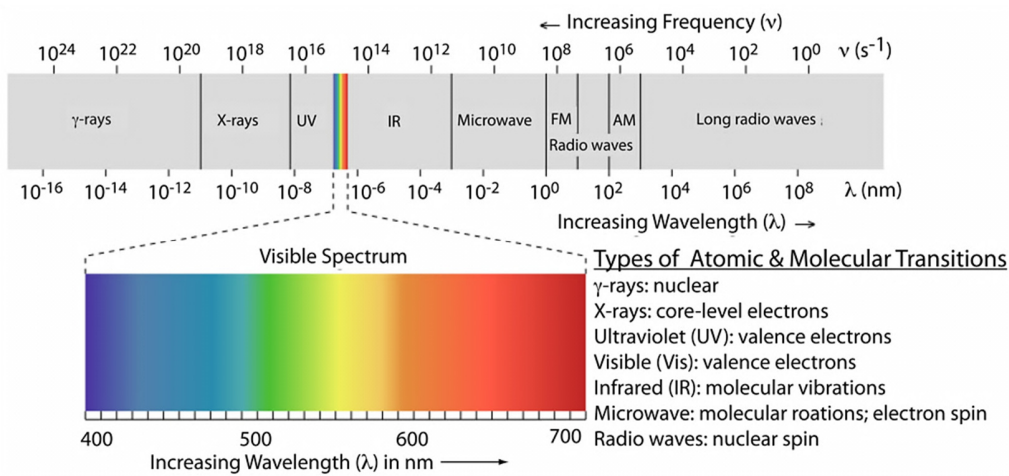


Figure 3.4 The electromagnetic spectrum showing the boundaries between different regions and the type of atomic or molecular transition responsible for the change in energy. The colored inset shows the visible spectrum. (www.chemwiki.ucdavis.edu)

● UV-visible spectroscopy (UV-Vis)

UV-Vis is one of the oldest spectroscopic techniques that are widely used for the quantitative analysis of the analyte in a sample (mostly solution). The incident light from UV-Vis is in the UV and visible range where molecules of the sample undergo electronic transitions upon absorbing the energy. UV-Vis then measures the transition of electrons from the ground state to the excited state (i.e. the absorption). (Rajarathnam, 1953) In a typical UV-Vis test, samples are typically placed in a cuvette, which are typically rectangular-shaped container with an internal width of 1 cm (i.e. path length L). According to Beer-Lambert law shown in Equation 3.1, the absorbance of a solution has a linear relationship with the concentration of the absorbing species in the solution at a fixed path length:

$$\text{Equation 3.1} \quad A = \epsilon lc$$

where A is the absorbance (no unit), ϵ is the absorption coefficient ($\text{L mol}^{-1} \text{cm}^{-1}$), l is the path length (cm), and c is the concentration (mol L^{-1}). Therefore, UV/Vis spectroscopy can be used to quantitatively determine the concentration of the analyte in a solution.(Calloway, 1997)

Since the absorption spectrum reveals information on electronic transition from the occupied molecular orbital to the unoccupied molecular orbital, the shift in wavelengths of absorption peaks can also be correlated to band gap change of semiconductor or conjugated polymers. Figure 3.5(a) shows the four possible electronic transitions in a molecule where $\sigma \rightarrow \sigma^*$ and $n \rightarrow \sigma^*$ transitions

require relatively higher energy (i.e. short wavelength) while $n \rightarrow \pi^*$ and $\pi \rightarrow \pi^*$ occur in lower energy longer wavelength UV region. A typical UV spectrum for tetraphenylcyclopentadienon is also provided in Figure 3.5(b) where two electron transitions within UV region can be observed. Therefore, UV-Vis is also used to study the effect of chemical modification of conjugated polymers on their bandgap properties. For instance, a higher conjugation degree can lead to a redshift and more intense absorption peak of conjugated polymers in UV spectra.

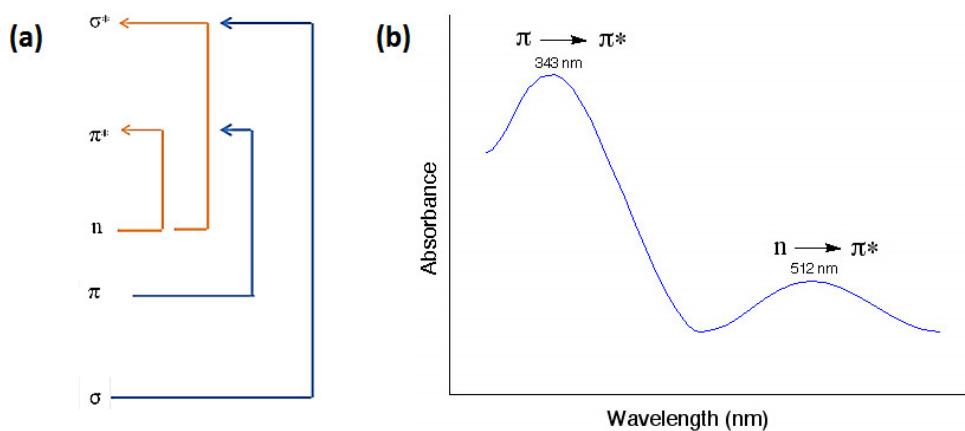


Figure 3.5 (a) Four types of possible electronic transitions in molecules and (b) An UV-vis spectrum of tetraphenylcyclopentadienon. (<http://plasticphotovoltaics.org>)

● Fourier transform infrared spectroscopy (FTIR) and Raman spectroscopy (RS)

FTIR and RS are two complimentary techniques widely used to characterize the vibrational energy of nanomaterials. As a vibrational spectroscopy, FTIR is more sensitive to the asymmetrical vibrations (dipolar bond) and RS is more sensitive to symmetrical vibrations (symmetrical bond). In FTIR, light consisting of a broadband in IR region is passed through the sample simultaneously. The light is then absorbed in different amount at distinct frequencies (i.e. vibrational frequency) by different bonds in the sample and get measured. The resulting spectrum provides a molecular fingerprint which correspond to the vibrations frequencies of different bonds in a sample. Though quantitative measurement is possible by correlating the peak intensity with the amount of material present in a sample, FTIR is mostly used to qualitatively identify the type of material existed. Moreover, only vibrations due to dipole oscillating is IR active, therefore FTIR is more sensitive for identifying hetero-nuclear functional group vibrations and polar bonds. RS, in contrast, uses a monochromatic light source to excite vibration of bonds in a sample, and the relative frequencies at which samples scattered light are measured. Also, RS relies on a change in polarizability of a

molecule, and is more sensitive to homo-nuclear molecular bonds (e.g. C-C, C=C and C≡C bonds). This is extremely suitable for the characterization of graphite compounds.

In this research, all the FTIR characterizations were conducted using a Bruker Tensor 27 FT-IR spectrometer. Before detection, the dried samples were mixed with KBr (1:100 mass ratio), well grinded, and then compressed into pellets. FTIR spectra was scanned at a resolution of 4 cm^{-1} between 400 and 4000 cm^{-1} and averaged over 32 scans. Raman scattering spectra were recorded on a HORIBA Scientific LabRAM HR system using a 532.4 nm laser. There is no specific sample preparation for RS and the materials in the powder form are simply loaded onto a glass slide (less than 5 mg), gently flattened on the surface using another glass slide and then transferred into the detection chamber under the microscope. Since it is a non-destructive technique, multiple detection can be performed on the same sample.

● X-ray diffraction (XRD)

XRD is a technique commonly used to identify the crystalline materials. XRD works by shooting a high energy electron beam to a metal plate to generate X-rays. Then the X-rays pass through a slit and hit the sample from a certain angle. During an XRD test, a series of angles will be tested by changing the X-ray arm and the scattered X-rays from the sample surface further hit a photographic film and get counted. For crystalline materials, some of the rays will pass through the lattice while others hit the atoms and get scattered. The structures of crystals (e.g. lattice spacing) can thus been identified by XRD based on Bragg's law in Equation 3.2),

$$\text{Equation 3.2} \quad n\lambda = 2d\sin\theta$$

where n is an integer, λ is the wavelength of the x-ray, d is the spacing of the crystal layers in the atomic lattice, and θ = the incident angle (the angle between incident ray and the scattering plane). The law suggests that the scattered radiation will undergo constructive interference only when the angles of the generated x-rays are the same as the incident angle. Therefore, when this angle (Bragg angle) is satisfied, an intensive peak will be detected. Depending on the crystal structure of the sample, the peak can be associated with the interaction with a specific lattice plane.

Besides the lattice spacing d , XRD can also provide information about the crystallite size based on scherrer (Equation 3.3):

$$\text{Equation 3.3} \quad L_c = K\lambda / (\beta \cos\theta)$$

where L_c is the mean size of the ordered crystalline domains, K is a dimensionless shape factor, λ is the X-ray wavelength; β is the full width at half maximum of the peak in radians, θ is the Bragg angle. This equation provides a simple relationship between the size of the crystallite in the sample and the broadening of a peak in a diffraction pattern. In practice, a spectrum of diffraction intensity versus the angle between incident and diffraction beam will be directly compared to a huge database containing diffraction spectra of thousands of known crystalline substances to find a match.

● X-ray photoelectron spectroscopy (XPS)

XPS is a surface-sensitive quantitative spectroscopic technique to investigate the surface chemical composition of conducting and non-conducting samples. The technique is based on the photoelectric effect where an incident X-ray photon hits the sample, interact with a core electron, and result in the ejection of the electron from the atom Figure 3.6(a). The general layout of a XPS instrument is shown in Figure 3.6(b). The sample is exposed to an incident X-ray beam and once the photoelectric effect causes electrons to escape from the atom, the kinetic energies E_k of the emitted photoelectrons will be collected by the electron analyzer. E_k of the emitted electron is dependent on the incident X-ray and binding energy of the atomic orbital from which it originated Equation 3.4):

$$\text{Equation 3.4} \quad E_b = h\nu - E_k - \Phi_{\text{analyzer}}$$

where $h\nu$ is the energy of the incident X-ray, E_k is the kinetic energy of the emitted electron, Φ_{analyzer} is the work function of the electron analyzer. The XPS spectrum is usually given by intensity (counts per second) as a function of binding energy and each photoelectron peak elucidate a certain chemical element that can be identified by its characteristic energy.(Smart et al., 2011). An example XPS spectra determined from the XPS machine is not sensitive to light element such as hydrogen or helium, but can detect most of other elements.

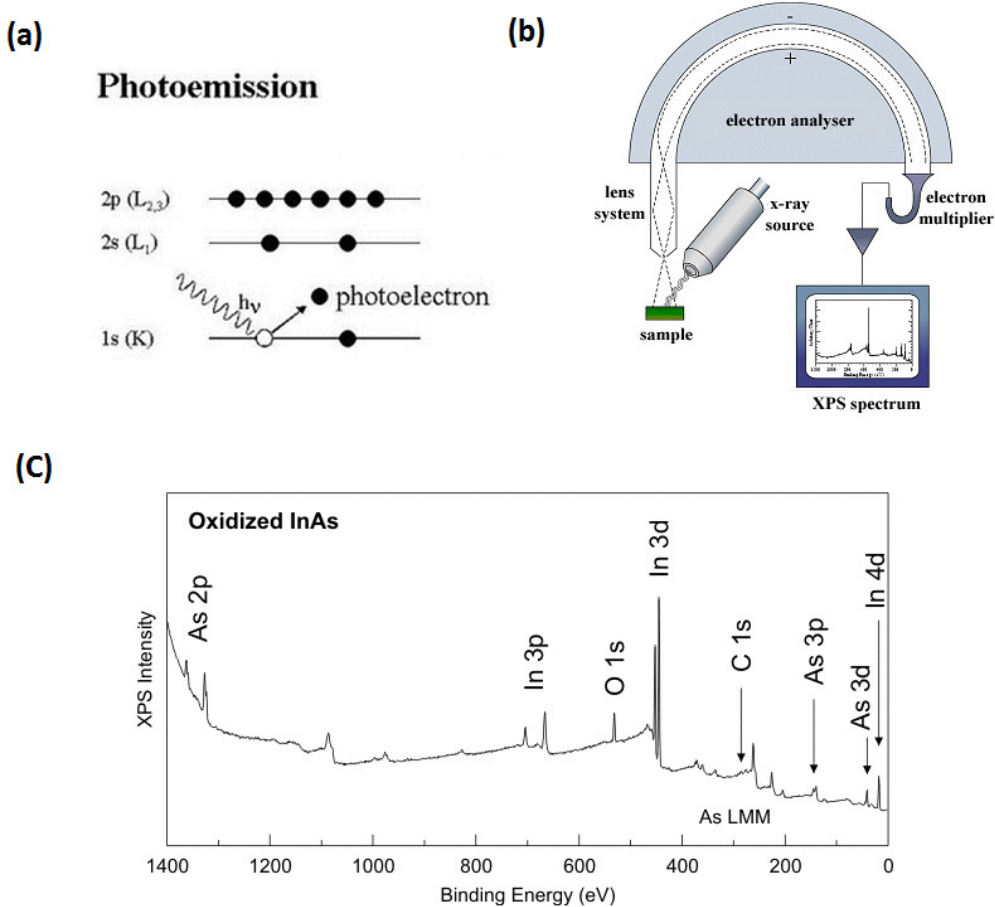


Figure 3.6 (a) Illustrate of the process of photoelectric effect, (b) typical configuration of XPS instrument (source: <http://www.tut.fi/en/home>) and (c) XPS spectra of an oxidized InAs surface (source: <http://biointerface.org/surface/xps/>).

3.1.3 CHNS Elemental analysis

As mentioned above, XPS is not sensitive to light element, therefore, CHNS elemental analysis is a good complementary technique since it can provide the precise measurement for the weight percentage of carbon (C), hydrogen (H), nitrogen (N) and sulfur (S) in a sample. In the elemental analysis, samples are exposed to a combustion process (up to 1800 °C) in an oxygen-rich atmosphere. As a result of the combustion, elements originally in the sample are converted to their combustion products: C to CO₂, H to H₂O, N to N₂ or NO_x, S to SO₂. Then these products will go through a series of cells for separation and where their mass are measured individually to calculate the composition of the initial sample. An illustration of a CHNS elemental analyzer is shown in Figure 3.7.

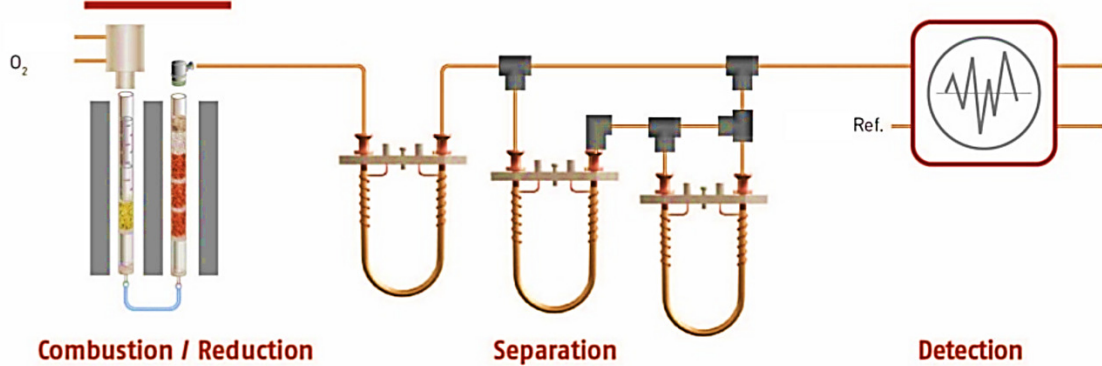


Figure 3.7 The functional diagram of a typical CHNS elemental analyzer. (Source: Elementar Americas Inc.)

3.1.4 Zeta potential (ζ -potential)

ζ -potential is a physical property displayed by any particle in a suspension and is a key parameter that critically determines the stability of particle suspension. The magnitude of the ζ -potential represents the strength of electrostatic repulsion between two particles. Based on electric double-layer theory, charged particles in a suspension will attract a layer of tightly bounded counter-ions and another layer of loosely bounded ions forming the diffuse layer. An example of a negatively charged particle in a suspension is shown in Figure 3.8(a). The diffuse layer has certain ionic mobility and travels with the particle and those outside remain stationary and the boundary in between is the so-called slipping plane. ζ - potential measures the potential difference between the particle surface to the slipping plane.

The measurement of ζ -potential is based on the electrophoretic mobility of the particles. Figure 3.8(b) shows the typical cell in the ζ -potential instrument where the suspension containing the charged particles was injected into the cell with two parallel electrode plates. When an oscillating electric field is turned on, particles will move towards the oppositely charged electrode and the velocity of the particles is measured. ζ -potential can then be readily resolved from the measured electrophoretic mobility of the particle based on Henry equation below:

$$\text{Equation 3.5} \quad U_e = 2\epsilon z f(Ka)/3\eta$$

where U_e is electrophoretic mobility, z is ζ -potential, ϵ is dielectric constant, $f(Ka)$ is Henry's function and Smoluchowski approximation is commonly applied were $f(Ka)$ is equal to 1.5, and η is viscosity.

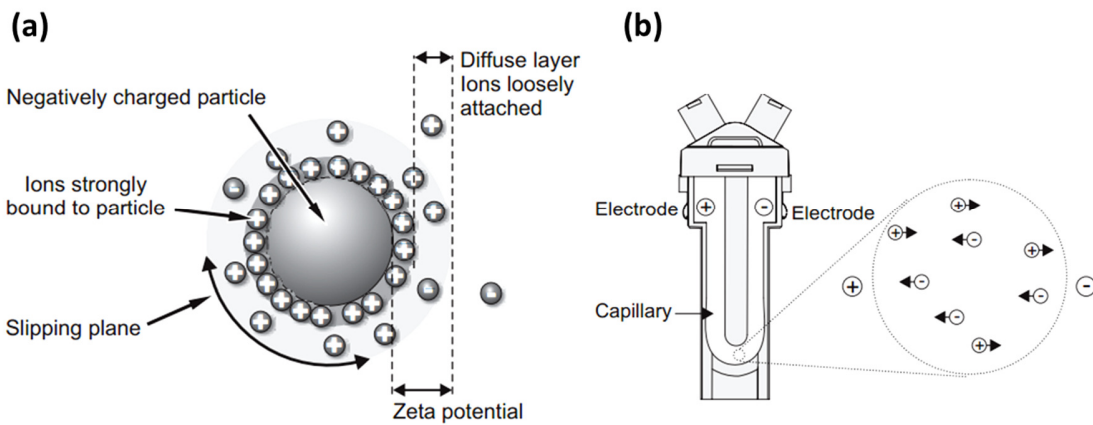


Figure 3.8 Illustration showing (a) zeta potential of a negatively charged particle in a suspension and (b) micro-electrophoresis system is a cell with electrodes. (Source: zetasizer nanoseries user manual)

3.1.5 Thermal dynamic analysis (TGA)

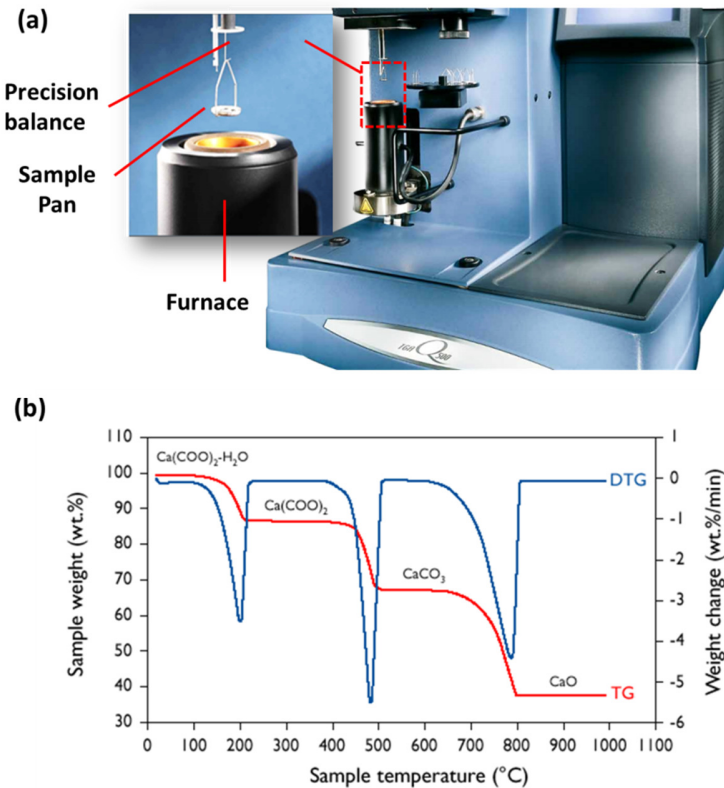


Figure 3.9 (a) Photos of TGA instrument showing the core units and (b) example of TGA measurement for calcium oxalate monohydrate showing both TG (red) and DTG (blue) curves. (Source: TA instrument user manual and Philips Research bulletin)

TGA is a thermal analysis that measures the weight loss of a material as a function of increasing temperature. TGA is a rather useful technique in material science for studying the thermal stability and decomposition patterns of the material, and the determination of organic/inorganic content in a sample. As shown in Figure 3.9, the key units of the TGA instrument include a sample pan that is hand down and supported by a precision balance, and a programmable furnace that can heat the sample at a controlled rate. The TGA instrument continuously weighs a sample as it is heated under the chosen atmosphere (e.g. air, Ar etc.) The result from the TGA measurement is provided in both TG curve where the remaining mass percentage of the material is plotted against the temperature, as well as DTG curve which is the 1st derivative of the TG curve. An example is shown in Figure 3.9(b). While TG curve provides information such as onset weight loss, weight decomposition pattern, and weight retention at different temperatures, DTG gives a clear picture of at which temperature the greatest weight loss takes place indicated by the sharp peak. For TGA measurement, samples have to be completely dried to avoid any interference of moisture at early stages of the test.

3.1.6 Brunauer-Emmett-Teller (BET) surface area analysis

Nanomaterials are known to have enormous surface area and often have interesting porous structure. BET analysis is the most commonly used technique that determines the external surface area of the particles and provide insight into the open pores (e.g. pore size, pore volume, *etc.*) The measurement is based on BET theory where the exposed surface area of a material is determined by the amount of physical adsorption of a gas on the surface. In BET analysis, N₂ is typically used due to its strong interaction with solids and the availability in high purity. Before samples are measured, a degas process is necessary to remove the pre-adsorbed gases and vapors reside in the material. To enhance the interaction between gas and the solid, the measurement is usually performed in liquid N₂. After the known amount of N₂ is released, BET will monitor the pressure change during the adsorption process. Once the surface of the sample is saturated with the adsorbed gas molecules, the sample is removed from N₂ and the adsorbed N₂ is released and quantified upon heating. The profile of the N₂ adsorption-desorption is presented in the form of a BET isotherm where the amount of gas adsorbed is plotted against relative pressure. According to IUPAC standard, isotherms can be classified into six types representing different pore features (i.e. texture) of the structure. (McCusker et al., 2001) Pores are defined as three categories:

- Micropores: size below 2 nm
- Mesopores: size of 2 nm-50 nm
- Macropores: size above 50 nm

As shown in Figure 3.10, Type I typically refer to microporous material with the exposed surface area almost exclusively inside the pores; Type II are usually observed for nonporous or macroporous solid; Type III refers to non-porous material with weak adsorbent-adsorbate interaction. Types IV with a hysteresis loop commonly associated with mesoporous material. Type VI isotherms are similar to Type III with weak adsorbent-adsorbate interaction except that the pores are mostly mesoporous. (Li et al., 2014) The adsorption/desorption isotherms can be used to calculate the specific surface area, pore volume, pore diameter of the measured samples. In practice, all the results can be generated in a form a report of summary or raw data for plotting.

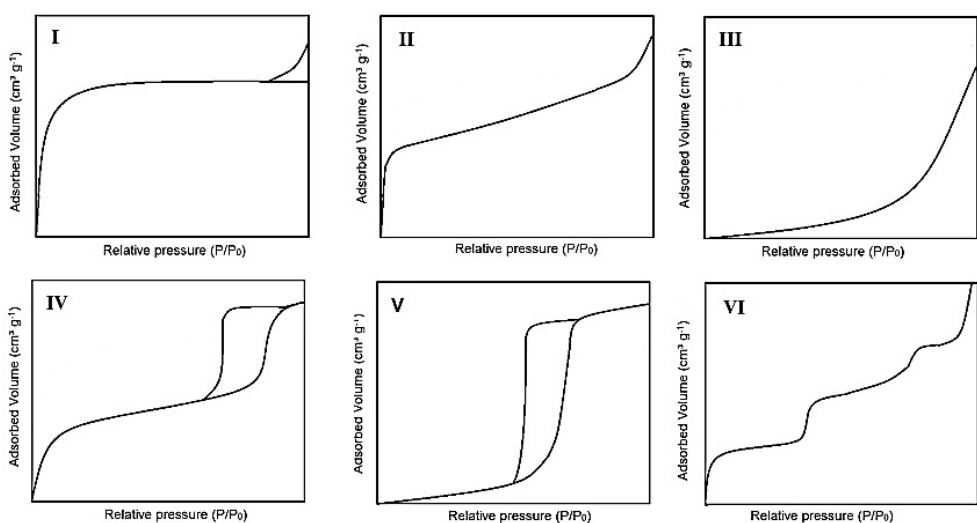


Figure 3.10 The IUPAC classification of isotherms. (McCusker et al., 2001)

3.2 Electrochemical characterization

3.2.1 Four-point probe conductivity measurement

Conductivity is one of the most important properties for semiconducting or conducting materials and they can be related to the structural defect and impurity of the sample. The four-point probe method is one of a most efficient and accurate way of measuring the bulk conductivity of the sample. As shown in Figure 3.11(a), the apparatus consists of four equally placed tungsten metal tips as electrodes that made to contact the surface of the sample during the test. A current is then passed through the outer two probes and the voltage across the inner two probes is measured. This technique is especially advantageous for measuring semiconducting materials since it avoids the contribution of contact resistance (R_c) between the probe tip and surface of the sample (R_c is cancelled out in calculating R in the circuit illustrated in Figure 3.11(b)). In comparison,

conventional two-probe apparatus tends to overestimate the resistance of the sample by counting in both R_c where the calculated conductivity tends to be lower than the real value.

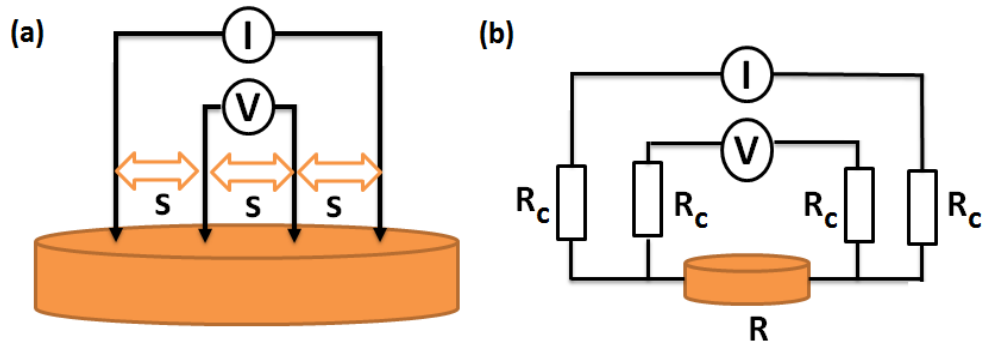


Figure 3.11 (a) Diagram of four-point probe conductivity measurement and (b) equivalent circuit for four-point probe setup.

Equation 3.6 is based on the assumption that the thickness t of the sample is less than half the distance between the probes S , from which the bulk resistivity of sample can be readily resolved from four-point probe measurement (Smits, 1958):

$$\text{Equation 3.6} \quad \rho = \frac{\pi}{\ln 2} t \left(\frac{V}{I} \right) = 4.523 t \left(\frac{V}{I} \right)$$

where ρ is the resistivity of the sample (inverse of conductivity), t is the sample thickness, V is the potential measured, I is the current applied. In practice, the material in powder form is pressed under high pressure using hydraulic press into a thin dense pellet. The measurement is performed on three different regions of the pellet and the average of the calculated conductivity is reported.

3.2.2 Half-cell design

Half-cell test is the mostly widely used lab protocol for investigating various electrochemical properties of the material. The general setup is a three-electrode electrochemical cell consisting of working electrode (WE) also named auxiliary electrode, a reference electrode (RE), and a counter electrode (CE) that are all immersed in the electrolyte solution within the cell. The experimental setup is illustrated in Figure 3.12, although N₂ purging and stirring are not necessary in some cases.

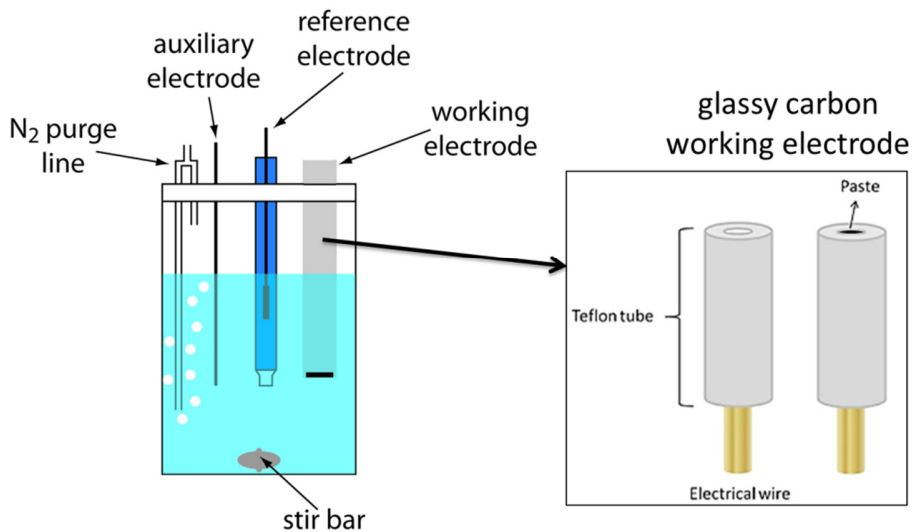


Figure 3.12 Illustration of a three-electrode electrochemical cell and the glassy carbon working electrode.
 (<http://chemwiki.ucdavis.edu> ; Lowinsohn et al. 2014)

In half cell testing, WE is the most important component since this is where the material of interest is loaded and the electrochemical phenomena are investigated. The most widely used WE is glassy carbon(GC) and Pt, Au, mercury electrode are also used. As shown in Figure 3.12, a typical GC electrode has a black center with a white Teflon coating. Only the black area is conductive and could serve as a current collector for loading. GC electrode has to be activated by polishing to mirror-like surface with micro-sized abrasives before use. After polishing, mild sonication is needed to remove the carbon particles and the remaining abrasives from the electrode. The process might be time consuming but it is highly important to expose fresh new surface for both coating quality and conductivity. Before fabricating the WE, active material of interest is formulated into a nicely dispersed ink at a known concentration of 1mg ml^{-1} (particles are commonly dispersed in a mixture of ethanol/water 50% V/V). Then $10\ \mu\text{L}$ of the prepared ink is pipetted twice onto the black area of the GC and dried to form a coating. If the coating material does not adhere well to the GC, a small amount of Nafion solution can be introduced as the binder to further coat on the formed film (in this project we use $5\ \mu\text{L}$ of 0.05 wt% Nafion). The RE is the electrode that holds a constant potential that it can be taken as the reference against which the potentials of the working electrode can be measured. Generally, RE can be a Hg/HgO, Ag/AgCl electrode, or saturated calomel electrode (SCE). The counter electrode is generally a platinum wire, and it completes the electric circuit and enable the current to flow. In a 3-electrode system, current flows between the WE and the CE and the potential at WE gets measured.

3.2.3 Cyclic voltammetry (CV) and galvanostatic charge-discharge (CD)

CV is a type of potentiodynamic electrochemical technique commonly applied for the investigation of capacitive materials or various electrochemical reactions. In CV test, the potential of WE experiences a linear ramp within a certain time, and the ramp is reversed back to the initial potential within the same time period. During the process, the response current is measured and plotted against the applied potential, forming a closed curve. In CV curve, the area beneath the curve can be used to calculate the specific capacitance based on Equation 3.7: (Yu et al., 2013):

$$\text{Equation 3.7 } C_s = \frac{\int idV}{2 \times m \times \Delta V \times S}$$

where C_s is the specific capacitance, $\int idV$ is the integrated area of the CV curve, m is the mass of active material, ΔV is the potential range, and S is the scan rate. Before each test, the electrode usually goes through a conditioning protocol and get cycled at a high scan rate of 0.1 V s^{-1} for 25 cycles to activate the electrode material. Conditioning is considered complete when the CV curves become invariant between cycles. Moreover, several cycles are performed at a fixed scan rate and various scan rate from low to high is performed to study the rate capacity of the material.

CD is another technique that can be used to determine the capacitance of the material and is more commonly used to conduct cycling stability test. In CD test, charge and discharge are performed by applying a constant current until a certain set voltage is reached. The capacitance can then be determined from the voltage window and discharge time using the Equation 3.8:

$$\text{Equation 3.8 } C_s = \frac{I}{(\frac{dV}{dt})}$$

where $dV dt^{-1}$ was calculated from the first half slope of the CD discharge curve (Stoller & Ruoff, 2010) and I is the charge current density (A g^{-1}). Energy density and power density of the material can further be attained from the above C_s results, using Equation 3.9 and Equation 3.10:

$$\text{Equation 3.9 } E = 1/2 \times C_s \times (\Delta V)^2$$

$$\text{Equation 3.10 } P_{av} = \frac{E}{\Delta t}$$

where E is energy density, ΔV is the potential range, P_{av} is the average power density, and Δt is the discharge time.

3.2.4 Electrochemical impedance spectroscopy (EIS)

EIS is a diagnostic technique used to characterize the limiting factor in the capacitive systems. In specific, it is able to determine the source and contributions of the resistance (e.g. charge transfer resistance) without significantly disturbing the system. In the EIS test, an AC sinusoidal potential in a wide range of frequencies was applied to an electrode surface, and the current responds (AC current signal) were analyzed as a sum of sinusoidal functions (Fourier series). The impedance can then be expressed in terms of a magnitude, Z_0 , and a phase shift, Φ as below:

$$\text{Equation 3.11 } Z(\omega) = \frac{E}{I} = Z_0 \exp(j\phi) = Z_0 (\cos\phi + j\sin\phi)$$

$Z(w)$ consists of a real and an imaginary part. When the real part is plotted as the X-axis and the imaginary part is plotted as the Y-axis of a chart, it is called "Nyquist Plot". An example Nyquist plot is shown in Figure 3.13, the first x-intercept represents the series resistance (ESR). The semicircular hump followed by the ESR which can be extrapolated back to the x-intercept, and the value is referred to as charge transfer resistance. After the semicircle follows the 45-degree curve, known as Warburg diffusion regime, which occurred at lower frequencies. This region is closely related to the transition diffusion resistance. In order to extract the detailed information from EIS result, the shape of the EIS curve is often simulated using a software to fit an equivalent circuit model for the cell.

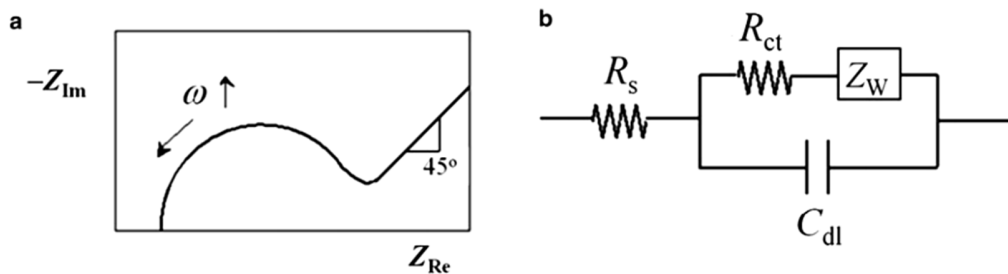


Figure 3.13 (a) Typical shape of Nyquist plot from EIS test and (b) equivalent circuit from simulation.
(Pyun et al., 2012)

3.3 Catalytic activity measurements

3.3.1 4-nitrophenol (4-NP) reduction reaction

The development of various MNPs of diverse shapes, sizes, or even porosities has received much attention in the field of catalysis. To facilitate the parallel comparison in catalytic performance

among different studies, the reduction of 4-nitrophenol (4-NP) by NaBH₄ has been universally adopted as a model reaction.(Aditya et al., 2015) Such reaction only takes place when both a reducing agent and a catalyst are present, and it proceeds in solution under mild conditions, yielding a single product (4-nitrophenol to 4-aminophenol). The progress of the reaction can be readily monitored using a UV-vis spectroscopy, since the reaction is accompanied with a successive decrease in intensity for peak at 400 nm which is the adsorption peak of 4-NP. The reaction is generally considered first-order reaction when excess NaBH₄ is and metal catalyst are used. The catalytic reaction follows the Langmuir-Hinshelwood model (Wunder et al., 2010) and was demonstrated to occur on the surface of the catalyst, and both the reactants will compete to be adsorbed on the surface sites. After the two reactants react, and 4-NP is converted to the reducing product 4-aminophenol (4-AP), they will then dissociate from the surface. As the scheme shown in Figure 3.14(a), in the proposed mechanism, the adsorbed NaBH₄ first react with Au NP to generate Au-H, which will further react with the adsorbed 4-NP to give 4-AP. An induction time t_0 is sometimes observed due to the catalysis-induced and the spontaneous dynamic surface restructuring and nanosized catalyst exhibit less t_0 compared to their bulk counterpart.(Zhou et al., 2010a)

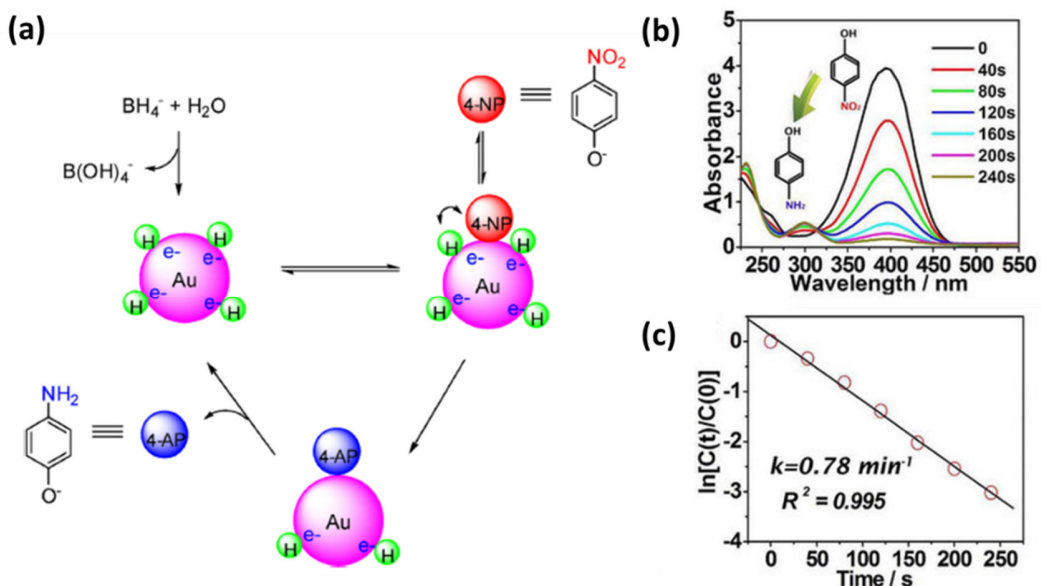


Figure 3.14 (a) Proposed mechanism for the reduction of 4-NP to 4-AP by Au NP in the presence of NaBH₄ based on Langmuir-Hinshelwood model, (b) example of typical spectra from UV measurement during 4-NP reduction and (c) Plot obtained from spectra in (b) to calculate the rate constant of the reaction.(Zhao et al., 2015b; Li et al., 2013d)

In a typical test, 4-NP solution is first well mixed with fresh NaBH₄ solution (in excess amount) under room temperature, then a certain volume of the mixture is introduced in the UV cell and mounted in the UV instrument. Then, a certain volume of the catalyst suspension (known concentration) is quickly mixed with the previous mixture in the UV cell followed by UV monitoring. During the reaction, UV spectra will be scanned at a certain time interval and the resultant spectra should appear like Figure 3.14(b). As Equation 3.12 suggests, the rate constant is proportional to the active surface area (S) of the catalyst:

$$\text{Equation 3.12} \quad -\frac{dc_t}{dt} = k_{app}C_t = k_1SC_t$$

where C_t is the concentration of 4-NP, K_{app} is the apparent rate constant, and k₁ is the rate constant that is independent of the catalyst surface, and S is the surface area of the catalyst. Furthermore, by further plotting ln(A_t/A₀) against time (t), the apparent rate constant of the reaction is resolved (as the example shown in Figure 3.14(c)), which is equal to the slope of the linear fit for the plot (Equation 3.13):

$$\text{Equation 3.13} \quad \ln\left(\frac{C_t}{C_0}\right) = \ln\left(\frac{A_t}{A_0}\right) = -k_{app}t$$

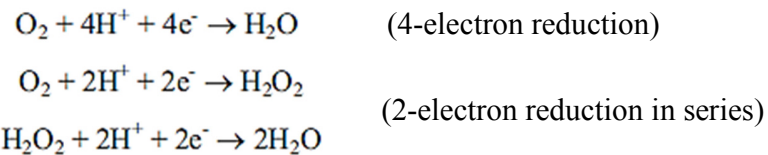
In practice, k_{app} is dependent on the different catalytic condition such as catalyst mass, and thus need to be normalized in order to compare the catalytic activity of the catalyst among various work. Turnover frequency (TOF) is widely used for this purpose and is defined the number of moles of 4-NP reduced per mole of catalyst per time (hour, minute, or second).

3.3.2 Catalytic oxygen reduction reaction (ORR) tests

ORR is a rather important reaction that takes place in various energy storage devices such as fuel cells (cathode). The reaction itself has very low efficiency without a catalyst, thus on a practical level, a suitable catalyst is highly desirable to speed up the process. Pt-based materials are currently the dominant technology for catalyzing ORR with superior efficiency. Other non-noble metals and even metal-free carbon-based materials are also under much investigation as alternatives to alleviate the high cost challenge associated with Pt-based catalyst in this area.

The mechanism of ORR reaction is quite complicated involving many intermediates and is closely related to the natures of the electrode material, catalyst, and the electrolyte. The reduction pathways could involve 1-electron, 2-electron, and 4-electrons depending on the applications. For example,

Pt catalyzed ORR reaction was demonstrated to involve either a direct 4-electron transfer process from O₂ to H₂O or it can involve a 2-electron reduction in series shown below:



Herein, techniques used to in this research to study the catalytic activity of different catalyst are introduced as below.

The ORR activity of catalyst is investigated with a rotating disc electrode (RDE) half-cell configuration that consists of catalyst coated glass carbon electrode (GCE) as working electrode, graphite rod as contour electrode and reversible hydrogen electrode (RHE) as the reference electrode (shown in Figure 3.15). A modulated speed rotator is used where working electrode is mounted and can be rotated at various speed inside the 3-electrode cell during testing. An illustrate of RDE is shown in the inset of Figure 3.15(a). To fabricate the working electrode, catalyst materials was first sonicate in the ethanol/ water mixture at a containing also 0.03% Nafion desired concentration. Then a certain volume of the suspension is drop cast using a pipette onto the glassy carbon disc of the RDE. Once the working electrode is fabricated, the three electrodes are immersed in the cell containing the electrolyte solution (acidic or alkaline).

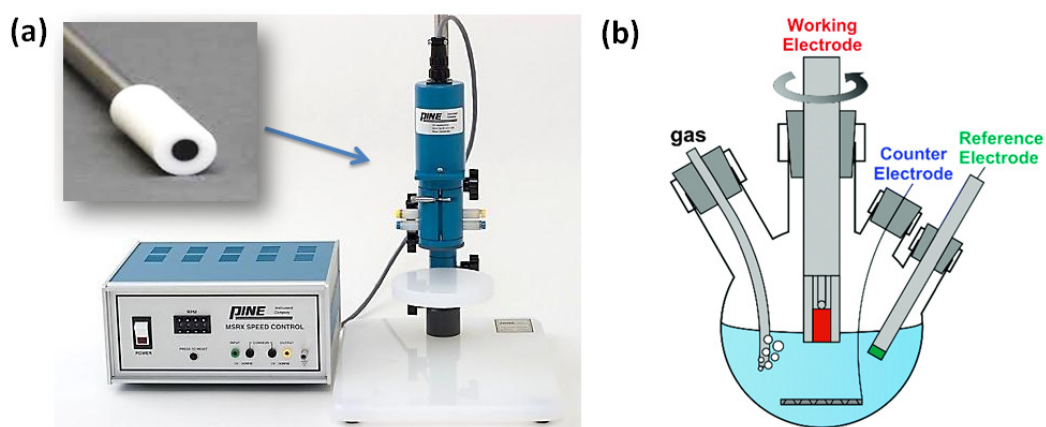


Figure 3.15 (a) Pine AFMSRX electrode rotator (inset: a rotating ring-disk electrode) and (b) typical electrochemical testing cell for ORR.(source: Pine Instrumentation Inc.)(Hong et al., 2015)

● Polarization curve

Polarization curves record the relationship between the current density and the potential, and can be obtained by measuring the current response to the linear potential sweep under O₂ saturated electrolyte. Baseline correction is conducted by performing the same scan in N₂ saturated electrolyte. The polarization curves are measured at different rotational speed of the working electrode at room temperature. A typical polarization curve is provided in Figure 3.16(a), and the test is very useful for studying the kinetics of the ORR reaction. At higher potentials indicated as A, ORR reaction is limited by electrochemical kinetics. A good catalyst will alleviate the effect of such limitation by bringing the potential where the reaction occurs as close to the reversible equilibrium potential (i.e. thermodynamic potential) as possible. This is indicated by a more positive on-set potential of the curve. At moderate potentials of region B, ORR is limited by mixed effect of electrochemical kinetics and mass transfer. At even lower potential region of C, the current response reaches a plateau. At this stage, ORR reaction proceeds fast enough and is only limited by the diffusion of O₂ species from the electrolyte to the surface of the catalyst. At higher rotational speed, this diffusion limited current is higher due to increased contact with O₂ saturated electrolyte which alleviate the diffusion limiting effect. Koutechy-Levich equation is applied to calculate the kinetic limited current density (i_k):

$$\text{Equation 3.14} \quad \frac{1}{j} = \frac{1}{j_k} + \frac{1}{B\omega^{1/2}}$$

where j is the measured current density, j_k is the kinetic current density and ω is the rotation speed of the electrode.(Xue et al., 2013) Therefore, by plotting 1/j against 1/ω known as K-L plot (example shown in Figure 3.16(b)), a linear curve is obtained from which j_k at different potentials can be calculated from the intercept. B can be determined by the slope of the K-L plots from which number of electrons transferred per oxygen (n) indicating the reaction pathway of ORR can be derived on the basis of the following equation:

$$\text{Equation 3.15} \quad B = 0.62nFC_{O_2}D_{O_2}^{2/3}\nu^{-1/6}$$

Where F is Faraday's constant (96485 C mol⁻¹), C_{O_2} means the bulk concentration of O₂, D_{O_2} denotes the diffusion coefficient of O₂ in the electrolyte, ν is the kinetic viscosity of the electrolyte. (Masa et al., 2014)

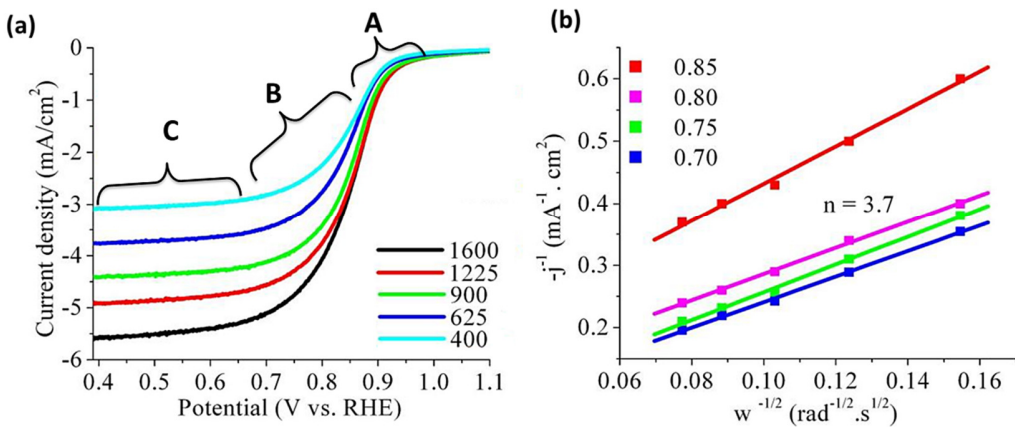


Figure 3.16 (a) Typical ORR polarization curves catalyzed by Pt/C solution at the different rotation speeds, and (b) corresponding K-L plots at various disk potentials.(Tiwari et al., 2013)

● Cyclic voltammetry (CV) curve

CV scan can quickly provide qualitative information on the electrochemically active surface area (ECSA) of the catalyst which is critical parameter for catalytic activity. CV scan is conducted under N_2 saturated electrolyte and a typical scan is shown in Figure 3.17. The pink areas are associated with H_2 adsorption/desorption and the stripe shaped area is related to the capacitance on the surface of the catalyst. The average area from the integration of the two peaks gives the charges involved in the adsorption/desorption of H_2 . By assuming that the catalyst is covered with a monolayer of H_2 species, ECSA ($\text{m}^2 \text{ g}^{-1}$) of the active catalyst can be calculated based on Equation 3.16:

$$\text{Equation 3.16 } \text{ECSA} = Q / 0.21m$$

where m is the specific loading of the active catalyst (mg cm^{-2}) on the electrode, Q (mC) is the averaged H_2 adsorption/desorption peak area. The constant 0.21 (mC cm^{-2}) comes from the electrical charge associated with monolayer adsorption of H_2 on the active catalyst.

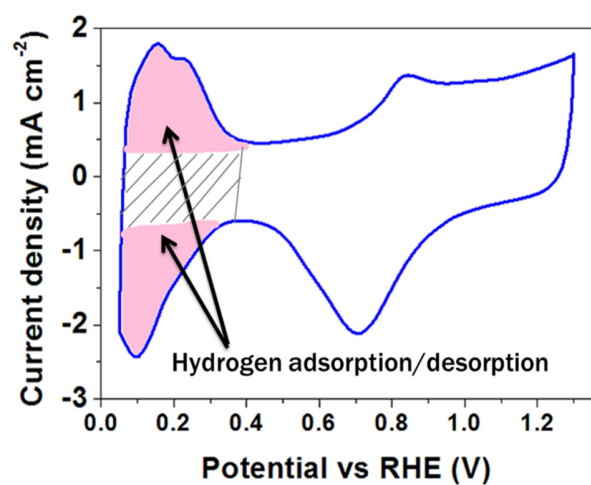


Figure 3.17 Example of cyclic voltammetry in ORR test to calculate electrochemically active surface area.

Chapter 4 Cost-effective and scalable chemical synthesis of conductive cellulose nanocrystals for high-performance supercapacitors

4.1 Introduction

The energy and environmental challenges facing the world are daunting, thus they call for the development of high-performance devices that can be manufactured with renewable materials at a low processing cost. Supercapacitors (SPs) are recognized as an important element in the overall energy storage system. SP can store far more energy than conventional capacitors, and they also possess a much longer cycle life than batteries.(Conway, 1991; Arico et al., 2005) Current commercial electrode materials for SPs are active carbon, metal oxides, carbon nanotubes (CNTs), and graphenes.(Yu et al., 2011, 2010) However, these materials present several challenges, such as high cost, greenhouse effect, metal-depletion, and low-biodegradability. To this end, intrinsically conductive polymers (ICPs), polypyrrole (PPy), polyaniline (PANI) and poly(3,4-ethylenedioxythiophene) (PEDOT) have gained increased attention due to their good conductivity, low cost, and attractive pseudo-capacitive behaviors that combine fast kinetics (i.e. high power) and superior specific capacitance. (Du Pasquier et al., 2002) PPy has been considered to be the most promising ICP for this purpose due to its facile synthesis, long-term stability, outstanding electrochemical properties, and low cost.(Ryu et al., 2002; Rudge et al., 1994) They are also believed to replace traditional battery or supercapacitor material to meet the demands for flexible, lightweight or even wearable electronic devices.(L.Nyholm, G.Nystrom, A. Mihranyan, and M. Stromme, 2011) However, the poor mechanical strength of ICPs limits their processability and results in poor stability due to degradation during charge-discharge cycles. (Paul et al., 2011) Another drawback is the compactness of the polymer film resulting in a low specific capacitance ($F\ g^{-1}$) due to the limited access for dopant ions. (Snook et al., 2007)

In order to strengthen the structure and increase the porosity of ICPs for supercapacitor application, many attempts have been made to produce ICP composite materials over various substrates, such as latex particles, CNTs(Zhang et al., 2011; Yu et al., 2005; Zhang et al., 2005; Zhou et al., 2010c; Sivakkumar & Kim, 2007; Wang et al., 2007), graphene oxides(An et al., 2001; K. Jurewicz, S. Delpeux, V. Bertagna, F. Beguin, E. Frackowiak, 2001; Frackowiak et al., 2000; Wang et al., 2007; Li et al., 2011), metal compounds(Gomez-Romero et al., 2005, 2003), inorganic oxides and hydroxides.(Huang et al., 2006; Mallouki et al., 2007) An outstanding example of these composite

materials is PPy/CNT which has been proposed for many applications(An et al., 2004, 2002; Sivakkumar et al., 2007; Chen et al., 2006; Sivakkumar & Kim, 2007). The enhanced electrochemical performance of this composite is generally believed to be due to the synergy between highly conductive CNTs and conductive polymers.

Recently, there has been a significant interest in the use of nanotechnology to rejuvenate the forest industry by producing value-added wood-derived nanomaterials with one application being their incorporation into ICPs. (Nyström et al., 2010; Li et al., 2010a; Ding et al., 2010; Olsson et al., 2012; Sasso et al., 2010; G.Nystrom, Ph.D. Thesis, 2012; Liew et al., 2010; Huang et al., 2005; Liew et al., 2013) Various PPy/cellulose hybrid system have been successfully fabricated via chemical oxidation polymerization in the presence of Pyrrole monomer (Pitchai-Mydeen & Ning, 2011; Xu et al., 2013a; Huang et al., 2005; Sasso et al., 2010) Recently, Wang et al.(Wang et al., 2013b) conducted a detailed investigation on the various polymerization parameters for achieving highly conductive composites of bacterial cellulose/PPy for supercapacitor applications. However, due to the length of microfibrillated cellulose system mentioned above, the end-product mostly achieved by forming the entangled films/mat, aerogel, or cake-form that have poor further processibility.(Huang et al., 2006) Currently, however, limited studies have focused on individually coated nanofibers, i.e. rods, or whiskers, that can be easily incorporated as conductive fillers into various matrices via mixing.(Flandin et al., 2000) An effective enhancement in electrochemical performance can be obtained by forming individual core-shell structure because it avoids the conductivity loss due to cross-linking network formed during ICP polymerization.(Ramya et al., 2013; Kricheldorf et al., 2005) In a most relevant work, CNCs derived from cotton has been successfully incorporated into PPy by Soon et al. using electrochemical co-deposition. In their work, the prepared CNC/PPy shows superior electrochemical performance even comparable to carbon nanotube/PPy synthesized and tested under the exact same conditions. (Liew et al., 2010) The exciting results strongly suggest that the substrate conductivity is not a prerequisite and CNC/PPy is a promising candidate for high performance supercapacitor applications. While electrochemical polymerization yield systems with better performance, the yield of product is limited to the surface area of the electrode not suitable for large-scale production and is gernerally produced as dense film limit its wide application.(Davies et al., 2011)

In this work, we describe a well-controlled synthesis of conductive CNCs *via* facile *in situ* chemical polymerization. Due to the good dispersibility of CNCs and an ideal dimension that is short enough to prevent entanglement, PPy can be readily polymerized to form a conductive shell on individual CNCs. The one-dimensional structure of CNC not only facilitates the efficient transportation of

electrons along one controllable direction, but also gives a very low percolation concentration of PPy/CNC to achieve a conductive network.(Lu et al., 2011) By using well documented chemistry, more negative charges (i.e. carboxylic groups) are introduced to the CNC surface in addition to the existing sulfate ester groups, which provide a stronger interaction (electrostatic attraction, hydrogen bonding) between CNC and PPy than the untreated-CNC. Compared with polymerization over the cellulose network in other studies (i.e. membrane, cake, hydrogel etc.), the polymerization confined to individual CNC fiber is more challenging to achieve. Controlled synthesis has to be designed to enhance the affinity of ICP to the surface of CNC and eliminate the bulk polymerization of PPy or agglomeration. Our optimized synthesis was developed by tuning the feed ratio of Py monomer to hydroxyl group (Py/OH). Zeta-potential measurements were monitored over the polymerization time to ensure an adequate PPy coating achieved. The effect of electrochemical change associated with different Py/OH ratio was thoroughly studied using various characterization techniques, and we were able to elucidate the phenomenon on the observed internal structural changes associate with their electrochemical behavior, which is believed, to the best of our knowledge, the first reported. The electrical conductivity of the prepared PPy/CNC approached 4 S/cm with an outstanding capacitance of 248 F/g. The nanostructure has the added advantage of being a sustainable and cost-effective nanomaterial for the fabrication of light, flexible, high-performance, and cheap energy storage devices. Our solution based synthesis is readily scalable using larger vessels or reactors: from 100 ml to 4-liter vessel, the yield of PPy/CNC from a single batch was increased from 0.2-0.3 g to 10-12g with the end product being fine powder form (after freeze dry) that is able to well redisperse in solution. The nanorod-shape nanocomposite using our approach is promising for a wide variety of applications, such as conductive inks for printable electronics, conductive fillers for various insulating matrix, sensors, conducting and antibacterial films etc. This is also significantly more versatile than the electrochemical method, where the product is somewhat limited to the deposition of a composite film on an electrode that restrict its both scalability and further processibility as well.

4.2 Experimental Section

4.2.1 Materials

Cellulose nanocrystal (CNC) was provided by FP Innovations and Celluforce Inc. The chemicals used in this study were analytical grade, purchased from Sigma-Aldrich, and used as received. The chemicals for reaction are: TEMPO reagent, sodium bromide (NaBr), sodium hypochlorite (NaClO), pyrrole monomer (Py) and ammonium persulfate (APS).

4.2.2 Methods

TEMPO-mediated oxidation was first performed on CNC, converting primary hydroxyls to carboxylate functionalities.(Habibi et al., 2006) Freeze-dried TEMPO-CNC was dispersed under sonication in a mixture of HClO₄ (1 M) and ethanol (V/V=1/1) to produce a 0.2 % wt suspension. Py monomers at different molar ratio to surface -OH groups of CNC were then added to the suspension and the mixture was transferred to a double-walled jacketed reaction vessel. The solution was vigorously stirred, and equal molar amounts of ammonium persulfate (APS) to pyrrole monomer was added slowly to initiate the polymerization. The color of the solution gradually turned from transparent to yellow, to dark green and finally to black, which is the color of PPy. The reaction was magnetically stirred below the room temperature overnight for sufficient polymerization. Finally, the reaction was quenched followed by repeated washing with DI water. For comparison, pure PPy was also synthesized under identical conditions in the absence of CNCs.

The molar amount of surface hydroxyl group on CNC was estimated based on anhydrous glucose (AGU) repeating units (MW 162 g mol⁻¹) discussed in Chapter 2, where each AGU unit contains three -OH and roughly 30% of the -OH are active and on the surface of CNC. Each gram of CNC contains 0.0037 mol of accessible surface -OH.

4.2.3 Characterization

The morphology of TEMPO-oxidized CNC, PPy/CNC system was characterized using a Philips CM10 electron microscope. SEM characterization was conducted with LEO FESEM 1530. ζ -potential of the PPy/CNC composite material was monitored throughout the polymerization process using a Malvern Zetasizer Nano ZS (Worcestershire, UK) by collecting the sample aliquots from the reaction vessel at different time intervals, filtered with DI water and measured. The thermal stability of the TEMPO-CNC and PPy/CNC systems were studied by thermal gravimetric analysis (TGA). Both samples were placed in an inert ceramic crucible and heated from 25 to 800 °C at a heating rate of 10°C min⁻¹ in 20 mL min⁻¹ of air. The interaction between PPy coating and CNC substrate, and the effect of Py/OH ratio on the final nanostructure were characterized using FT-IR, UV-Vis (Varian Cary 500 spectrophotometer), and Raman Spectroscopy (RS).

Conductivity was measured using a four-point probe station following the protocol described in Chapter 3. Cyclic voltammetry (CV), charge and discharge (CD), and electrochemical impedance spectroscopy (EIS) were performed using a CHI 760D electrochemical station (CH Instruments, USA) equipped with a three-electrode half-cell configuration (WE: glassy carbon (GC); CE: Pt wire;

RE: saturated calomel reference electrode (SCE)). All the above tests follow a 25-cycle CV activation between -0.6 and 0.4 V versus SCE in KCl electrolyte (0.5 M). The working electrode was fabricated following the protocol described in Chapter 3. A total of 20 µg of active material is loaded onto the sensing area of GC (diameter of the current collector: 3mm). The CV test was performed with scan rates of 1, 10, and 100 mV.s⁻¹ and CD tests were performed by applying a constant current density between 1 to 5 A g⁻¹. EIS was performed using a frequency range between 0.1Hz and 1MHz.

4.3 Results and discussion

4.3.1 Properties of PPy/Tempo-CNC nanocomposite

The synthesis of PPy/CNC based on an *in situ* chemical oxidation polymerization technique is illustrated in Figure 4.1(a). The carboxylic groups on TEMPO-oxidized CNC offer hydrogen bonding sites between the OH groups on CNC and NH groups of pyrrole monomers.(Sahoo et al., 2010) The polymerization proceeded along the CNC surface from these attached monomer sites to form the conductive coating. The color change in the solution from slightly yellow to black confirmed the successful polymerization of PPy (Figure 4.1(b)).

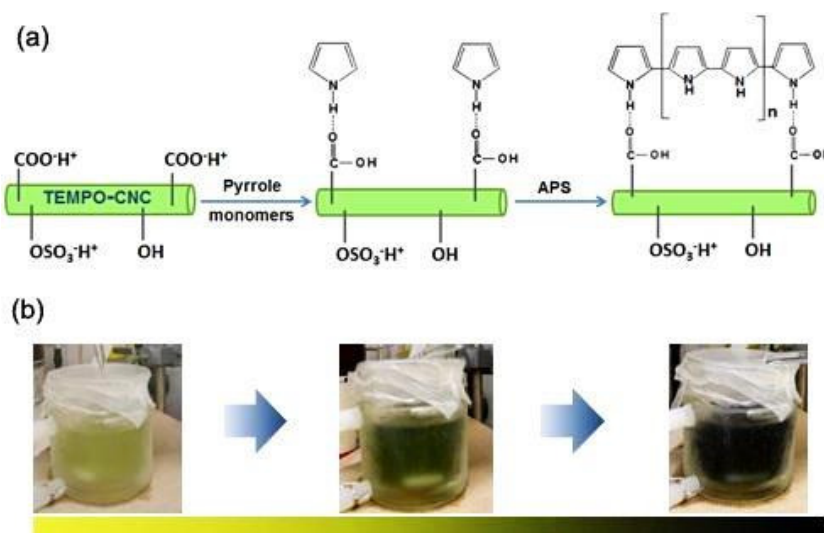


Figure 4.1 (a) In situ chemical oxidation polymerization for the synthesis of PPy/CNC nanostructures; (b) Color change of the reacting solution during the polymerization process.

PPy is hydrophobic and is insoluble in almost all solvents. However, CNCs by nature are hydrophilic, and they are well dispersed in water due to the electrostatic repulsion of negative

surface charges.(Habibi et al., 2010b) The hybrid nanostructure of PPy on CNC substrate inherits the good dispersibility of CNC and forms a homogeneous black colloidal dispersion. Once freeze dried, the powder could be readily redispersed to form a black aqueous dispersion. In comparison, pure PPy synthesized in the absence of CNC precipitated out from water in the form of flakes (Figure 4.2(a) and (b)). TEM images in Figure 4.2(c)(d) confirmed that the core-shell structured PPy/CNCs are successfully achieved with PPy coating grown on the surface of individual CNC nanorods. SEM images in Figure 4.3(a-b) shows the PPy synthesized under the same experimental condition without and with adding the CNC. It demonstrates a uniform coating of CNC on each individual rod-shaped CNC that have been achieved. Compared to the bulky spherical PPy, the nanocomposite material well preserves the fine structure of CNCs that significantly enhance the surface area by forming a porous network.

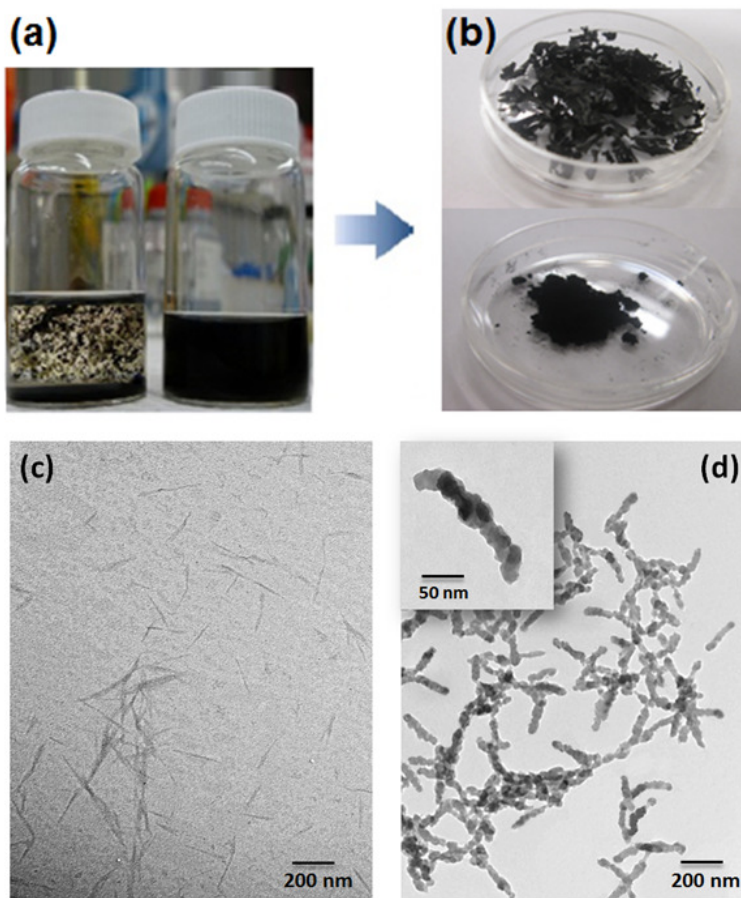


Figure 4.2(a) Comparison of a pure PPy suspension with visible flasks (left) and a homogenous PPy/CNC suspension (right); (b) Freeze-dried sample of pure PPy in the form of random flakes (top) and PPy/CNC in the form of powder (bottom); (c) TEM images of TEMPO-CNC and (d) PPy/CNC at Py/OH = 16.

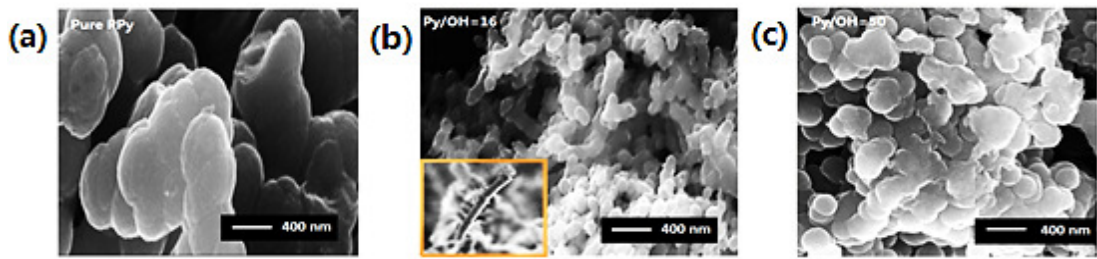


Figure 4.3 SEM image for (a) Pure PPy using bulk synthesis without adding CNC (b) PPy/CNC polymerized with Py/OH molar ratio of 16, the insert is the zoom-in HRSEM for a single nanorod of PPy/CNC; (c) PPy/CNC polymerized with Py/OH molar ratio of 50, showing thick PPy coating evolving from rod shape into spherical shape.

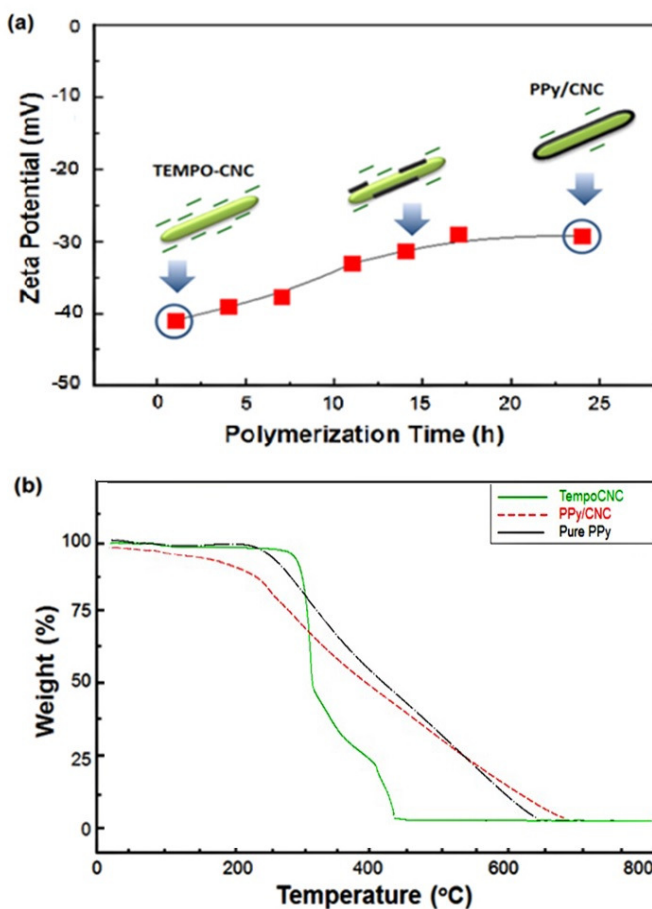


Figure 4.4 (a). Dynamic change of zeta potential of PPy/CNC particles during polymerization; (b). TGA curves of TEMPO-CNC (green line) and PPy/CNC (red line) with Py/OH =16 and bulk PPy (black line).

An important consequence of PPy coating is the neutralization of the surface negative charges on CNC due to the positively charged PPy backbone.(Zhang & Bai, 2003) Thus, the growth of PPy layer could be monitored throughout the 24 hours polymerization, by monitoring the changes in the zeta potential. Due to the negatively charged groups on the surface (i.e. OSO_3^- , COO^-), TEMPO-CNC without coating possessed a negative zeta potential of - 41 mV. Once PPy coating was deposited on the surface of CNC, the zeta potential became less negative, and approached a plateau of approximately -29 mV at a polymerization time of 24 hrs. The trend shown in Figure 4.4(a) provides clear evidence of the gradual formation of PPy coating on the CNC nanoparticles. The thermal stability of the PPy/CNC nanostructure was investigated using a thermal gravimetric analyzer (TGA). TGA curve for TEMPO-CNC, PPy/CNC and pure PPy are shown in Figure 4.4(b). The PPy/CNC system was thermally stable up to 250°C and displayed a large weight retention at high temperature (more than 40% up to 400°C). The weight loss in the first stage of PPy/CNC decreased by 30% compared to pristine CNCs, which is attributed to the higher thermal stability of the PPy shell.

4.3.2 Effect of Py/OH ratio on PPy coating and the electrochemical properties

The effect of Py/OH ratio on electrochemical properties of PPy/CNC was investigated by preparing the hybrid material at various Py/OH ratio of 1:1, 2:1, 4:1, 8:1, 12:1, 16:1, 25:1, and 50:1. At low monomer feed ratios, bulk polymerization of PPy was not observed from the TEM micrographs. However, beyond the ratio of 25, the existence of high Py content led to the formation of bulk PPy particles that formed a black coating on the interior wall of the reaction vessel and stirrer bar. It is known that the polymerization rate is controlled by the reactant concentration, and an optimum condition to yield only polymer coating on the CNC can be determined.(Gregory et al., 1989) At a low Py concentration, more pyrrole monomers were adsorbed on the high surface CNCs, resulting in a preferential nucleation and polymerization of polymer chains on CNC. While at a high Py concentration, a fast reaction kinetic process induced excess activation of PPy oligomers resulting in an accumulation of polymer in bulk before they could be effectively transported and polymerized on the CNC surface.

4.3.2.1 Conductivity

The conductivity changes of PPy/CNC with increasing Py/OH ratio displayed three transitions (Figure 4.5(a)): At low Py/OH ratios, the electrical conductivity increased slowly with a low magnitude, suggesting a poor electrical contact of PPy/CNC rods due to insufficient polymer

coating. A sudden rise in the conductivity of pressed pellets occurred after a threshold ratio of Py/OH=4, after which an almost linear increase in conductivity was observed. The increasing trend in the conductivity was reversed above Py/OH = 16, which could be related to the saturation of PPy or poor PPy coating. Considering the fact that the conductivity of PPy/CNC decreased instead of reaching the plateau, the latter factor is believed to dominate. From the conductivity curve, the optimal feeding Py/OH ratio of 16 was observed, where the conductivity reached a maximum of 4.5 S cm⁻¹. An illustration of the effectiveness of its conductivity is shown in Figure 4.5(b), when the PPy/CNC sheets can conduct electricity to light the bulbs.

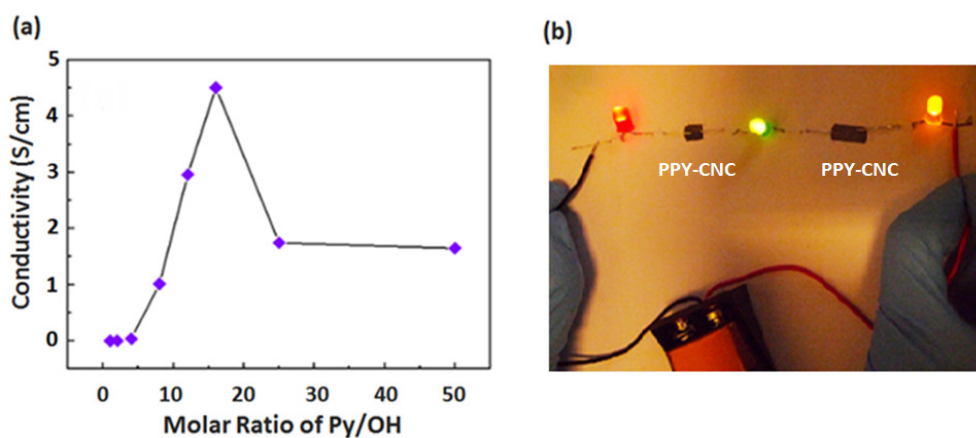


Figure 4.5(a) Effect of feeding ratio of Py/OH on the conductivity of PPy/CNC, (b) An illustration of how conductive PPy/CNC (black sheet pressed from PPy/CNC powder prepared at Py/OH =16) can conduct electricity in a circuit to light the bulbs.

4.3.2.2 Optical characteristics

To better understand the growth of PPy oligomers on CNCs at various Py/OH ratios and the associated changes in the electrochemical property, several spectroscopic measurements, such as UV-Vis, FT-IR and Raman spectroscopy were performed on PPy/CNC samples. These techniques are complementary in providing additional insights on the changes in the polymer structure, bonds, interactions and composition. FT-IR provides information on the interaction between the constituent polymers, such as chemical bonds, Raman spectra provides information on the conjugation length of the polymer, and UV-Vis provides information on the shift in PPy's electronic band energies. (Mohammad, 2007)

The FT-IR spectra of chemically modified CNCs, PPy and PPy/CNC are shown in Figure 4.6(a). The characteristic bands due to the newly formed carboxylic groups of CNCs after Tempo-mediated

oxidation were clearly observed and the IR bands at 3403, 2902, and 1620 cm⁻¹ were consistent with the O-H stretching, C-O stretching, C=O stretching in the Tempo-oxidized CNC, respectively.(Way et al., 2012) For the CNC-PPy hybrid nanostructure, no new peaks were observed for the hybrid material in addition to those belonging to TEMPO-CNC and pure PPy, which suggests that no new chemical bonds were formed between CNC and PPy. More importantly, two important trends were observed: (i) all the carboxylic related peaks were greatly influenced by formation of PPy on CNC. The band at 3430 cm⁻¹ (N-H stretching vibration) gradually replaced the peak at 3403 cm⁻¹ (O-H stretching) and the peak was shifted to a higher wavenumber compared to pure PPy. Moreover, the peaks at 2902 cm⁻¹, 1620 cm⁻¹ and 1061 cm⁻¹ were significantly reduced. These changes suggest that the interfacial interaction between the PPy coating and CNC is associated with the hydrogen bonding between carboxylic and amine functional groups on CNC and PPy respectively. The phenomenon was similarly observed when carbon nanotubes were coated with PPy.(Wu et al., 2009) (ii) a small peak at 1701 cm⁻¹ appeared at lower Py/OH ratios which indicates the presence of a typical side reaction during PPy synthesis where water forms a carbonyl group that inhibits the polymer chain growth.(Maia et al., 1994) This shows the poor polymerization kinetics at low pyrrole monomer concentration, which directly corresponds to the low conductivity. At higher monomer concentration, most of the characteristic peaks for pure PPy were observed in the PPy/CNC hybrid nanostructures, including: the fundamental C-C ring vibration at 1560 cm⁻¹ (asymmetric ring stretching), C–N in-plane ring deformation at 1480 cm⁻¹ (symmetric ring stretching), C-H in-plane vibration at 1320 cm⁻¹ and the C-N stretching vibration appearing at 1178 cm⁻¹. (Sahoo et al., 2010)

The most important scattering peak for PPy/CNC in the RS in Figure 4.6(b) was at ~1580 cm⁻¹, assigned to the C=C stretching of PPy backbone. Previous studies have established clear correlation between this peak and the conductivity since it is very sensitive to the conjugation length and structural order of PPy.(Liu, 2004) Kim et al. showed that the peak shifted to a higher wave number when the conjugation length of PPy was reduced due to aging.(Kim et al., 1995) Tain and Zerbi reported a downshift of the wavenumber when PPy possessed a lower doping level.(Tian & Zerbi, 1990) In our case, the band revealed interesting shift in correlation to various Py/OH feed ratio: the peak position continued to shift to lower wavenumber with increasing Py/OH ratio, while beyond the critical point of Py/OH=16, the shift was reversed. This trend agrees well with the conductivity change observed in Figure 4.5(a) and supports the highest conductivity observed at Py/OH=16 due to the longest conjugation length. When excess pyrrole is present during the reaction, the rough polymer structure and poor stacking on CNC surface (fast polymerization kinetics) inhibits the electron transport along the backbone due to steric hindrance, thus lowering the conductivity. When

compared to pure polypyrrole, all the peaks for PPy/CNC synthesized at a ratio of $\text{Py}/\text{OH} > 4$ at this position were red-shifted suggesting that the polymerization proceeded more orderly with a higher conjugation degree with the CNC templating.

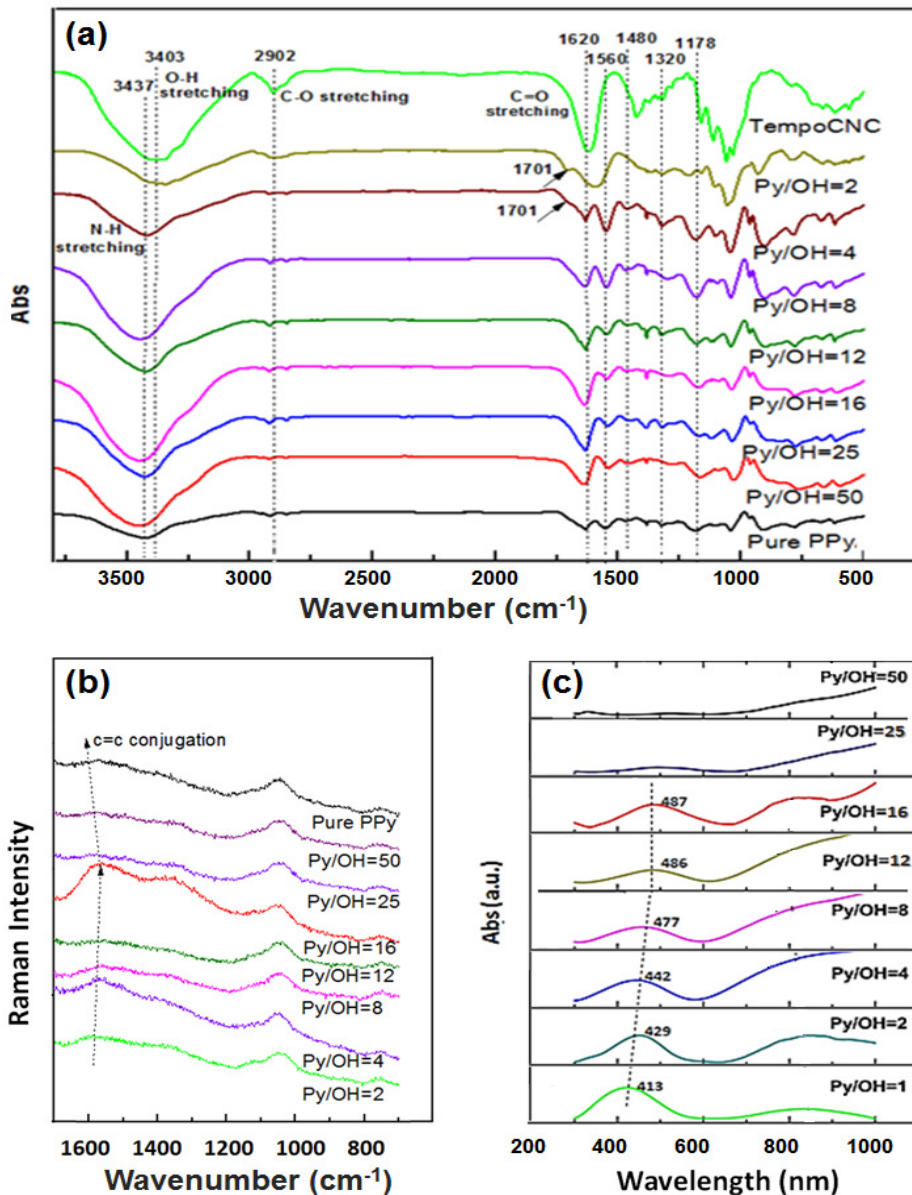


Figure 4.6 (a) FT-IR; (b) Raman Scattering; (c) UV-Vis spectra of PPy/CNC system synthesized with various Py/OH ratios of 1:1, 2:1, 4:1, 8:1, 12:1, 16:1, 25:1, and 50:1.

Figure 4.6(c) shows the UV-Vis spectra of PPy/CNC synthesized at different Py/OH molar ratios. A broad band peak around 800 nm is due to the conduction electrons that only presents in the oxidized PPy. A significant growth in intensity with increasing Py/OH ratio reflects the conductivity

increase of the materials. The other typical peak at about 430 is attributed to the transitions from valence band to the polaron/bipolaron bands formed upon doping.(Brédas et al., 1984; Kaufman et al., 1984; Singh & Prakash, 2008) The significant red-shift of the peak maxima from 413 nm to 490 nm (energy decrease) with increasing Py/OH ratio corresponds to a reduction in the bandgap due to longer conjugation length/higher doping level.(Brédas et al., 1984) However, when the Py/OH ratio was increased to 50 and 100, both peaks broadened extensively and decreased in intensity, which suggests the existence of more disorder or defects introduced within the polymeric chains. This observation agrees with the RS analyses.

4.3.2.3 Electrochemical behavior

Figure 4.7 (a) and (b) illustrate the typical Cyclic Voltammetry (CV) at scan rates of 0.01, 0.05, and 0.1 V/s determined for the PPy/CNC samples prepared from different Py/OH ratios. For practical issue, the specific capacitance was calculated based on the real composite material (PPy + CNC), and not only on active material (PPy). The trend of Py/OH feed ratio on the capacitance of PPy/CNC is similar to conductivity results. The optimal ratio for the supercapacitor performance was at Py/OH=16 and the rectangular shape of the CV confirmed its outstanding, reversible capacitive behavior. The highest capacitances were determined to be 248, 238, and 230 F g⁻¹ at scan rates of 0.01, 0.05 and 0.1 V s⁻¹, respectively. More importantly, PPy/CNC retained more than 90% of their capacitance when the scan rate was increased from 0.01 to 0.1 V s⁻¹, suggesting excellent charge transfer kinetics. Similar to the conductivity profiles, the supercapacitor performance of PPy/CNC began to dissipate above Py/OH of 16. At a higher feed ratio of Py/OH, the rough and poor PPy stacking on CNC surface induce steric hindrance to the ionic penetration, while the poor conductivity reduces the transfer of electrons, both resulting in a lower capacitance and retention. The capacitance of pure PPy synthesized under the same condition in the absence of CNC was also performed. A significantly lower capacitance of 90 F g⁻¹ was observed at scan rate of 0.01 V s⁻¹, which was less than half the capacitance of PPy-CNC system. Clearly, the combination of CNC and polypyrrole greatly enhanced the electrochemical properties of the polymer itself. In Figure 4.7(c), CD curves are shown based on the various charge current densities. The discharge curve of PPy/CNC is almost symmetric to the corresponding charge curve with a slight curvature, representing the pseudocapacitance behavior.(Han et al., 2010) The calculated capacitance approached 250 F g⁻¹ at 5 A g⁻¹ showing that the optimized PPy coating on CNC maintains a very good capacitive behavior at high charge current. Moreover, the IR drop in CD curves due to internal resistance of the electrode material was barely observed in the PPy/CNC system.

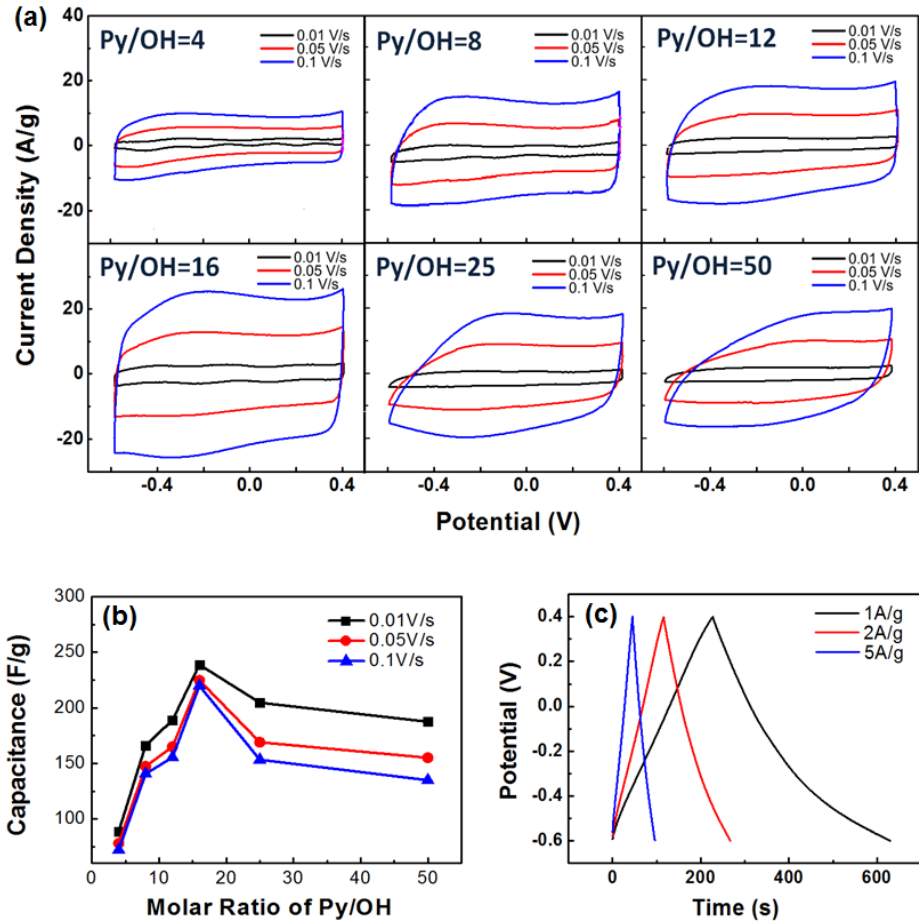


Figure 4.7 (a) CV curves of PPy/CNC prepared with different Py/OH feeding ratios at scan rates of 0.01 V/s, 0.05 V/s and 0.1 V/s. (b) Effect of Py/OH on the capacitance of PPy/CNC; (c) Charge and discharge test at different charge currents of 1A/g, 2A/g, and 5A/g for PPy/CNC where Py/OH = 16.

Electrochemical impedance spectroscopy (EIS) was used to further monitor the behavior for various PPy/CNC samples between 10 mHz and 1MHz. The Nyquist plots obtained from EIS are summarized in Figure 4.8. The results illustrate that PPy/CNC at Py/OH = 16 possesses the lowest charge transfer resistance in the high frequency region and the short steep line in the low frequency charge diffusion region indicates low charge diffusion resistance. Below the Py/OH feed ratio of 16, the diffusion resistance due to the inadequate PPy coating increased and this resistance decreased with increasing PPy coating. However, at a feed ratio above Py/OH of 16, significant charge transfer resistance existed in the high frequency region due to the poor PPy coating that impeded the efficient charge transfer. Such assumption is also proved in the SEM image in Figure

4.3(b-c) where at Py/OH = 50, it starts to lose the high-aspect rod-shape and form granular thick agglomerates. The conclusion is consistent with our analysis from other characterization techniques.

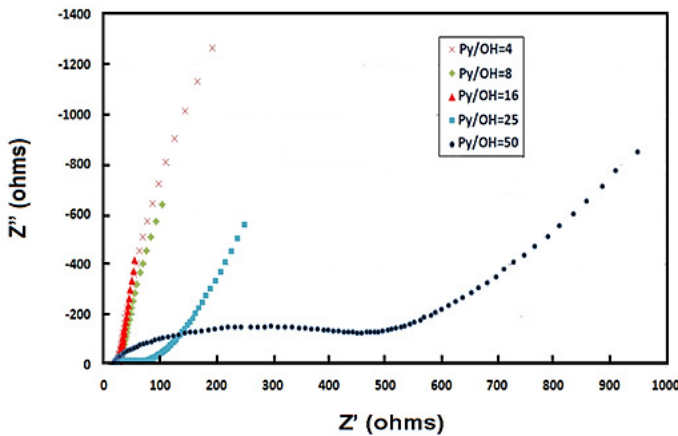


Figure 4.8 Nyquist plots obtained from EIS for different PPy/CNC samples in 0.5 M KCl where Py/OH=4, 8, 16, 25, 32 respectively.

4.3.3 Comparison of specific capacitance (Cs) with other electrode materials

Within the supercapacitor field, carbon nanotube (single walled/multi-walled) and graphene have aroused tremendous interest in the past due to their super-conductive characteristics. Table 4.1 compares the capacitance of the carbon nanotube, and graphene systems with the PPy/CNC system developed in this study together with similar system reported recently via electrochemical approach. It is clear that the PPy/CNC system performs better than the other systems and our product achieved using chemical polymerization is comparable to the relevant work using electrochemical approach in capacitance. As well, the CNC substrate is derived from abundant and sustainable sources and thus is relatively inexpensive, environmentally sound and renewable. The methodology is easily scale up and cost effective.

The exceptional supercapacitor performance of PPy/CNC is attributed to the following factors: (i) the favorable polymerization of PPy facilitated by the CNC substrate; (ii) the strong interaction between the PPy shell and the CNC core stabilizes the electrochemical sites of PPy during cycles; (iii) the porous hybrid nanostructure of PPy/CNC film on the electrode that facilities ion and solvent transport; (iv) the extremely low density of the CNC with an ultrathin coating of PPy enhances the specific capacitance. These advantages make PPy/CNC a promising and attractive candidate for the production of supercapacitor devices that are efficient, lightweight, cost effective, and environmental sound.

Table 4.1 Capacitance measured in different studies on Single-walled carbon nanotube (SWCT), Multi-walled carbon nanotube (MWCT) , PPy-coated MWCT, graphene sheet, hybrid nanostructure of PPy/graphene and CNC/PPy fabricated using a) in situ chemical polymerization method in our work b) Electrochemical co-deposition method(An et al., 2001; Frackowiak et al., 2000; Zhang et al., 2011; Li et al., 2011; Han et al., 2010; Liew et al., 2013)

Material	Electrolyte	Scan Rate [mV s ⁻¹]	Specific Capacitance [F g ⁻¹]	Reference
SWCT	7.5 M KOH	100	180	<i>An et al., 2001</i>
MWCT	6 M KOH	10	135	<i>Frackowiak et al. 2000</i>
PPy/MWCT	1 M KCl	100	200	<i>B. Zhang et al. 2011</i>
Graphene	1 M Na ₂ SO ₄	10	135	<i>Y. Li et al. 2011</i>
PPy/Graphene	1 M KCl	10	223	<i>Y.Han et al. 2010</i>
PPy/CNC ^a	0.5 M KCl	10	248	<i>Current Work</i>
		100	230	
PPy/CNC ^b	2 M KCl	10	240	<i>S. Y. Liew et al. 2013</i>

4.4 Conclusion

Conductive CNCs were successfully prepared by the polymerization of PPy on individual CNC surfaces via a facile in situ chemical polymerization technique. By tuning the feed ratio of Py/OH under controlled synthesis, an optimal polymerization condition was achieved to produce novel capacitive materials with superior electrochemical properties. Systematic and comprehensive studies are also conducted to associate, for the first time, the internal structural changes with the observed trend at different Py/OH feeding ratio. FT-IR studies indicated strong hydrogen bonding interactions between the CNC substrate and PPy coating. UV-Vis and Raman spectra both suggested that the optimal growth (i.e. conjugation length) of PPy on CNC occurred at a Py/OH feed ratio of 16. The quality of PPy coating is directly related to the electrochemical performance and despite the insulating nature of CNC, the conductivity of PPy/CNC synthesized under the optimal feed ratio approached a high value of 4.5 S cm⁻¹. PPy/CNC also exhibited outstanding supercapacitor behavior with capacitance of 248 F g⁻¹ at the scan rate of 0.01 V s⁻¹, retaining 90% capacitance at up to 0.1 V s⁻¹. The excellent electrochemical behavior of PPy/CNC is mainly attributed to the ideal CNC templating characteristics. The methodology proposed in this paper on the preparation of PPy/CNC is scalable and the nanomaterials produced can be adapted to many applications, such as printable electronics, antibacterial coating, tissue scaffold etc. Considering the cost and environmental benefits, the novel hybrid material of PPy/CNC is expected to be a promising system for the development of sustainable energy storage system in the future.

Chapter 5 Conductive cellulose nanocrystals with high cycling stability for supercapacitor applications

5.1 Introduction

The increasing demand for various consumer electronics and hybrid vehicles capable of delivering a high power in short pulses with an extremely long cycle life has prompted renewed interest in supercapacitors (SPs). Polypyrrole (PPy) has been extensively studied for decades as a promising electrode material for SPs due to its ease of synthesis, low cost, good conductivity, stability (Ryu et al., 2002; Rudge et al., 1994) and excellent specific capacitance (Cs). (Snook et al., 2011) However, being mechanically weak, PPy experiences significant structural breakdown resulting from volumetric swelling/shrinkage resulting in a fast capacitance decay over extended cycles (less than 50% retention of the initial capacitance after 1000 cycles). (Wang et al., 2012b; Liu et al., 2014; Zhao et al., 2013a) Another drawback is the poor processibility and unsatisfactory specific capacitance (Cs) (F/g) due to agglomeration resulting from strong intermolecular, intramolecular interactions and possible cross-linking of PPy chains. (Fan & Maier, 2006; Hsu & Wu, 2012)

The key to addressing these shortcomings will depend on the controlled synthesis of the active material. Generally, a large surface area between electrode material and electrolyte is critical for improving the capacitance, because of enhanced ion mobility. A thin and uniform coating of active material is also critical for a fast and effective ion diffusion in the polymer matrix. With the advent of nanotechnology, various PPy-based nanocomposites were developed by polymerizing PPy as a thin layer on another template material, such as graphite ⁹, carbon nanotubes (CNT)(Wang et al., 2007; Zhang et al., 2011; Yu et al., 2005; Zhang et al., 2005; Zhou et al., 2010c; Sivakkumar & Kim, 2007),, graphene oxides (GO) (Wang et al., 2007; An et al., 2001; K. Jurewicz, S. Delpoux, V. Bertagna, F. Beguin, E. Frackowiak, 2001; Frackowiak et al., 2000; Li et al., 2011). Large increase in the surface area arising from the nano-size effect of these PPy-based hybrid nanocomposites produced higher Cs compared to their bulk counterparts. Improved cycling stability was also achieved due to the enhanced reinforcement, e.g. PPy deposited/reduced GO achieved 249 F/g of Cs with 81% of the Cs retention after 1000 cycles under 0.3 A/g. (Zhang & Zhao, 2012) A Cs of 183.2 F/g at a high current density of 8 A g⁻¹ was obtained for CNT embedded PPy network with Cs retention of 85% after 1000 cycles at 1 A/g. (Fu et al., 2013)

Recently, several research efforts have been devoted to PPy/cellulose nanocomposites, due to their abundance, lightweight, good mechanical property, abundant hydroxyl group for further

functionalization, biodegradability and low cost. Many PPy/nanocellulose hybrids were synthesized via chemical oxidation polymerization in the form of films, gels, or cakes, due to the length of entangled cellulose network. (Müller et al., 2011; Pitchai-Mydeen & Ning, 2011; Sasso et al., 2010; Xu et al., 2013a; Wang et al., 2013b; Huang et al., 2006) More recently, individually coated nanocellulose was achieved on cellulose nanocrystals (CNCs) (Wu et al., 2014; Liew et al., 2010, 2013). These rice-shaped nanoparticles (100-400 nm long, 5-20 nm in diameter) are extracted from cellulose fibers by removing the amorphous region via acid hydrolysis yielding well-dispersed nanoparticles with high density of surface sulfuric acid groups. Liew *et al.* reported the successful synthesis of PPy/CNC via electrochemical deposition and demonstrated that the capacitance was comparable to PPy/CNTs synthesized under similar conditions. The high capacitance is largely attributed to the highly porous structure, thin coating of PPy on individual fibers, and rigidity of CNC substrate. (Liew et al., 2010, 2013) However, the end product from electrodeposition is a dense film on the electrode that limits further processing. Using a facile *in situ* chemical polymerization, our recent study on a PPy/CNC system with a core-shell structure possessed attractive supercapacitor behavior. (Wu et al., 2014)

Despite the success in the development of PPy-coated nanocomposites, the precise control of a uniform and thin PPy morphology at nanoscale remain a significant scientific challenge, hindering the commercial application of these composite electrode material. It is difficult to fully prevent the formation of free PPy particles in bulk solution, and deposited conjugated polymers on the nanoparticles are often irregular and thick. In most cases, the PPy-based hybrid material loses its fine fibril structure due to agglomerations. (Huang et al., 2005) Our previous strategy to improve the affinity between CNC and PPy coating via additional hydrogen bonding sites did not completely eliminate the formation of PPy particles and the irregular PPy coatings. (Wu et al., 2014) Previous studies have found that conductive polymers such as PPy favor the growth on CH₃ terminated hydrophobic regions than hydrophilic OH groups. (Huang, Z., Wang, P. C., MacDiarmid, A. G., Xia, Y., Whitesides, 1997) Several studies have demonstrated that the deposition of PPy onto relatively hydrophobic polystyrene latex particles (Lascelles & Armes, 1997) led to a much smoother, and continuous coating, while the deposition onto more hydrophilic poly (methyl methacrylate) latex produced discontinuous and patchy PPy coating. (Burchell & Armes, 2011; Ormond-Prout et al., 2009) Studies on PPy coated micro-sized silica particles with hydrophilic silanol groups led to highly globular-surfaced particles that aggregated to form ‘raspberry’-like structure. (Armes et al., 1991) This problem can be addressed through a simple pretreatment with either silanes via chemical grafting, or coating of a monolayer of poly (N-vinylpyrrolidone) (PVP),

to yield a uniform PPy coating on the substrate. (Lovett et al., 2014; Dai et al., 2007; Hao et al., 2003; Marini et al., 2008)

In this paper, we report on the development of a core-shell PPy/PVP/CNC nanorod that displays a smooth and uniform PPy coating. Surface modification on CNC was achieved through the physical adsorption of PVP to alter the hydrophilic nature of CNC for the favorable growth of PPy. PVP also acts as a steric stabilizer to prevent PPy-coated hybrid particles from further agglomeration. The degree of surface modification of CNC was also systematically evaluated since it is a crucial parameter to achieve an optimal PPy deposition. The optimally synthesized PPy/PVP/CNC on an insulating template possesses superior conductivity and demonstrates improved capacitance and cycling stability for SP applications. The current synthesis and characterizations were compared to the PPy/Tempo-CNC system reported recently by our group.

5.2 Experimental section

5.2.1 Materials

Cellulose nanocrystal (CNC) was provided by FP Innovations and Celluforce Inc. The chemicals used in this study were reagent grade, purchased from Sigma-Aldrich, and used as received. The chemicals for reaction are: poly (N-vinylpyrrolidone) (PVP) (MW 10,000 Da), Iron (III) chloride (97%), and pyrrole (98%).

5.2.2 Synthesis of PPy/PVP/CNC hybrid nanostructure

The experimental strategy for the synthesis of the core-shell structured PPy/PVP/CNC is illustrated in Figure 5.1. Surface modified CNC is simply achieved by mixing PVP with CNC. After PVP is physically adsorbed on the CNC surface, the oxidant and the monomer are then introduced. In specific, surface-modified CNCs were first prepared by mixing 0.2 wt% CNC solution with PVP at different PVP/CNC mass ratio of 100/0, 40/60, 10/90, 5/95, and 0/100 (samples denoted as PVP100/CNC, PVP40/CNC, PVP10/CNC, PVP5/CNC and PVP0/CNC respectively). The dispersion was mixed for 24 hours to ensure sufficient adsorption of PVP on CNC surface, which refer herein as PVP/CNC. In one typical polymerization for PPy/PVP/CNC, 15 ml of PVP/CNC solution was transferred to a double-jacketed reaction vessel kept in an ice water bath at 0 °C. Then 364.5 mg of FeCl₃ dissolved in 5ml water was added dropwise to the suspension and vigorously stirred. After an hour, 106.5 µl of pyrrole monomer (Py) dissolved in 5 ml water was added slowly and the polymerization was left to mix under mild stirring for 16 hours, and the reaction was

quenched by repeated washing with DI water in an ultrafiltration cell. Finally, the precipitates were freeze-dried, and the dried fine powder was pressed into pellet for conductivity measurements.

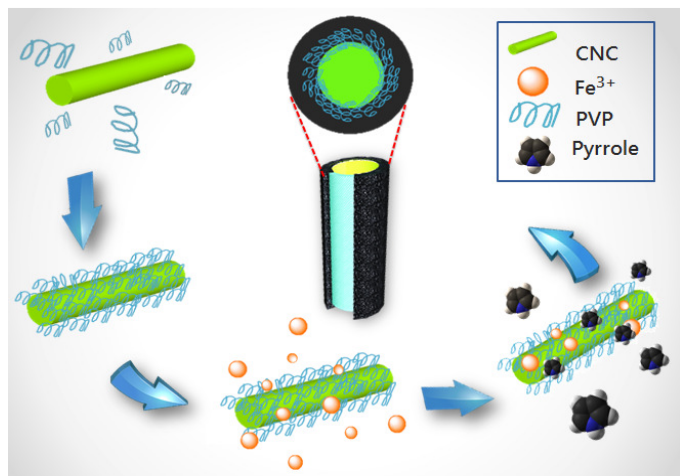


Figure 5.1 Schematic illustrating the formation of proposed core-shell PPy coated CNC. PVP was adsorbed onto the CNC surface prior to the polymerization to promote the homogeneous growth of PPy shell.

5.2.3 Characterization

The morphology of PPy/PVP/CNC system was characterized using a Philips CM10 electron microscope. The same TEM sample grid was used directly for scanning electron microscopy (SEM) imaging (Philips XL-30 microscope) and by attaching onto the carbon tape. The zeta potential of the PPy/CNC system was monitored throughout the polymerization process using a Malvern Zetasizer Nano ZS (Worcestershire, UK). Sample aliquots were collected from the reaction vessel at different time intervals, filtered with DI water and measured. The thermal stability of the PPy/PVP/CNC systems were studied by thermal gravimetric analysis (TGA). All samples were placed in an inert ceramic crucible and heated from 25 to 800 °C at a heating rate of 10°C min⁻¹ in 20 mL min⁻¹ air flow.

Conductivity was measured using a four-probe station in following the protocol in Chapter 3. Cyclic voltammetry (CV), charge and discharge (CD), and electrochemical impedance spectroscopy (EIS) were conducted using a CHI 760D electrochemical station (CH Instruments, USA) equipped with a three-electrode half-cell configuration (WE: glassy carbon(GC), CE: Pt wire and RE: saturated calomel reference electrode (SCE)). All measurements are performed after a 25-cycle CV for conditioning purposes between -0.6 and 0.4 V versus SCE in KCl electrolyte (0.5 M). The working

electrode was fabricated by repeated casting (twice) of the PPy/CNC (1 mg mL⁻¹ in 50% water/ethanol) dispersion onto the graphite carbon (GC) electrode (3 mm in diameter) at 10 µL each time and dried (mass loading on the electrode for testing is 20 µg). The CV test was performed with scan rates of 1, 10, and 100 mV.s⁻¹. Cycling stability test is carried out under the same experimental setup at the scan rate of 100 mV.s⁻¹. CD tests were performed by applying a constant current density between 2 to 10 A g⁻¹. Cycling stability using CD setup was performed with the same testing setup at 10 A g⁻¹.

5.3 Results and discussions

5.3.1 Effect of surface modification with PVP on PPy growth

The degree of CNC surface modification with PVP and its effect on PPy growth were characterized with a TEM and shown in Fig. Figure 5.2. A noticeable size expansion was observed in Figure 5.2(b) - (f) for all the PPy/CNCs synthesized at different PVP/CNC ratio confirming the successful polymerization of PPy shell. The fibril shape of CNCs with 150-250 nm in length was preserved after PPy coating. The most attractive feature of the PPy coating using this protocol is the continuous and uniform PPy coating. During our synthesis, we observed an appreciable increase in the polymerization kinetics from PVP100/CNC to PVP0/CNC based on the accelerating color change from light yellow to black, which was confirmed using a TEM. In Figure 5.2(b), CNCs were not completely covered by PPy and the magnified image clearly showed some exposed CNC surface that was not coated with PPy. By decreasing the PVP/CNC mass ratio to 10, a more uniform PPy coating with a thicker shell was formed on the CNC. When the PVP/CNC ratio was decreased, the PPy coating became inhomogeneous (Figure 5.2 (e)). When no PVP was added, the PPy coatings were irregular and rougher caused by the fast polymerization rate with also agglomerations appear (Figure 5.2 (f)).

Thermal gravimetric analyses (TGA) were conducted to qualitatively estimate the mass loading of PPy coating with different degree of CNC modification with PVP. Due to the higher thermal stability of PPy shell, the higher PPy loading should demonstrate milder decomposition closer to the bulk PPy sample synthesized under the same condition only in the absence of CNC nanoparticles or PVP. As shown in Figure 5.3, compared with PVP/CNC ratio 100 and 10, the higher PVP addition resulting in the lower PPy loading (35% mass retention for PPy/PVP100/CNC versus 48% PPy/PVP10/CNC at 400°C. When no PVP is added to modify CNC, the PPy loading is comparably

low as PPy/PVP100/CNC sample demonstrating incomplete PPy coating or a low PPy polymerization efficiency.

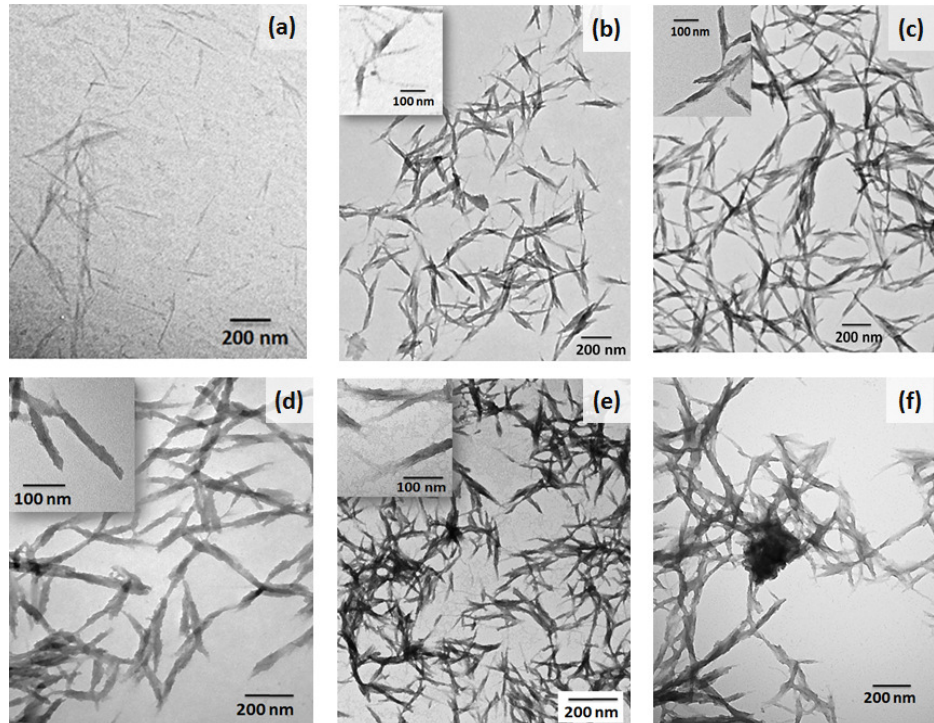


Figure 5.2 TEM images for (a) pristine CNC; (b) PPy/PVP100/CNC; (c) PPy/PVP40/CNC; (d) PPy/PVP10/CNC; (e) PPy/PVP5/CNC; (f) PPy/PVP0/CNC

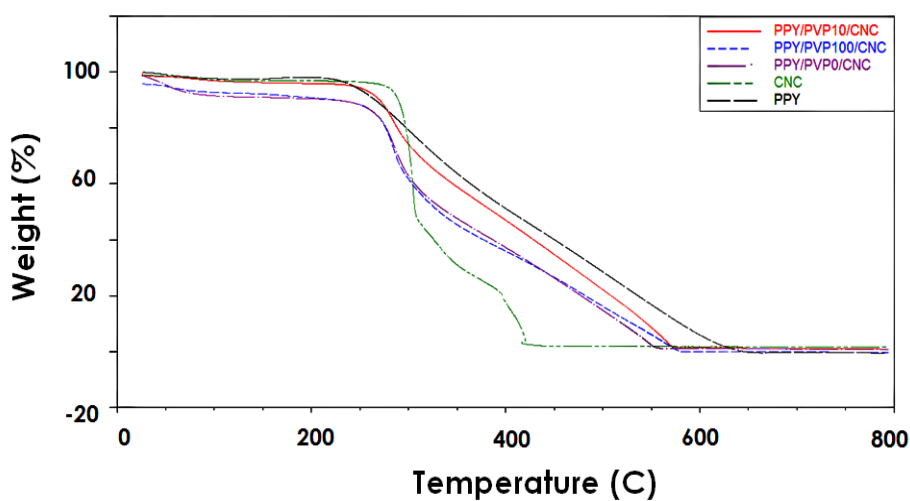


Figure 5.3 TGA curve for Pristine CNC, PPy, PPy/PVP100/CNC, PPy/PVP10/CNC, PPy/PVP0/CNC. All samples were placed in an inert ceramic crucible and heated from 25 to 800 °C at a heating rate of 10°C/min in 20 mL/min in air atmosphere.

To highlight the important role of PVP in the synthesis process, we mixed equal mass of pristine CNC with PVP modified CNC, and performed the polymerization in the same reaction vessel. Interestingly, the TEM image revealed two dramatically different phenomena: PPy was exclusively grown on PVP coated CNC, while those without PVP displayed inhomogeneously coated and globular PPy particles deposited on CNC surface. (Figure 5.4) The PVP is believed to serve two functions: (i) firstly, being an amphiphilic polymer, PVP provides hydrophobic domain that promotes a favorable growth of PPy on CNC surface; (ii) secondly, being a macromolecule, it acts as steric stabilizers that minimizes the agglomeration of PPy/CNC particles producing stable PPy/PVP/CNC hybrid nanoparticles in aqueous solution.(Dai et al., 2007) In addition, hydrogen bonding between the carbonyl groups of PVP and the N-H group of Py promotes a uniform growth of PPy on PVP-coated CNC.

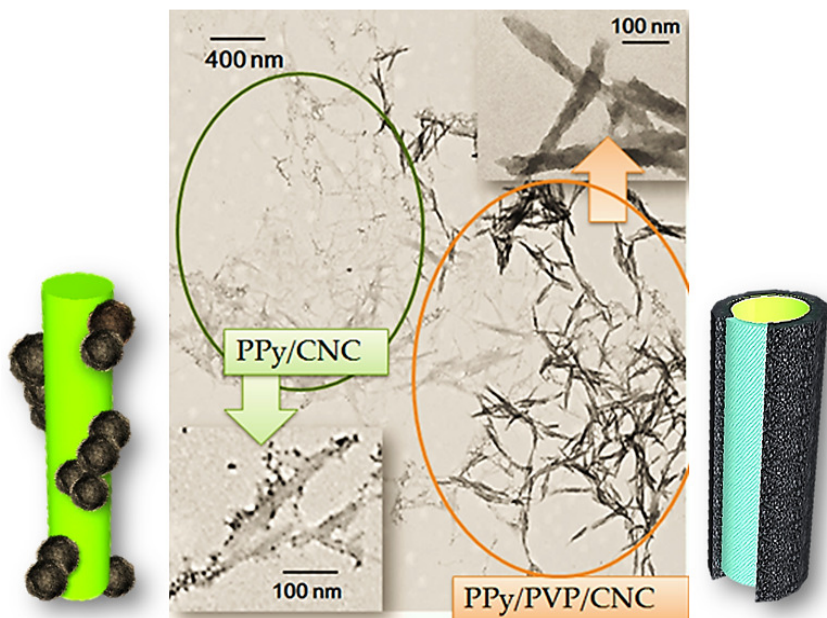


Figure 5.4 PPy polymerization in the presence of equal amounts of pristine CNCs and PVP/CNCs with cartoon illustrating the two drastically different morphologies of the end products.

The conductivity of PPy/PVP/CNC samples prepared at different PVP/CNC ratio were evaluated and summarized in Figure 5.5(a) together with the zeta potential (ZP). Due to the negatively charged sulfuric acid groups on the surface (i.e. OSO_3^-), CNC possessed a negative ZP of -55 mV and is extremely stable in aqueous solution. Coating of PPy neutralized the surface negative charges on CNC by the positively charged PPy backbone. From PPy/CNC10/CNC, the ZP increased sharply to a positive value signifying a homogeneous coating of PPy on CNC (i.e. CNCs are fully covered

with PPy layers, thereby shielding the sulfuric acid groups). This correlates with the conductivity data, where PPy/CNC10/CNC possessed the highest conductivity and the most positive ZP. However, when PVP addition was insufficient (less than PVP 5%), the ZP decreased to a negative value, indicating a non-uniform PPy coating on the CNC. The conclusions based on ZP measurements agreed with the TEM observations for all the samples prepared at different PVP/CNC as shown in Figure 5.3(b)-(f).

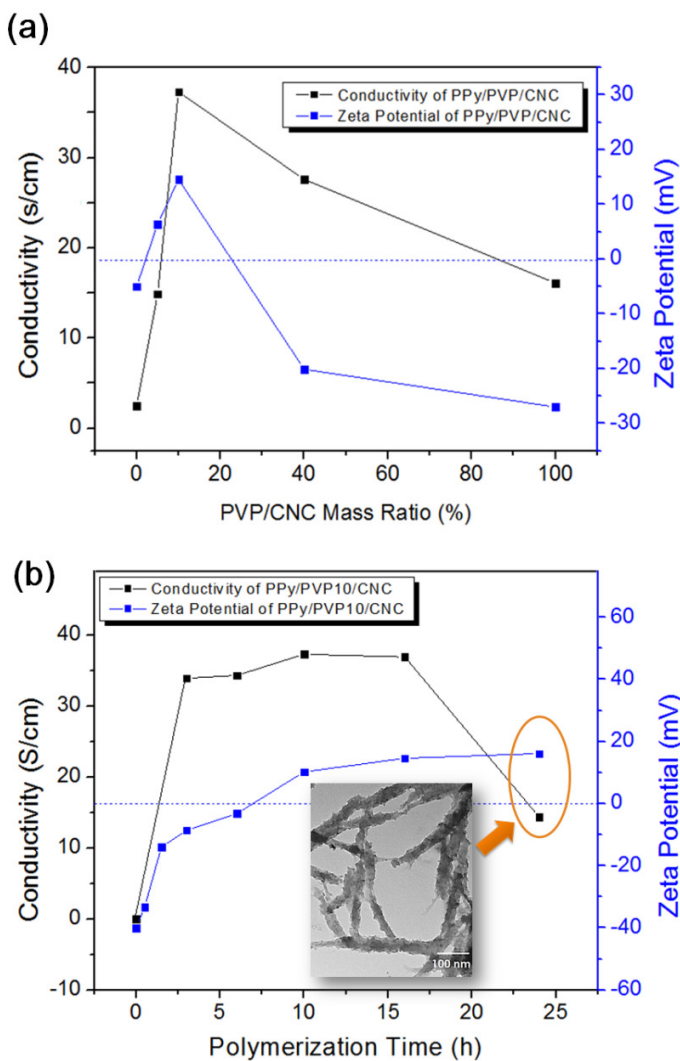


Figure 5.5 (a) The effect of the degree of surface modification on CNC on the zeta-potential and conductivity of the hybrid material of PPy/PVP/CNC after polymerization, and (b) Kinetic study: the effect of polymerization time on the conductivity and zeta-potential of PPy/PVP10/CNC. TEM image shows the morphology of PPy/PVP10/CNC sample under polymerization time of 24 hours.

The reaction kinetics of the PPy/PVP10/CNC sample were examined by monitoring the changes in

ZP over a period of 24 hours, and Figure 5.5(b) summarises the conductivity and zeta potential as a function of time. The ZP results suggested that the polymerization occurred rapidly in the first 3 hours, and it plateau after 10 hrs. The PPy growth on the surface of CNC approached the conducting percolation threshold at 3 hours with the conductivity reaching a plateau and remained constant for the next 10 hrs and it decreased rapidly after 16 hours. This is not unexpected since extended polymerization often leads to over-oxidation that disrupts the ordered conjugation structure in conductive polymer systems.(Marcus, 1956) The inset TEM image shows the PPy/PVP10/CNC sample at 24 hours. Compared with the sample at 16 hours (Figure 5.3 (d)), the surface morphology of PPy layer at 24-hours polymerization was much rougher and fluffier, which confirmed our earlier hypothesis.

5.3.2 Effect of PVP modification on electrochemical behaviour of PPy/PVP/CNC

Cyclic Voltammetry (CV) was conducted on different PPy/PVP/CNC systems. The specific capacitance (C_s) result from CV tests of different PPy/PVP/CNC samples were plotted and compared in Figure 5.6(a). The specific capacitance continued to increase from 3 hours until it approached a peak value of between 260 to 320 F/g at 16 hours, and decreased sharply after that. It is interesting to compare the CV results with the conductivity data in Figure 5.6(b). Though the conductivity approached a threshold at 3 hours, the capacitance did not. The capacitance reached its optimal levels when CNC/PVP was evenly coated with PPy. The sharp decrease in the capacitance was attributed to the thick and rough PPy coating, which hindered the ion diffusion and charge transfer. The best performance of PPy/PVP10/CNC in the CV test possessed a capacitance of 323 F g^{-1} . The superior C_s is mainly due to the nano-porous network formed by the 1D rod-shaped PPy/PVP/CNCs that possessed significant active surface area for the efficient ion diffusion and transport (the FESEM image of the deposited PPy/PVP/CNC film on the working electrode shown in the bottom of Figure 5.6(a)). Moreover, the lightweight substrate material of CNC and ultrathin and uniform layer of PPy coating also contribute to the high C_s .

To further investigate electrochemical performances of the PPy/PVP/CNC nanocomposite system, galvanostatic charge-discharge (CD) process was performed on PPy/PVP10/CNC sample, which is considered our optimal synthesis, at various current densities (Figure 5.6b). The CD curves in general appear the triangular symmetry and linear slopes, consolidating its good electrochemical performance. When lower current density is applied, the discharge curve has a slight curvature, representing the pseudocapacitance behaviour. The calculated capacitance approaches 338.6 F g^{-1} at 2 A g^{-1} . It is also worth noting that the PPy/PVP/CNC electrode displays only a moderate

drop, i.e. 5.4% of the Cs, when the current density increases from 2 to 10 A g⁻¹. This indicates that the utilization efficiency of the active material of PPy coating maintains at a high level at high charge current. Moreover, the IR drop in CD curves due to internal resistance of the electrode material was not observed in the PPy/PVP/CNC system. The stability during charge and discharge is a critical issue that is closely associated with the properties/morphologies of the active material. Figure 5.6(c) shows the cycling stability of the as-prepared PPy/PVP10/CNC nanostructures by conducting CD tests at a current density of 10 A g⁻¹. The Cs retained 87.3% of its initial value over 2000 cycles, indicating a good stability. Moreover, the sharpest drop in Cs occurred in the first 400 cycles, presumably due to the loss of active material that was only loosely attached on the carbon electrode. The decrease of Cs becomes much milder over extended cycles, which implies a good mechanical stability and capacitive behaviour of the composite material of PPy/PVP/CNC.

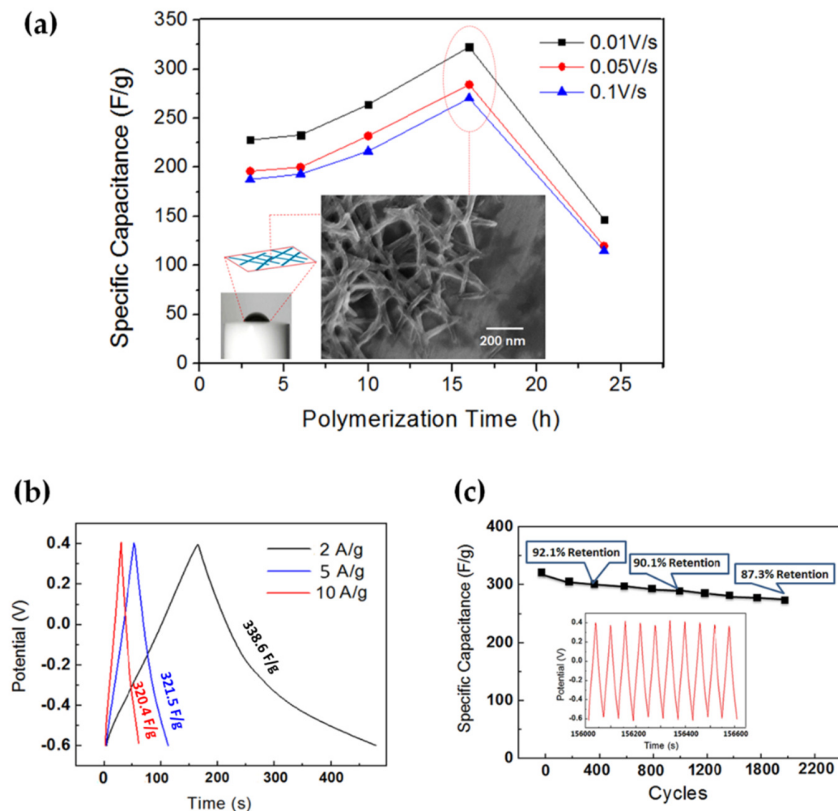


Figure 5.6 (a) Specific capacitance from CV test for PPy/PVP10/CNC polymerized at different time intervals. The FESEM image shows the porous structure formed by drop casting PPy/PVP10/CNC solution on the working electrode. (b) charge-discharge curves of PPy/PVP10/CNC electrode at different current densities. (c) Cycling performance of the PPy/PVP10/CNC electrode at the current density of 10 A g⁻¹. The inset shows the charge-discharge curves of the last 10 cycles.

5.3.3 Comparison of PPy/PVP/CNC and PPy/TempoCNC

We compared the current improved synthesis with our previous system prepared using TEMPO-oxidized CNCs (Table 5.1). (Wu et al., 2014) The key advantages of the new approach are: (i) the synthesis is conducted in mild pH condition, instead of extremely low pH environment needed for TEMPO-CNC; (ii) physical adsorption of PVP onto CNC is much simpler than TEMPO-mediated oxidation of CNC for enhanced affinity between the substrate and PPy. The important properties of PPy coated CNC using two different approaches are summarized and compared in Table 5.1. Firstly, the ZP of PPy/PVP10/CNC was positive while PPy/Tempo-CNC possessed a negative ZP at -31mV, suggesting that a more uniform and better coating of PPy was achieved for PVP/CNC system. Secondly, the conductivity of PPy/PVP/CNC increased 7 fold (conductivity increased from 4.9 to 36.9 S/cm), which is largely attributed to the improved PPy coating as confirmed by TEM images of both samples (Figure 5.7 b and c). PPy/Tempo-CNC produced a globular PPy coating morphology with sporadic coverage on the CNC nanorods, whereas PPy/PVP/CNC displayed a uniform core-sheath structure covering most of the CNC surface. An enhancement of 35% in the specific capacitance was observed for the PPy/PVP/CNC system.

Table 5.1 Comparison in synthesis and key characterizations of the improved PPy/PVP/CNC and PPy/Tempo-CNC system.

		PPy/TempoCNC	PPy/PVP/CNC
Synthesis	PH	Low	Neutral
	Surface modification of CNC	TEMPO-mediated Oxidation	PVP adsorption
Zeta Potential		- 31mV	+ 16.1 mV
Conductivity		4.9 S/cm	36.9 S/cm
Specific Capacitance	0.01 V/s	238.8 F/g	322.6 F/g
	0.05 V/s	224.7 F/g	284.2 F/g
	0.1 V/s	219.8 F/g	270.4 F/g
Capacitance Loss after 1000 cycles		36.9%	8.9%

The same CV stability tests were also performed on PPy/Tempo-CNC (Py/OH=16) and PPy/PVP16/CNC. The CV curves at different cycling numbers are shown in Figure 5.7(a) and 6(b), and the capacitance loss over cycling was plotted in Figure 5.7(c)). The cycling stability was greatly enhanced in the PPy/PVP/CNC system with less than a 9% capacitance loss compared to a 35% loss for the PPy/Tempo-CNC system. The superior cycling stability is attributed to a more uniform

PPy deposition that facilitates the charge transfer and diffusion. In addition, the affinity between PVP and PPy driven by hydrophobic interaction and hydrogen bonding provided a stronger and robust PPy coating. The enhanced cycling stability could also be due to the pseudo-3-layer structure of the PPy/PVP/CNC. The layer in the middle formed by PVP polymer chains serves as a buffer that effectively releases stress induced by ion diffusion/electron transfer within the hybrid material (illustrated in Figure 5.7(d)). This is especially advantageous compared to the 2-layered PPy/CNC model where there is no binder at the interface to provide flexibility between the substrate and the PPy sheath.

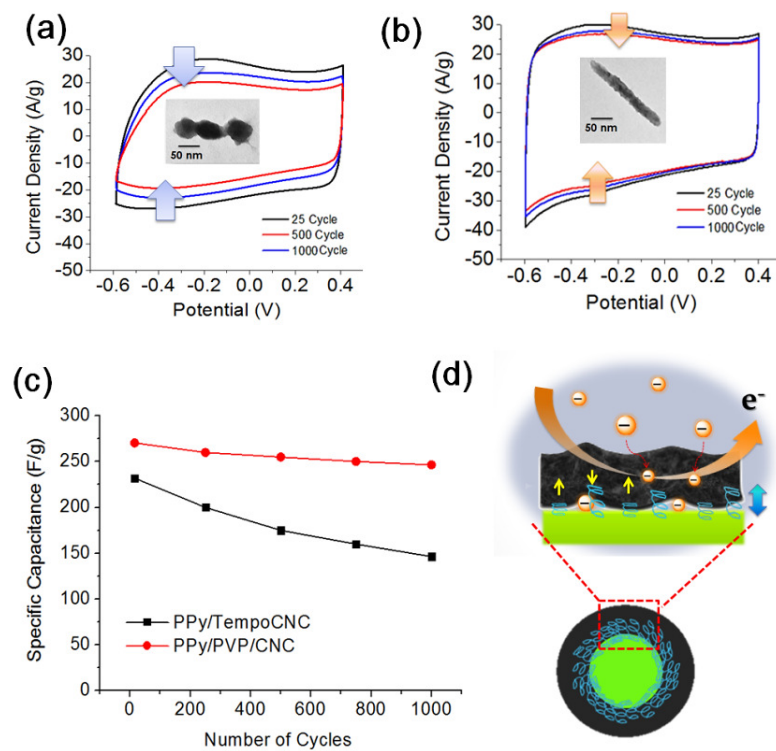


Figure 5.7 (a) CV curve of different cycles for sample PPy/TempoCNC during 1000 cycles at 0.1 V/s scan rate. The TEM image shows the typical morphology of PPy/Tempo-CNC. (b) CV curve of different cycles for sample PPy/PVP/CNC during 1000 cycles at 0.1 V/s scan rate. The TEM image shows the typical morphology of PPy/PVP/CNC. (c) Comparison of Capacitance loss between PPy/PVP10/CNC and PPy/Tempo-CNC (d) Proposed mechanism that PVP layer as a binder releases the stress and provides better accommodation for the conformational change for PPy during cycling.

5.4 Conclusion

We reported the synthesis of a core-shell PPy/CNC hybrid nanostructure with uniform and smooth PPy coating deposited on the pretreated PVP/CNC surface. The physical adsorption of PVP onto CNC surface prior to the introduction of pyrrole plays a critical role in ensuring a uniform PPy coating. PVP introduces hydrophobicity to CNC surface making it much more favorable for the growth of the hydrophobic PPy shell that acts as steric stabilizer preventing further agglomeration of the nanoparticles. An outstanding conductivity of 36.9 S/cm was achieved for the PPy/PVP/CNC synthesized with 10% PVP to CNC mass ratio. The calculated capacitance approaches 338.6 F g^{-1} at 2 A g^{-1} with a good Cs retention of 87.3% over 2000 cycles. The same CV measurement was performed and compared with our previous traditional chemical synthesis conducted over PPy coated Tempo-CNC system. An enhancement of 35% in the specific capacitance was observed for the PPy/PVP/CNC system with much improved cycling stability (less than 9% Cs loss over 1000 cycles) at 0.1 V/s fast scan rate. The current system displayed a more efficient and uniform growth of PPy coating with improved electrochemical behaviors (conductivity, Cs, Cycling stability). We believe the proposed approach of surface functionalization with PVP offers an attractive approach to produce conductive hybrid composite system with enhanced electrochemical performance.

Chapter 6 Nitrogen-enriched porous carbon nanorods templated by cellulose nanocrystals as high performance supercapacitor electrode

6.1 Introduction

Supercapacitors (SCs) have received ever increasing attention because of the demand for future energy storage devices capable of delivering high power density with an extremely long cycle life. SCs are highly desirable for a wide range of applications including regenerative braking, hybrid electric vehicles, consumer electronics, uninterrupted power sources, and industrial power management.(Gu & Yushin, 2014; Ibrahim et al., 2008) Based on different charge storage mechanisms, there are two types of SCs: electrical double layer capacitors (EDLCs) and pseudocapacitors (PCs). For EDLCs, charge/discharge occurs on the electrode interface, while PCs store energy *via* reversible redox reactions at the surface of the active material. PCs typically offer higher energy density than EDLCs, however they suffer from poor cycling stability and retention capability which also resulted from the redox reactions. Therefore, EDLCs are still preferred industrially. The electrode material in today's commercial SPs mainly comprises of active carbon due to its good electrochemical properties and relatively low cost.(Wang et al., 2012b)

To enhance the energy density to the level of a secondary battery, there is significant effort and activity on increasing surface area and porosity via advanced carbonaceous nanomaterials. Various carbon systems were proposed including activated carbon, carbide derived carbon, zeolite-templated carbon, carbon aerogel, onion-like carbon, carbon spheres, and carbon fibers were developed. (Zhai et al., 2011; Wei et al., 2012; Yang et al., 2013; Pech et al., 2010; Ma et al., 2014; Liu et al., 2015b; Zhao et al., 2015d) The well-controlled porous structure and high surface area achieved in the above systems have greatly enhanced the rate and capacitive performance of the carbon-based electrode material. However, achieving high surface area and porosity often necessitates the use of complicated template synthesis and a tedious activation processes. A further issue is that the conductivity decreases with increasing porosity.(Xu et al., 2008) Carbon nanotubes (CNTs) and graphene are two very attractive materials as high performance carbon-based SP electrode materials. Both have high electrical conductivity and exceptional theoretical surface area. (Arico et al., 2005; Du et al., 2011; Zhu et al., 2011b; Liu et al., 2010a) However, the production of good-quality CNTs and graphene is costly and achieving high surface area is challenging due to aggregation and stacking. An alternative to enhancing the energy density for carbon-based materials is via heteroatom-doping with elements such as boron(Kwon et al., 2009; Cermignani et al., 1995;

Wang et al., 2008b), phosphorus (Wang et al., 2013a; Paraknowitsch & Thomas, 2013; Paraknowitsch et al., 2013), sulphur (Hasegawa et al., 2011), and nitrogen (N) (Tan et al., 2013; Wen et al., 2012; Chen et al., 2013c, 2012a; Qin et al., 2009; Chen et al., 2013b; Jeon et al., 2014) into the carbon framework. Significantly higher specific capacitance (C_s) is achieved from enhanced electrochemical activity, such as higher conductivity and the PC effect. Improved wettability of porous carbons with electrolytes is also achieved by doping.(Lee et al., 2011; Paraknowitsch & Thomas, 2013; Li et al., 2010b; Kim et al., 2007)

Recently, nitrogen (N) doping has shown great promise, resulting in highly enhanced C_s while maintaining a superb cycling durability. (Zhao et al., 2015c; Zhu et al., 2015; Wang et al., 2013a; Cao et al., 2011; Jeon et al., 2014; Zhao et al., 2015a) The superior doping effect of N is believed to be the attraction between five valence electrons and protons that enhances the charge density of the space-charge layer (Wang et al., 2012a). Two strategies are commonly used to introduce N into carbon matrices: post-treatment with bases, such as ammonium, amine, urea; and in-situ doping with N-rich precursors. The first strategy normally results in surface doping with relatively low N content(Cao et al., 2011; Jurewicz et al., 2004; Kim et al., 2008; Jurewicz et al., 2008) while the second typically results in a more efficient, higher and uniform N doping that also allow the adjustment of N content via controlling the pyrolysis condition. (Li et al., 2010b; Kim et al., 2008; Jurewicz et al., 2008; Fuertes & Centeno, 2005) However, the second approach often involves the harsh etching of expensive templates such as mesoporous silica for the impregnation of N precursors, such as nucleobases and polyaniline, after pyrolysis (Fuertes & Centeno, 2005; Ania et al., 2007) or a time-consuming activation process, *via* direct carbonization of N-rich precursors, necessary for generating good pore structure. (Lota et al., 2007; Shrestha & Mustain, 2010) The production of carbonaceous electrode materials for SCs from biomass has attracted much interest (Raymundo-Piñero et al., 2006; Li et al., 2012b; Wu et al., 2013c; Chen et al., 2012a; Nguyen et al., 2014; Long et al., 2014; Chen et al., 2013a) providing a sustainable and cost-effective starting material. However, to date, the carbon materials produced from biomass typically have low surface area ($< 20 \text{ m}^2 \text{ g}^{-1}$) and are non-porous in the absence of activation or templating.(Zhao et al., 2010) Therefore, the task of developing carbon-based electrode materials with high surface area, porosity, and effective heteroatom doping using simple and cost effective methods still remains.

In this work, we report on the novel fabrication of N-enriched carbon nanorods (NCNR) with high surface area and porosity based on melamine formaldehyde coated cellulose nanocrystals (MFCNCs). CNCs extracted from wood fibers are typically 200 nm long and 2-5 nm in diameter, and they are good templates for the controlled-growth of MF on CNC to yield a core-shell-structured

MFCNC. The good water dispersibility of CNC allows the individual coating of MF in aqueous solution. The production of hierarchically porous carbon nanorods and the required nitrogen doping was readily achieved through a one-step pyrolysis of MFCNC without any activation process or the use of sacrificial templates. The optimal capacitance of 350 F g^{-1} was obtained for NCNR with robust cycling stability when 1M sulfuric acid was used as the electrolyte. The superior supercapacitive behavior of NCNR were also demonstrated in neutral and alkaline electrolytes, indicating the versatility of NCNRs as supercapacitor electrode materials. The enhancement in capacitance due to N doping becomes apparent when compared to the carbonized system based on pristine CNCs.(Asefa, 2012) To the best of our knowledge, this is the first synthesis of MF coated CNCs, as well as the first report of N-doped carbonized CNCs for supercapacitor application.

6.2 Experimental section

6.2.1 Materials

Cellulose nanocrystals (CNCs) were provided by FP Innovations and Celluforce Inc. All the chemicals used in this study were analytical grade, purchased from Sigma-Aldrich, and used as received.

6.2.2 Synthesis of NCNR

The schematic for the preparation of NCNR is shown in Figure 6.1. MF precursor was mixed with CNCs to allow for the in-situ polycondensation on the surface of CNCs. Then the core-shell structured MFCNC was carbonized to N-MFCNC under various temperatures. This synthesis is simple in terms of the procedure and apparatus, and it is highly efficient and industrially scalable. The experiment can be divided into the following steps and is explained in detail below:

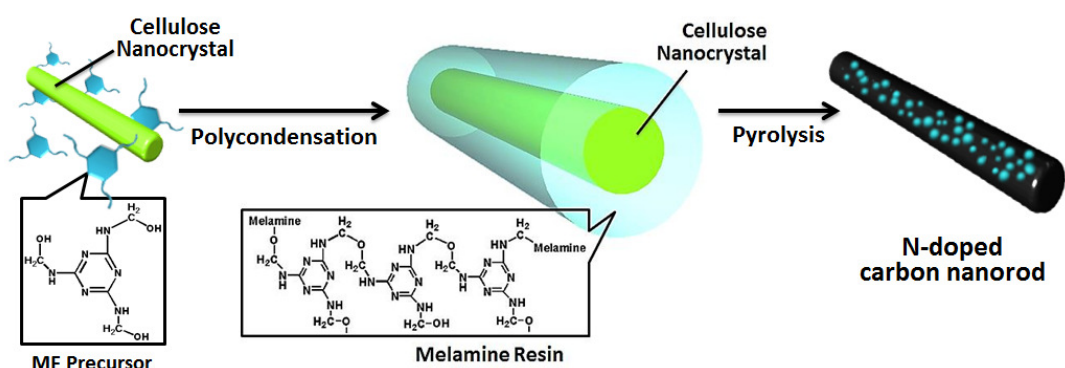


Figure 6.1 Schematic of 2-step synthesis of nitrogen-doped carbon nanorods.

6.2.2.1 Synthesis of melamine-formaldehyde (MF) pre-polymer

In a typical synthesis, 2.2 g of melamine and 4.0 mL of formaldehyde (37% in water) was mixed in 10 mL deionized water in a 50 mL flask, followed by pH adjustment to between 8 and 9 using NaOH solution. The temperature was increased to 80 °C under mechanical or magnetic stirring. The solution turns from cloudy to transparent within about 5 min. After 30 min, the precursor is ready for the next step.

6.2.2.2 Synthesis of Melamine-Formaldehyde coated Cellulose Nanocrystals (MFCNCs)

100 mL of 1% CNC suspension was mixed with the MF precursor from step 1, followed by adjusting the pH to between 4 and 5 with HCl solution. The suspension was stirred for 2 h at 80 °C. During the process, the cross-linked melamine formaldehyde resin condenses on the CNC surface and forms a coating. The suspension was then allowed to cool to room temperature and purified by repeated filtration and washing with DI water. MF resin was synthesized under the exact same condition in the absence of CNC.

6.2.2.3 Synthesis of N-doped mesoporous carbon nanorod (NCNRs)

NCNR were prepared by carbonizing the freeze-dried MFCNCs in a quartz tube under a flow of Ar₂ up to a desired temperature. Three different temperature for pyrolysis is conducted, 800, 900, and 1000 °C, respectively with a ramping speed of at 5 °C min⁻¹. Upon reaching each temperature, the sample was held for another 2 hours before cooling. MFCNCs carbonized at various temperatures are denoted as NCNR800, NCNR900, NCNR1000.

6.2.3 Characterization

The morphology of MFCNC and CNC was characterized using a Philips CM10 transmission electron microscope (TEM) and JEM-2100 High resolution TEM. The CNC sample was stained with 2% (w/w) uranyl acetate negative stain for high resolution imaging. The surface charge of the MFCNC and CNC were measured using a Malvern Zetasizer Nano ZS (Worcestershire, UK). The coating of MF on CNC was further confirmed by FT-IR (Bruker Tensor 27 FT-IR). The composition of the synthesized MFCNC was estimated from thermal gravimetric analysis (TGA) by assuming that the thermos degradation process of MFCNC is exactly the same as that of CNC and MFCNC separately. Samples of MFCNC, CNC and MF were placed in an inert ceramic crucible and heated from 25 to 800 °C at a heating rate of 10 °C min⁻¹ with a flow of N₂ of 20 ml min⁻¹. X-ray diffraction (XRD) was performed with the Rigaku D/MAX-RB diffractometer using filtered Cu K α radiation.

The analysis of the surface area, pore diameter and volume of NCNRs was determined by N₂ adsorption analysis with an autosorb iQ-AG instrument (Quantachrome Co., USA) at 77 K using the multipoint BET (Brunauer–Emmett–Teller) model to eliminate any interference from weakly adsorbed species. Prior to measurements, the samples were degassed overnight at 150 °C under vacuum. Raman scattering spectra was recorded with a HORIBA Scientific LabRAM HR system (532.4 nm laser).

Cyclic voltammetry (CV), charge and discharge (CD), and electrochemical impedance spectroscopy (EIS) were conducted using an electrochemical work station (Zahner-Electrik, Germany) equipped with a three-electrode half-cell configuration with a Pt wire as the counter electrode. For testing in 2 M KCl, 6 M KOH, 1M H₂SO₄ electrolytes, Hg/HgCl, Hg/HgO, Ag/AgCl were used as the reference electrodes respectively. To fabricate the working electrode, the NCNRs were dispersed in a water/ethanol mixture (V/V=50/50) to form an aqueous 2 mg ml⁻¹ ink and well sonicated. Then 10 µl of ink was pipetted twice onto the graphite carbon (GC) electrode (3 mm in diameter). The CV test was performed with scan rates between 1 to 400 mV s⁻¹. Charge and discharge (CD) tests were performed by applying a constant current density between 5 to 20 A g⁻¹. Cycling stability was measured with the same testing setup as CD at 20 A g⁻¹. EIS was conducted in the frequency range from 0.1 Hz to 200 kHz at an open circuit potential with AC amplitude of 5 mV.

6.3 Results and discussion

6.3.1 Characterization of MFCNC composite

To confirm the presence of MF in the MFCNC system, FTIR spectra were acquired and compared with those of MFCNC and CNC (Figure 6.2(a)). Several peaks in the MFCNC spectrum are absent in the CNC spectrum. The new peaks are due to the 1, 3, 5-triazine ring (at 1556 and 812 cm⁻¹) and the methylene C-H bending vibration (at 1330 cm⁻¹) of melamine. (Wu et al., 2013d) Further evidence was provided by zeta potential measurements, where pristine CNC with a zeta-potential of -54 mV was dramatically increased to + 35 mV for MFCNCs, suggesting the good coverage of MF on the surface of CNCs. The MF content in the composite material was determined by thermogravimetric analysis (TGA), shown in Figure 6.2(b). The thermo degradation curves showed that the residue at 600°C was 14.6% for CNC, 25.6% for MFCNC, and 33.5% for pure MF resin. From this information, the MF resin content in MFCNC was calculated to be 58.2% based on Equation 6.1 and Equation 6.2:

$$\text{Equation 6.1} \quad C_{\text{CNC}} + C_{\text{MF}} = 1$$

$$\text{Equation 6.2} \quad 0.146C_{\text{CNC}} + 0.335C_{\text{MF}} = 0.256$$

where C_{CNC} is the content of CNC in MFCNC, and C_{MF} is the content of MF in MFCNC.

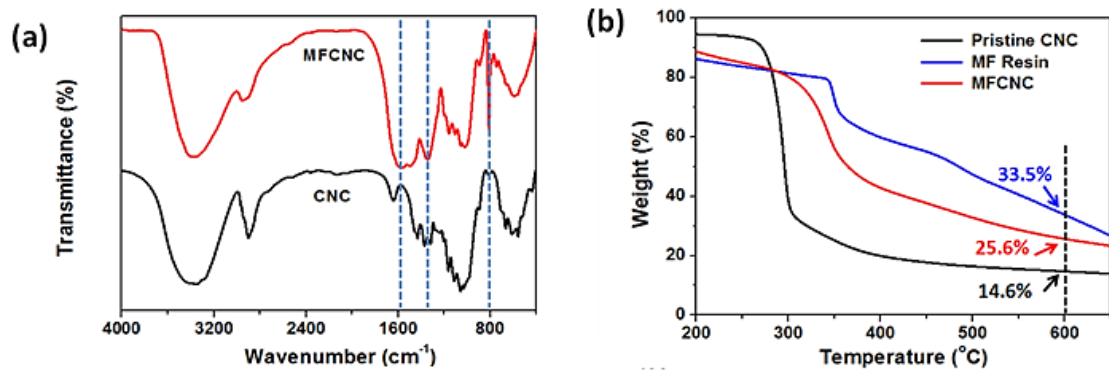


Figure 6.2 (a) FTIR characterization for the freeze-dried MFCNC and CNC powder, and (b) TGA measurement for MF resin, MFCNC and CNC under N_2

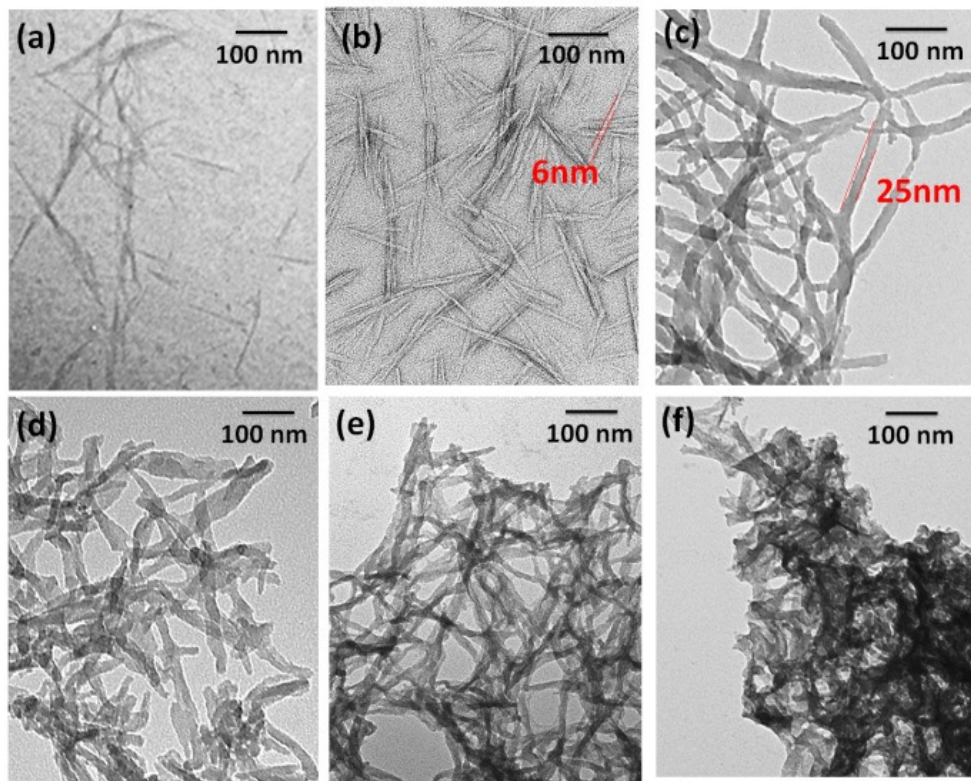


Figure 6.3 (a) TEM image for pristine CNCs, (b) High resolution TEM for pristine CNCs with uranyl acetate staining, and TEM images for (c) MFCNCs, (d) NCNR800, (e) NCNR 900, and (f) NCNR 1000.

The synthesized MFCNC was directly imaged using TEM (Figure 6.3(a)-(c)). CNCs without staining are very lightly colored in TEM images due to their low density. A more defined edge was shown in Figure 6.3(b) for stained CNC, and a typical diameter was observed to be around 6 nm. MFCNCs however, appear much darker in color (Figure 6.3 (c)) with a noticeable increase in diameter to around 25 nm, indicating the successful coating by the MF resin. The hybrid material preserves the rod-shape of the CNC with a smooth and thick MF surface. MFCNCs after synthesis remain well dispersed in solution and appear milky in color. TEM images for MFCNC after carbonization at various temperatures are shown in Figure 6.3(c)-(e). By increasing the temperature of pyrolysis from 800 to 900 °C, NCNR shows a slight shrinkage in diameter while maintaining a well-defined shape. However, further increase in the carbonization temperature to 1000 °C results in some structural breakdown which is shown in Figure 6.3(f).

The degree of graphitization of all NCNRs was investigated with XRD shown in Figure 6.4(a). The peaks at $2\theta=18.5^\circ$ and 40° are most relevant in assessing carbonization. These peaks show that NCNRs consists of graphitized carbon after carbonization. In particular, increasing the temperature from 800 to 900°C increases the peak intensity, suggesting a higher degree of graphitization at higher temperature. When the temperature reaches 1000 °C, both peaks are significantly quenched due to the poorly organized carbon structure (also supported by TEM observation), which will also affect the electrochemical performance. Raman spectrometry (RS) is a sensitive technique to investigate the structural defects in carbon systems and was performed on all the NCNR samples shown in Figure 6.4(b). Two peaks at 1350 and 1590 cm^{-1} , corresponding to the D and G band for carbon materials, can be observed in the RS of all NCNR samples. Since the D band changes with defects in the graphitic structures, the intensity of the D peak relative to that of G peak (I_D/I_G) is related to the amount of defects in the carbon materials.(Nemanich & Solin, 1979) By increasing the pyrolytic temperature from 800 to 900 °C, there was a decrease in I_D/I_G from 1.13 to 1.06 presumably due to both an increase in graphitization degree and a decrease in the nitrogen doping content.(Xiao et al., 2012) A sharp increase to 1.14 in the ratio of the D to G bands when the temperature was increased to 1000 °C indicating a higher amount of disorder and defective sites introduced to the carbon structure. This is in good agreement with the TEM micrographs which show many structural defects in the samples carbonized at 1000 °C (Figure 6.3 (f)).

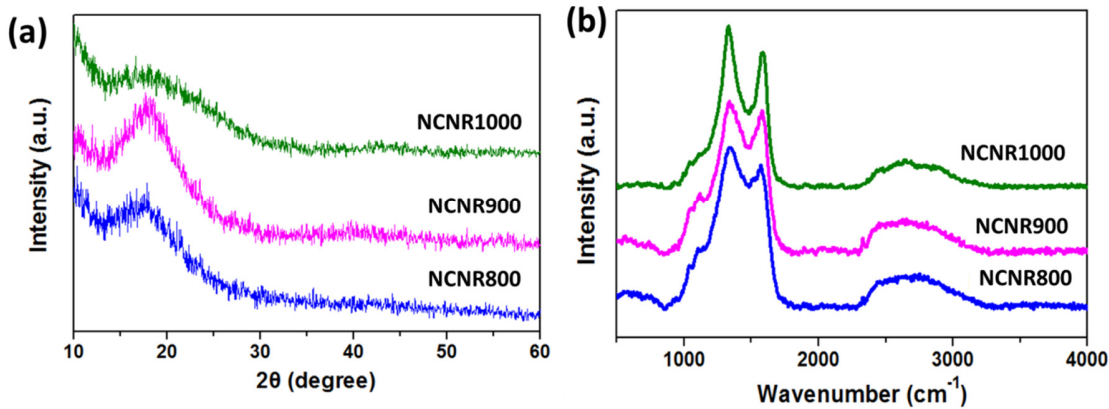


Figure 6.4 (a) XRD and (b) RAMAN spectra characterization for N-MFCNC prepared at various carbonization temperatures

6.3.2 Effect of pyrolysis temperature on physiochemical properties of NCNRs

Since carbonization temperature can significantly affect the physical and chemical properties of the carbon material, the composition, pore structure, and surface area were carefully investigated for NCNR samples prepared at 800, 900 and 1000 °C respectively. The last 2 rows of Table 6.1 summarize the composition by elemental analysis of MFCNC before and after pyrolysis showing the efficient N doping from MF coating. The N doping depends on the pyrolysis temperature: 15.6% for NCNR800, 8.45% for NCNR900 and 4.28% for NCNR1000. The decreased nitrogen content with increased temperature is in good agreement with previous studies and the phenomenon was proposed to be due to the evolution of nitrogenous volatile products such as HCN.(Hulicova et al., 2005; Hirata et al., 1991; Devallencourt et al., 1995) The texture of the material described by the pore size distribution (PSD), pore volume, and pore type is a critical for the supercapacitor performance and this is greatly affected by the carbonization temperature. To investigate the temperature effects on porosity, PSD curves and isotherms were developed and the results were plotted and summarized in Figure 6.5 and Table 6.1.

The isotherms of all samples exhibited the representative type III behavior defined by IUPAC with a H_3 type hysteresis loop. The sharp capillary condensation step at high relative pressures $P/P_0 > 0.90$ suggests the existence of large mesopores and macropores as indicated in the PSD graph. Moreover, NCNR900 shows a noticeable increased adsorption in the low pressure region suggesting the existence of micropores (Tripathi et al., 2014; Liu et al., 2015b), while in the case of NCNR800 and NCNR1000, almost adsorption was observed. The observation is in agreement with the results summarized in Table 6.1, NCNR900 possessed an optimal pore structure with the largest specific

surface area of $564.2 \text{ m}^2 \text{ g}^{-1}$ that contributed to the improved capacitive performance both EDLC and PC devices due to enhanced interactions with the electrolyte. Compared to NCNR800, the increase in V_{total} is mainly contributed by the development of mesopores as indicated in the PSD graph where both micropores and mesopores are much better developed with intensified peaks at 1.5 nm, 2.5 nm and in the 4-5 nm region. Compared with MFCNC without annealing, NCNR samples carbonized at 800 and 900 °C showed an apparent increase in the surface area and a better developed pore structure. The sharp decrease in V_{total} and surface area was observed for NCNR1000 which is mainly attributed to the destruction of the rod structure causing pore blockage (which is in agreement with the TEM observation). It is evident in the PSD curve that some isolated peaks from NCNR800 and NCNR900 merged into a much broader peak that decreased significantly in intensity. For example, the peaks at 2.5 nm and 4 nm for NCNR900 became a broad weak peak at 3.3 nm. It has been demonstrated that a hierarchy of pores enhances the capacitance in several ways(Li et al., 2013c; Wang et al., 2008c): the macropores may serve as ion-buffering reservoirs, shortening the diffusion path to the interior pore surface; the mesopores may reduce the ion transport resistance and the micropores may enhance the EDLC capacitance. Therefore, NCNR900 with an optimal hierarchical porous structure with a moderate N-doping content is expected to be most favourable for supercapacitor applications.

Table 6.1 Summary of physicochemical characterization by BET and the composition of various N-MFCNCs by elemental analysis

	MFCNC	NCNR800	NCNR 900	NCNR 1000
BET surface area (m^2/g)	212.8	358.9	564.2	97.5
Total pore volume (cm^3/g)	0.07	0.50	2.03	0.40
Mean pore diameter (nm)	1.34	2.00	1.65	1.93
N Content (%)	34.73	15.60	8.45	4.28
C Content (%)	38.09	68.59	75.53	83.65

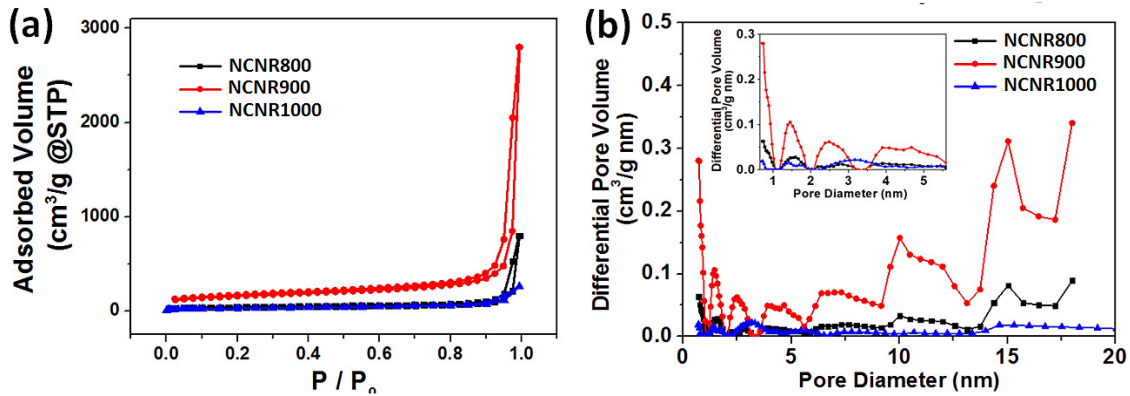


Figure 6.5 (a) N₂ adsorption/desorption isotherms and (b) the corresponding PSDs of samples carbonized at different temperatures.

6.3.3 Effect of pyrolysis temperature on electrochemical behavior of NCNRs

To assess this expectation, a series of electrochemical tests were conducted and the results are presented below. The electrochemical performances of the NCNRs were investigated in a three electrode cell with a 1M sulfuric acid aqueous electrolyte. The CV curve for N-MFCNC samples carbonized at various temperatures all demonstrated a quasi-rectangular shape which suggests the combined effect of double-layer capacitor and pseudo-capacitive mechanisms in our system (Figure 6.6 (a)). The deformation of the CV curve at higher voltages is mainly due to the heteroatoms present in the carbon frame that causes a surface polarity phenomenon. NCNR900 possesses the best Cs reaching 328.5 F g⁻¹ at a 0.01 V s⁻¹ sweep rate, followed by 287.3 F g⁻¹ and 177.5 F g⁻¹ for NCNR800 and NCNR1000 respectively. The prominent redox hump along the current-potential axis at 0.1-0.2 V for NCNR800 is due to the Faradaic reaction from richer nitrogen functionalities. The presence of N in the carbon frame introduces basicity to the carbon framework that will further enhance the interaction with acidic electrolyte. The overall good capacitive behavior for all NCNRs is due to the combined contribution of double layer capacitance from high surface area and the pseudocapacitance from N functionality. N doping also increases conductivity and improves wettability that further enhance the supercapacitive performance.(Paek et al., 2013; Kwon et al., 2009) It is worth noting that the capacitance of NCNR900 surpasses the other two samples despite the lower N content of the NCNR800, which shows the crucial role that the hierarchical porous structure has on supercapacitor performance. Moreover, the relationship between scan rate and capacitance (Figure 6.6 (b)) suggests good capacitance retention when the scan rate was increased from 0.01V s⁻¹ to 0.4 V s⁻¹, indicating efficient charge transfer kinetics. As shown in Figure 6.6(c), the CV curve preserves its shape even at an increased scan rate up to 0.4 V s⁻¹. Further increasing

of the carbonization temperature from 900 to 1000°C, however, results in a significant reduction in the capacitance due to the loss in N-doping, surface area, and pore structure.

To further investigate the supercapacitive behavior of NCNR900, CD characterization within the same voltage window as CV tests was performed at 5 A g^{-1} , 10 A g^{-1} , and 20 A g^{-1} and the results are given in Figure 6.6(d). The obtained V-I relationship is approximately linear with a slight curvature due to Faradaic reaction, implying that the material is behaving as a capacitor with high charge and discharge efficiency. The capacitance was calculated to be 352 F g^{-1} , 320 F g^{-1} , 295 F g^{-1} , and 263 F g^{-1} at high charge/discharge rates of 5 A g^{-1} , 10 A g^{-1} , 20 A g^{-1} , and 40 A g^{-1} respectively.

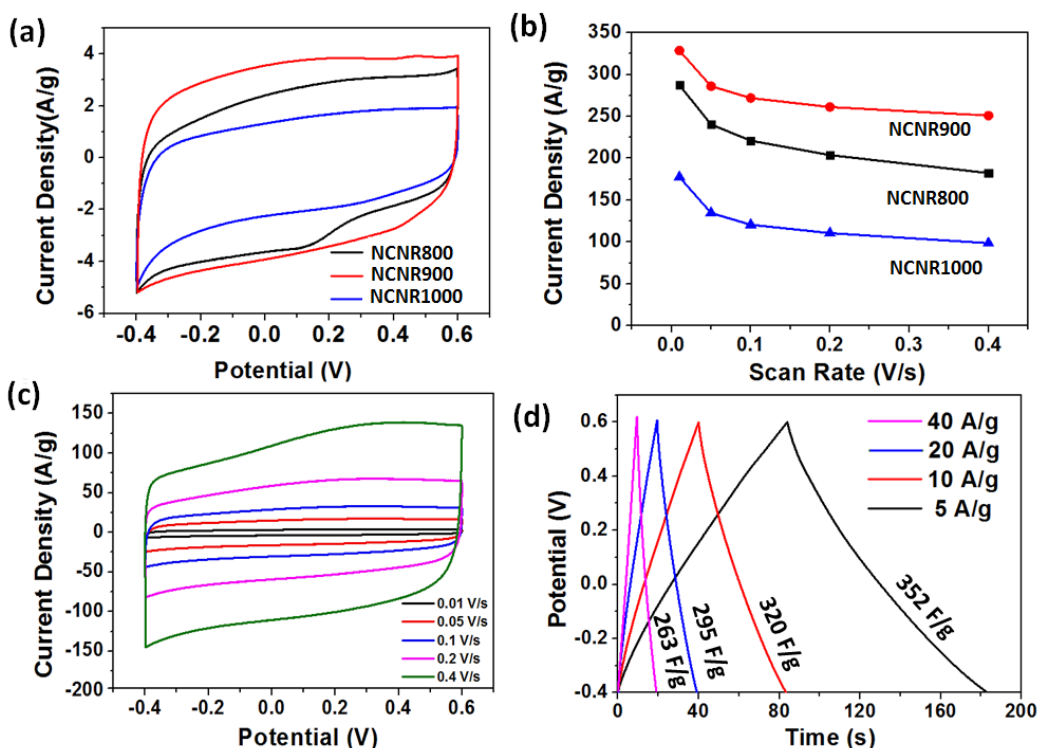


Figure 6.6 (a) Cyclic Voltammetry curves for NCNR800, NCNR900, NCNR1000 with the same scan rate of 0.01 V/s ; (b) Capacitance retention profiles with increasing scan rates for NCNR800 NCNR900 and NCNR1000; (c) Cyclic Voltammetry curves for NCNR900 at various scan rates; and (d) Charge/discharge curves for NCNR900 at various current density.

In spite of the lower surface area compared with another reported carbonized CNC system using the more challenging silica template approach(Asefa, 2012) ($546 \text{ m}^2 \text{ g}^{-1}$ versus $400 \text{ m}^2 \text{ g}^{-1}$), our NCNR still yields excellent Cs (352 F g^{-1} at 5 A g^{-1} versus 170 F g^{-1} at 0.23 A g^{-1}). This comparison further demonstrates the crucial role of introducing N-functionality to enhance electrochemical properties. The specific energy density and power density were further calculated from the CD characterization.

The excellent energy density reaches 48.8 Wh kg^{-1} at a current density of 5 A g^{-1} and maintains a rather impressive value of 36.5 Wh kg^{-1} at a current density of 40 A g^{-1} . The value is significantly higher than that of the commercial carbon supercapacitors which is in the range of $4\text{-}5 \text{ kWh kg}^{-1}$.(Burke, 2007) Furthermore, the high power density of 39.85 kW kg^{-1} was achieved at the current density 40 A g^{-1} which is almost twice the power target of the PNGV (Partnership for a New Generation of Vehicles) which is 15 kW kg^{-1} .(Wang et al., 2008c)

Since cycling stability is a critical issue for most of the pseudocapacitive electrode materials due to material degradation from irreversible Faradaic redox reactions, the stability test was conducted at a harsh charge-discharge rate of 20 A g^{-1} for 2000 cycles for NCNR900. From the results shown in Figure 6.7(a), the capacitance loss was only 4.6% even under such a high current density, indicating a durable structure and an efficient ion transfer mechanism for MFCNC900. EIS testing of all NCNR samples was performed to elucidate the capacitive behavior and the results are shown in Figure 6.7(b). A much steeper linear shape in the low frequency region was observed for NCNR900 compared to the other two samples demonstrating an ideal capacitive behavior with the lowest ion diffusion resistance. (Conway, 2013)

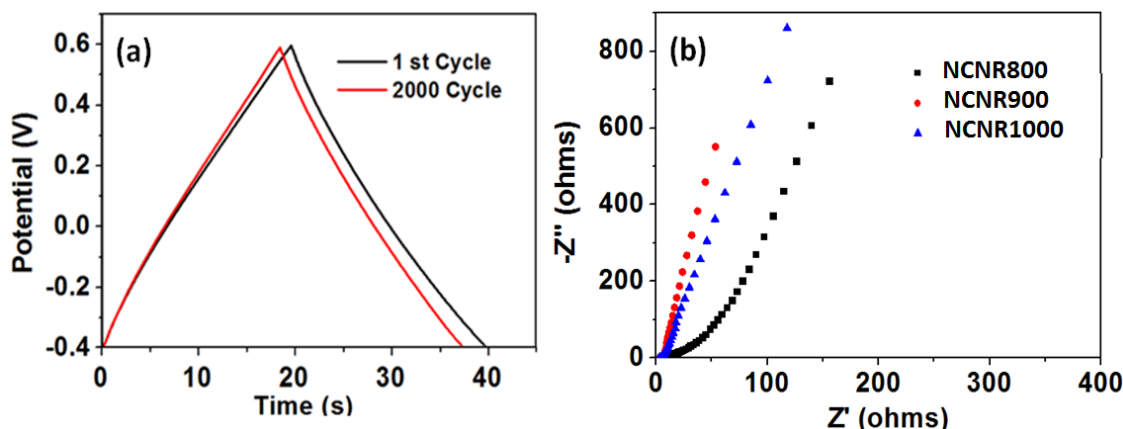


Figure 6.7 (a) Stability test for NCNR900 at 20 A/g charge/discharge rate for 2000 cycles, and (b) electrochemical Impedance Spectroscopy for NCNR800 NCNR900, NCNR1000 under 5 mV (AC voltage).

To further explore the versatility of our NCNR, we carried out a series of electrochemical tests in two other common electrolytes- 2 M KCl and 6 M KOH . Excellent performance was also observed for NCNR900 showing capacitances of 237.2 F g^{-1} and 289.5 F g^{-1} in neutral and alkaline electrolyte respectively (a summary of capacitance performance in various electrolytes is shown in Table 6.2). The capacitance performance for N-MFCNC samples follows the same order in all three electrolytes: NCNR900 > NCNR 800 > NCNR 1000. It was found that the CV curve for NCNR

900 in neutral electrolyte displays the most rectangular shape (Figure 6.8(a)), suggesting that the contribution for capacitance at neutral electrolyte is mainly from the EDLC mechanism. Therefore, the overall capacitive performance is lower than in acidic and basic electrolytes due to the lack of pseudocapacitance. Further evidence is revealed in CV curves for various NCNR (Figure 6.8 (c)(d)). No visible redox peaks were evident in any of the three NCNR samples when tested in neutral electrolyte while the CV curves in basic electrolyte, both NCNR 800 and NCNR900 exhibited obvious peaks due to the Faradaic contribution from the nitrogen functionalities. However, NCNR900 conducted in neutral electrolyte demonstrates better cycling stability compared to that in acidic (4.6% loss) and alkaline electrolyte (4.3% loss); no capacitance loss over 2000 cycles was observed at the fast charge and discharge rate of 20 A g^{-1} . This trend in cycling stability is to be expected for N-MFCNC in different types of electrolyte as it should follow the degree of Faradaic reaction. The strong performance in the neutral electrolyte originates primarily from the electrostatic nature of the charge storage for double layer capacitors, while the basicity of MFCNC resulting from nitrogen functionality enhances the pseudocapacitive performance *via* Faradaic reaction in acidic solution.

Table 6.2 Summary of capacitance performance of MFCNC 800 MFCNC900 MFCNC1000 in neutral, alkaline and acidic electrolytes.

Capacitance in various electrolytes (F/g)										
Scan	2M KCl				6M KOH				1M H ₂ SO ₄	
Rate	NCNR	NCNR	NCNR	NCNR	NCNR	NCNR	NCNR	NCNR	NCNR	NCNR
(V/s)	800	900	1000	800	900	1000	800	900	1000	1000
0.01	214.2	237.2	96.5	213.3	289.5	160.4	287.3	328.5	177.5	
0.05	199.4	202.4	81.8	189.4	258.4	122.2	240.4	286.1	134.7	
0.1	179.5	192.4	76.9	179.0	255.5	101.0	221.0	272.0	120.7	
0.2	160.9	183.0	72.8	169.3	243.3	79.8	203.8	261.2	110.6	
0.4	150.0	176.0	68.8	158.8	231.0	61.6	182.3	250.9	98.6	

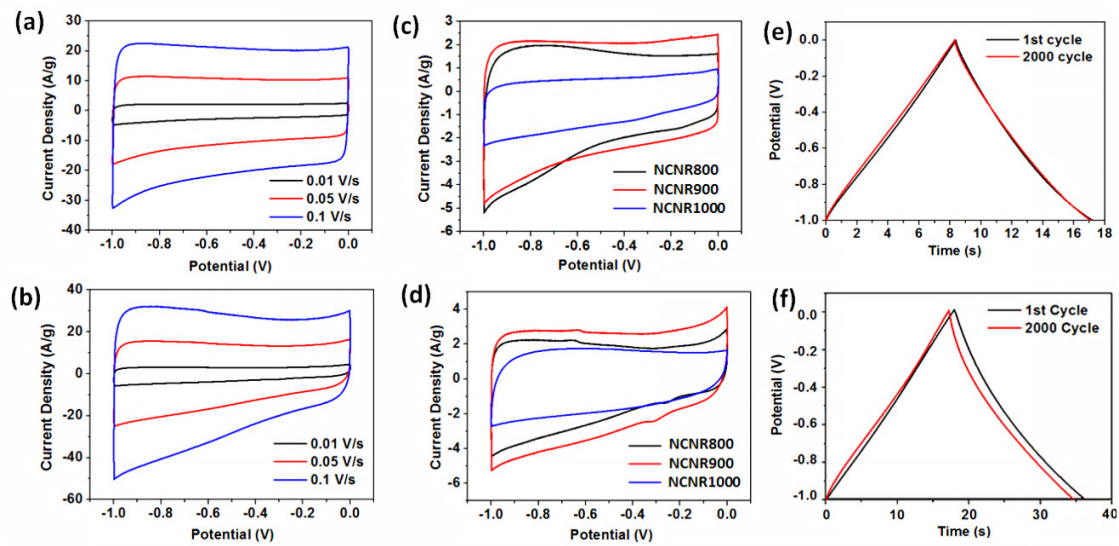


Figure 6.8 (a) CV for NCNR900 with the scan rate of 0.01 V s^{-1} , 0.05 V s^{-1} and 0.1 V s^{-1} in 2M KCl; (b) CV for NCNR900 with the scan rate of 0.01 V s^{-1} , 0.05 V s^{-1} and 0.1 V s^{-1} in 6M KOH; (c) CV for NCNR800, NCNR900, and NCNR1000 at the same scan rate of 0.01 V s^{-1} in 2M KCl; (d) CV for NCNR800, NCNR900, and NCNR1000 at the same scan rate in 6M KOH; (e) Cycling stability in 2M KCl electrolyte of NCNR900 at 20 A g^{-1} current density and (f) Cycling stability test in 6M KOH electrolyte for NCNR900 at a 20 A/g current density

6.3.4 Comparison of supercapacitive performance of NCNRs with other works

We finally compared our results with various N-enriched carbon materials presented in recent years (summarized in Table 6.3) (Chen et al., 2012b; Han et al., 2014; Hou et al., 2015; Zhao et al., 2015a; Lota et al., 2007; Hulicova et al., 2005) on Cs and other major characteristics including electrolytes and the electrode material. Remarkably, our NCNR900 exhibits much higher Cs value than that of those reported systems. The overall good performance is attributed to the combined effect of a high nitrogen doping level (greatly improving the electronic properties and wettability of the material) as well as a well-developed porous structure and high surface area (enhancing the accessibility of electrolyte and facilitating the electron/ion transport).

Table 6.3 Comparison of the Cs value of various N-doped Carbon Systems reported in recent years.

Electrode Material	Cs (F g ⁻¹)	Electrolyte	Reference
Nitrogen-doped porous carbon nanofibers from bacterial cellulose	202	6 M KOH	(Chen et al., 2012b)
Nitrogen-doped porous hollow carbon spheres	213	6 M KOH	(Han et al., 2014)
Hierarchical nitrogen-doped Carbon Nanocages	313	6 M KOH	(Zhao et al., 2015a)
Hierarchical porous nitrogen-doped carbon nanosheets from silk	242	EMIMBF ₄	(Hou et al., 2015)
N-doped multiwalled carbon nanotube	167	1 M H ₂ SO ₄	(Lota et al., 2007)
Melamine-based Carbon	205	1 M H ₂ SO ₄	(Hulicova et al., 2005)
This work	352	1 M H₂SO₄	

6.4 Conclusion

The synthesis of a highly-porous N-enriched carbon nanorods was reported. Cellulose nanocrystal was used both as the carbon source and template to facilitate the controlled growth of nitrogen precursor into core-shell structured MFCNC nanorods. The abundant micro-, meso-, and macropores in the carbon structure are obtained without using any sacrificial templates or an activation process. The effect of pyrolysis temperature on nitrogen doping content, surface area, and pore structures was carefully studied with respect to their effect on different electrochemical behaviors. A carbonization temperature of 900 °C was found to be most optimal in terms of capacitive performance which was achieved through the balance between a well-developed pore structure, high surface area and moderate nitrogen doping content. The synthesized NCNRs possesses superior capacitance in all three of the most commonly used electrolytes - 2M KCl, 1M H₂SO₄ and 6M KOH – with good retention capability and excellent cycling stability. The best capacitance performance was as high as 352 F g⁻¹ at a current density of 5 A g⁻¹ when 1M H₂SO₄ electrolyte was used. The basicity introduced by N-doping was believed to be particularly beneficial for an enhanced interaction in the acidic environment. The work presented here provides an attractive route for the fabrication of a high performance capacitive electrode carbon materials through the transformation of cheap, abundant and renewable biomaterials.

Chapter 7 N-enriched mesoporous carbon derived from biomass as metal-free catalyst

7.1 Introduction

Catalysts play a pivotal role in 90% of the chemical process and the manufacturing of over 60% of the chemical products.(Horváth, 2003) Various homogeneous or heterogeneous metals, metal oxides, or hybrid composite materials have been extensively explored since they are among the most vibrant catalysts for a wide range of reactions in modern chemistry. However, the challenges associated with the real world application of these catalysts are most commonly related to nanoparticle agglomeration, catalyst leaching, and reusability, which directly lead to the decay of catalytic performance, economics and environmental problems. Moreover, the high cost and low abundance of the metal-based material further restrict their usage industrially. Increasing research activities are directed towards the exploration of metal-free, and cost-effective catalyst materials derived from the abundant resources as sustainable alternatives to traditional metal-based catalysts. Within the context, ‘carbocatalyst’ has evolved as a new class of catalysts and the materials used are carbonaceous materials composed predominantly of carbon. In this case, carbon is used exclusively as catalysts rather than as the support for traditional metal/metal oxides. In recent years, zero-dimensional fullerene, one-dimensional carbon nanotubes, two-dimensional graphene and various three-dimensional carbon nanostructures have been proposed. (Lu et al., 2013; Duan et al., 2015a; X. Kong, Z. Sun, M.Chen, 2013; Chen et al., 2014; Su & Loh, 2013; Xue et al., 2013; Wong et al., 2013) It was further demonstrated experimentally and theoretically that doping with heteroatoms can effectively enhance the catalytic activity of carbocatalysts as the result of the unique electronic properties due to heteroatom-induced charge transfer and delocalization (Liang et al., 2012; Paraknowitsch & Thomas, 2013). Nitrogen (N) is the most widely investigated doping element and various N-doped carbon materials including carbon nanotube (Mo et al., 2012; Vikkisk et al., 2013), carbon nanofiber (Maldonado & Stevenson, 2005; Liu et al., 2013a), porous carbon (Pan et al., 2014; Lu et al., 2013), graphene (Chang et al., 2015a; Zhou et al., 2015; Geng et al., 2011; Zhang et al., 2012b; Lee et al., 2010; Sun et al., 2012) *etc.* have been developed. Within the context, most of the studies on N-carbocatalyst focused on catalyzing oxygen reduction reaction (ORR) and their results suggest an excellent catalytic activity with long-term durability, and higher tolerance to poisoning than metal-based catalysts. (Jiao et al., 2014; Liang et al., 2013b; He et al., 2014a; Silva et al., 2013) In other studies, N-doped graphene was shown to have promising catalytic activity towards the reduction of 4-nitrophenol whereas N-free graphene did not show any catalytic

effect.(X. Kong, Z. Sun, M.Chen, 2013) Moreover, N-doped single-walled carbon nanotubes (Duan et al., 2015b) or graphene (Duan et al., 2015a) have both been used for catalyzing phenol oxidation reaction. In these studies, the high catalytic activity surpassing metal-based catalyst was achieved, and the critical role of N doping was clearly demonstrated.

Despite its promise, significant challenge still remains for achieving adequate and homogeneous N doping using simple procedure and apparatus that meets the practical considerations. (Fuentes & Centeno, 2005; Ania et al., 2007; Lota et al., 2007; Shrestha & Mustain, 2010) It is also highly desirable to engineer the carbon structure with controlled mesopores (pores within 2nm - 50nm) that were demonstrated to efficiently reduce the mass transfer and accelerate the reaction kinetics. (Zhu et al., 2016) Current strategies to achieve N-doped mesoporous carbon structures often necessities the use of exotic hard templates, expensive surfactants, high-cost polymeric carbon sources and complicated procedures, which is costly, energy-consuming and low in yield. (Fuentes & Centeno, 2005; Ania et al., 2007; Lota et al., 2007; Shrestha & Mustain, 2010) Post-activation at an extremely high temperature (>1000 °C) are also applied for generating the desired porosity. Therefore, the motivation of this research is to develop a facile synthesis of mesoporous N-doped carbon as high efficient metal-free catalysts using abundant and environmental benign resources for practical applications.

As a new class of nanomaterial derived from renewable biomass, cellulose nanocrystal (CNCs) can be extracted from plants and marine animals. The high aspect ratio, superior mechanical properties, water dispersibility and highly reactive surface, make CNC an ideal platform for various functionalizations.(Peng et al., 2011) The material itself is an ideal carbon source and is also promising for templating various carbon structures. (Shopsowitz et al., 2011) Moreover, Canada has commissioned a demonstration plant that can produce 1000 kg per day of CNC, giving tremendous impetus to its wide application.

In this research, mesoporous N-doped carbon nanorods (NCNRs) were fabricated from melamine formaldehyde (MF) coated cellulose nanocrystals (CNCs). CNC with unique rod-structure serve as the main carbon precursor for self-templated carbon nanorod. It also serve as an ideal template to induce the controlled MF polymerization on the surface of CNCs prior to pyrolysis. The functionalization of highly porous MF resin not only introduces desired N-doping but also generates favorable mesoporous structure after pyrolysis. Moreover, the coating of MF resin was demonstrated to critically protect and stabilize the fiberous shape of CNCs during carbonization, contributing to the high surface area and pore volume of NCNR. A very high N-doping content and

mesoporous carbon structure was achieved through a facile one-step pyrolysis without using any sacrificing template or activation process. The potential of NCNR as high-efficient carbocatalyst was further evaluated by catalyzing the reduction of 4-nitrophenol (4-NP) and oxygen reduction reaction (ORR) as two model reactions. A pseudo-zero order reaction profile was observed with a high catalytic activity ($k = 1.67 \times 10^{-7} \text{ mol L}^{-1} \text{ s}^{-1}$) in the reduction reaction of 4-NP. The result is more superior than that of N-graphene. NCNRs also exhibit excellent catalytic activity for ORR, with a high on-set potential of 0.87V (vs RHE), a half-wave potential of 0.73V (vs RHE) as well as a great selectivity to four electron reduction pathway of oxygen. We believe that our strategy of synthesizing mesoporous N-doped carbon nanostructure from widely available biomass with low cost processing provides a practical and sustainable alternative as metal-free catalyst for a wide range of electrochemical or chemical applications.

7.2 Experimental section

7.2.1 Materials

Cellulose nanocrystals (CNCs) were provided by FPInnovations and Celluforce Inc. All the chemicals used in this study were of analytical grade, purchased from Sigma-Aldrich, and used as received.

7.2.2 Synthesis of NCNR

The strategy of preparing NCNR is illustrated in Figure 7.1. The first step involving the preparation of MFCNC has been described in Chapter 6 (experimental section). The mesoporous nitrogen-doped carbonized MFCNCs (NCNRs) were prepared by one-step carbonization of the dried MFCNCs in a furnace tube under a flow of Ar₂ at 900 °C over 2 hours with a ramping rate of 5 °C min⁻¹. After naturally cooling to room temperature, NCNRs were collected and ground to fine powders. As a comparison, pristine CNCs was well mixed physically with the same amount of melamine powder (MeCNC) and carbonized under the exact same condition (cMeCNC).

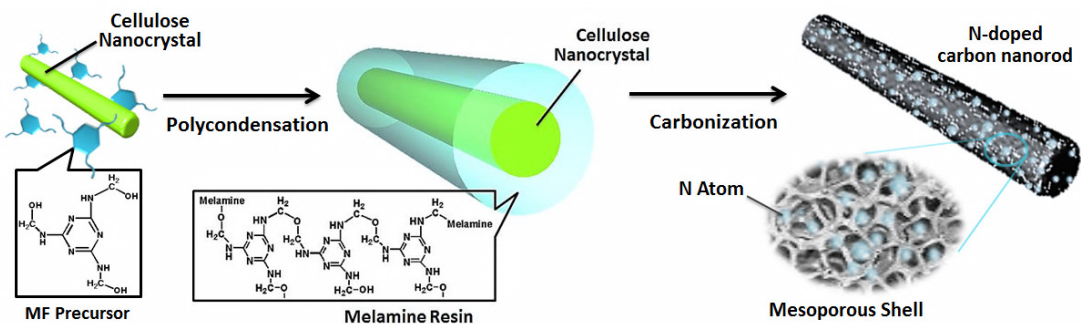


Figure 7.1 Strategy for preparing mesoporous nitrogen-doped carbon nanorods (NCNR).

7.2.3 Characterization

7.2.3.1 Physical and chemical characterization

The morphology of sample CNC was characterized with JEM-2100 high resolution TEM. Before imaging, the CNCs were stained with 2% (w/w) uranyl acetate negative stain for better contrast. The morphology of MFCNC, NCNR, cCNC, cMeCNC were characterized using a Philips CM10 transmission electron microscope (TEM). The successful coating of MF on CNCs was confirmed by measuring the zeta potential of pristine CNCs and MFCNCs with Malvern Zetasizer Nano ZS (Worcestershire, UK). The zeta potential of the particles was calculated from the electrophoretic mobility values using the Smoluchowski equation. The composition of CNCs, MFCNCs, the carbonized sample of NCNR were further characterized with FT-IR (PerkinElmer 1720 FT-IR spectrometer). For FT-IR spectrum, freeze-dried samples were mixed with KBr and then compressed into pellets for measurements at a resolution of 4 cm^{-1} . The analysis of the surface area, pore diameter and volume was determined by N_2 adsorption analysis with an autosorb iQ-AG instrument (Quantachrome Co., USA) at 77 K using the multipoint BET (Brunauer–Emmett–Teller) model to eliminate any interference from weakly adsorbed species. Prior to measurements, the samples were degassed overnight at 150 °C under vacuum.

7.2.3.2 Catalytic activity of NCNR for 4-nitrophenol reduction reaction

The catalytic activity of the above synthesized NCNR was evaluated using the model catalytic reaction of the reduction of 4-nitrophenol (4-NP) to 4-aminophenol (4-AP) with NaBH_4 as the reducing agent. In a typical test, 4-NP (0.24 mM) solution was first well mixed with fresh NaBH_4 (0.24 M) solution in the same volume under room temperature. For the UV test, 1 ml of the mixture solution was pipetted out and transferred to the UV-vis cuvette. Then 50 μL of NCNR suspension

(1mg/ml) was introduced into the cuvette followed by rapid mixing with a pipette for 2 seconds. After that, the kinetics of the reaction was monitored every minute with UV-vis at room temperature between 250 and 600 nm.

7.2.3.3 Catalytic activity of NCNR for oxygen reduction reaction

The ORR activity of catalyst was investigated with a rotating disc electrode (RDE) half-cell that consists of catalyst coated glass carbon electrode (GCE) as working electrode, graphite rod as contour electrode and reversible hydrogen electrode (RHE) as the reference electrode. Typical ink for testing was prepared by well-sonicating the mixture of 10 mg of NCNR catalyst, 750 μ L isopropanol (IPA) and 250 μ L 0.25% Nafion IPA solution. Then 16 μ L was pipetted from the ink and drop casted the surface of GCE (a catalyst loading of 0.6 mg cm^{-2}). All the electrochemical experiments were performed on a computer-controlled bipotentiostat (Pine Instrument Company, USA) at room temperature. Cyclic voltammetry (CV) curves were recorded at scan rate of 50 mV s^{-1} in the O_2/N_2 saturated electrolyte of 0.1 mol L^{-1} KOH. Steady-state ORR polarization curves were obtained with linear staircase voltammetry (LCSV) under different rotational speed in the O_2 saturated electrolyte.

7.3 Results and discussion

7.3.1 Material characterization

The morphologies of samples from each experimental step were confirmed with TEM imaging in Figure 7.2. Compared with the pristine CNCs shown in Figure 7.2(a), MFCNCs appeared much thicker in diameter and were well dispersed, indicating the successful MF resin coating on individual CNC and the formation of the proposed core-shell structure of MFCNCs (Figure 7.2 (b)). The smooth surface of MFCNCs also suggest a rather homogeneous polymerization of MF resin, which is mainly attributed to the remarkable suspension stability in water, high surface area and one-dimensional structure of the templating substrate of CNCs. Figure 7.2 (c) shows the well-preserved fibrous morphology for the NCNR with a slight shrinkage in diameter. Our strategy of introducing N-doping by forming a uniform layer of N precursor on the carbon precursor is believed to be rather beneficial for a homogeneous N atom doping in the carbon frame after pyrolysis.

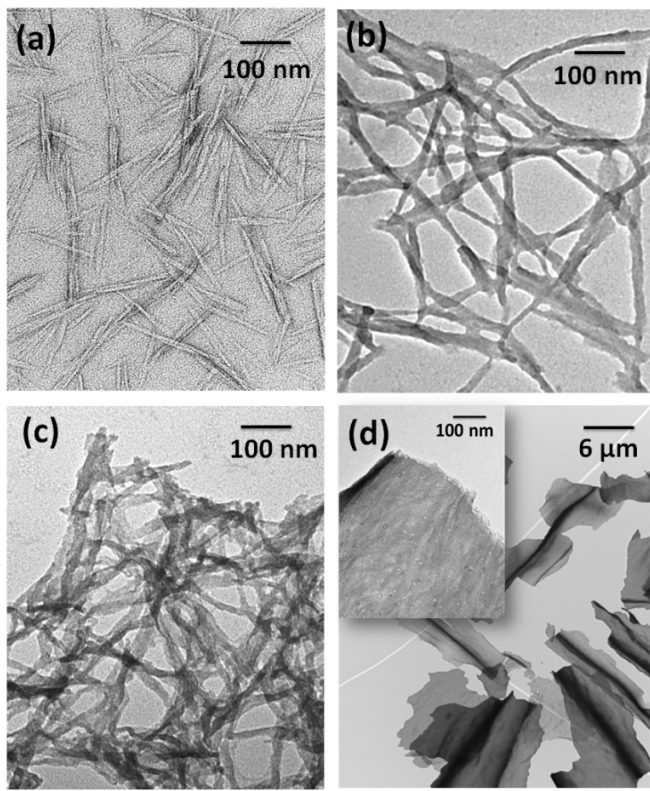


Figure 7.2 (a) HRTEM image for pristine CNCs, and TEM images for (b) MFCNCs, (c) NCNRs and (d) cMeCNC

It is also worthwhile to point out the critical role of MF layer for protecting and stabilizing the structure CNCs. As shown in Figure 7.2(d), when N-precursor of melamine is only physically mixed with CNCs for carbonization, no fibre shape can be found in the carbonized system and CNCs all collapse and diffuse into large aggregated sheets up to micro-meter in dimension. The inset image in Figure 7.2 (d), also shows that these sheets are rather thick and consist of multiple layers tightly stacking together. Compared with the collapse structure of cMeCNCs, the well-dispersed fibrous structure of NCNR in nanoscale is rather advantageous for catalysts application providing increased surface area and active sites for enhanced utilization efficiency and solution accessibility.

The characterization for MFCNC was described in Chapter 6 and thus will not be discussed here. As shown in Figure 7.3(a), after pyrolysis, most of the adsorption peaks from MFCNC diminished in NCNR, due to the loss of functional groups during carbonization. A new peak, however, was shown at around 1381 nm^{-1} , representing C-N stretch, indicating the successful N doping in the carbon framework. Similar peak was also observed for N-doped graphene and N-doped carbon dots.(Xu et al., 2013b; X. Kong, Z. Sun, M.Chen, 2013) The characterization of surface area,

porosity of CNC before and after MF resin coating is listed in Table 7.1. The results confirmed our prediction that MF resin in MFCNC composite dramatically increased the surface area (10 times higher) and pore volume of CNC (70 times higher) with its highly crosslinked sponge-like structure. Elemental analysis revealed that the N content in the composite material of MFCNC is as high as 34.78%wt. The carbonized MFCNC gained an extremely high surface area of $564.2 \text{ m}^2 \text{ g}^{-1}$ and pore volume of $0.07 \text{ cm}^3 \text{ g}^{-1}$. In contrast, the carbon structure resulted from physically mixed melamine and CNCs yielded a much lower surface area of $82.7 \text{ m}^2 \text{ g}^{-1}$ and pore volume of 0.004 cm^3 . This confirmed our conclusion from TEM imaging that the collapse of fibrous nanostructure and the formation of stacked sheets of cMeCNC lead to significant loss in surface area. It also confirmed that the porous MF resin is key in generating highly porous carbon structure. Further elemental analysis confirmed a remaining N doping content as high as 8.45% after carbonization.

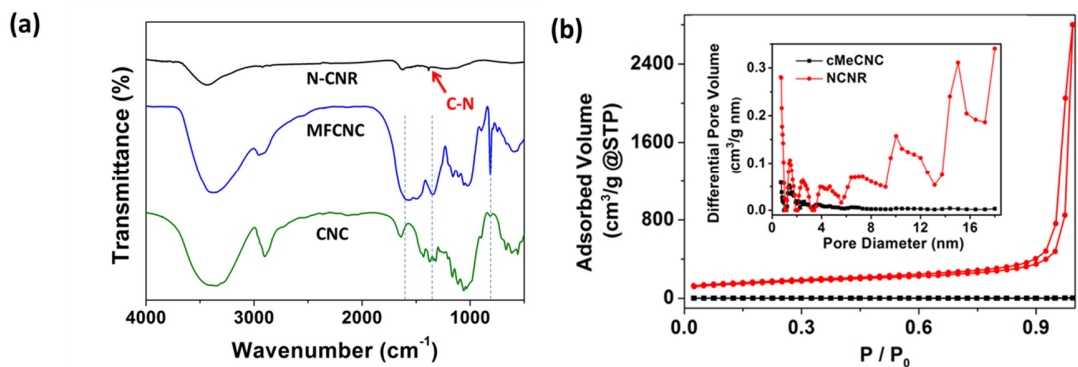


Figure 7.3 (a) FTIR spectra for pristine CNC, MFCNC and NCNR sample, and (b) N_2 adsorption/desorption isotherms for sample NCNR in comparison with and cMeCNC. Inset: the comparison of pore size distribution between NCNR and cMeCNC.

The detailed structural features of the prepared NCNRs was investigated with BET characterisation since it is closely related to the catalytic performance. Figure 7.3(b) shows the N_2 adsorption/desorption isotherms and pore size distribution (PSD) curve of NCNR and cMeCNC. The isotherms of NCNR exhibited the representative type III behavior defined by IUPAC with a H_3 type hysteresis loop. The sharp capillary condensation step at high relative pressures $P/P_0 > 0.90$ suggests the existence of abundant mesopores in NCNR nanostructure. The result agreed well with the PSD characterization, where it displayed a well-developed mesoporous structure with intensive peaks throughout mesopore region. This is expected to be rather beneficial for the enhanced catalytic activity due to favorable contact with the reactants. The isotherm and PSD profile for cMeCNC, however, suggest a nearly non-porous structure with rather low volume adsorption

observed. Since the catalytic reaction occurs on the surface of the catalysts, the efficiency of the reaction is critically determined by its accessible active sites. Therefore, the N-doped mesoporous NCNR with widely accessible surface area should be an ideal candidate as highly efficient catalyst.

Table 7.1 Summary of the surface area and pore properties from BET measurement for CNC, MFCNC, cMeCNC and NCNR samples.

	CNC	MFCNC	cMeCNC	NCNR
BET surface area (m²/g)	24.12	212.8	82.7	564.2
Total pore volume (cm³/g)	0.001	0.07	0.004	2.03
Mean pore diameter (nm)	0.95	1.34	1.41	1.65

7.3.2 Catalytic activity in 4-NP reduction reaction

Catalytic activity in the reduction of 4-NP in waste waters is desirable since it is anthropogenic, toxic and inhibitory. (Isayev et al., 2006) The conversion of nitro to amino is also of great industrial importance for a wide range of applications, such as photographic developer for films, precursor for analgesic and antipyretic drugs, intermediate for paracetamol synthesis. (Woo & Lai, 2001; Snethlage & Wendler, 1999; Zhao et al., 2015b) In particular, the catalytic reduction of p-NP by borohydride ions (BH^{4-}) is considered to be an ideal model reaction and has been widely used to evaluate the catalytic activity of various metallic nanoparticle systems. (Hervés et al., 2012) To the best of knowledge, only two studies have reported the use of hetero-doped carbocatalysts to catalyze such reaction. (Gao et al., 2014; X. Kong, Z. Sun, M.Chen, 2013).

The catalytic reaction of 4-nitrophenol in the presence of excess NaBH_4 as the reducing agent and NCNR as the catalyst was conducted. The kinetics of the reaction was continuously monitored using a UV-Vis instrument. Upon mixing with NaBH_4 , the light yellow solution of 4-NP immediately turned intense greenish yellow due to the formation of 4-nitrophenolate ions, and the peak displayed a strong UV adsorption at 400 nm (Figure 7.4 (a)). Further addition of catalyst initiates the reduction of 4-NP to 4-aminophenol (AP) accompanied with the successive reduction in the UV adsorption of peak at 400nm and a developed new peak at 300nm associated with 4-AP. The cessation of the reduction is also evidenced by the ultimate bleaching of the yellow color of the 4-NP mixture. As shown in Figure 7.4(a), the reaction in the presence of NCNR as the catalyst was completed within 12 minutes. To exclude the possibility that the color fading of 4-NP solution is through the physical adsorption of 4-NP by high-surface-area NCNRs rather than catalytic reduction, the same experiment was carried out in the absence of the reducing agent NaBH_4 . No color change was

observed over several hours after mixing NCNRs with 4-NP, suggesting that the observed reduction is due to catalytic reaction instead of physical absorbance.

The reduction reaction of 4-NP is generally considered pseudo first-order for most of the metal-based catalysts. However, the reaction catalyzed by NCNR was found to better fit in the pseudo-zero-order model where the adsorption intensity at 400 nm changes linearly with time (Figure 7.4 (b)). The phenomenon was similarly observed and first reported by previous study when N-doped graphene was used as catalyst for such reaction. (X. Kong, Z. Sun, M.Chen, 2013) The pseudo-zero-order rate constant was calculated to be $k = 1.67 \times 10^{-7} \text{ mol L}^{-1} \text{s}^{-1}$, which is higher than the reported catalytic activity of N-doped graphene (X. Kong, Z. Sun, M.Chen, 2013) as well as some noble metal catalyst. (Li et al., 2013b) Moreover, unlike the previous findings, the so-called ‘activation time’ or ‘induction time’(Gao et al., 2007; X. Kong, Z. Sun, M.Chen, 2013) related to substrate diffusion limitation was not observed in our reaction with NCNRs. This strongly suggest the efficient mass transfer and ion diffusion in the catalyst structure due to its abundant catalytic active sites and optimal mesopores.

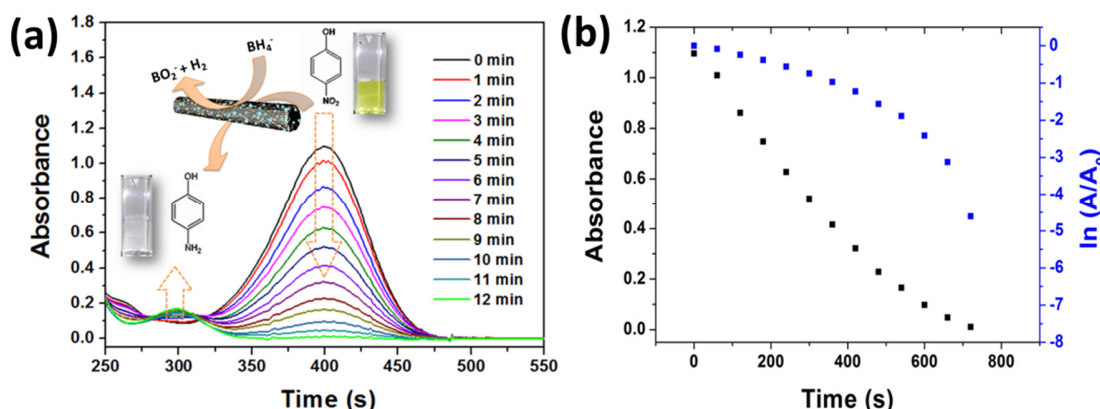


Figure 7.4 (a) Time-dependent UV-vis spectra of 4-nitrophenol reduction catalyzed by NCNR and (b) Plot of adsorption intensity A of peak at 400 nm and $\ln(A/A_0)$ against the reaction time t for 4-nitrophenol reduction catalyzed by NCNR.

7.3.3 Electrocatalytic activity in ORR

ORR is an essential reaction in many energy conversion and storage devices, such as fuel cells (Meng et al., 2014; Liang et al., 2013b; He et al., 2014a; Silva et al., 2013), metal-air batteries (Nam et al., 2014; Zhu et al., 2011a). However, without the assistance of a suitable catalyst, the sluggish ORR could not proceed effectively, efficiently and practically. In recent year, heteroatom-doped

carbon materials are recognized a promising metal-free alternative to replace traditional catalysts in this area that heavily relies on noble metals. Herein, the catalytic activity of our proposed NCNR was evaluated electrochemically for catalyzing ORR. The CV curve for NCNR under both N₂ and O₂ saturated electrolyte is plotted in Figure 7.5(a). A significant redox peak with current density of 1.23 mA cm⁻² at 0.7V vs RHE was observed with O₂-saturated electrolyte compared to the quasi-rectangular profile in the presence of N₂, clearly indicating the capability of NCNR to catalyze ORR. Polarization curves of NCNR under different rotational speeds were recorded by RDE. The polarization curves under 900 rpm gives an on-set potential of 0.87V and a half-wave potential of 0.73V, indicating an excellent ORR activity of NCNR (Figure 7.5). Moreover, the high diffusion-limited current density obtained (4.21 mA cm⁻²) was comparable to the commercial Pt/C catalyst in the literature (Silva et al., 2013) This is mainly due to the high surface area, mesoporous structure and the abundant catalytic active sites of NCNR that facilitate the mass transfer and ion diffusion. In order to further analyze the ORR activity, Koutecky–Levich equation as follows is applied:

$$\text{Equation 3.14} \quad \frac{1}{j} = \frac{1}{j_k} + \frac{1}{B\omega^{1/2}}$$

where j is the measured current density, j_k is the kinetic current density and ω is the rotation speed of the electrode. B is determined by the slope of the K-L plots (Figure 7.5c) on the basis of the following equation:

$$\text{Equation 3.15} \quad B = 0.62nFC_{O_2}D_{O_2}^{2/3}\nu^{-1/6}$$

where n is the overall number of electrons transferred per oxygen, F is Faraday's constant (96485 C mol⁻¹), C_{O_2} means the bulk concentration of O₂ (1.2×10⁻⁶ mol cm⁻³), D_{O_2} denotes the diffusion coefficient of O₂ in 0.1 M KOH electrolyte (1.9×10⁻⁵ cm² s⁻¹), ν is the kinetic viscosity of the electrolyte (0.01 cm² s⁻¹). The linear and parallel curves in the K-L plots indicate the first-order reaction kinetics associated with O₂ on NCNR. (Zhu et al., 2011a) The number of transferred electrons of NCNR reaches 3.83 (Figure 7.5c, inset), suggesting that quasi four-electron reduction pathway dominates the reaction. Tafel plot was further applied to study the ORR activity of NCNR (Figure 7.5d). Two distinct Tafel regions at low and high over potentials were observed with different slopes being 66 mV dec⁻¹ and 359 mV dec⁻¹, respectively. The slope at low over potential region, where the ORR reaction is mainly controlled by kinetic reaction on the surface of NCNR, is similar to the reported values of N-doped graphene or CNT in the literature. (Liang et al., 2013b;

He et al., 2014a; Meng et al., 2014; Zhu et al., 2011a) This could be attributed to the change in the electron cloud density on the carbon structure due to N doping functionality.(He et al., 2014a)

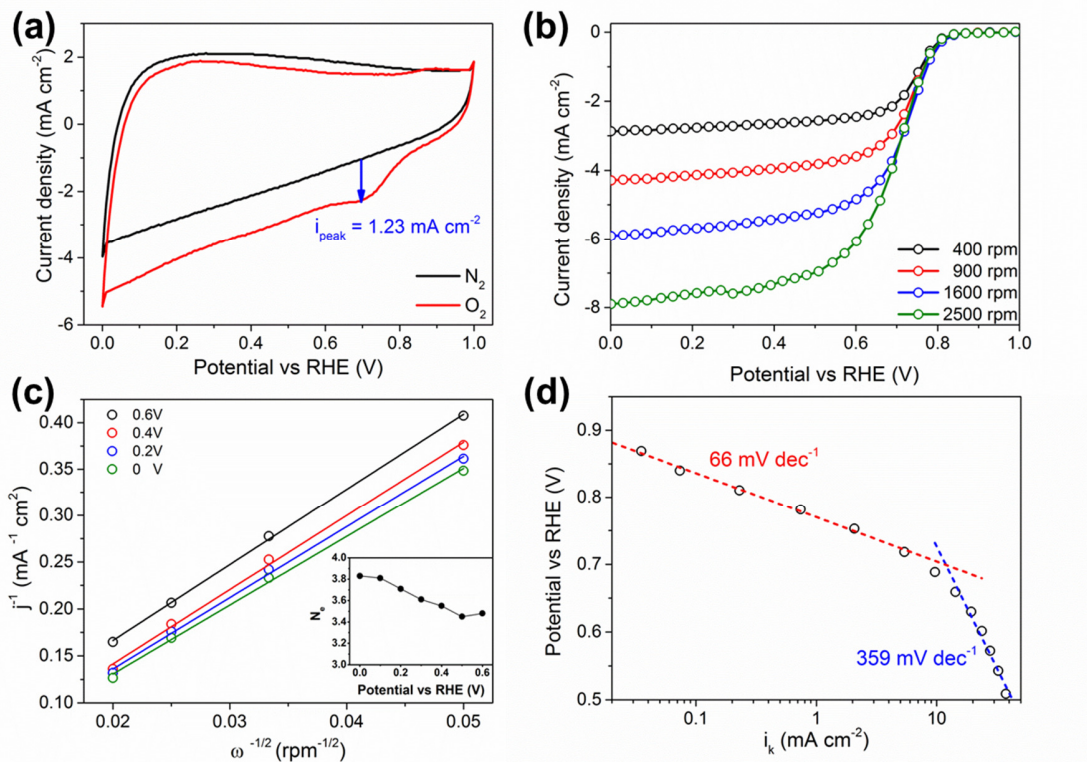


Figure 7.5 ORR performance of N-CNR: (a) CV curves under both N_2 and O_2 saturated 0.1 mol L^{-1} KOH; (b) LSV curves under different rotating speeds; (c) Koutechy–Levich plots under different potential vs RHE with transferred number of electrons (insert plot); and (d) Tafel plot.

XPS analysis was further performed to study the binding configuration of the N atom in the carbon frame and further understand the ORR catalytic behavior of NCNR. Based on the results from high resolution spectrum of N 1s (Figure 7.6a), four different nitrogen species could be identified, namely pyridinic (398 eV), pyrrolic (399.9 eV), graphitic (400.9 eV) and oxide (402.8 eV). Among them, pyridinic and graphitic nitrogen are most responsible for the ORR activity (Guo et al., 2016; He et al., 2014a; Meng et al., 2014; Silva et al., 2013; Nam et al., 2014), and the adjacent carbon atoms to pyridinic nitrogen is considered as the major active site in N-doped carbon materials. (Guo et al., 2016) Therefore, the N functionality with high ratio of pyridinic (36%) and graphitic (34%) nitrogen could be used to account for the high ORR activity observed for NCNR (Figure 7.6b). Besides, the high surface area and mesoporous structure greatly improve the reactant accessibility and diffusion

to the active sites of NCNR(Liang et al., 2013b; He et al., 2014a), which is closely related to the activity in the diffusion-controlled region with high over potential in Figure 7.5(d).

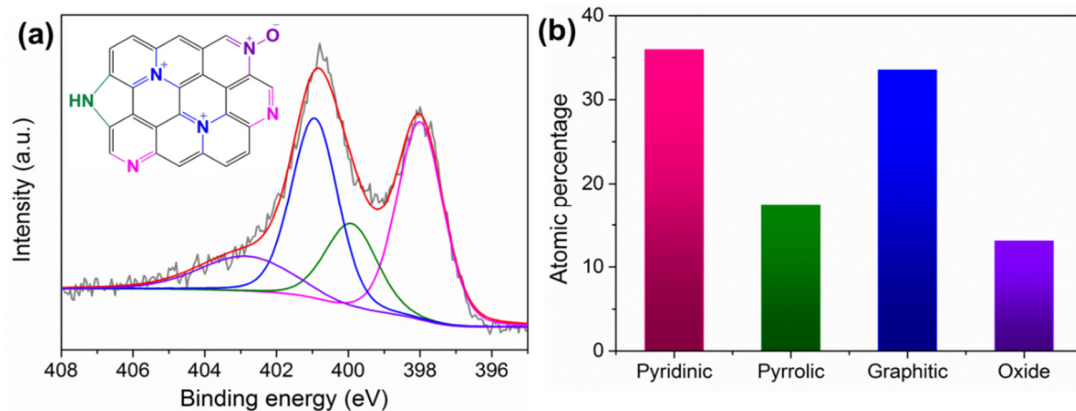


Figure 7.6(a) High resolution XPS spectrum of N 1s and the structure of different nitrogen species; (b) composition of nitrogen species in N-CNR.

7.4 Conclusions

In conclusion, novel N-doped mesoporous carbon nanorods were developed using abundant and renewable carbon source, cost-effective synthesis, and easily accessible apparatus. Core-shell structured MFCNC with a rather smooth surface validates the homogeneous coating of MF templated by CNCs. The strategy of MF functionalization introduces efficient N-doping, mesoporosity as well as critical stabilizing effect for the fibrous-structure of NCNR through one-step pyrolysis. The prepared NCNCR demonstrated promising catalytic activity in both the catalytic reduction reaction of 4-NP and the electrocatalytic reaction of ORR. The superior catalytic performance is mainly attributed to the high N-doping content introducing abundant active sites, as well as high surface area mesoporous structure leading to high solution accessibility of active sites and efficient reactant transfer and diffusion.

Chapter 8 Polydopamine-modified N-doped mesoporous carbon derived from biomass for supporting highly dispersed metal nanocatalysts

8.1 Introduction

Downscaling the metal catalyst is a popular research topic in nanotechnology, since metal nanoparticles (MNPs) offer unprecedented efficiency compared to their bulk counterparts due to extremely large surface area and active sites.(Campelo et al., 2009) The improved catalytic efficiency of MNPs enables reduced loading of expensive metal catalyst while still maintaining or even improve the fuel cell performance. However, challenges with synthesizing MNPs are associated with the tendency of the NPs to minimize surface energy leading to aggregation, resulting in a loss of catalytic activity. A further issue pertains to the recyclability of these MNPs due to their small size that possess both economic and environmental concerns. (White et al., 2009) One promising strategy to address the above issue is to support MNPs with a suitable solid substrate. Nano-carbonaceous materials, active carbon (Kang et al., 2013; Zhang et al., 2014a), graphene (Shang et al., 2014; Julkapli & Bagheri, 2015), and carbon nanotube (Li et al., 2012a; Deng et al., 2014) etc. are popular candidates due to their high surface area, physical robustness, chemical stability, and electrical conductivity. (Fang & Wang, 2013) Current challenge for carbon-supported metal nanocatalysts lies in the lack of metal-support interaction, leading to poorly dispersed MNPs and/or stabilization. (Li et al., 2013e) Significant loss in active surface area of the above carbon supports were also reported due to their hydrophobicity/poor wettability. (Guo et al., 2012)

The development of nanostructured carbon with well-controlled surface area and mesoporous texture is receiving increasing attention. These materials greatly promote the metal dispersion with their high active sites and provide confinement effect for the MNP growth within their pores. Mesopores (i.e. 2-50 nm) may also enhance the catalytic efficiency by facilitating mass transfer.(Li et al., 2013e) However, current technologies to fabricate mesoporous carbon using either soft or hard templating method are either too complicated, costly or low in yield that barely meet the practical demands. High temperature activation with highly toxic and corrosive agents for generating desired porous texture are also widely used. (Lu & Schüth, 2006; Xu et al., 2008; Banham et al., 2011).

Recently, the strategy of N-doping in carbon has demonstrated to greatly improve the MNP synthesis in terms of better dispersion and finer size. (Liang et al., 2013a; He et al., 2013; Lee et al., 2014; Mabena et al., 2011) Enhanced catalytic activity and durability were observed for these

supported metal systems compared to their N-free counterpart with prominent examples that include: Pt/N-carbon catalyzing p-nitrophenol (p-NP) reduction;(Liu et al., 2012b) Pd/N-magnetic carbon catalyzing Heck, Suzuki, and Sonogashira coupling reactions (Yoon et al., 2007); Au/N-graphene catalyzing selective oxidation of benzylic alcohols (Xie et al., 2012); Pt/N-graphene or Pt/N-carbon nanotube catalyzing electrochemical reactions of oxygen reduction reaction (ORR) (Gasteiger et al., 2005; Li et al., 2010c) and methanol oxidation reaction. It has been demonstrated both experimentally and theoretically that N dopants in the carbon framework act as “tethers” (chemical binding sites), improving dispersion of the MNPs, providing resistance to nanoparticle agglomeration and coarsening, and improved stabilization effect. (Zhou et al., 2010b; Li & Antonietti, 2013; Mabena et al., 2011; Wong et al., 2013; Li et al., 2013e) It was also suggested that N-doping may serve as active sites that further contribute to the catalytic activity by tuning the electronic properties around. (Wong et al., 2013) Two strategies are commonly used to introduce N into carbon matrices: post-treatment with bases, such as ammonium, amine, urea; and ‘in-situ’ doping with N-rich precursors during carbon fabrication. The first strategy normally results in surface doping with relatively low N content (Cao et al., 2011; Jurewicz et al., 2004; Kim et al., 2008; Jurewicz et al., 2008) while the second one typically results in a more efficient, higher and uniform N doping and techniques such as CVD (e.g. acetonitrile, pyrrole) (Xia & Mokaya, 2005; Yang et al., 2005; Hou et al., 2005) or liquid impregnation (Liu et al., 2010c; Lu et al., 2004; Shrestha & Mustain, 2010) have been used.

In light of the above discussion, an ideal carbon material for supporting MNPs as catalysts should possess the following features: (i) high surface area with mesoporous structure (ii) N-doping (iv) surface wettability. However, strategies for developing such platform are not common. Herein, we report a novel synthesis of modified N-enriched mesoporous carbon nanorods (NCNRs) as promising substrate for supporting highly dispersed MNP as catalysts. Both mesoporous structure and N-doping were achieved through one-step pyrolysis of melamine-formaldehyde coated cellulose nanocrystals (MFCNC). CNCs derived from wood fibers were used as carbon source and non-sacrifice template. Melamine as N-precursor was introduced in-situ by forming highly cross-linked network of MF resin that homogeneously condensed on CNCs. Further bio-inspired polydopamine (PDA) modification was performed on the prepared NCNRs that dramatically improve the dispersion and loading of the reduced MNPs through strong chelation with metals. In addition, PDA modification provides remarkable suspension stability of the prepared hybrid metal catalysts against precipitation over months. Further catalytic activity of the prepared Pd/PDA-NCNR was evaluated by catalyzing 4-NP reaction and an excellent turnover frequency of 148.5 min^{-1} was

observed, much higher than that of commercial Pd/C and the previously reported value for Pd-based catalyst. Outstanding catalytic activity of synthesized Pt/PDa-NCNR towards ORR was also observed that outperform the commercial Pt/C in terms of half-wave potential (0.89V vs RHE), ECSA ($120 \text{ m}^2 \text{ g}_{\text{Pt}}^{-1}$) and mass activity ($200 \text{ A g}_{\text{Pt}}^{-1}$) with comparable stability. The exceptional catalytic activity is mainly attributed to the high dispersion of the reduced MNPs with narrowly-distributed small size enabled by modified N-doped mesoporous carbon matrix, which provide high density active sites for reactions to occur. The strong interaction between metal-substrate will further improve the stability and durability of the supported catalysts. Our strategy is simple in terms of the procedure and apparatus, and it is highly efficient and scalable.

8.2 Experimental section

8.2.1 Materials

Cellulose nanocrystals (CNCs) were provided by FPInnovations and Celluforce Inc. All the chemicals used in this study were analytical grade, purchased from Sigma-Aldrich, and used as received.

8.2.2 Synthesis

Our strategy for preparing MNP/PDa-NCNR is illustrated in Figure 8.1. Our strategy for preparing Pt/PDa-NCNR is illustrated in Figure 8.1.

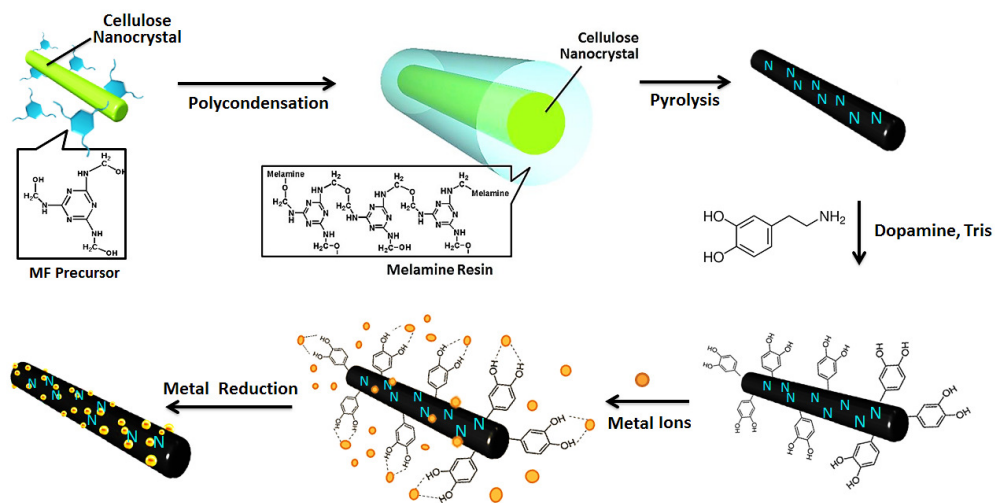


Figure 8.1 Schematic of our experimental strategy for preparing Pt and Pd heterogeneous nanocatalysts supported by PDa-NCNR.

The NCNR have been described in Chapter 7 and will be omitted herein. 10 mg NCNR powder was first dispersed in 0.1%wt suspension and sonicated. Then 12 mg Tris buffer and 2 mg dopamine hydrochloride was added to the suspension. After vigorous stirring in ambient air with an open cap for about 24 h, the reaction was stopped by repeated filtration. 10 mg of PDa-NCNR was dispersed in 20 ml of ethylene glycol and well sonicated. Then 20 mg of chloroplatinic acid hexahydrate (37.5% metal basis) or 12 mg potassium tetrachloropalladate (II) (98% purity) was added to the above solution and the pH was adjusted to 8.0 with NaOH. Then the mixture was refluxed at 110 °C for 2 h followed by filtration. Pd/NCNR and Pt/NCNR were prepared under exactly the same condition but without the coating of PDa on NCNC.

8.2.3 Characterization

8.2.3.1 Physical and chemical characterization

The morphology of samples synthesized from each steps were imaged using a Philips CM10 transmission electron microscope (TEM). In particular, CNC was imaged with JEM-2100 high resolution TEM (HRTEM) and the sample was stained with 2% (w/w) uranyl acetate negative stain for high resolution imaging. The surface charge of the MFCNC and CNC were measured using a Malvern Zetasizer Nano ZS (Worcestershire, UK) where the zeta potential of the particles was calculated from the electrophoretic mobility values using the Smoluchowski equation. The mass loading of MF coating in the composite material of MFCNCs was determined by thermal gravimetric analysis (TGA) where samples were heated from 25 to 800 °C at a heating rate of 10 °C min⁻¹ under 10 ml min⁻¹ N₂ flow. The functional groups of CNC, MFCNC, and NCNR was characterized by FT-IR (PerkinElmer 1720 FT-IR spectrometer). For sample preparation, freeze-dried samples were mixed with KBr and then compressed into pellets for measurements at a resolution of 4 cm⁻¹. The loading of Pt and Pd in the hybrid material of Pt/PDa-NCNR was determined from thermal gravimetric analysis (TGA) where samples were heated from 25 to 800 °C at a heating rate of 10 °C min⁻¹ under 10 ml min⁻¹.air flow. X-ray diffraction (XRD) was used to confirm the crystalline phases of supported MNPs and was performed with the Rigaku D/MAX-RB diffractometer using filtered Cu K α radiation. X-ray photoelectron spectroscopy (XPS) was conducted to determine the surface composition of the composite material using a Thermal Scientific K-Alpha XPS spectrometer.

8.2.3.2 Catalytic performance of Pd/PDa-NCNR for 4-NP reduction reaction

The catalytic activity of the synthesized Pd/PDa-NCNR was evaluated in the catalytic reduction of 4-nitrophenol (4-NP) to 4-aminophenol (4-AP) with NaBH₄ as the reducing agent. In a typical test, the same volume of 4-NP (0.24 mM) was first mixed with fresh NaBH₄ (0.48 M) aqueous solution (the molar ratio between NaBH₄ to 4-NP is 200:1) from which 1 ml of the mixture solution was transferred to the UV-vis cuvette. Then 20 µL of Pd/MFCNC (0.005 mg/ml) was pipetted into the cuvette followed by rapid mixing with pipette twice. After that, the kinetics of the reaction was monitored every minute with UV-vis (Agilent Model 8453 UV-vis spectroscopy) at room temperature between 250 and 600 nm. Apparent kinetic constants were obtained from the decay of UV-Vis spectra of the reactant assuming the reaction follows pseudo-first-order.

8.2.3.3 Catalytic performance of Pt/PDa-NCNR for ORR

The catalytic reaction of ORR was carried out using a typical three-electrode system with modified reversible hydrogen electrode (RDE) as the working electrode, Pt wire as the counter electrode, (RHE) as the reference electrode. The catalytic activity of commercial carbon supported platinum catalysts (28% Pt/C, TKK) was also evaluated for comparing purpose. The catalyst ink was first formulated by dispersing the active material in mixed ethanol/water solution (0.03% Nafion) at a certain concentration. Then 10 µL ink was coated onto the glassy carbon disc of the RDE using a pipette, achieving a Pt loading of 20 µg cm⁻² on the electrode surface. Cyclic voltammetry (CV) curves were obtained by performing linear voltage sweep between 0.05 and 1.05 V at 50 mV s⁻¹ in 0.1 mol L⁻¹ HClO₄ as the electrolyte (N₂ saturated). All potentials presented are relative to RHE, and current densities were normalized by the geometric area of the working electrode. Electrochemically active surface area (ECSA) of the Pt (m² g⁻¹) can be calculated based on the hydrogen under-potential adsorption and de-sorption (H-UPD) technique using the following equation:

$$\text{Equation 3.16 ECSA} = \frac{Q}{0.21m}$$

where m is the specific loading of the active catalyst (mg cm⁻²) on the electrode, Q (mC) is the averaged H₂ adsorption/desorption peak area. The constant 0.21 (mC cm⁻²) comes from the electrical charge associated with monolayer adsorption of H₂ on the active catalyst. Further ORR polarization curves were obtained via linear sweep voltammetry with scanning rate of 5 mV s⁻¹ ranging from 0.05 to 1.05 V under O₂ saturated electrolyte. In order to remove the capacity contribution, the capacitative currents obtained in the N₂ saturated electrolyte as the baseline were deducted and the

electrolyte resistance were also applied to compensate and correct the obtained ORR current densities. The stabilities of catalysts were evaluated by accelerated degradation testing (ADT), i.e. repeating cyclically scanning electrode at a rate of 50 mV s^{-1} from 0.6 to 1.0 V for 3000 cycles. Mass activity (MA) and specific activity (SA) were calculated by normalizing the kinetic current to the Pt loading and ECSA.

8.3 Results and discussion

8.3.1 Material characterization

The characterization of MFCNC and NCNR has been described in Chapters 6 and 7 and will not be discussed here. After carbonization, NCNRs still maintain the well-defined fibrous shape with a slight shrinkage in diameter (Figure 8.2c). Due to hydrophobicity of the carbon structure, once suspended in solution, NCNR particles easily precipitate within hours (inset of Figure 8.2c). The morphology changes of PDA-NCNR in Figure 8.2(d) compared to NCNRs is rather subtle, confirming the limited modification of PDA on the surface. However, dramatically improved water solubility was observed for PDA-NCNRs indicating the existence of PDA on NCNRs.

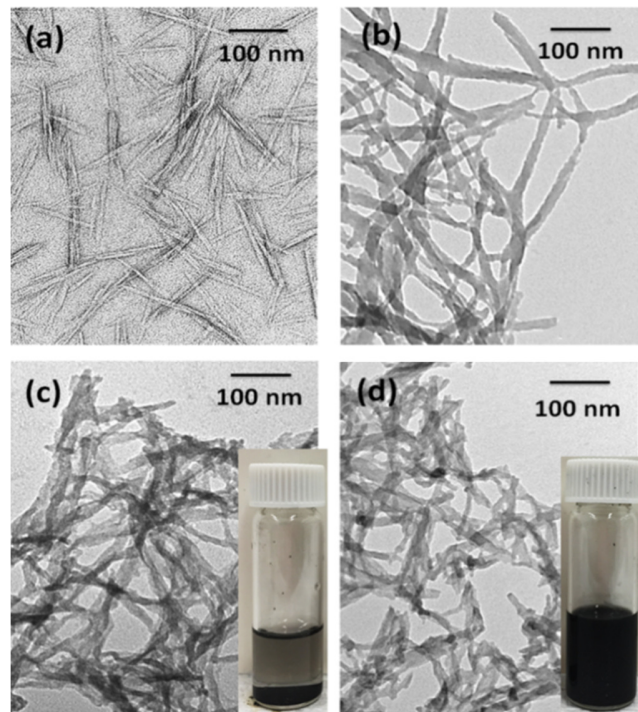


Figure 8.2 (a) HRTEM image for pristine CNCs, and TEM images for (b) MFCNC (c) NCNR and (d) PDA-NCNR. Inset of (c) and (d) shows the particle dispersion over 1 hour.

Figure 8.3 shows the comparison between Pt & Pd NPs supported by PDa-modified NCNRs and NCNRs. For the modified substrate, both Pt and Pd were homogeneously reduced and dispersed over the carbon support with astonishing fine size of 1-2 nm. The results from the same synthesis but on unmodified NCNR substrate showed a much less inhomogeneous metal dispersion for both Pt and Pd reduction with slightly larger particle size. The comparison confirmed the important role of PDa modification in promoting the optimal MNP reduction and immobilization. Moreover, pictures shown in Figure 8.3(e) and (f) for suspensions of supported Pt and Pd particles after leaving them undisturbed for 3 months. Both Pt and Pd supported by PDa-NCNR catalysts remained stable in solution while those supported by PDa-free catalysts completely precipitated. The highly dispersed ultrafine MNPs obtained in our experiment and the extraordinary dispersion stability of the heterogeneous catalysts are beneficial for catalyst application. Greatly enhanced utilization efficiency of metal catalysts can be gained due to high density active site exposed to the reactants.

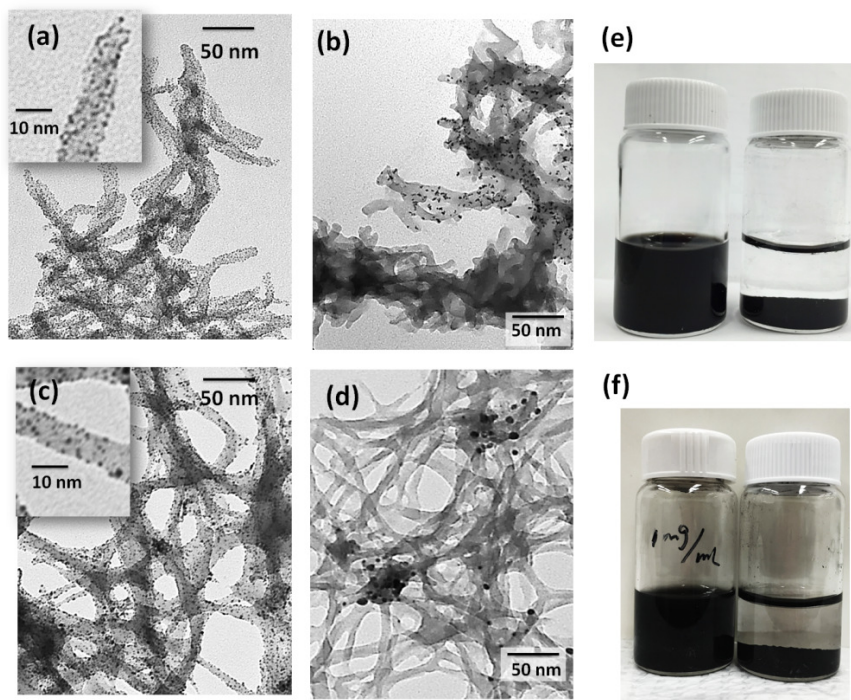


Figure 8.3 TEM images of (a) Pt/PDA-NCNR (b) Pt/NCNR (c) Pd/PDA-NCNR (d) Pd/NCNR and comparison of dispersion stability after 3 months undisturbed (e) Pt/PDA-NCNR(left) and Pt/NCNR(right), and (f) Pd/PDA-NCNR (left) and Pd/NCNR(right).

To further probe the crystalline phases of the synthesized Pt and Pd supported by NPs/PDA-NCNRs, XRD characterizations were performed. As shown in Figure 8.4(a), XRD patterns displayed clear

reflection peaks for (111), (200), (220) and (311) face-centered cubic Pt and Pd NPs (JCPDS, No. 04-0802) with (111) peak being the sharpest, and the peak is the most relevant for high catalytic activity. The diffraction peak at around 22° is attributed to graphitized carbon substrate. XRD result confirmed that neither the crystallinity of MNPs nor the underlying carbon substrate is affected by the presence of PDA modification. The highly efficient MNP reduction was further confirmed by thermogravimetric analysis (TGA) shown in Figure 8.4(b). The loading of Pt and Pd NP were determined to be 40.46% (theoretical value: 42.86%) in Pt/PDA-NCNR and 36.27% (theoretical value: 38.34%) for Pd in Pd/PDA-NCNR respectively. TGA results indicate that both metal reductions are highly efficient and more than 94% of the MNPs were reduced within 2 hours. The results prove that PDA functionalization is an extremely versatile and facile way to effectively tune the surface properties of various carbon substrates without disrupting their structural feature.

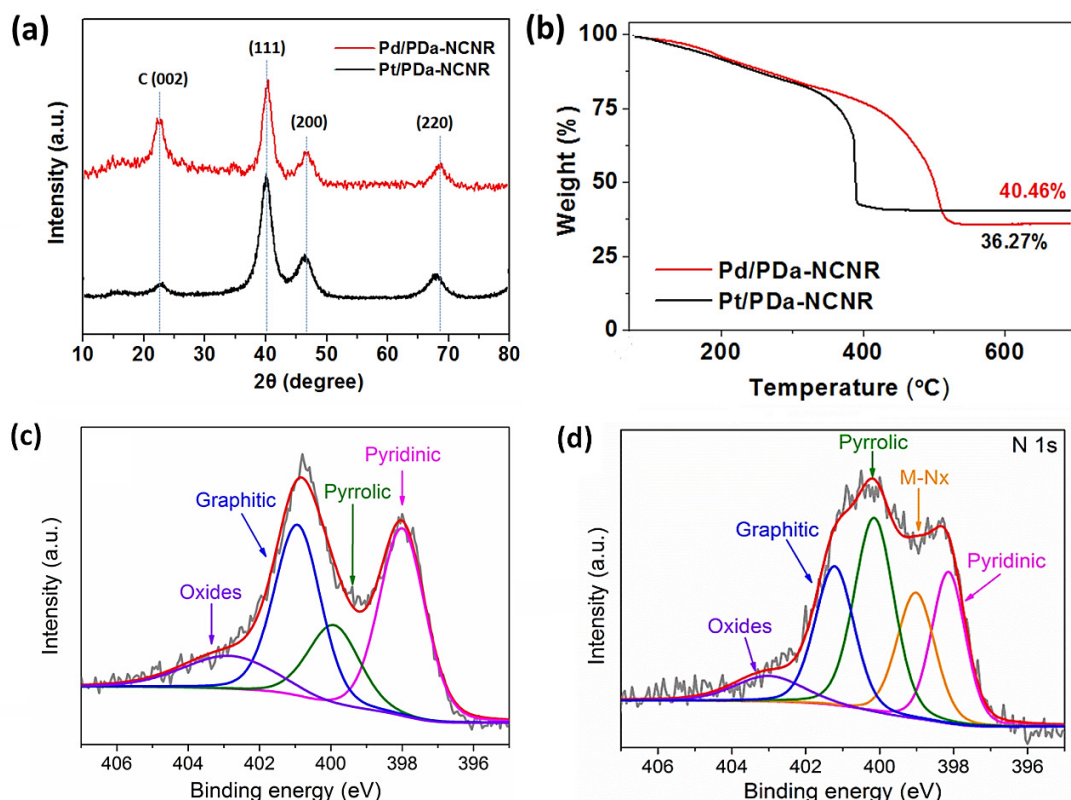


Figure 8.4 (a) XRD and (b)TGA characterization in N_2 flow of Pt/PDA-NCNR and Pd/PDA-NCNR and the N 1s XPS high resolution spectrum of (c) NCNRs and (d) Pt/PDA-NCNRs

To investigate different N species on the surface of the carbon support as well as confirm the metal-substrate interactions, XPS was performed for Pt/PDA-NCNR and comparison with NCNR and their N1s spectrum re shown in Figure 8.4(c)(d). When comparing with the XPS result of NCNRs, a new

peak representing metal-N interaction shows up in the Pt/PDa-NCNR spectra, providing direct evidence of Pt-substrate interaction (Figure 8.4d). Peaks representing various N species doped in the carbon structure graphitic N are also shown, where pyridinic N at the edge plane sites of the carbon frame is generally considered to induce strong interaction with the Pt (Zhou et al., 2010b). It has also been suggested that N-doping induce certain electronic effect on MNP resulting in the preferential growth of higher activity facets (e.g. Pt 111) which is confirmed in our XRD results. The peak representing pyrrolic N(399.9 eV) is much higher than NCNR, which confirmed the existence of PDa and the N is also responsible for providing high density nucleation sites for Pt NPs growth.

8.3.2 Catalytic activity of Pd/PDa-NCNR in 4-NP reduction reaction

The reduction of 4-NP is widely considered an ideal ‘model catalytic reaction’ for evaluating various metallic catalytic systems. It is thus used to assess the catalytic activity of the synthesized Pd/PDa-NCNR. Experimentally, 4-NP has a strong absorption peak at 400 nm, which allows the easy and reliable way of studying the reaction kinetics with UV-vis spectroscopy.(Zhao et al., 2015b) Once the reaction proceeds, the conversion of 4-NP to 4 aminophenol (4-AP) was indicated by the successive reduction in the peak intensity. Simultaneously, a new peak appeared at 310 nm corresponding to 4-AP. The reaction is also accompanied by the fading of green-yellow color of the solution (photos in Figure 8.5). The inset of Figure 8.5 shows the time-dependent UV-Vis adsorption for the 4-NP reduction catalyzed by Pd/PDa-NCNR. The reaction progressed over 97% within 10 min and completed within 15 min. In contrast, virtually no reduction occurred when the same amount of PDa-NCNR was used as the catalyst within the same time slot, suggesting that the effect of substrate is negligible for catalyzing the reduction of 4-NP to 4-AP.

The reaction is generally considered pseudo first-order when excess amount of NaBH₄ is used, and is independent of borohydride content. The general rate law for the 4-NP reduction with NaBH₄ is governed by the following equation from which the apparent pseudo first-order rate constants (k_{app}) can be readily determined:

$$\text{Equation 3.13} \quad \ln\left(\frac{C_t}{C_0}\right) = \ln\left(\frac{A_t}{A_0}\right) = -k_{app}t$$

where A_t , A_0 and C_0 , C_t are the absorption intensity at peak 400 nm and concentration of 4-NP initially and at time t respectively. To calculate the apparent rate constant k_{app} , $\ln(A_t/A_0)$ was plotted

against time (t) in Figure 8.5. A good linear fit through zero consistent with the theoretical pseudo first-order model was obtained and the slope k_{app} of 0.007 s^{-1} .

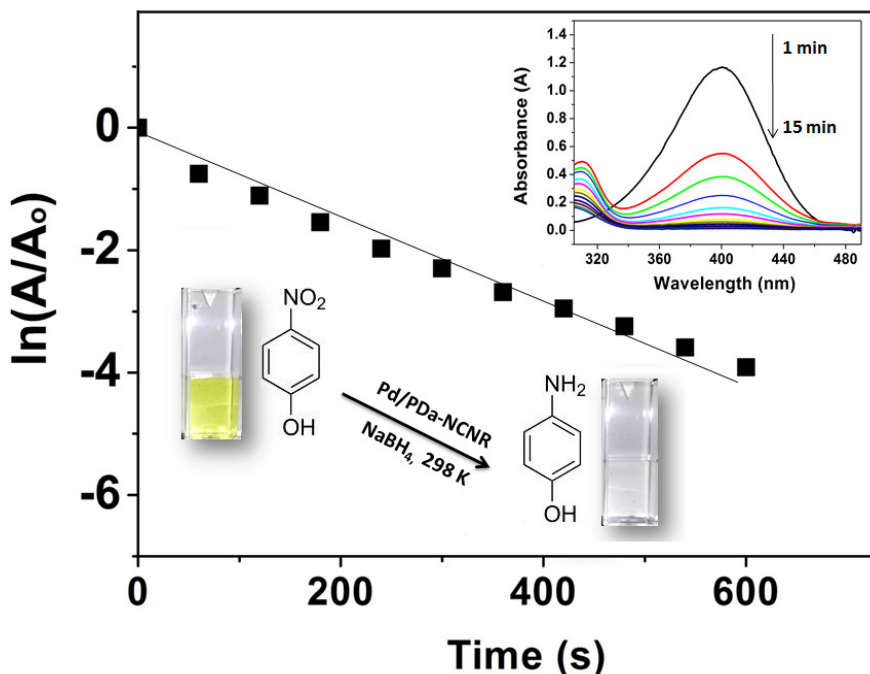


Figure 8.5 The plot of $\ln(A_t/A_0)$ against time for the reduction of 4-NP at 298 K catalyzed by Pd/PDA-NCNR. Inset: The time-dependent absorption spectra of the 4-NP reduction reaction catalyzed by Pd/PDA-NCNR.

Since catalytic reaction occurs on the surface of PdNP, the efficiency of the reaction is critically determined by the accessible active sites on the catalysts. In our test, the ‘activation time’ or ‘induction time’(Gao et al., 2007) related to substrate diffusion limitation was observed, both point to the high active surface area and reactant accessibility of supported Pd systems. To interpret the catalytic efficiency in comparison to other supported Pd nanocatalysts, the turnover frequency (TOF, defined as number of moles of 4-NP reduced per mole Pd catalyst per min) was calculated. Table 8.1 summarizes the TOF value of Pd nanocatalysts systems supported by various substrates together with their Pd NP size, and the reducing method. Our PDA-NCNR supported Pd NP displayed rather competitive catalytic performance with outstanding TOF value approaching 148.5 min^{-1} , much higher than other systems. The superior catalytic efficiency of our Pd/PDA-NCNR is largely attributed to the highly dispersed and finely sized Pd NP size achieved by PDA-NCNR substrate. Improved wettability and solubility from to PDA modification further promote the accessibility of reactant to the surface of the catalyst.

Table 8.1 Comparison of the catalytic performance and origins of Pd nanocatalyst supported on various substrates for 4-NP reduction.

Catalyst Support/Template	Reducing Reagent/Method	Palladium Size (nm)	TOF (min ⁻¹)	Reference
CNT/PiHP	PiHP	2.1, 31.6	6.3	(Li et al., 2012a)
Covalently functionalized CNT	H ₂	1.5	18	(Gu et al., 2014)
Fe ₃ O ₄ @SiO ₂ @CeO ₂	NaBH ₄	3	110.8	(Wang et al., 2013c)
Microgels	NaBH ₄	2.4	13.7	(Mei et al., 2007)
PPy/TiO ₂	PPy	2	5.4	(Lu et al., 2012)
Mesoporous silica SBA-15	Supercritical CO ₂	7-10	0.1	(Morère et al., 2011)
Cellulose Nanocrystal	Hydrothermal	1-40	14.7	(Wu et al., 2013b)
PDa-NCNR	Ethylene Glycol	1-2	148.5	This Work

8.3.3 Catalytic activity of Pt/PDa-NCNR in ORR

Carbon supported platinum (Pt/C) is commercially used as catalyst to accelerate oxygen reduction reaction (ORR) in the polymer electrolyte membrane fuel cells (PEMFCs). In industry, the high cost of Pt-based catalyst remains a top concern. To enhance the specific catalytic activity of Pt so that the reaction can proceed with much lower Pt loading is a subject of active research activity. Herein, our proposed supported Pt/PDa-NCNR catalyst was used in catalyzing ORR and Figure 8.6(a) shows a typical CV of Pt catalyst and Pt/PDa-NCNR over the range 0.05 – 1.05 V vs RHE in N₂ saturated electrolyte. Compared to the commercial Pt/C catalyst, more intense peaks representing H-UPD region (0.05 - 0.40 V vs RHE) and oxygen reduction peaks (0.77 V vs RHE) were obtained, indicating a much higher electrochemical activity of Pt/PDa-NCNR.(Wang et al., 2013d) In addition, a higher capacitive current was also observed in CV curve of Pt/PDa-NCNR as opposed to Pt/C, which is mainly attributed to the high surface area of the carbon support (NCNR). The ECSA of Pt/PDa-NCNR determined based on charge transferred within H-UPD region exhibits more than twice the number of ECSA of commercial Pt/C, i.e. 120 m² g_{Pt}⁻¹ vs 53 m² g_{Pt}⁻¹ (Figure

8.6b). The high ECSA could be attributed to the well-dispersed and narrowly-distributed small Pt NPs on the PDA-NCNRs.

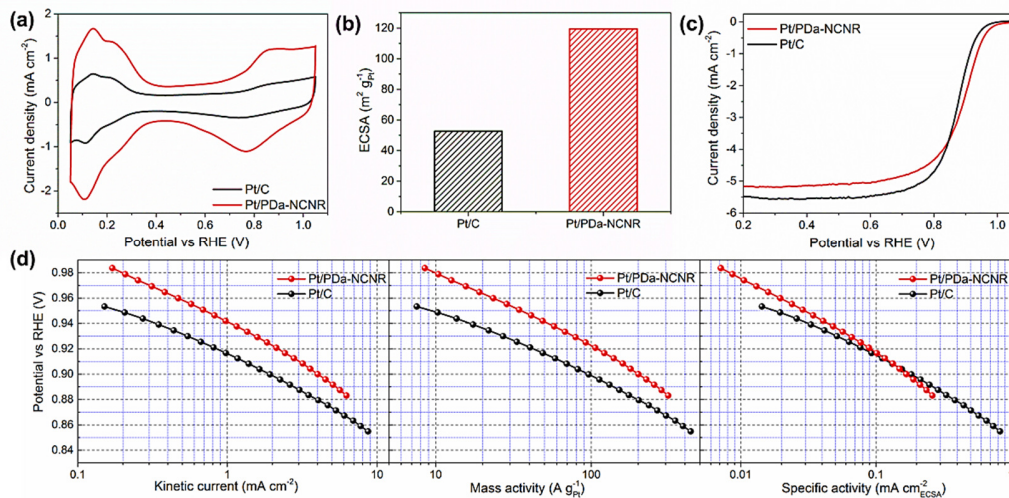


Figure 8.6 The ORR activity comparison of Pt/PDA-NCNR with commercial Pt/C in (a) cyclic voltammetry, (b) ECSA, (c) polarization curves and (d) potential as functions of different catalytic activities (kinetic current, mass activity and specific activity).

The ORR polarization curves of Pt/PDA-NCNR and Pt/C are compared in Figure 8.6(c), and both of them displayed similar characteristic profiles of the mixed kinetic/diffusion controlled region above 0.8 V and diffusion-controlled region below 0.8 V. (Wang et al., 2013d) Although the limiting current of Pt/PDA-NCNR is slightly lower than commercial catalyst, the half-wave potential of Pt/PDA-NCNR (0.89V vs RHE) is 20 mV higher than that of Pt/C (0.87V vs RHE). To further illustrate the high activity of Pt/PDA-NCNR, the Tafel plots associated with the kinetic current, mass activity and specific activity are presented in Figure 8.6(d). The Tafel slopes of Pt/PDA-NCNR is the same as that for Pt/C (61mV dec^{-1}), indicating its attractive kinetic activity. (Higgins et al., 2014; Khudhayer et al., 2011) Similar to ECSA, mass-transport corrected kinetic current densities as well as mass activity of Pt/PDA-NCNR at 0.9V vs RHE, $4.0 \text{ mA cm}_{\text{geo}}^{-2}$ and $200 \text{ A g}_{\text{Pt}}^{-1}$ respectively, are also two times higher than those of commercial catalyst ($1.9 \text{ mA cm}_{\text{geo}}^{-2}$ and $96 \text{ A g}_{\text{Pt}}^{-1}$). Considering that the mass activity is the parameter directly related the real application of PEMFC, Pt/PDA-NCNR has proven to be a promising catalyst for ORR in PEMFC. (Zhang et al., 2012a) Besides the high ECSA of Pt/PDA-NCNR, the specific activity of Pt/PDA-NCNR at 0.9V vs RHE ($0.168 \text{ mA cm}_{\text{ECSA}}^{-2}$) is also comparable to that of Pt/C ($0.182 \text{ mA cm}_{\text{ECSA}}^{-2}$), indicating the similar intrinsic catalytic activity of Pt/PDA-NCNR to the commercial catalyst for ORR. (Zhang et al., 2012a) In other words,

the high ECSA of Pt/PDa-NCNR contributes greatly to its high ORR activity. Notably, Pt/PDa-NCNR shows much higher specific activity at low over-potential (0.95V vs RHE) as opposed to Pt/C, such as 0.030 vs 0.018 mA cm_{ECSA}⁻², demonstrating its excellent intrinsic activity at high potential.

Furthermore, the stability of Pt/PDa-NCNR for ORR was evaluated in the accelerated degradation tests (ADTs). As shown in Figure 8.7(a), both Pt/PDa-NCNR and Pt/C degraded to certain extend as indicated by the reduced area in the CV curves. The calculated reduction in ECSA is illustrated in Figure 8.7(c), where Pt/PDa-NCNR even still shows higher ECSA after ADT tests as opposed to Pt/C. ORR polarization curves after the ADT test were obtained and compared with that using fresh samples in Figure 8.7(b). The decrease in the half-wave potential for Pt/PDa-NCNR is 48mV which is comparable to that of Pt/C (39mV). The calculated mass activity of Pt/PDa-NCNR at 0.9V vs RHE in Figure 8.7(c) remained at 81 A g_{Pt}⁻¹, which still outperforms that of commercial catalyst (47 A g_{Pt}⁻¹). As for specific activity at 0.9V vs RHE, Pt/PDa-NCNR (0.091 mA cm_{ECSA}⁻²) is comparable to that of Pt/C (0.108 mA cm_{ECSA}⁻²). The good stability could be associated with the N-doping induced binding interaction as well as strong chelation interaction introduced by PDa coating between metal-substrate, providing enhanced stability of Pt NPs against dissolution, migration and agglomeration during the cycles.

The superior activity and durability of our Pt/PDa-NCNR in catalyzing ORR is largely benefited from the modified N-doped mesoporous substrate which serves multiple roles: (i) the high surface area, mesoporous structure provides an ideal matrix for supporting and controlling the MNP dispersion and growth; (ii) N-C species due to N-doping induces tethering effect on the carbon substrate that facilitates the nucleation, binding, and prevent the agglomeration of MNPs; (iii) N-doping also provides synergy that further enhances the catalytic activity; (iv) PDa modification introduces strong chelation effect with MNP and further promote anchoring and stabilization effect; (v) PDa introduces remarkable solubility of the composite catalyst that increase the solution accessibility and the utilization efficiency of the catalyst, and improve the coating property on the working electrode.

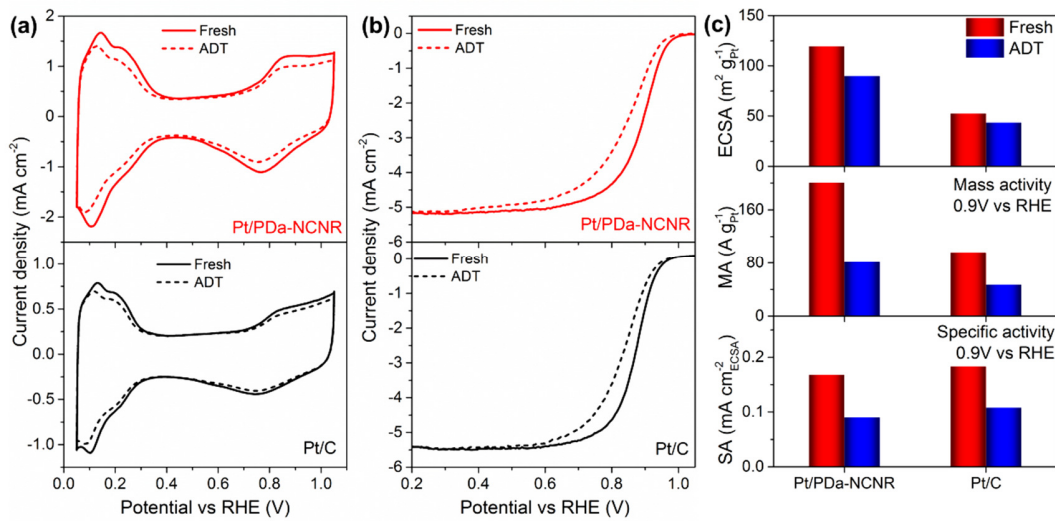


Figure 8.7 Cyclic voltammetry curves (a), ORR polarization curves (b) and the summary of ECSA, mass and specific activities at 0.9 V vs. RHE before and after 3000 cycles in ADT test for Pt/PDa-NCNR with commercial Pt/C.

8.4 Conclusions

In summary, we developed an innovative strategy to prepare modified N-doped mesoporous carbon support for highly dispersed synthesis of Pt and Pd nanocatalysts. The carbon support was prepared from a one-step pyrolysis of MF functionalized CNC which is derived from widely available biomass. A bio-inspired PDa modification was further performed on the prepared carbon surface that dramatically promotes the homogenous dispersion of MNPs during reduction as well as improving the dispersability of the supported metal composite, both critical for the catalytic activity of the catalyst. An outstanding TOF of 148.5 min^{-1} was achieved in the catalytic reaction of 4-NP reduction with Pd/PDa-NCNR. Outstanding catalytic activity of synthesized Pt/PDa-NCNR towards ORR was also demonstrated, which outperformed the commercial Pt/C in terms of half-wave potential, ECSA and mass activity with comparable durability. We believe that our PDa-NCNR system can be extended to various metal and metal oxide nanoparticle synthesis towards the development of high performance heterogeneous catalysts for industrial-scale applications.

Chapter 9 Highly dispersed Pt supported by N-doped mesoporous carbon for ultrasensitive non-enzymatic glucose sensing

9.1 Introduction

Electrochemical sensors constitute the most rapidly growing class of chemical sensors in analytical chemistry and the technique is widely demanded the industry for environmental monitoring and disease control. Central to all electrochemical sensors is the working electrode where the transduction of the sensing molecules to the electrical signal occurs. The working electrode is an integrated system consisting of a conducting material as current collector (e.g. glassy carbon), a transducer that is deposited on the surface of the current collector for desired functionality (e.g. selectively binding and catalyzing target analyte). Significant attention has been drawn to utilizing carbon materials as electrode modifiers due to the advances in material science allowing various nanostructured porous carbon materials to be fabricated with precisely controlled pore size within mesopore region (2-50 nm)(Ryoo et al., 1999). Mesoporous materials have many unique features that are highly advantageous for electrochemical sensors, including (i) enormous specific surface area exposing more active sites for sensing; (ii) easily accessible pores greatly facilitating mass transport of the analyte; (iii) good conductivity enabling direct charge transfer to the electrode and (iv) chemical stability and mechanical strength.(Walcarius, 2013, 2008) Due to the above reasons, the sensing performance of mesoporous carbon-modified electrodes were often found to outperform those modified with carbon nanotube (CNT) and graphene (G) in terms of sensitivity, extended linear range, and lower detection limit in sensing applications.(Zhu et al., 2008; Zhou et al., 2008)

Moreover, mesoporous carbon can serve as an ideal matrix for further supporting of various metal nanoparticles (MNPs). In many electrochemical sensing reactions, MNPs are highly needed for catalyzing the reaction so that it can occur within an appropriate detection window (e.g. Pt for non-enzymatic glucose sensing). It has been demonstrated in many heterogeneous catalyst systems that metal synthesis in the presence of mesoporous carbon as templates can greatly improve the dispersion of the reduced MNPs and provide confinement effect for particle growth, leading to enhanced catalytic activity.(Li et al., 2013e) Often the challenge faced in this area is that carbon materials lack surface functional groups to stabilize MNPs, leading to low metal loading, metal leaching and/or agglomeration. The poor water solubility due to their highly hydrophobic structure is also a crucial drawback for carbon materials, resulting in dramatically decreased surface area and poor reactant accessibility.(Li et al., 2013e; Guo et al., 2012) Effective functionalization for these

carbon to enhance the interaction with MNPs as well as to improved the wettability/solubility of the support materials has therefore received much research effort.(Stein et al., 2009) Recently, the strategy of N-doping in carbon was shown to effectively reduce the mobility of MNPs and establish favorable N-metal interaction, providing improved MNP reduction and stabilization.(Li & Antonietti, 2013; Mabena et al., 2011; Wong et al., 2013; Li et al., 2013e) Therefore, MNPs supported by N-doped carbon also show enhanced catalytic activity and durability compared to their N-free counterparts.(Liang et al., 2013a; He et al., 2013; Lee et al., 2014; Mabena et al., 2011) However, current technologies in achieving N-doped mesoporous carbons necessitates the use of sophisticated techniques and apparatus such as chemical vapor deposition (CVD)(Wang et al., 2010d) or cold plasma treatment(Gong et al., 2009), tedious procedures like soft/hard template synthesis(Fuertes & Centeno, 2005; Ania et al., 2007), or energy-consuming activation process sometimes involving corrosive reagents. (Lu & Schüth, 2006; Xu et al., 2008; Banham et al., 2011; Lota et al., 2007; Shrestha & Mustain, 2010) Hence, the development of N-doped mesoporous carbon materials using simple and cost-effective synthesis remains a hot research topic in the fields of catalysis and in electrochemical sensing.

Diabetes is a well-illustrated case where electrochemical glucose bio-sensors are universally applied for its control and monitoring. Conventional enzymatic glucose sensors have the significant drawback of enzyme denaturation from changes in temperature, pH, humidity etc. Alternatives in the form of non-enzymatic sensing materials that exhibit oxidation ability are being explored due to their extended lifetime and overall superior stability. Various Pt or Pt alloys have been developed as suitable transducers that enables direct glucose detection.(Yuan et al., 2005; Park et al., 2003; Wang et al., 2008d; Ryu et al., 2010) Effort to improve the catalytic activity of Pt-based biosensor electrode has focused on downscaling the particle size into nanoscale range resulting in increased activity and resistance against poisoning for the Pt NPs.(Rong et al., 2007) This has been made possible by reducing Pt precursors onto various high surface area carbon support such as CNT and G to form Pt NPs. (Joo et al., 2001; Yuan et al., 2005; Rong et al., 2007; Chang et al., 2015b; Hoa et al., 2015) However, most of the developed non-enzymatic glucose sensors exhibit long response time and can only operate at high pH or in alkaline conditions.(Rathod et al., 2010; Rong et al., 2007; Ndamanisha & Guo, 2009) Moreover, CNTs and G as metal support have the problem of low surface area due to poor wettability, stacking/entanglement, and inaccessible porosity. The most promising systems to date is mesoporous carbon supported Pt or Pt alloy composite materials as they enable the direct electrocatalytic detection of glucose at low over-potentials in media close to neutrality (e.g., physiological pH).(Bo et al., 2010b; Su et al., 2010) With the development of more

N-doped mesoporous carbons, promising candidates for supporting Pt NPs to achieve high performance enzyme-free glucose sensing especially at neutral pH should arise.

In this work, N-doped mesoporous carbon nanorods (NCNRs) were fabricated via a facile one-step pyrolysis of melamine-formaldehyde resin (MF) coated cellulose nanocrystals (CNCs). CNCs of 200 nm in length and 5 nm in diameter are extracted from wood fibers and serve as both carbon precursor and non-sacrificial template. MF was demonstrated to be an effective N-precursor for doping in addition to help generating the mesoporous structure of the carbonized NCNRs. Polydopamine (PDA) functionalization was further performed on NCNR to induce a strong chelation effect with metal ions/metals to achieve remarkable dispersion of the prepared carbon material. Highly dispersed Pt NPs of 1-2 nm in size were homogeneously reduced onto the PDA-NCNRs by ethylene glycol in the absence of any capping agent. The developed Pt composite is further used for non-enzymatic glucose sensing in neutral media. The fast current response to the addition of glucose reaches steady-state signal within 10 s with very low detection limit of 0.01 mM and a remarkable sensitivity of $81.24 \mu\text{A mM}^{-1} \text{cm}^2$. The exceptional sensing performance is mainly attributed to the optimal synthesis of MNPs assisted with N-doping and favorable mesoporous structure of the PDA modified CNR substrate. This work, to the best of our understanding, is the very first reported synthesis of the supported Pt by carbonized CNCs for electrochemical sensing application.

9.2 Experimental section

The materials used, the synthesis, and the characterization techniques for Pt/PDA-NCNR have been described in Chapter 7 and 8 and will be omitted herein.

Sensors were fabricated by drop casting 10 μL of catalyst ink onto the gold working electrode of a screen-printed electrodes (SPEs - DropSens). Reference and counter electrode consisted of solid state Ag/AgCl and Pt, respectively. The ink was formulated by dispersing the catalyst powder in 1%wt nafion (ethanol) in a 7:3 ratio (catalyst:nafion). Chronoamperometric (CA) measurements were performed at a suitable potential of +0.28 V. Potentials presented herein relate to glucose sensing are relative to Ag/AgCl. Successive additions of glucose were performed in 1xPBS (pH 7.4) under stirred conditions. Ivium Technologies CompactStat potentiostat was used for all characterization.

9.3 Results and discussion

The material characterization for MFCNC, NCNR, PDa-NCNR, and Pt/PDa-NCNR has been discussed in Chapter 7 and 8, and will be omitted herein.

Figure 9.1(a) presents the CVs of Pt/PDA-NCNR in phosphate buffered saline (PBS, pH 7.4) containing increasing amounts of glucose (0, 5, 10, 15, 20, 25, 30 mM). Multiple peaks attributed to the oxidation of glucose and resulting intermediates are observed. The peaks in the spectra are in agreement with the well-established electro-oxidation mechanism of glucose on Pt electrodes in neutral pH environment.(Ernst et al., 1979; de Mele et al., 1982; de Mele, 1982; Park et al., 2006) Peak A is attributed to reaction and oxidation of the hemiacetal group of glucose with the Pt-based electrode surface and is observed at approximately -0.55 V vs. Ag/AgCl, followed by a shoulder at -0.4 V (peak B) and a signal at 0.10 V (peak C) for indicating further oxidation of intermediates. When scanning the potential towards more positive values, Pt undergoes to electrochemical oxidization indicated by a broad response (peak D) starting from +0.3 V. Correspondingly, the reduction peak E of Pt oxides appears at around 0.15 V in the negative scan. The reduction of Pt oxides give rise to more active sites for glucose oxidation. Furthermore, the typical behavior displayed at peak F due to the electrochemical oxidation of glucose was observed in the ‘reversible hydrogen region’, and is unique only when Pt-based materials are used as the working electrode.(Ernst et al., 1979) Successive increase in peak current and a positive shift in peak potential is observed at peak F with increasing glucose concentration. Operation of glucose sensor in physiological conditions can be challenging since reactant concentration, pH and temperature are predefined by the physiological environment. Physiological species present in bodily fluid such as uric acid (UA), and ascorbic acid (AA) produce a significant increase in current leading to overestimation of the glucose signal. The interference test of most studies in this field adopt 0.02-0.1 mM UA and AA and 1-5 mM glucose that mimicking the physiological conditions of human tears and blood.(Kloke et al., 2011; Köhler et al., 2014) As illustrated in Figure 9.1(b), the current response of Pt/PDa-NCNR for AA, UA, and glucose varies at different voltages. Notably, the response towards glucose is highest at +0.5V, however due to a large response observed from UA and AA at that potential, +0.28V was chosen as the optimal voltage. The inset of Figure 9.1(b) demonstrates that addition of AA and UA at +0.28V barely produces a notable interference for glucose sensing, indicating potential use of Pt-PDa-NCNR in various sensing applications.

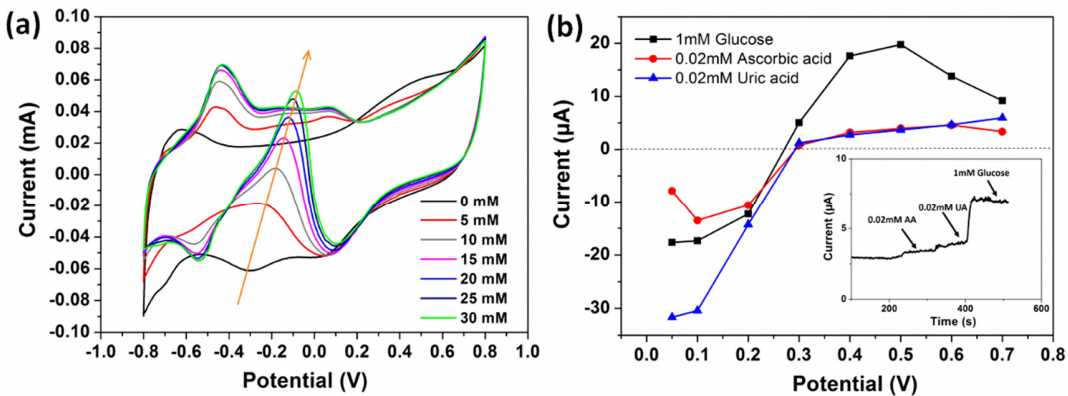


Figure 9.1 (a) CV of Pt/PDA-NCNR in 1xPBS (pH 7.4) containing glucose in the range of 0–30 mM at 100 mV/s scan rate. The arrow shows the increasing of the peak current and the shifting of peak potential with increasing glucose concentration, and (b) Amperometric current response of Pt/PDA-NCNR in 1mM Glucose, 0.02 mM Ascorbic acid (AA), and 0.02 mM Uric Acid (UA) solutions (1x PBS pH 7.4, continuously stirred, N₂ purged) at varying voltages with inset showing amperometric current measured at +0.28V in response to an addition of 0.02 mM AA, 0.02 mM UA, and 1mM glucose.

Figure 9.2(a) shows the amperometric responses of Pt/PDA-NCNR to successive addition of glucose at +0.28 V. The results showed a stepwise profile of current in accordance to the glucose addition. As indicated in the inset of Figure 9.2(a), the proposed biosensor exhibits fast amperometric response and equilibrium rate towards glucose oxidation producing steady-state signal within 10 s. The current response was further plotted against glucose concentration shown in Figure 9.2(b). Interestingly, the sensor exhibits two linear responses to glucose up to 30 mM with a higher sensitivity of $81.24 \mu\text{A mM}^{-1} \text{cm}^{-2}$ at lower glucose concentration of 0.01 – 2 mM and a lower sensitivity of $7.65 \mu\text{A mM}^{-1} \text{cm}^{-2}$ at higher glucose concentration of 2 – 30 mM. The superior sensitivity with low detection limit of 0.01 mM can be attributed to the dramatic increase of catalytic sites for glucose oxidation due to the highly dispersed Pt NPs. The excellent electrical conductivity and mesoporous structure of the carbon support further facilitates the electron transfer from the Pt NP to the electrode thereby reducing the mass diffusion pathway of the analyte to the catalytic sites. The fabrication reproducibility of the Pt/PDA-NCNR glucose sensing electrode was further evaluated by comparing sensitivities of four sensors. A relative standard deviation (RSD) value of 5.24% (N=4) from the amperometric testing was obtained. Table 9.1 compares the performance of Pt/PDA-NCNR with other recent-reported Pt-based glucose sensors tested in physiological PH. It is apparent that the sensor developed in this work exhibits superior sensing behavior in various parameters such as detection range, lowest detection limit, and sensitivity.

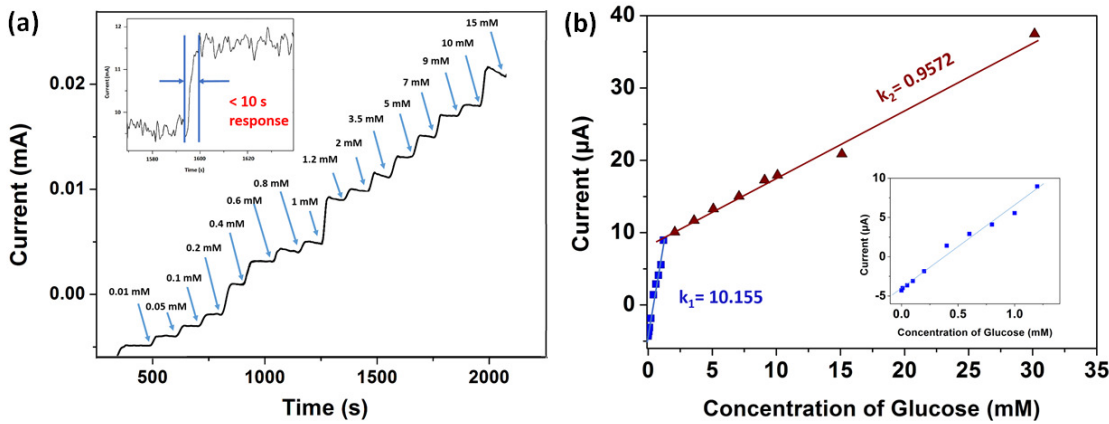


Figure 9.2 (a) Amperometric current response of the Pt/PDA-NCNR upon successive addition of glucose at +0.28 V in 1xPBS (7.4 pH). Inset: Glucose response time, and (b) calibration curve displaying 2 linear ranges: 0.01 mM to 2 mM and 2 mM to 30 mM Inset: Lower concentration linear range between 0.01 mM and 1.2 mM glucose.

Table 9.1 Comparison of performance of Pt based non-enzymatic glucose sensors in neutral PH.

Electrode	Linear range (mM)	Detection Limit (mM)	Sensitivity ($\mu\text{A mM}^{-1} \text{cm}^{-2}$)	Reference
Pt/mesoporous carbon	0.5-4.5	0.13	16.69	(Bo et al., 2010b)
Pt/Au nanocorals	0-22	0.028	2.1	(Liu et al., 2012a)
Macroporous Au-Pt hybrid	1-20	0.025	39.53	(Lee & Park, 2011)
Pt/poly(glutamic acid)	0.05-5.95	0.011	0.88	(Zhou et al., 2013)
Pt-replaced Cu foams	1-11	0.385	9.62	(Hu et al., 2015)
Pt nanoflower/rGO	0.002-10.3	0.002	1.26	(Wu et al., 2013a)
This work	0.01-2	0.01	81.24	
		2-30	7.65	

9.4 Conclusion

In summary, we developed an innovative N-doped mesoporous carbon support for highly dispersed synthesis of Pt NPs for non-enzymatic glucose sensing. The carbon support with high N-doping and mesoporous structure was prepared from one-step pyrolysis of MF coated CNC. A further bio-inspired PDa modification on the carbonized material effectively added desired functionalities without affecting the electrical conductivity and structural features of the carbon substrate. Highly homogeneous reduction of Pt NPs immobilized onto the carbon substrate was achieved with a narrow distributed small size of 1-2. The composite material exhibits remarkable water solubility and stability for months with no observed precipitation thanks to the introduced hydrophilic functionalities of PDa. An excellent sensitivity of $81.24 \mu\text{A mM}^{-1} \text{cm}^2$ in 1xPBS (pH 7.4) was achieved for glucose detection with great reproducibility as well. The outstanding performance of the non-enzymatic glucose sensor is attributed to the well-controlled high density catalytic sites due to homogeneously dispersed Pt NPs supported by PDa modified NCNRs. The high aspect ratio, excellent conductivity, and mesoporous structure of the NCNR further promote a fast kinetics of the electrochemical sensing process by facilitating the mass and electron transfer. Our strategy of using PDa-NCNR as a novel platform, can be further applied to the synthesis of other metal or metal oxide NPs as electrode material for ultra-sensitive electrochemical sensing devices.

Chapter 10 Conclusions and Recommendation for Future Studies

10.1 Conclusion and contributions

This thesis is devoted to the transformation of biomass-derived material, cellulose nanocrystals (CNCs), into high value-added conductive materials. A summary of the research journey is sketched in Figure 10.1. Two strategies have been developed to produce CNC-based conductive materials: (i) *in situ* polymerization of conductive polymer onto CNCs to form a core-shell structured hybrid material and (ii) carbonizing CNCs into carbon-based material. The carbon materials synthesized from the second strategy are further modified using simple chemistry to be an ideal platform for supporting highly dispersed metal nanoparticles (MNPs). The potential of synthesized conductive CNC systems was evaluated for various electrochemical applications include supercapacitors, catalysts, and sensors. Herein, the major contributions of this thesis are summarized below:

- Core-shell structured polypyrrole (PPy)/CNC was successfully synthesized by polymerizing PPy *in situ* on the surface of TEMPO-oxidized CNCs (Gen1). The favorable interaction established between the surface carboxylic group of CNCs and the pyrrole monomer induced a controlled growth of PPy along one-dimension. The synthesized PPy/CNC demonstrates outstanding specific capacitance outperforming carbon nanotube and graphene, promising for supercapacitor applications. By incorporating CNC into conductive polymer nanocomposites, significantly enhanced dispersion stability was observed, resolving the processing challenge associated with conductive polymers.
- Core-shell structured PPy/ PVP /CNC was successfully synthesized by polymerizing PPy *in situ* on the surface of CNC pre-modified by poly(vinylpyrrolidone)(PVP) (Gen2). With PVP simply adsorbed onto CNC through physical interaction, it dramatically conditioned the surface properties of CNCs that favors highly uniform PPy coating. The Gen 2 PPy/PVP/CNC displayed an improved electrochemical behavior compared to Gen1 with simpler experimental procedure. Higher capacitance and cycling stability were also obtained with Gen 2.
- N-enriched mesoporous carbon nanorods (NCNRs) was fabricated from melamine-formaldehyde (MF) coated CNCs. CNCs serve as carbon source and non-sacrifice template. Melamine as N-precursor was introduced by forming a highly crosslinked network of MF resin and condensed on the CNCs. Through a one-step pyrolysis, NCNRs preserving the

original CNC morphology were obtained with high N-doping content and mesoporous texture as well. MF resin was also found to play a key role in stabilizing the structure of CNC through the pyrolysis. Pyrolysis temperature was studied in detail to optimize the product. The prepared NCNRs showed promising capacitive behaviour in various electrolyte with excellent cycling stability as well.

- The potential of developing NCNR as metal-free catalyst was demonstrated by catalyzing 4-nitrophenol (NP) reduction reaction and oxygen reduction reaction (ORR). The superior catalytic performance is mainly attributed to the high N-doping content effectively tuning the electronic properties of carbon and generating catalytic active sites. High surface area mesoporous structure further contributes to the catalytic efficiency by enhancing solution accessibility and enabling efficient reactant transfer and diffusion.
- An ideal platform of modified NCNR for supporting highly dispersed metal nanocatalysts was developed. A bio-inspired PDa modification was the key to promotes the homogenous dispersion of MNPs onto carbon substrate as well as improves the solubility of the supported metal composite, both are critical for enhancing catalytic activity of the catalyst. Pt and Pd as model metal were homogeneously reduced onto the modified carbon substrate exhibiting narrowly distributed size of 1-2 nm and high density dispersion without agglomeration. The favorable interaction of metal-substrate was elucidated.
- The catalytic activity of the synthesized Pd/PDa-NCNR was demonstrated in catalyzing 4-NP reduction with an outstanding TOF of 148.5 min^{-1} achieved surpasses other reported Pd-based catalyst. Outstanding catalytic activity of synthesized Pt/PDa-NCNR towards ORR was also demonstrated that outperform the commercial Pt/C in terms of half-wave potential, ECSA and mass activity with comparable durability. The superior catalytic activity was mainly due to the high density active sites of evenly dispersed MNPs supported by PDa modified NCNRs.
- The synthesized Pt/PDa-NCNRs were used as sensing agent that enable high sensitivity non-enzymatic glucose sensing in neutral PH

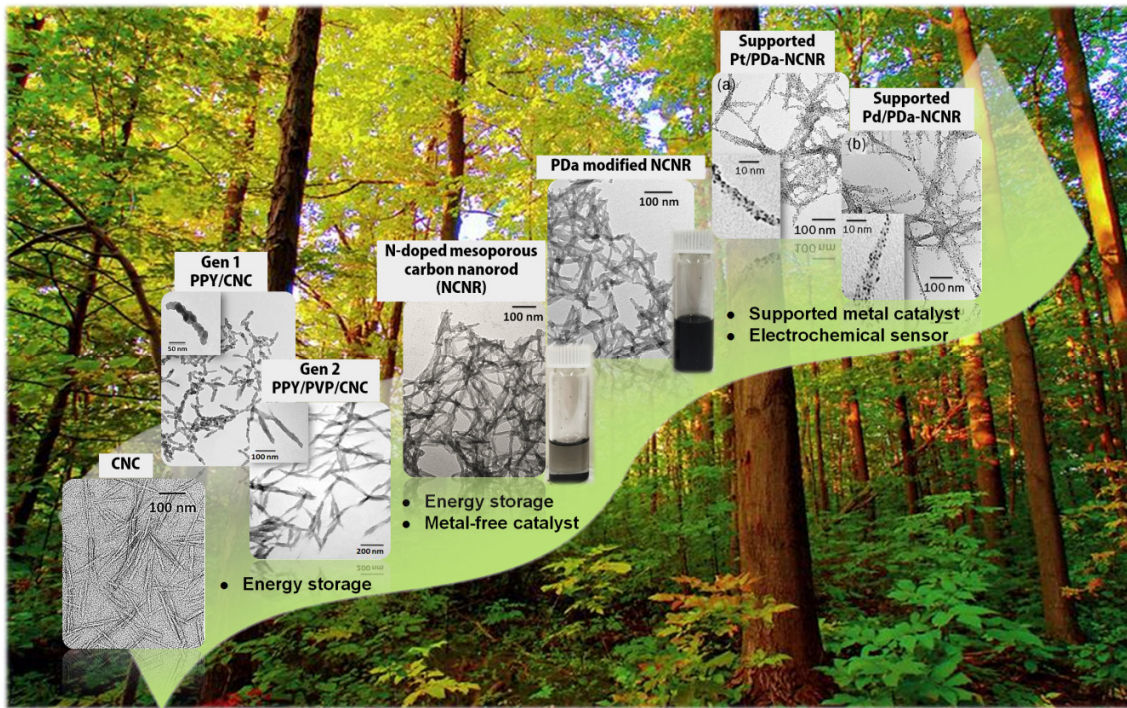


Figure 10.1 Summary of research topics in this work.

10.2 Future work

The work conducted in this thesis opens a wide variety of opportunities and many of them have the potential to transform into innovative commercial products. Herein, some of the unfinished work and unexplored possibilities are recommended:

- The conductive CNCs developed in Chapter 4 and 5 can be easily formulated into ink or gel for 2D or 3D printing. The advantages of using PPy/CNC for conductive ink application are: low percolation threshold due to 1D structure; printing friendly due to proper size; less non-conductive binder/surfactant needed due to high water dispersibility, etc. In addition, these conductive particles can be directly applied as conductive fillers for various polymeric matrix for enhanced mechanical strength with electrochemical properties at the same time. Since PPy and CNC are both biocompatible, the composite material is especially promising for bio-related applications, such as conductive reinforces for tissue engineering heart scaffold.
- The strategy for developing hybrid system of PPy and CNC in Chapter 4 and 5 can be extended to a series conductive polymers, polyaniline, poly(3,4-ethylenedioxothiophene), etc. Using CNC as templates combines the advantages of both components including the physical

properties of CNCs (highly dispersible, high aspect ratio, mechanically robust etc.) and the electrochemical properties of conductive polymers, making the hybrid system highly intriguing. Based on diverse properties of conductive polymer, and composite material of CNC/conductive polymer can be used for application such as color switchable film based on conductive polymers that are able to change color at different potential or doping state; pH sensor; gas sensor based on conductive polymers changing resistance upon interacting with different analyte gases, etc.

- The strategy for developing NCNR system in Chapter 6 can also be extended to other doping elements by introducing different precursors that might exhibit new electrochemical properties and functionalities. Since CNCs are relatively consistent in physiochemical properties, they can be used as model carbon precursors to study and compare various doping effect.
- The platform of PDa modified NCNR system developed in Chapter 8 is rather promising for supporting not only various metal and non-metal nanocatalyst. In many catalytic reactions in industry, non-noble cheaper metals such as copper are becoming increasingly popular to replace noble metals as catalyst. Therefore, PDa-NCNR will be an ideal substrate for supporting purposes. Also, various metal oxides have great potential for supercapacitors due to high theoretical pseudocapacitance. However, since charges are mostly stored on the top layers of the material, downscaling particle size will significantly increase the capacitance. By supporting metal oxides onto PDa-NCNR, greatly enhanced capacitance should be observed due to reduced particle size as well as synergy from the substrate.

References

- Aditya, T., Pal, A. & Pal, T. (2015). Nitroarene reduction: a trusted model reaction to test nanoparticle catalysts. *Chem. Commun.* 51 (100). p. pp. 9410–9431.
- Ahmadpour, A. & Do, D.D. (1996). The preparation of active carbons from coal by chemical and physical activation. *Carbon*. 34 (4). p. pp. 471–479.
- Alexeyeva, N., Shulga, E., Kisand, V., Kink, I. & Tammeveski, K. (2010). Electroreduction of oxygen on nitrogen-doped carbon nanotube modified glassy carbon electrodes in acid and alkaline solutions. *Journal of Electroanalytical Chemistry*. 648 (2). p. pp. 169–175.
- An, K.H., Jeon, K.K., Heo, J.K., Lim, S.C., Bae, D.J. & Lee, Y.H. (2002). High-capacitance supercapacitor using a nanocomposite electrode of single-walled carbon nanotube and polypyrrole. *Journal of The Electrochemical Society*. 149 (8). p. pp. A1058–A1062.
- An, K.H., Jeong, S.Y., Hwang, H.R. & Lee, Y.H. (2004). Enhanced Sensitivity of a Gas Sensor Incorporating Single-Walled Carbon Nanotube–Polypyrrole Nanocomposites. *Adv Mater.* 16 (12). p. pp. 1005–1009.
- An, K.H., Kim, W.S., Park, Y.S., Moon, J.M., Bae, D.J., Lim, S.C., Lee, Y.S. & Lee, Y.H. (2001). Electrochemical Properties of High-Power Supercapacitors Using Single-Walled Carbon Nanotube Electrodes. *Advanced Functional Materials*. 11 (5). p. pp. 387–392.
- Anglès, M.N. & Dufresne, A. (2001). Plasticized Starch / Tunicin Whiskers Nanocomposite Materials . 2 . Mechanical Behavior. *Macromolecules*. 34 (9). p. pp. 2921–2931.
- Ania, C.O., Khomenko, V., Raymundo-Piñero, E., Parra, J.B. & Béguin, F. (2007). The large electrochemical capacitance of microporous doped carbon obtained by using a zeolite template. *Advanced Functional Materials*. 17 (11). p. pp. 1828–1836.
- Anon (2009). Polysaccharide Materials: Performance by Design, Copyright, Foreword. In: *Polysaccharide Materials: Performance by Design*. ACS Symposium Series. American Chemical Society, pp. i–v.
- Antolini, E. (2012). Graphene as a new carbon support for low-temperature fuel cell catalysts. *Applied Catalysis B: Environmental*. 123-124 p. pp. 52–68.
- Araki, J., Wada, M. & Kuga, S. (2001). Steric stabilization of a cellulose microcrystal suspension by poly (ethylene glycol) grafting. *Langmuir*. 17 (1). p. pp. 21–27.
- Araki, J., Wada, M., Kuga, S. & Okano, T. (1998). Flow properties of microcrystalline cellulose suspension prepared by acid treatment of native cellulose. *Colloids and Surfaces A: Physicochemical and Engineering Aspects*. 142 (1). p. pp. 75–82.
- ArboraNano (2014). *Annual Report 2013-2014: Canadian Forest NanoProducts Network, Canada*.

[Online]. (July). p.pp. 1–50. Available from: <http://www.arboranano.ca/pdfs/Annual Report 2013-2014.pdf>.

- Arico, A.S., Bruce, P., Scrosati, B., Tarascon, J.M. & Van Schalkwijk, W. (2005). Nanostructured materials for advanced energy conversion and storage devices. *Nature Materials*. 4 (5). p.pp. 366–377.
- Armes, S.P., Gottesfeld, S., Beery, J.G., Garzon, F. & Agnew, S.F. (1991). Conducting polymer-colloidal silica composites. *Polymer*. 32 (13). p.pp. 2325–2330.
- Asefa, T. (2012). Chiral nematic mesoporous carbons from self-assembled nanocrystalline cellulose. *Angewandte Chemie - International Edition*. 51 (9). p.pp. 2008–2010.
- Auer, E., Freund, a., Pietsch, J. & Tacke, T. (1998). Carbons as supports for industrial precious metal catalysts. *Applied Catalysis A: General*. 173 (2). p.pp. 259–271.
- Banham, D., Feng, F., Fürstenhaupt, T., Pei, K., Ye, S. & Birss, V. (2011). Effect of Pt-loaded carbon support nanostructure on oxygen reduction catalysis. *Journal of Power Sources*. 196 (13). p.pp. 5438–5445.
- Bell, A.T. (2003). The impact of nanoscience on heterogeneous catalysis. *Science (New York, N.Y.)*. 299 (5613). p.pp. 1688–1691.
- Berlizoz, S., Molina-Boisseau, S., Nishiyama, Y. & Heux, L. (2009). Gas-phase surface esterification of cellulose microfibrils and whiskers. *Biomacromolecules*. 10 (8). p.pp. 2144–2151.
- Berry, R., Hashaikeh, R. & Hu, T. (2010). *Crystalline sulphated cellulose II and its production from sulphuric acid hydrolysis of celulose*. WO/2010/12 (EP20100771944).
- Bezerra, C.W.B., Zhang, L., Lee, K., Liu, H., Marques, A.L.B., Marques, E.P., Wang, H. & Zhang, J. (2008). A review of Fe-N/C and Co-N/C catalysts for the oxygen reduction reaction. *Electrochimica Acta*. 53 (15) p.pp. 4937–4951.
- Bichat, M.P., Raymundo-Piñero, E. & Béguin, F. (2010). High voltage supercapacitor built with seaweed carbons in neutral aqueous electrolyte. *Carbon*. 48 (15). p.pp. 4351–4361.
- Biermann, C.J. (1996). *Handbook of Pulping and Papermaking*.
- Biyani, M. V., Foster, E.J. & Weder, C. (2013). Light-healable supramolecular nanocomposites based on modified cellulose nanocrystals. *ACS Macro Letters*. 2 (3). p.pp. 236–240.
- Bo, X., Bai, J., Ju, J. & Guo, L. (2010a). A sensitive amperometric sensor for hydrazine and hydrogen peroxide based on palladium nanoparticles/onion-like mesoporous carbon vesicle. *Analytica Chimica Acta*. 675 (1). p.pp. 29–35.
- Bo, X., Bai, J., Yang, L. & Guo, L. (2011). The nanocomposite of PtPd nanoparticles/onion-like mesoporous carbon vesicle for nonenzymatic amperometric sensing of glucose. *Sensors and*

Actuators B: Chemical. 157 (2). p.pp. 662–668.

- Bo, X., Ndamanisha, J.C., Bai, J. & Guo, L. (2010b). Nonenzymatic amperometric sensor of hydrogen peroxide and glucose based on Pt nanoparticles/ordered mesoporous carbon nanocomposite. *Talanta*. 82 (1). p.pp. 85–91.
- Bondeson, D. & Oksman, K. (2007). Dispersion and characteristics of surfactant modified cellulose whiskers nanocomposites. *Composite Interfaces*. 14 (7-9). p.pp. 617–630.
- Braun, B. & Dorgan, J.R. (2009). Single-step method for the isolation and surface functionalization of cellulosic nanowhiskers. *Biomacromolecules*. 10 (2). p.pp. 334–341.
- Brédas, J., Scott, J., Yakushi, K. & Street, G. (1984). Polarons and bipolarons in polypyrrole: Evolution of the band structure and optical spectrum upon doing. *Physical Review B*. 30 (2). p.pp. 1023–1025.
- Bulota, M., Tanpichai, S., Hughes, M. & Eichhorn, S.J. (2012). Micromechanics of TEMPO-oxidized fibrillated cellulose composites. *ACS Applied Materials and Interfaces*. 4 (1). p.pp. 331–337.
- Burchell, M.J. & Armes, S.P. (2011). Impact ionisation spectra from hypervelocity impacts using aliphatic poly(methyl methacrylate) microparticle projectiles. *Rapid Communications in Mass Spectrometry*. 25 (4). p.pp. 543–550.
- Burke, A. (2007). R&D considerations for the performance and application of electrochemical capacitors. *Electrochimica Acta*. 53 (3). p.pp. 1083–1091.
- Burke, A. (2000). Ultracapacitors: why, how, and where is the technology. *Journal of Power Sources*. 91 (1). p.pp. 37–50.
- Calloway, D. (1997). Beer-Lambert Law. *Journal of Chemical Education*. 74 (7). p.p. 744.
- Campelo, J.M., Luna, D., Luque, R., Marinas, J.M. & Romero, A.A. (2009). Sustainable preparation of supported metal nanoparticles and their applications in catalysis. *ChemSusChem*. 2 (1). p.pp. 18–45.
- Cao, B., Zhang, B., Jiang, X., Zhang, Y. & Pan, C. (2011). Direct synthesis of high concentration N-doped coiled carbon nanofibers from amine flames and its electrochemical properties. *Journal of Power Sources*. 196 (18). p.pp. 7868–7873.
- Cao, Y. & Mallouk, T.E. (2008). Morphology of template-grown polyaniline nanowires and its effect on the electrochemical capacitance of nanowire arrays. *Chemistry of Materials*. 20 (16). p.pp. 5260–5265.
- Cermignani, W., Paulson, T.E., Onneby, C. & Pantano, C.G. (1995). Synthesis and characterization of boron-doped carbons. *Carbon*. 33 (4) p.pp. 367–374.

- Çetin, N.S., Tingaut, P., Özmen, N., Henry, N., Harper, D., Dadmun, M. & Sèbe, G. (2009). Acetylation of cellulose nanowhiskers with vinyl acetate under moderate conditions. *Macromolecular Bioscience*. 9. p.pp. 997–1003.
- Chai, G.S., Yoon, S.B., Yu, J.-S., Choi, J.-H. & Sung, Y.-E. (2004). Ordered Porous Carbons with Tunable Pore Sizes as Catalyst Supports in Direct Methanol Fuel Cell. *The Journal of Physical Chemistry B*. 108 (22). p.pp. 7074–7079.
- Chang, D.W., Choi, H.-J. & Baek, J.-B. (2015a). Wet-Chemical Nitrogen-Doping of Graphene Nanoplatelets as Electrocatalysts for Oxygen Reduction Reaction. *Journal of Materials Chemistry A*. 3. p.pp. 7659–7665.
- Chang, G., Shu, H., Huang, Q., Oyama, M., Ji, K., Liu, X. & He, Y. (2015b). Synthesis of highly dispersed Pt nanoclusters anchored graphene composites and their application for non-enzymatic glucose sensing. *Electrochimica Acta*. 157. p.pp. 149–157.
- Chen, G., Dufresne, A., Huang, J. & Chang, P.R. (2009). A novel thermoformable bionanocomposite based on cellulose nanoerystal-graft-Poly(e-caprolactone). *Macromolecular Materials and Engineering*. 294 (1). p.pp. 59–67.
- Chen, L., Zhang, X., Liang, H. & Kong, M. (2012a). Synthesis of nitrogen-doped porous carbon nanofibers as an efficient electrode material for supercapacitors. *ACS nano*. 6 (8). p.pp. 7092–7102.
- Chen, L.-F., Huang, Z.-H., Liang, H.-W., Yao, W.-T., Yu, Z.-Y. & Yu, S.-H. (2013a). Flexible all-solid-state high-power supercapacitor fabricated with nitrogen-doped carbon nanofiber electrode material derived from bacterial cellulose. *Energy & Environmental Science*. 6 (11). p.p. 3331.
- Chen, L.-F., Zhang, X.-D., Liang, H.-W., Kong, M., Guan, Q.-F., Chen, P., Wu, Z.-Y. & Yu, S.-H. (2012b). Synthesis of nitrogen-doped porous carbon nanofibers as an efficient electrode material for supercapacitors. *ACS nano*. 6 (8). p.pp. 7092–7102.
- Chen, P., Wang, L.-K., Wang, G., Gao, M.-R., Ge, J., Yuan, W.-J., Shen, Y.-H., Xie, A.-J. & Yu, S.-H. (2014). Nitrogen-doped nanoporous carbon nanosheets derived from plant biomass: an efficient catalyst for oxygen reduction reaction. *Energy Environ. Sci.* 7 (12). p.pp. 4095–4103.
- Chen, P., Yang, J.J., Li, S.S., Wang, Z., Xiao, T.Y., Qian, Y.H. & Yu, S.H. (2013b). Hydrothermal synthesis of macroscopic nitrogen-doped graphene hydrogels for ultrafast supercapacitor. *Nano Energy*. 2 (2). p.pp. 249–256.
- Chen, X.Y., Chen, C., Zhang, Z.J., Xie, D.H., Deng, X. & Liu, J.W. (2013c). Nitrogen-doped porous carbon for supercapacitor with long-term electrochemical stability. *Journal of Power Sources*. 230 (15). p.pp. 50–58.
- Chen, Y., Zhang, X., Yu, P. & Ma, Y. (2010). Electrophoretic deposition of graphene nanosheets

- on nickel foams for electrochemical capacitors. *Journal of Power Sources*. 195 (9). p.pp. 3031–3035.
- Chen, Z.W., Xu, L.B., Li, W.Z., Waje, M. & Yan, Y.S. (2006). Polyaniline nanofibre supported platinum nanoelectrocatalysts for direct methanol fuel cells. *Nanotechnology*. 17 (20). p.pp. 5254–5259.
- Cirtiu, C.M., Dunlop-Brière, A.F. & Moores, A. (2011). Cellulose nanocrystallites as an efficient support for nanoparticles of palladium: application for catalytic hydrogenation and Heck coupling under mild conditions. *Green Chemistry*. 13 (2). p.pp. 288–291.
- Conway, B. (1999). *Electrochemical supercapacitors: scientific fundamentals and technological applications (POD)*. Kluwer Academic/Plenum: New York.
- Conway, B.E. (2013). *Electrochemical supercapacitors: scientific fundamentals and technological applications*. Springer Science & Business Media.
- Conway, B.E. (1991). Transition from ‘Supercapacitor’ to ‘Battery’ Behavior in Electrochemical Energy Storage. *J. Electrochem. Soc.* 138 (6). p.pp. 1539–1548.
- Conway, B.E., Birss, V. & Wojtowicz, J. (1997). The role and utilization of pseudocapacitance for energy storage by supercapacitors. *Journal of Power Sources*. 66 (1). p.pp. 1–14.
- Daems, N., Sheng, X., Vankelecom, I.F.J. & Pescarmona, P.P. (2014). Metal-free doped carbon materials as electrocatalysts for the oxygen reduction reaction. *Journal of Materials Chemistry A*. 2 (12). p.pp. 4085–4110.
- Dai, T., Yang, X. & Lu, Y. (2007). Conductive composites of polypyrrole and sulfonic-functionalized silica spheres. *Materials Letters*. 61 (14-15). p.pp. 3142–3145.
- Davies, A., Audette, P., Farrow, B., Hassan, F., Chen, Z.W., Choi, J.Y. & Yu, A.P. (2011). Graphene-Based Flexible Supercapacitors: Pulse-Electropolymerization of Polypyrrole on Free-Standing Graphene Films. *Journal of Physical Chemistry C*. 115 (35). p.pp. 17612–17620.
- Davis, E.M. & Davis, R.J. (2003). *Fundamentals of Chemical Reaction Engineering*.
- von Deak, D., Biddinger, E.J., Luthman, K.A. & Ozkan, U.S. (2010). The effect of phosphorus in nitrogen-containing carbon nanostructures on oxygen reduction in PEM fuel cells. *Carbon*. 48 (12). p.pp. 3637–3639.
- Deng, J., Ren, P., Deng, D., Yu, L., Yang, F. & Bao, X. (2014). Highly active and durable non-precious-metal catalysts encapsulated in carbon nanotubes for hydrogen evolution reaction. *Energy & Environmental Science*. 7 (6). p.pp. 1919–1923.
- Deutschmann, O., Knüzinger, H., Kochloefl, K. & Turek, T. (2000). *Heterogeneous Catalysis and*

Solid Catalysts.

- Devallencourt, C., Saiter, J., Fafet, A. & Ubrich, E. (1995). Thermogravimetry/Fourier transform infrared coupling investigations to study the thermal stability of melamine formaldehyde resin. *Thermochimica Acta*. 259 (1). p.pp. 143–151.
- Diallo, M.S., Fromer, N.A. & Jhon, M.S. (2014). Nanotechnology for sustainable development: Retrospective and outlook. In: *Nanotechnology for Sustainable Development, First Edition*. pp. 1–16.
- Ding, C., Qian, X., Yu, G. & An, X. (2010). Dopant effect and characterization of polypyrrole-cellulose composites prepared by in situ polymerization process. *Cellulose*. 17 (6). p.pp. 1067–1077.
- Dong, S. & Roman, M. (2007). Fluorescently labeled cellulose nanocrystals for bioimaging applications. *Journal of the American Chemical Society*. 129 (45). p.pp. 13810–13811.
- Dong, X.U.E.M.I.N. (1998). Effect of microcrystallite preparation conditions on the formation of colloid crystals of cellulose. *Water*. 5 (1). p.pp. 19–32.
- Drogat, N., Granet, R., Sol, V., Memmi, A., Saad, N., Koerkamp, C.K., Bressollier, P. & Krausz, P. (2011). Antimicrobial silver nanoparticles generated on cellulose nanocrystals. *Journal of Nanoparticle Research*. 13 (4). p.pp. 1557–1562.
- Du, F., Yu, D., Dai, L., Ganguli, S., Varshney, V. & Roy, A.K. (2011). Preparation of tunable 3D pillared carbon nanotube-graphene networks for high-performance capacitance. *Chemistry of Materials*. 23 (21). p.pp. 4810–4816.
- Du, Q., Zheng, M., Zhang, L., Wang, Y., Chen, J., Xue, L., Dai, W., Ji, G. & Cao, J. (2010). Preparation of functionalized graphene sheets by a low-temperature thermal exfoliation approach and their electrochemical supercapacitive behaviors. *Electrochimica Acta*. 55 (12). p.pp. 3897–3903.
- Duan, X., Ao, Z., Sun, H., Indrawirawan, S., Wang, Y., Kang, J., Liang, F., Zhu, Z.H. & Wang, S. (2015a). Nitrogen-doped graphene for generation and evolution of reactive radicals by metal-free catalysis. *ACS applied materials & interfaces*. 7 (7). p.pp. 4169–78.
- Duan, X., Sun, H., Wang, Y., Kang, J. & Wang, S. (2015b). N-Doping-Induced Nonradical Reaction on Single-Walled Carbon Nanotubes for Catalytic Phenol Oxidation. *ACS Catalysis*. 5 (2). p.pp. 553–559.
- Dugan, J.M., Gough, J.E. & Eichhorn, S.J. (2010). Directing the morphology and differentiation of skeletal muscle cells using oriented cellulose nanowhiskers. *Biomacromolecules*. 11 (9). p.pp. 2498–2504.
- Dujardin, E., Blaseby, M. & Mann, S. (2003). Synthesis of mesoporous silica by sol-gel

- mineralisation of cellulose nanorod nematic suspensions. *Journal of Materials Chemistry*. 13. p.pp. 696–699.
- Dvir, T., Timko, B.P., Kohane, D.S. & Langer, R. (2011). Nanotechnological strategies for engineering complex tissues. *Nature nanotechnology*. 6 (1). p.pp. 13–22.
- Egerton, R.F. (2005). *Physical principles of electron microscopy: An introduction to TEM, SEM, and AEM*.
- Elazzouzi-Hafraoui, S., Nishiyama, Y., Putaux, J.L., Heux, L., Dubreuil, F. & Rochas, C. (2008). The shape and size distribution of crystalline nanoparticles prepared by acid hydrolysis of native cellulose. *Biomacromolecules*. 9 (1). p.pp. 57–65.
- Ernst, S., Heitbaum, J. & Hamann, C.H. (1979). The Electrooxidation of Glucose in Phosphate Buffered Solutions - Part I. Reactivity and Kinetics Below 350 mV/RHE. *Journal of Electroanalytical Chemistry*. 100. p.pp. 173–183.
- Esmaeili, C., Abdi, M.M., Mathew, A.P., Jonoobi, M., Oksman, K. & Rezayi, M. (2015). Synergy effect of nanocrystalline cellulose for the biosensing detection of glucose. *Sensors (Switzerland)*. 15 (10). p.pp. 24681–24697.
- Fan, L.Z. & Maier, J. (2006). High-performance polypyrrole electrode materials for redox supercapacitors. *Electrochemistry Communications*. 8 (6). p.pp. 937–940.
- Fang, B., Kim, J.H., Kim, M. & Yu, J.-S. (2009). Ordered Hierarchical Nanostructured Carbon as a Highly Efficient Cathode Catalyst Support in Proton Exchange Membrane Fuel Cell. *Chemistry of Materials*. 21 (5). p.pp. 789–796.
- Fang, Y. & Wang, E. (2013). Simple and direct synthesis of oxygenous carbon supported palladium nanoparticles with high catalytic activity. *Nanoscale*. 5 (5). p.pp. 1843–1848.
- Flandin, L., Bidan, G., Brechet, Y. & Cavaille, J.Y. (2000). New nanocomposite materials made of an insulating matrix and conducting fillers: Processing and properties. *Polymer Composites*. 21 (2). p.pp. 165–174.
- Fleming, K. & Gray, D. (2000). Cellulose crystallites: a new and robust liquid crystalline medium for the measurement of residual dipolar couplings. *Journal of the American* 122 (21). p.pp. 5224–5225.
- Frackowiak, E., Khomenko, V., Jurewicz, K., Lota, K. & Beguin, F. (2006). Supercapacitors based on conducting polymers/nanotubes composites. *Journal of Power Sources*. 153 (2). p.pp. 413–418.
- Frackowiak, E., Metenier, K., Bertagna, V. & Beguin, F. (2000). Supercapacitor electrodes from multiwalled carbon nanotubes. *Applied Physics Letters*. 77 (15). p.pp. 2421–2423.

- Frenzel, B., Kurzweil, P. & Rönnebeck, H. (2011). Electromobility concept for racing cars based on lithium-ion batteries and supercapacitors. *Journal of Power Sources*. 196 (12). p.pp. 5364–5376.
- Fu, H., Du, Z., Zou, W., Li, H. & Zhang, C. (2013). Carbon nanotube reinforced polypyrrole nanowire network as a high-performance supercapacitor electrode. *Journal of Materials Chemistry A*. 1 (47). p.pp. 14943–14950.
- Fuertes, A.B. & Centeno, T.A. (2005). Mesoporous carbons with graphitic structures fabricated by using porous silica materials as templates and iron-impregnated polypyrrole as precursor. *Journal of Materials Chemistry*. 15 (10). p.pp. 1079–1083.
- G.Nystrom, Ph.D. Thesis (2012). *Nanocellulose and Polypyrrole Composites for Electrical Energy Storage*. Uppsala University.
- Gao, L., Li, R., Sui, X., Chen, C. & Chen, Q. (2014). Conversion of chicken feather waste to N-doped carbon nanotubes for the catalytic reduction of 4-nitrophenol. *Environmental Science and Technology*. 48 (17). p.pp. 10191–10197.
- Gao, Y., Ding, X., Zheng, Z., Cheng, X. & Peng, Y. (2007). Template-free method to prepare polymer nanocapsules embedded with noble metal nanoparticles. *Chemical communications (Cambridge, England)*. (36). p.pp. 3720–3722.
- Garcia de Rodriguez, N.L., Thielemans, W. & Dufresne, A. (2006). Sisal cellulose whiskers reinforced polyvinyl acetate nanocomposites. *Cellulose*. 13 (3). p.pp. 261–270.
- Gasteiger, H.A., Kocha, S.S., Sompalli, B. & Wagner, F.T. (2005). Activity benchmarks and requirements for Pt, Pt-alloy, and non-Pt oxygen reduction catalysts for PEMFCs. *Applied Catalysis B: Environmental*. 56 (1-2 SPEC. ISS.) p.pp. 9–35.
- Gavrilov, N., Pašti, I.A., Mitić, M., Travas-Sejdić, J., Ćirić-Marjanović, G. & Mentus, S. V. (2012). Electrocatalysis of oxygen reduction reaction on polyaniline-derived nitrogen-doped carbon nanoparticle surfaces in alkaline media. *Journal of Power Sources*. 220. p.pp. 306–316.
- Geng, D., Chen, Y., Chen, Y., Li, Y., Li, R., Sun, X., Ye, S. & Knights, S. (2011). High oxygen-reduction activity and durability of nitrogen-doped graphene. *Energy & Environmental Science*. 4 (3). p.pp. 760–764.
- Georgakilas, V., Otyepka, M., Bourlinos, A.B., Chandra, V., Kim, N., Kemp, K.C., Hobza, P., Zboril, R. & Kim, K.S. (2012). Functionalization of graphene: Covalent and non-covalent approaches, derivatives and applications. *Chemical Reviews*. 112 (11) p.pp. 6156–6214.
- George, J., Sajeevkumar, V.A., Ramana, K.V., Sabapathy, S.N. & Siddaramaiah (2012). Augmented properties of PVA hybrid nanocomposites containing cellulose nanocrystals and silver nanoparticles. *Journal of Materials Chemistry*. 22. p.pp. 22433–22439.

- Goffin, a. L., Raquez, J.M., Duquesne, E., Siqueira, G., Habibi, Y., Dufresne, A. & Dubois, P. (2011). Poly(ϵ -caprolactone) based nanocomposites reinforced by surface-grafted cellulose nanowhiskers via extrusion processing: Morphology, rheology, and thermo-mechanical properties. *Polymer*. 52 (7). p.pp. 1532–1538.
- Golikand, A.N., Asgari, M. & Lohrasbi, E. (2011). Study of oxygen reduction reaction kinetics on multi-walled carbon nano-tubes supported Pt-Pd catalysts under various conditions. *International Journal of Hydrogen Energy*. 36 (20). p.pp. 13317–13324.
- Gómez, H., Ram, M.K., Alvi, F., Villalba, P., Stefanakos, E. & Kumar, A. (2011). Graphene-conducting polymer nanocomposite as novel electrode for supercapacitors. *Journal of Power Sources*. 196 (8). p.pp. 4102–4108.
- Gomez-Romero, P., Chojak, M., Cuentas-Gallegos, K., Asensio, J.A., Kulesza, P.J., Casan-Pastor, N. & Lira-Cantu, M. (2003). Hybrid organic-inorganic nanocomposite materials for application in solid state electrochemical supercapacitors. *Electrochemistry Communications*. 5 (2). p.pp. 149–153.
- Gomez-Romero, P., Cuentas-Gallegos, K., Lira-Cantu, M. & Casan-Pastor, N. (2005). Hybrid nanocomposite materials for energy storage and conversion applications. *Journal of Materials Science*. 40 (6). p.pp. 1423–1428.
- Gong, K., Du, F., Xia, Z., Durstock, M. & Dai, L. (2009). Nitrogen-doped carbon nanotube arrays with high electrocatalytic activity for oxygen reduction. *Science*. 323 (5915). p.pp. 760–764.
- Goussé, C., Chanzy, H., Excoffier, G., Soubeyrand, L. & Fleury, E. (2002). Stable suspensions of partially silylated cellulose whiskers dispersed in organic solvents. *Polymer*. 43 (9). p.pp. 2645–2651.
- Gregory, R. V., Kimbrell, W.C. & Kuhn, H.H. (1989). Conductive textiles. *Synthetic Metals*. 28 (1–2). p.pp. 823–835.
- Gu, W. & Yushin, G. (2014). Review of nanostructured carbon materials for electrochemical capacitor applications: advantages and limitations of activated carbon, carbide-derived carbon, zeolite-templated carbon, carbon aerogels, carbon nanotubes, onion-like carbon, and graphene. *Wiley Interdisciplinary Reviews: Energy and Environment*. 3 (5). p.pp. 424–473.
- Gu, X., Qi, W., Xu, X., Sun, Z., Zhang, L., Liu, W., Pan, X. & Su, D. (2014). Covalently functionalized carbon nanotube supported Pd nanoparticles for catalytic reduction of 4-nitrophenol. *Nanoscale*. 6 (12). p.pp. 6609–6616.
- Guo, D., Shibuya, R., Akiba, C., Saji, S., Kondo, T. & Nakamura, J. (2016). Active sites of nitrogen-doped carbon materials for oxygen reduction reaction clarified using model catalysts. *Science*. 351 (6271). p.pp. 361–365.
- Guo, L., Liu, Q., Li, G., Shi, J., Liu, J., Wang, T. & Jiang, G. (2012). A mussel-inspired

- polydopamine coating as a versatile platform for the in situ synthesis of graphene-based nanocomposites. *Nanoscale*. 4. p.pp. 5864–5867.
- Guo, Y., He, J., Wang, T., Xue, H., Hu, Y., Li, G., Tang, J. & Sun, X. (2011). Enhanced electrocatalytic activity of platinum supported on nitrogen modified ordered mesoporous carbon. *Journal of Power Sources*. 196 (22). p.pp. 9299–9307.
- Habibi, Y. (2014). Key advances in the chemical modification of nanocelluloses. *Chemical Society reviews*. 43 (5). p.pp. 1519–1542.
- Habibi, Y., Chanzy, H. & Vignon, M.R. (2006). TEMPO-mediated surface oxidation of cellulose whiskers. *Cellulose*. 13 (6). p.pp. 679–687.
- Habibi, Y. & Dufresne, A. (2008). Highly filled bionanocomposites from functionalized polysaccharide nanocrystals. *Biomacromolecules*. 9 (7). p.pp. 1974–1980.
- Habibi, Y., Goffin, A.-L., Schiltz, N., Duquesne, E., Dubois, P. & Dufresne, A. (2008). Bionanocomposites based on poly(ϵ -caprolactone)-grafted cellulose nanocrystals by ring-opening polymerization. *Journal of Materials Chemistry*. 18 (41). p.pp. 5002–5010.
- Habibi, Y., Hoeger, I., Kelley, S.S. & Rojas, O.J. (2010a). Development of Langmuir - Schaeffer cellulose nanocrystal monolayers and their interfacial behaviors. *Langmuir*. 26 (2). p.pp. 990–1001.
- Habibi, Y., Lucia, L.A. & Rojas, O.J. (2010b). Cellulose nanocrystals: chemistry, self-assembly, and applications. *Chemical Reviews*. 110 (6). p.pp. 3479–3500.
- Hagen, J. (2006). *Industrial Catalysis: A Practical Approach: Second Edition*.
- Han, J., Xu, G., Ding, B., Pan, J., Dou, H. & MacFarlane, D.R. (2014). Porous nitrogen-doped hollow carbon spheres derived from polyaniline for high performance supercapacitors. *Journal of Materials Chemistry A*. 2 (15). p.pp. 5352–5357.
- Han, S., Sohn, K. & Hyeon, T. (2000). Fabrication of new nanoporous carbons through silica templates and their application to the adsorption of bulky dyes. *Chemistry of Materials*. 12 (10). p.pp. 3337–3341.
- Han, Y.Q., Ding, B. & Zhang, X.G. (2010). Preparation of Graphene/polypyrrole Composites for Electrochemical Capacitors. *Journal of New Materials for Electrochemical Systems*. 13 (4). p.pp. 315–320.
- Hao, L., Zhu, C., Chen, C., Kang, P., Hu, Y., Fan, W. & Chen, Z. (2003). Fabrication of silica core-conductive polymer polypyrrole shell composite particles and polypyrrole capsule on monodispersed silica templates. *Synthetic Metals*. 139 (2). p.pp. 391–396.
- Hasegawa, G., Aoki, M., Kanamori, K., Nakanishi, K., Hanada, T. & Tadanaga, K. (2011).

Monolithic electrode for electric double-layer capacitors based on macro/meso/microporous S-Containing activated carbon with high surface area. *Journal of Materials Chemistry*. 21 (7). p.pp. 2060–2063.

He, D., Jiang, Y., Lv, H., Pan, M. & Mu, S. (2013). Nitrogen-doped reduced graphene oxide supports for noble metal catalysts with greatly enhanced activity and stability. *Applied Catalysis B: Environmental*. 132-133. p.pp. 379–388.

He, W., Jiang, C., Wang, J. & Lu, L. (2014a). High-rate oxygen electroreduction over graphitic-N species exposed on 3D hierarchically porous nitrogen-doped carbons. *Angewandte Chemie - International Edition*. 53 (36). p.pp. 9503–9507.

He, X., Xiao, Q., Lu, C., Wang, Y., Zhang, X., Zhao, J., Zhang, W., Zhang, X. & Deng, Y. (2014b). Uniaxially aligned electrospun all-cellulose nanocomposite nanofibers reinforced with cellulose nanocrystals: Scaffold for tissue engineering. *Biomacromolecules*. 15 (2). p.pp. 618–627.

Hervés, P., Pérez-Lorenzo, M., Liz-Marzán, L.M., Dzubiella, J., Lu, Y. & Ballauff, M. (2012). Catalysis by metallic nanoparticles in aqueous solution: model reactions. *Chemical Society Reviews*. 41 (17) p.pp. 5577–5587.

Higgins, D.C., Wang, R., Hoque, M.A., Zamani, P., Abureden, S. & Chen, Z. (2014). Morphology and composition controlled platinum-cobalt alloy nanowires prepared by electrospinning as oxygen reduction catalyst. *Nano Energy*. 10. p.pp. 135–143.

Hirata, T., Kawamoto, S. & Okuro, A. (1991). Pyrolysis of melamine-formaldehyde and urea-formaldehyde resins. *Journal of Applied Polymer Science*. 42 (12). p.pp. 3147–3163.

Hoa, L.T., Sun, K.G. & Hur, S.H. (2015). Highly sensitive non-enzymatic glucose sensor based on Pt nanoparticle decorated graphene oxide hydrogel. *Sensors and Actuators, B: Chemical*. 210. p.pp. 618–623.

Hong, W.T., Risch, M., Stoerzinger, K.A., Grimaud, A., Suntivich, J. & Shao-Horn, Y. (2015). Toward the rational design of non-precious transition metal oxides for oxygen electrocatalysis. *Energy & Environmental Science*. 8 (5). p.pp. 1404–1427.

Horváth, I. (2003). Encyclopedia of catalysis. *Encyclopedia of catalysis*.

Hossain, K.M.Z., Ahmed, I., Parsons, A.J., Scotchford, C. a., Walker, G.S., Thielemans, W. & Rudd, C.D. (2012). Physico-chemical and mechanical properties of nanocomposites prepared using cellulose nanowhiskers and poly(lactic acid). *Journal of Materials Science*. 47 (6). p.pp. 2675–2686.

Hou, J., Cao, C., Idrees, F. & Ma, X. (2015). Hierarchical Porous Nitrogen-Doped Carbon Nanosheets Derived from Silk for Ultrahigh-Capacity Battery Anodes and Supercapacitors. *ACS nano*. 9 (3). p.pp. 2556–2564.

- Hou, P.-X., Orikasa, H., Yamazaki, T., Matsuoka, K., Tomita, A., Setoyama, N., Fukushima, Y. & Kyotani, T. (2005). Synthesis of Nitrogen-Containing Microporous Carbon with a Highly Ordered Structure and Effect of Nitrogen Doping on H₂O Adsorption. *Chemistry of Materials*. 17 (20). p.pp. 5187–5193.
- Hsieh, C.T. & Teng, H. (2002). Influence of oxygen treatment on electric double-layer capacitance of activated carbon fabrics. *Carbon*. 40 (5). p.pp. 667–674.
- Hsu, F.-H. & Wu, T.-M. (2012). In situ synthesis and characterization of conductive polypyrrole/graphene composites with improved solubility and conductivity. *Synthetic Metals*. 162 (7-8). p.pp. 682–687.
- Hu, Y., Niu, X., Zhao, H., Tang, J. & Lan, M. (2015). Enzyme-Free Amperometric Detection of Glucose on Platinum-Replaced Porous Copper Frameworks. *Electrochimica Acta*. 165. p.pp. 383–389.
- Huang, Z., Wang, P. C., MacDiarmid, A. G., Xia, Y., Whitesides, G. (1997). Selective deposition of conducting polymers on hydroxyl-terminated surfaces with printed monolayers of alkylsiloxanes as templates. *Langmuir*. 13 (24). p.pp. 6480–6484.
- Huang, J., Ichinose, I. & Kunitake, T. (2005). Nanocoating of natural cellulose fibers with conjugated polymer: hierarchical polypyrrole composite materials. *Chemical Communications*. (13). p.pp. 1717–1719.
- Huang, L.M., Wen, T.C. & Gopalan, A. (2006). Electrochemical and spectroelectrochemical monitoring of supercapacitance and electrochromic properties of hydrous ruthenium oxide embedded poly (3,4-ethylenedioxythiophene)-poly (styrene sulfonic acid) composite. *Electrochimica Acta*. 51 (17). p.pp. 3469–3476.
- Hulicova, D., Yamashita, J., Soneda, Y., Hatori, H. & Kodama, M. (2005). Supercapacitors prepared from melamine-based carbon. *Chemistry of Materials*. 17 (5). p.pp. 1241–1247.
- Hulicova-Jurcakova, D., Seredych, M., Lu, G.Q. & Bandosz, T.J. (2009). Combined effect of nitrogen- and oxygen-containing functional groups of microporous activated carbon on its electrochemical performance in supercapacitors. *Advanced Functional Materials*. 19 (3). p.pp. 438–447.
- Ibrahim, H., Ilinca, A. & Perron, J. (2008). Energy storage systems-Characteristics and comparisons. *Renewable and Sustainable Energy Reviews*. 12 (5) p.pp. 1221–1250.
- Isayev, O., Rasulev, B., Gorb, L. & Leszczynski, J. (2006). Structure-toxicity relationships of nitroaromatic compounds. *Molecular Diversity*. 10 (2). p.pp. 233–245.
- Isogai, A. & Kato, Y. (1998). Preparation of polyuronic acid from cellulose by TEMPO-mediated oxidation. *Cellulose*. 5 (3). p.pp. 153–164.

- Jackson, J.K., Letchford, K., Wasserman, B.Z., Ye, L., Hamad, W.Y. & Burt, H.M. (2011). The use of nanocrystalline cellulose for the binding and controlled release of drugs. *International journal of nanomedicine*. 6. p.pp. 321–330.
- Jang, J. (2006). Conducting polymer nanomaterials and their applications. In: *Emissive Materials Nanomaterials*. Springer, pp. 189–260.
- Jeon, J.W., Sharma, R., Meduri, P., Arey, B.W., Schaef, H.T., Lutkenhaus, J.L., Lemmon, J.P., Thallapally, P.K., Nandasiri, M.I., McGrail, B.P. & Nune, S.K. (2014). In situ one-step synthesis of hierarchical nitrogen-doped porous carbon for high-performance supercapacitors. *ACS Applied Materials and Interfaces*. 6 (10). p.pp. 7214–7222.
- Ji, X., Lee, K.T. & Nazar, L.F. (2009). A highly ordered nanostructured carbon-sulphur cathode for lithium-sulphur batteries. *Nature materials*. 8 (6). p.pp. 500–506.
- Jiang, Y., Zhang, J., Qin, Y.-H., Niu, D.-F., Zhang, X.-S., Niu, L., Zhou, X.-G., Lu, T.-H. & Yuan, W.-K. (2011). Ultrasonic synthesis of nitrogen-doped carbon nanofibers as platinum catalyst support for oxygen reduction. *Journal of Power Sources*. 196 (22). p.pp. 9356–9360.
- Jiao, Y., Zheng, Y., Jaroniec, M. & Qiao, S.Z. (2014). Origin of the electrocatalytic oxygen reduction activity of graphene-based catalysts: A roadmap to achieve the best performance. *Journal of the American Chemical Society*. 136 (11). p.pp. 4394–4403.
- Joo, S.H., Choi, S.J., Oh, I., Kwak, J., Liu, Z., Terasaki, O. & Ryoo, R. (2001). Ordered nanoporous arrays of carbon supporting high dispersions of platinum nanoparticles. *Nature*. 412 (6843). p.pp. 169–172.
- Ju, M.J., Kim, J.C., Choi, H.J., Choi, I.T., Kim, S.G., Lim, K., Ko, J., Lee, J.J., Jeon, I.Y., Baek, J.B. & Kim, H.K. (2013). N-doped graphene nanoplatelets as superior metal-free counter electrodes for organic dye-sensitized solar cells. *ACS Nano*. 7 (6). p.pp. 5243–5250.
- Julkapli, N.M. & Bagheri, S. (2015). Graphene supported heterogeneous catalysts: An overview. *International Journal of Hydrogen Energy*. 40 (2) p.pp. 948–979.
- Junior de Menezes, A., Siqueira, G., Curvelo, a. a S. & Dufresne, A. (2009). Extrusion and characterization of functionalized cellulose whiskers reinforced polyethylene nanocomposites. *Polymer*. 50 (19). p.pp. 4552–4563.
- Jurewicz, K., Babcik, K., Ziolkowski, A. & Wachowska, H. (2004). Capacitance behaviour of the ammoniated coal. In: *Journal of Physics and Chemistry of Solids*. 2004, pp. 269–273.
- Jurewicz, K., Pietrzak, R., Nowicki, P. & Wachowska, H. (2008). Capacitance behaviour of brown coal based active carbon modified through chemical reaction with urea. *Electrochimica Acta*. 53 (16). p.pp. 5469–5475.
- K. Jurewicz, S. Delpeux, V. Bertagna, F. Beguin, E. Frackowiak (2001). Supercapacitors from

- nanotubes/polypyrrole composites. *J. Power Sources*. 822. p.pp. 97–98.
- Kan, K.H.M., Li, J., Wijesekera, K. & Cranston, E.D. (2013). Polymer-grafted cellulose nanocrystals as pH-responsive reversible flocculants. *Biomacromolecules*. 14 (9). p.pp. 3130–3139.
- Kang, J., Li, O.L. & Saito, N. (2013). A simple synthesis method for nano-metal catalyst supported on mesoporous carbon: the solution plasma process. *Nanoscale*. 5 (15). p.pp. 6874–6882.
- Kang, Y.J., Kim, B., Chung, H. & Kim, W. (2010). Fabrication and characterization of flexible and high capacitance supercapacitors based on MnO₂/CNT/papers. *Synthetic Metals*. 160 (23-24). p.pp. 2510–2514.
- Karn, B. (2008). The road to green nanotechnology. *Journal of Industrial Ecology*. 12 (3) p.pp. 263–266.
- Kaufman, J., Colaneri, N., Scott, J. & Street, G. (1984). Evolution of Polaron States into Bipolarons in Polypyrrole. *Physical Review Letters*. 53 (10). p.pp. 1005–1008.
- Khudhayer, W.J., Kariuki, N.N., Wang, X., Myers, D.J., Shaikh, A.U. & Karabacak, T. (2011). Oxygen Reduction Reaction Electrocatalytic Activity of Glancing Angle Deposited Platinum Nanorod Arrays. *Journal of The Electrochemical Society*. 158 (8). p.pp. B1029–B1041.
- Kim, D.Y., Lee, J.Y., Moon, D.K. & Kim, C.Y. (1995). Stability of reduced polypyrrole. *Synthetic Metals*. 69 (1–3). p.pp. 471–474.
- Kim, J., Montero, G., Habibi, Y., Hinestroza, J.P., Genzer, J., Argyropoulos, D.S. & Rojas, O.J. (2009). Dispersion of cellulose crystallites by nonionic surfactants in a hydrophobic polymer matrix. *Polymer Engineering & Science*. 49 (10). p.pp. 2054–2061.
- Kim, N.D., Kim, W., Joo, J.B., Oh, S., Kim, P., Kim, Y. & Yi, J. (2008). Electrochemical capacitor performance of N-doped mesoporous carbons prepared by ammoniation. *Journal of Power Sources*. 180 (1). p.pp. 671–675.
- Kim, Y.J., Abe, Y., Yanagiura, T., Park, K.C., Shimizu, M., Iwazaki, T., Nakagawa, S., Endo, M. & Dresselhaus, M.S. (2007). Easy preparation of nitrogen-enriched carbon materials from peptides of silk fibroins and their use to produce a high volumetric energy density in supercapacitors. *Carbon*. 45 (10). p.pp. 2116–2125.
- Klemm, D., Philipp, B., Heinze, T., Heinze, U. & Wagenknecht, W. (2004). *General Considerations on Structure and Reactivity of Cellulose: Section 2.1–2.1. 4*. Wiley Online Library.
- Kloke, A., Biller, B., Kräling, U., Kerzenmacher, S., Zengerle, R. & Von Stetten, F. (2011). A single layer glucose fuel cell intended as power supplying coating for medical implants. *Fuel Cells*. 11 (2). p.pp. 316–326.

- Koga, H., Saito, T., Kitaoka, T., Nogi, M., Suganuma, K. & Isogai, A. (2013). Transparent, conductive, and printable composites consisting of TEMPO-oxidized nanocellulose and carbon nanotube. *Biomacromolecules*. 14 (4). p.pp. 1160–1165.
- Koga, H., Tokunaga, E., Hidaka, M., Umemura, Y., Saito, T., Isogai, A. & Kitaoka, T. (2010). Topochemical synthesis and catalysis of metal nanoparticles exposed on crystalline cellulose nanofibers. *Chemical communications (Cambridge, England)*. 46. p.pp. 8567–8569.
- Köhler, C., Frei, M., Zengerle, R. & Kerzenmacher, S. (2014). Performance Loss of a Pt-Based Implantable Glucose Fuel Cell in Simulated Tissue and Cerebrospinal Fluids. *ChemElectroChem*. 1 (11). p.pp. 1895–1900.
- Köhnke, T., Lin, A., Elder, T., Theliander, H. & Ragauskas, A.J. (2012). Nanoreinforced xylan-cellulose composite foams by freeze-casting. *Green Chemistry*. 14 (7). p.pp. 1864–1869.
- Kötz, R. & Carlen, M. (2000). Principles and applications of electrochemical capacitors. *Electrochimica Acta*. 45 (15). p.pp. 2483–2498.
- Kricheldorf, H.R., Nuyken, O. & Swift, G. (2005). GBA466581 bnbPlastics engineering ; 70Previous ed. published in two volumes: c1992. Includes bibliographical references and index. Formerly CIP. Uk. *Handbook of polymer synthesis*. 2nd ed. New York, Great Britain: Marcel Dekker.
- Ku, K., Kim, B., Chung, H. & Kim, W. (2010). Characterization of graphene-based supercapacitors fabricated on Al foils using Au or Pd thin films as interlayers. *Synthetic Metals*. 160 (23-24). p.pp. 2613–2617.
- Kumar, B., Asadi, M., Pisasale, D., Sinha-Ray, S., Rosen, B. a, Haasch, R., Abiade, J., Yarin, A.L. & Salehi-Khojin, A. (2013). Renewable and metal-free carbon nanofibre catalysts for carbon dioxide reduction. *Nature communications*. 4. p.p. 2819.
- Kwon, T., Nishihara, H., Itoi, H., Yang, Q.H. & Kyotani, T. (2009). Enhancement mechanism of electrochemical capacitance in nitrogen-boron-doped carbons with uniform straight nanochannels. *Langmuir*. 25 (19). p.pp. 11961–11968.
- L.Nyholm, G.Nystrom, A. Mihranyan, and M. Stromme (2011). Toward Flexible Polymer and Paper-Based Energy Storage Devices. *Advanced Materials*. 23. p.pp. 3751–3769.
- La, Y., Park, C., Shin, T.J., Joo, S.H., Kang, S. & Kim, K.T. (2014). Colloidal inverse bicontinuous cubic membranes of block copolymers with tunable surface functional groups. *Nature chemistry*. 6 (6). p.pp. 534–541.
- Laforgue, A., Simon, P., Fauvarque, J.F., Mastragostino, M., Soavi, F., Sarrau, J.F., Lailler, P., Conte, M., Rossi, E. & Saguatti, S. (2003). Activated carbon/conducting polymer hybrid supercapacitors. *Journal of The Electrochemical Society*. 150 (5). p.pp. A645–A651.

- Lam, E., Hrapovic, S., Majid, E., Chong, J.H. & Luong, J.H.T. (2012). Catalysis using gold nanoparticles decorated on nanocrystalline cellulose. *Nanoscale*. 4 (3). p.pp. 997–1002.
- Lascelles, S.F. & Armes, S.P. (1997). Synthesis and characterization of micrometre-sized, polypyrrole-coated polystyrene latexes. *Journal of Materials Chemistry*. 7 (8). p.pp. 1339–1347.
- Lee, J., Yoon, S., Hyeon, T., Oh, S.M. & Kim, K.B. (1999). Synthesis of a new mesoporous carbon and its application to electrochemical double-layer capacitors. *Chemical Communications*. (21). p.pp. 2177–2178.
- Lee, K.R., Lee, K.U., Lee, J.W., Ahn, B.T. & Woo, S.I. (2010). Electrochemical oxygen reduction on nitrogen doped graphene sheets in acid media. *Electrochemistry Communications*. 12 (8). p.pp. 1052–1055.
- Lee, W.J., Maiti, U.N., Lee, J.M., Lim, J., Han, T.H. & Kim, S.O. (2014). Nitrogen-doped carbon nanotubes and graphene composite structures for energy and catalytic applications. *Chemical communications (Cambridge, England)*. 50 (52). p.pp. 6818–6830.
- Lee, Y.H., Lee, Y.F., Chang, K.H. & Hu, C.C. (2011). Synthesis of N-doped carbon nanosheets from collagen for electrochemical energy storage/conversion systems. *Electrochemistry Communications*. 13 (1). p.pp. 50–53.
- Lee, Y.J. & Park, J.Y. (2011). A coral-like macroporous gold-platinum hybrid 3D electrode for enzyme-free glucose detection. *Sensors and Actuators, B: Chemical*. 155 (1). p.pp. 134–139.
- Li, C., Wang, H. & Yamauchi, Y. (2013a). Electrochemical Deposition of Mesoporous Pt–Au Alloy Films in Aqueous Surfactant Solutions: Towards a Highly Sensitive Amperometric Glucose Sensor. *Chemistry – A European Journal*. 19 (7). p.pp. 2242–2246.
- Li, H., Cheng, L. & Xia, Y. (2005). A hybrid electrochemical supercapacitor based on a 5 V Li-ion battery cathode and active carbon. *Electrochemical and Solid-State Letters*. 8 (9). p.pp. A433–A436.
- Li, H., Han, L., Cooper-White, J. & Kim, I. (2012a). Palladium nanoparticles decorated carbon nanotubes: facile synthesis and their applications as highly efficient catalysts for the reduction of 4-Li, H., Han, L., Cooper-White, J. & Kim, I. (2012). Palladium nanoparticles decorated carbon nanotubes: facile. *Green Chemistry*. 14 (3). p.pp. 586–591.
- Li, H., Liao, J., Du, Y., You, T., Liao, W. & Wen, L. (2013b). Magnetic-field-induced deposition to fabricate multifunctional nanostructured Co, Ni, and CoNi alloy films as catalysts, ferromagnetic and superhydrophobic materials. *Chem Commun (Camb)*. 49 (17). p.pp. 1768–1770.
- Li, J., Qian, X.R., Chen, J.H., Ding, C.Y. & An, X.H. (2010a). Conductivity decay of cellulose–polypyrrole conductive paper composite prepared by in situ polymerization method.

Carbohydrate Polymers. 82 (2). p.pp. 504–509.

- Li, L., Liu, E., Li, J., Yang, Y., Shen, H., Huang, Z., Xiang, X. & Li, W. (2010b). A doped activated carbon prepared from polyaniline for high performance supercapacitors. *Journal of Power Sources.* 195 (5). p.pp. 1516–1521.
- Li, M.-C., Wu, Q., Song, K., Lee, S., Qing, Y. & Wu, Y. (2015). Cellulose Nanoparticles: Structure–Morphology–Rheology Relationships. *ACS Sustainable Chemistry & Engineering.* 3 (5). p.pp. 821–832.
- Li, T., Yang, G., Wang, J., Zhou, Y. & Han, H. (2013c). Excellent electrochemical performance of nitrogen-enriched hierarchical porous carbon electrodes prepared using nano-CaCO₃ as template. *Journal of Solid State Electrochemistry.* 17 (10). p.pp. 2651–2660.
- Li, W., Kuai, L., Chen, L. & Geng, B. (2013d). ‘Re-growth etching’ to large-sized porous gold nanostructures. *Scientific reports.* 3. p.p. 2377.
- Li, W., Liang, C., Zhou, W., Qiu, J., Sun, G. & Xin, Q. (2003). Preparation and Characterization of Multiwalled Carbon Nanotube-Supported Platinum for Cathode Catalysts of Direct Methanol Fuel Cells. *The Journal of Physical Chemistry B.* 107 (26). p.pp. 6292–6299.
- Li, W., Wu, Z., Wang, J., Elzatahry, A.A. & Zhao, D. (2014). A perspective on mesoporous TiO₂ materials. *Chemistry of Materials.* 26 (1) p.pp. 287–298.
- Li, X., Park, S. & Popov, B.N. (2010c). Highly stable Pt and PtPd hybrid catalysts supported on a nitrogen-modified carbon composite for fuel cell application. *Journal of Power Sources.* 195 (2). p.pp. 445–452.
- Li, X.-H. & Antonietti, M. (2013). Metal nanoparticles at mesoporous N-doped carbons and carbon nitrides: functional Mott-Schottky heterojunctions for catalysis. *Chemical Society reviews.* 42 (16). p.pp. 6593–6604.
- Li, Y.M., van Zijll, M., Chiang, S. & Pan, N. (2011). KOH modified graphene nanosheets for supercapacitor electrodes. *Journal of Power Sources.* 196 (14). p.pp. 6003–6006.
- Li, Z., Liu, J., Xia, C. & Li, F. (2013e). Nitrogen-Functionalized Ordered Mesoporous Carbons as Multifunctional Supports of Ultrasmall Pd Nanoparticles for Hydrogenation of Phenol. *ACS Catalysis.* 3 (11). p.pp. 2440–2448.
- Li, Z., Zhang, L., Amirkhiz, B.S., Tan, X., Xu, Z., Wang, H., Olsen, B.C., Holt, C.M.B. & Mitlin, D. (2012b). Carbonized chicken eggshell membranes with 3D architectures as high-performance electrode materials for supercapacitors. *Advanced Energy Materials.* 2 (4). p.pp. 431–437.
- Liang, C., Li, Z. & Dai, S. (2008). Mesoporous carbon materials: Synthesis and modification. *Angewandte Chemie - International Edition.* 47 (20) p.pp. 3696–3717.

- Liang, H.W., Wei, W., Wu, Z.S., Feng, X. & Müllen, K. (2013a). Mesoporous metal-nitrogen-doped carbon electrocatalysts for highly efficient oxygen reduction reaction. *Journal of the American Chemical Society*. 135 (43). p.pp. 16002–16005.
- Liang, J., Du, X., Gibson, C., Du, X.W. & Qiao, S.Z. (2013b). N-doped graphene natively grown on hierarchical ordered porous carbon for enhanced oxygen reduction. *Advanced Materials*. 25 (43). p.pp. 6226–6231.
- Liang, J., Jiao, Y., Jaroniec, M. & Qiao, S.Z. (2012). Sulfur and nitrogen dual-doped mesoporous graphene electrocatalyst for oxygen reduction with synergistically enhanced performance. *Angewandte Chemie - International Edition*. 51 (46). p.pp. 11496–11500.
- Liew, S.Y., Thielemans, W. & Walsh, D.A. (2010). Electrochemical Capacitance of Nanocomposite Polypyrrole/Cellulose Films. *Journal of Physical Chemistry C*. 114 (41). p.pp. 17926–17933.
- Liew, S.Y., Walsh, D. a. & Thielemans, W. (2013). High total-electrode and mass-specific capacitance cellulose nanocrystal-polypyrrole nanocomposites for supercapacitors. *RSC Advances*. 3 (24). p.pp. 9158–9162.
- Lin, N. & Dufresne, A. (2013). Supramolecular hydrogels from in situ host-guest inclusion between chemically modified cellulose nanocrystals and cyclodextrin. *Biomacromolecules*. 14 (3). p.pp. 871–880.
- Lin, N. & Dufresne, A. (2014). Surface chemistry, morphological analysis and properties of cellulose nanocrystals with gradiended sulfation degrees. *Nanoscale*. 6 (10). p.pp. 5384–5393.
- Lin, N., Huang, J., Chang, P.R., Feng, J. & Yu, J. (2011a). Surface acetylation of cellulose nanocrystal and its reinforcing function in poly(lactic acid). *Carbohydrate Polymers*. 83 (4). p.pp. 1834–1842.
- Lin, N., Huang, J., Chang, P.R., Feng, L. & Yu, J. (2011b). Effect of polysaccharide nanocrystals on structure, properties, and drug release kinetics of alginate-based microspheres. *Colloids and Surfaces B: Biointerfaces*. 85 (2). p.pp. 270–279.
- Lin, N., Huang, J. & Dufresne, A. (2012). Preparation, properties and applications of polysaccharide nanocrystals in advanced functional nanomaterials: a review. *Nanoscale*. 4 (11). p.pp. 3274–3294.
- Lin, Z., Liu, Y., Yao, Y., Hildreth, O.J., Li, Z., Moon, K. & Wong, C.P. (2011c). Superior capacitance of functionalized graphene. *Journal of Physical Chemistry C*. 115 (14). p.pp. 7120–7125.
- Ling, T.R., Li, C.S., Jow, J.J. & Lee, J.F. (2011). Mesoporous nickel electrodes plated with gold for the detection of glucose. *Electrochimica Acta*. 56 (3). p.pp. 1043–1050.
- Liu, C., Yu, Z., Neff, D., Zhamu, A. & Jang, B.Z. (2010a). Graphene-based supercapacitor with an

ultrahigh energy density. *Nano Letters*. 10 (12). p.pp. 4863–4868.

Liu, D., Zhang, X., Sun, Z. & You, T. (2013a). Free-standing nitrogen-doped carbon nanofiber films as highly efficient electrocatalysts for oxygen reduction. *Nanoscale*. 5 (20). p.pp. 9528–9531.

Liu, G., Li, X., Ganesan, P. & Popov, B.N. (2010b). Studies of oxygen reduction reaction active sites and stability of nitrogen-modified carbon composite catalysts for PEM fuel cells. *Electrochimica Acta*. 55 (8). p.pp. 2853–2858.

Liu, H., Wang, D., Shang, S. & Song, Z. (2011a). Synthesis and characterization of Ag-Pd alloy nanoparticles/carboxylated cellulose nanocrystals nanocomposites. *Carbohydrate Polymers*. 83 (1). p.pp. 38–43.

Liu, H., Wang, D., Song, Z. & Shang, S. (2011b). Preparation of silver nanoparticles on cellulose nanocrystals and the application in electrochemical detection of DNA hybridization. *Cellulose*. 18 (1). p.pp. 67–74.

Liu, J., Czerw, R. & Carroll, D.L. (2005). Large-scale synthesis of highly aligned nitrogen doped carbon nanotubes by injection chemical vapor deposition methods. *Journal of Materials Research*. 20 (02). p.pp. 538–543.

Liu, J., Liu, Y., Liu, N., Han, Y., Zhang, X., Huang, H., Lifshitz, Y., Lee, S.-T., Zhong, J. & Kang, Z. (2015a). Metal-free efficient photocatalyst for stable visible water splitting via a two-electron pathway. *Science*. 347 (6225). p.pp. 970–974.

Liu, L., Deng, Q.-F., Ma, T.-Y., Lin, X.-Z., Hou, X.-X., Liu, Y.-P. & Yuan, Z.-Y. (2011c). Ordered mesoporous carbons: citric acid-catalyzed synthesis, nitrogen doping and CO₂ capture. *Journal of Materials Chemistry*. 21 (40). p.pp. 16001–16009.

Liu, M., Qian, J., Zhao, Y., Zhu, D., Gan, L. & Chen, L. (2015b). Core-shell ultramicroporous@microporous carbon nanospheres as advanced supercapacitor electrodes. *Journal of Materials Chemistry A*. 3 (21). p.pp. 11517–11526.

Liu, R., Cho, S. Il & Lee, S.B. (2008). Poly (3, 4-ethylenedioxythiophene) nanotubes as electrode materials for a high-powered supercapacitor. *Nanotechnology*. 19 (21). p.p. 215710.

Liu, R., Wu, D., Feng, X. & Müllen, K. (2010c). Nitrogen-doped ordered mesoporous graphitic arrays with high electrocatalytic activity for oxygen reduction. *Angewandte Chemie (International ed. in English)*. 49. p.pp. 2565–2569.

Liu, T., Finn, L., Yu, M., Wang, H., Zhai, T., Lu, X., Tong, Y. & Li, Y. (2014). Polyaniline and Polypyrrole Pseudocapacitor Electrodes with Excellent Cycling Stability. *Nano Letters*. 14 (5). p.pp. 2522–2527.

Liu, Y., Ding, Y., Zhang, Y. & Lei, Y. (2012a). Pt-Au nanocorals, Pt nanofibers and Au microparticles prepared by electrospinning and calcination for nonenzymatic glucose sensing

in neutral and alkaline environment. *Sensors and Actuators, B: Chemical*. 171-172. p.pp. 954–961.

Liu, Y., Li, Y., Yang, G., Zheng, X. & Zhou, S. (2015c). Multi-stimulus-responsive shape-memory polymer nanocomposite network cross-linked by cellulose nanocrystals. *ACS Applied Materials and Interfaces*. 7 (7). p.pp. 4118–4126.

Liu, Y., Zhao, Y., Sun, B. & Chen, C. (2013b). Understanding the toxicity of carbon nanotubes. *Accounts of Chemical Research*. 46 (3). p.pp. 702–713.

Liu, Y.C. (2004). Characteristics of vibration modes of polypyrrole on surface-enhanced Raman scattering spectra. *Journal of Electroanalytical Chemistry*. 571 (2). p.pp. 255–264.

Liu, Z., Zhang, C., Luo, L., Chang, Z. & Sun, X. (2012b). One-pot synthesis and catalyst support application of mesoporous N-doped carbonaceous materials. *Journal of Materials Chemistry*. 22 (24). p.pp. 12149–12154.

Long, C., Qi, D., Wei, T., Yan, J., Jiang, L. & Fan, Z. (2014). Nitrogen-Doped Carbon Networks for High Energy Density Supercapacitors Derived from Polyaniline Coated Bacterial Cellulose. *Advanced Functional Materials*. 24 (25). p.pp. 3953–3961.

Lota, G., Lota, K. & Frackowiak, E. (2007). Nanotubes based composites rich in nitrogen for supercapacitor application. *Electrochemistry Communications*. 9 (7). p.pp. 1828–1832.

Lota, K., Khomenko, V. & Frackowiak, E. (2004). Capacitance properties of poly (3, 4-ethylenedioxythiophene)/carbon nanotubes composites. *Journal of Physics and Chemistry of Solids*. 65 (2). p.pp. 295–301.

Lovett, J.R., Fielding, L. a., Armes, S.P. & Buxton, R. (2014). One-Pot Preparation of Conducting Polymer-Coated Silica Particles: Model Highly Absorbing Aerosols. *Advanced Functional Materials*. 24 (9). p.pp. 1290–1299.

Lowinsohn, D., Lee, P.T. & Compton, R.G. (2014). Electrocatalytic detection of glutathione - the search for new mediators. *Journal of the Brazilian Chemical Society*. 25. p.pp. 1614–1620.

Lozano-Castello, D., Lozano-Castello, D., Cazorla-Amoros, D., Cazorla-Amoros, D., Linares-Solano, a, Linares-Solano, a, Shiraishi, S., Shiraishi, S., Kurihara, H., Kurihara, H., Oya, a & Oya, a (2003). Influence of pore structure and surface chemistry on electric double layer capacitance in non-aqueous electrolyte. *Carbon*. 41. p.pp. 1765–1775.

Lu, A., Kiefer, A., Schmidt, W. & Schüth, F. (2004). Synthesis of Polyacrylonitrile-Based Ordered Mesoporous Carbon with Tunable Pore Structures. *Chemistry of Materials*. 16 (1). p.pp. 100–103.

Lu, A.H. & Schüth, F. (2006). Nanocasting: A versatile strategy for creating nanostructured porous materials. *Advanced Materials*. 18 (14). p.pp. 1793–1805.

- Lu, J., Bo, X., Wang, H. & Guo, L. (2013). Nitrogen-doped ordered mesoporous carbons synthesized from honey as metal-free catalyst for oxygen reduction reaction. *Electrochimica Acta*. 108. p.pp. 10–16.
- Lu, X., Bian, X., Nie, G., Zhang, C., Wang, C. & Wei, Y. (2012). Encapsulating conducting polypyrrole into electrospun TiO₂ nanofibers: a new kind of nanoreactor for in situ loading Pd nanocatalysts towards p-nitrophenol hydrogenation. *Journal of Materials Chemistry*. 22 (25). p.pp. 12723–12730.
- Lu, X., Zhang, W., Wang, C., Wen, T.-C. & Wei, Y. (2011). One-dimensional conducting polymer nanocomposites: Synthesis, properties and applications. *Progress in Polymer Science*. 36 (5). p.pp. 671–712.
- Ly, B., Thielemans, W., Dufresne, A., Chaussy, D. & Belgacem, M.N. (2008). Surface functionalization of cellulose fibres and their incorporation in renewable polymeric matrices. *Composites Science and Technology*. 68 (15-16). p.pp. 3193–3201.
- Ma, X., Gan, L., Liu, M., Tripathi, P.K., Zhao, Y., Xu, Z., Zhu, D. & Chen, L. (2014). Mesoporous size controllable carbon microspheres and their electrochemical performances for supercapacitor electrodes. *Journal of Materials Chemistry A*. 2 (22). p.pp. 8407–8415.
- Ma, Y., Zhang, J., Zhang, G. & He, H. (2004). Polyaniline Nanowires on Si Surfaces Fabricated with DNA Templates. *Journal of the American Chemical Society*. 126 (22). p.pp. 7097–7101.
- Mabena, L.F., Sinha Ray, S., Mhlanga, S.D. & Coville, N.J. (2011). Nitrogen-doped carbon nanotubes as a metal catalyst support. *Applied Nanoscience*. 1 (2). p.pp. 67–77.
- Maia, G., Ticianelli, E.A. & Nart, F.C. (1994). Ftir Investigation of the Polypyrrole Oxidation in Na₂so₄ and Nano₃ Aqueous-Solutions. *Zeitschrift Fur Physikalische Chemie-International Journal of Research in Physical Chemistry & Chemical Physics*. 186 (Part_2). p.pp. 245–257.
- Maldonado, S. & Stevenson, K.J. (2005). Influence of nitrogen doping on oxygen reduction electrocatalysis at carbon nanofiber electrodes. *Journal of Physical Chemistry B*. 109. p.pp. 4707–4716.
- Mallouki, M., Tran-Van, F., Sarrazin, C., Simon, P., Daffos, B., De, A., Chevrot, C. & Fauvarque, J. (2007). Polypyrrole-Fe₂O₃ nanohybrid materials for electrochemical storage. *Journal of Solid State Electrochemistry*. 11 (3). p.pp. 398–406.
- Marcus, R.A. (1956). On the Theory of Oxidation-Reduction Reactions Involving Electron Transfer. *The Journal of Physical Chemistry*. 24. p.pp. 966–978.
- Marini, M., Pilati, F. & Pourabbas, B. (2008). Smooth Surface Polypyrrole-Silica Core-Shell Nanoparticles: Preparation, Characterization and Properties. *Macromolecular Chemistry and Physics*. 209 (13). p.pp. 1374–1380.

- Martin, C.R. (1994). Nanomaterials: A Membrane-Based Synthetic Approach. *Science*. 266 (5193). p.pp. 1961–1966.
- Masa, J., Batchelor-McAuley, C., Schuhmann, W. & Compton, R.G. (2014). Koutecky-Levich analysis applied to nanoparticle modified rotating disk electrodes: Electrocatalysis or misinterpretation. *Nano Research*. 7 (1). p.pp. 71–78.
- Mastragostino, M., Arbizzani, C. & Soavi, F. (2001). Polymer-based supercapacitors. *Journal of Power Sources*. 97–98. p.pp. 812–815.
- McCusker, L.B., Liebau, F. & Engelhardt, G. (2001). Nomenclature of structural and compositional characteristics of ordered microporous and mesoporous materials with inorganic hosts(IUPAC Recommendations 2001). *Pure and Applied Chemistry*. 73 (2). p.pp. 381–394.
- Mei, Y., Lu, Y., Polzer, F., Ballauff, M. & Drechsler, M. (2007). Catalytic activity of palladium nanoparticles encapsulated in spherical poly electrolyte brushes and core-shell microgels. *Chemistry of Materials*. 19 (5). p.pp. 1062–1069.
- de Mele, M.F.L. (1982). Potentiodynamic Study of Glucose Electro-Oxidation at Bright Platinum Electrodes. *Journal of The Electrochemical Society*. 129 (10). p.pp. 2207–2213.
- de Mele, M.F.L., Videla, H.A. & Arvia, A.J. (1982). c. *Journal of Electroanalytical Chemistry*. 141 (4). p.pp. 469–487.
- Meng, Y., Gu, D., Zhang, F., Shi, Y., Cheng, L., Feng, D., Wu, Z., Chen, Z., Wan, Y., Stein, A. & Zhao, D. (2006). A family of highly ordered mesoporous polymer resin and carbon structures from organic-organic self-assembly. *Chemistry of Materials*. 18 (18). p.pp. 4447–4464.
- Meng, Y., Gu, D., Zhang, F., Shi, Y., Yang, H., Li, Z., Yu, C., Tu, B. & Zhao, D. (2005). Ordered mesoporous polymers and homologous carbon frameworks: Amphiphilic surfactant templating and direct transformation. *Angewandte Chemie - International Edition*. 44 (43). p.pp. 7053–7059.
- Meng, Y., Voiry, D., Goswami, A., Zou, X., Huang, X., Chhowalla, M., Liu, Z. & Asefa, T. (2014). N-, O-, and S-Tridoped nanoporous carbons as selective catalysts for oxygen reduction and alcohol oxidation reactions. *Journal of the American Chemical Society*. 136 (39). p.pp. 13554–13557.
- De Mesquita, J.P., Donnici, C.L., Teixeira, I.F. & Pereira, F. V. (2012). Bio-based nanocomposites obtained through covalent linkage between chitosan and cellulose nanocrystals. *Carbohydrate Polymers*. 90 (1). p.pp. 210–217.
- Mo, Z., Liao, S., Zheng, Y. & Fu, Z. (2012). Preparation of nitrogen-doped carbon nanotube arrays and their catalysis towards cathodic oxygen reduction in acidic and alkaline media. *Carbon*,. 50 (7). p.pp. 2620–2627.

- Mohammad, F. (2007). *Specialty Polymers: Materials and Applications*. I.K. International Publishing House Pvt. Limited.
- Moon, R.J., Martini, A., Nairn, J., Simonsen, J. & Youngblood, J. (2011). Cellulose nanomaterials review: structure, properties and nanocomposites. *Chem Soc Rev.* 40 (7). p.pp. 3941–3994.
- Morère, J., Tenorio, M.J., Torralvo, M.J., Pando, C., Renuncio, J.A.R. & Cabañas, A. (2011). Deposition of Pd into mesoporous silica SBA-15 using supercritical carbon dioxide. *The Journal of Supercritical Fluids.* 56 (2). p.pp. 213–222.
- Müller, D., Rambo, C.R., D.O.S.Recouvreux, Porto, L.M. & Barra, G.M.O. (2011). Chemical in situ polymerization of polypyrrole on bacterial cellulose nanofibers. *Synthetic metals.* 161 (1–2). p.pp. 106–111.
- Muñiz, J., Marbán, G. & Fuertes, A.. (2000). Low temperature selective catalytic reduction of NO over modified activated carbon fibres. *Applied Catalysis B: Environmental.* 27 (1). p.pp. 27–36.
- Nam, G., Park, J., Kim, S.T., Shin, D. Bin, Park, N., Kim, Y., Lee, J.S. & Cho, J. (2014). Metal-free Ketjenblack incorporated nitrogen-doped carbon sheets derived from gelatin as oxygen reduction catalysts. *Nano Letters.* 14 (4). p.pp. 1870–1876.
- Ndamanisha, J.C. & Guo, L. (2009). Nonenzymatic glucose detection at ordered mesoporous carbon modified electrode. *Bioelectrochemistry.* 77 (1). p.pp. 60–63.
- Nemanich, R.J. & Solin, S.A. (1979). First- and second-order Raman scattering from finite-size crystals of graphite. *Physical Review B.* 20 (2). p.pp. 392–401.
- Nguyen, T.-D., Shopsowitz, K.E. & MacLachlan, M.J. (2014). Mesoporous nitrogen-doped carbon from nanocrystalline chitin assemblies. *Journal of Materials Chemistry A.* 2 (16). p.pp. 5915–5921.
- Nielsen, L.J., Eyley, S., Thielemans, W. & Aylott, J.W. (2010). Dual fluorescent labelling of cellulose nanocrystals for pH sensing. *Chemical communications (Cambridge, England).* 46 (47). p.pp. 8929–8931.
- Nyström, G., Mihranyan, A., Razaq, A., Lindström, T., Nyholm, L. & Strømme, M. (2010). A nanocellulose polypyrrole composite based on microfibrillated cellulose from wood. *The Journal of Physical Chemistry B.* 114 (12). p.pp. 4178–4182.
- Oh, H.-S., Oh, J.-G., Lee, W.H., Kim, H.-J. & Kim, H. (2011). The influence of the structural properties of carbon on the oxygen reduction reaction of nitrogen modified carbon based catalysts. *International Journal of Hydrogen Energy.* 36 (14). p.pp. 8181–8186.
- Öhlmann, G. (1999). Handbook of Heterogeneous Catalysis. *Zeitschrift für Physikalische Chemie.* 208. p.pp. 274–278.

- Olsson, H., Carlsson, D.O., Nystrom, G., Sjodin, M., Nyholm, L. & Stromme, M. (2012). Influence of the cellulose substrate on the electrochemical properties of paper-based polypyrrole electrode materials. *Journal of Materials Science*. 47 (13). p.pp. 5317–5325.
- Ormond-Prout, J., Dupin, D., Armes, S.P., Foster, N.J. & Burchell, M.J. (2009). Synthesis and characterization of polypyrrole-coated poly(methyl methacrylate) latex particles. *J. Mater. Chem.* 19 (10). p.pp. 1433–1442.
- Padalkar, S., Capadona, J.R., Rowan, S.J., Weder, C., Moon, R.J. & Stanciu, L. a. (2011). Self-assembly and alignment of semiconductor nanoparticles on cellulose nanocrystals. *Journal of Materials Science*. 46 (17). p.pp. 5672–5679.
- Padalkar, S., Capadona, J.R., Rowan, S.J., Weder, C., Won, Y.-H., Stanciu, L.A. & Moon, R.J. (2010). Natural Biopolymers: Novel Templates for the Synthesis of Nanostructures. *Langmuir*. 26 (11). p.pp. 8497–8502.
- Paek, E., Pak, A.J., Kweon, K.E. & Hwang, G.S. (2013). On the origin of the enhanced supercapacitor performance of nitrogen-doped graphene. *Journal of Physical Chemistry C*. 117 (11). p.pp. 5610–5616.
- Pan, F., Cao, Z., Zhao, Q., Liang, H. & Zhang, J. (2014). Nitrogen-doped porous carbon nanosheets made from biomass as highly active electrocatalyst for oxygen reduction reaction. *Journal of Power Sources*. 272. p.pp. 8–15.
- Pan, L., Qiu, H., Dou, C., Li, Y., Pu, L., Xu, J. & Shi, Y. (2010). Conducting polymer nanostructures: template synthesis and applications in energy storage. *International journal of molecular sciences*. 11 (7). p.pp. 2636–2657.
- Pang, Q., Tang, J., Huang, H., Liang, X., Hart, C., Tam, K.C. & Nazar, L.F. (2015). A Nitrogen and Sulfur Dual-Doped Carbon Derived from Polyrhodanine@ Cellulose for Advanced Lithium–Sulfur Batteries. *Advanced Materials*. 27 (39). p.pp. 6021–6028.
- Paraknowitsch, J.P. & Thomas, A. (2013). Doping carbons beyond nitrogen: an overview of advanced heteroatom doped carbons with boron, sulphur and phosphorus for energy applications. *Energy & Environmental Science*. 6 (10). p.pp. 2839–2855.
- Paraknowitsch, J.P., Zhang, Y., Wienert, B. & Thomas, A. (2013). Nitrogen- and phosphorus-co-doped carbons with tunable enhanced surface areas promoted by the doping additives. *Chemical communications (Cambridge, England)*. 49 (12). p.pp. 1208–1210.
- Park, S., Boo, H. & Chung, T.D. (2006). Electrochemical non-enzymatic glucose sensors. *Analytica Chimica Acta*. 556 (1). p.pp. 46–57.
- Park, S., Chung, T.D. & Kim, H.C. (2003). Nonenzymatic glucose detection using mesoporous platinum. *Analytical Chemistry*. 75 (13). p.pp. 3046–3049.

- Du Pasquier, A., Laforgue, A., Simon, P., Amatucci, G.G. & Fauvarque, J.-F. (2002). A Nonaqueous Asymmetric Hybrid Li₄Ti₅O₁₂/Poly (fluorophenylthiophene) Energy Storage Device. *Journal of The Electrochemical Society*. 149 (3). p.pp. A302–A306.
- Patil, A.O., Ikenoue, Y., Basescu, N., Colaneri, N., Chen, J., Wudl, F. & Heeger, A.J. (1987). Self-doped conducting polymers. *Synthetic metals*. 20 (2). p.pp. 151–159.
- Paul, S., Kim, J.H. & Kim, D.W. (2011). Cycling Performance of Supercapacitors Assembled with Polypyrrole/Multi-Walled Carbon Nanotube/Conductive Carbon Composite Electrodes. *Journal of Electrochemical Science and Technology*. 2. p.pp. 91–96.
- Pech, D., Brunet, M., Durou, H., Huang, P., Mochalin, V., Gogotsi, Y., Taberna, P.-L. & Simon, P. (2010). Ultrahigh-power micrometre-sized supercapacitors based on onion-like carbon. *Nature nanotechnology*. 5 (9). p.pp. 651–654.
- Pede, G., Iacobazzi, A., Passerini, S., Bobbio, A. & Botto, G. (2004). FC vehicle hybridisation: An affordable solution for an energy-efficient FC powered drive train. *Journal of Power Sources*. 125 (2). p.pp. 280–291.
- Pei, A., Zhou, Q. & Berglund, L. a. (2010). Functionalized cellulose nanocrystals as biobased nucleation agents in poly(l-lactide) (PLLA) - Crystallization and mechanical property effects. *Composites Science and Technology*. 70 (5). p.pp. 815–821.
- Peng, B.L., Dhar, N., Liu, H.L. & Tam, K.C. (2011). Chemistry and applications of nanocrystalline cellulose and its derivatives: A nanotechnology perspective. *The Canadian Journal of Chemical Engineering*. 89 (5). p.pp. 1191–1206.
- Peng, C., Jin, J. & Chen, G.Z. (2007). A comparative study on electrochemical co-deposition and capacitance of composite films of conducting polymers and carbon nanotubes. *Electrochimica Acta*. 53 (2). p.pp. 525–537.
- Petersson, L., Kvien, I. & Oksman, K. (2007). Structure and thermal properties of poly(lactic acid)/cellulose whiskers nanocomposite materials. *Composites Science and Technology*. 67 (11-12). p.pp. 2535–2544.
- Pinna, F. (1998). Supported metal catalysts preparation. *Catal. Today*. 41 (1-3). p.pp. 129–137.
- Pitchai-Mydeen, S.A. & Ning, Y. (2011). *Method of producing electrically conductive polymer and cellulose nanocomposites*. U.S. Paten (U.S. Patent CA 2796988).
- Place, E.S., Evans, N.D. & Stevens, M.M. (2009). Complexity in biomaterials for tissue engineering. *Nature materials*. 8 (6). p.pp. 457–470.
- Pooyan, P., Kim, I.T., Jacob, K.I., Tannenbaum, R. & Garmestani, H. (2013). Design of a cellulose-based nanocomposite as a potential polymeric scaffold in tissue engineering. *Polymer (United Kingdom)*. 54. p.pp. 2105–2114.

- Pooyan, P., Tannenbaum, R. & Garmestani, H. (2012). Mechanical behavior of a cellulose-reinforced scaffold in vascular tissue engineering. *Journal of the Mechanical Behavior of Biomedical Materials*. 7. p.pp. 50–59.
- Pyun, S.-I., Shin, H.-C., Lee, J.-W. & Go, J.-Y. (2012). *Electrochemistry of insertion materials for hydrogen and lithium*. Springer Science & Business Media.
- Qin, C.L., Lu, X., Yin, G.P., Bai, X.D. & Jin, Z. (2009). Activated nitrogen-enriched carbon/carbon aerogel nanocomposites for supercapacitor applications. *Transactions of Nonferrous Metals Society of China*. 19. p.pp. S738–S742.
- Rajarathnam, D. (1953). Instrumental Chemical Analysis. *Analytical Chemistry*. 25 (6). p.pp. 998–998.
- Rajender Reddy, K., Kumar, N.S., Surendra Reddy, P., Sreedhar, B. & Lakshmi Kantam, M. (2006). Cellulose supported palladium(0) catalyst for Heck and Sonogashira coupling reactions. *Journal of Molecular Catalysis A: Chemical*. 252 (1-2). p.pp. 12–16.
- Ramya, R., Sivasubramanian, R. & Sangaranarayanan, M. V (2013). Conducting polymers-based electrochemical supercapacitors—Progress and prospects. *Electrochimica Acta*. 101. p.pp. 109–129.
- Ranby, B.G. (1951). Fibrous macromolecular systems. Cellulose and muscle. The colloidal properties of cellulose micelles. *Discuss. Faraday Soc.* 11. p.pp. 158–164.
- Rathod, D., Dickinson, C., Egan, D. & Dempsey, E. (2010). Platinum nanoparticle decoration of carbon materials with applications in non-enzymatic glucose sensing. *Sensors and Actuators, B: Chemical*. 143 (2). p.pp. 547–554.
- Raymundo-Piñero, E., Leroux, F. & Béguin, F. (2006). A high-performance carbon for supercapacitors obtained by carbonization of a seaweed biopolymer. *Advanced Materials*. 18 (14). p.pp. 1877–1882.
- Reddy, A.L.M. & Ramaprabhu, S. (2007). Nanocrystalline metal oxides dispersed multiwalled carbon nanotubes as supercapacitor electrodes. *Journal of Physical Chemistry C*. 111 (21). p.pp. 7727–7734.
- Reynolds, J.R., Baker, C.K., Jolly, C.A., Poropatic, P.A. & Ruiz, J.P. (1989). Electrically conductive polymers. In: *Conductive Polymers and Plastics*. Springer, pp. 1–40.
- Rojas, O.J., Montero, G.A. & Habibi, Y. (2009). Electrospun nanocomposites from polystyrene loaded with cellulose nanowhiskers. *Journal of Applied Polymer Science*. 113 (2). p.pp. 927–935.
- Roman, M. & Winter, W.T. (2004). Effect of sulfate groups from sulfuric acid hydrolysis on the thermal degradation behavior of bacterial cellulose. *Biomacromolecules*. 5 (5). p.pp. 1671–

- Rong, L.-Q., Yang, C., Qian, Q.-Y. & Xia, X.-H. (2007). Study of the nonenzymatic glucose sensor based on highly dispersed Pt nanoparticles supported on carbon nanotubes. *Talanta*. 72 (2). p.pp. 819–824.
- Rowland, S.P. & Roberts, E.J. (1972). The nature of accessible surfaces in the microstructure of cotton cellulose. *Journal of Polymer Science Part A-1: Polymer Chemistry*. 10 (8). p.pp. 2447–2461.
- Rudge, A., Raistrick, I., Gottesfeld, S. & Ferrairis, J.P. (1994). A Study of the Electrochemical Properties of Conducting Polymers for Applications in Electrochemical Capacitors. *Electrochim. Acta*. 39 (2). p.pp. 273–287.
- Ryoo, R., Joo, S.H. & Jun, S. (1999). Synthesis of Highly Ordered Carbon Molecular Sieves via Template-Mediated Structural Transformation. *The Journal of Physical Chemistry B*. 103 (37). p.pp. 7743–7746.
- Ryu, J., Kim, K., Kim, H.-S., Hahn, H.T. & Lashmore, D. (2010). Intense pulsed light induced platinum-gold alloy formation on carbon nanotubes for non-enzymatic glucose detection. *Biosensors & bioelectronics*. 26 (2). p.pp. 602–607.
- Ryu, K.S., Kim, K.M., Park, N.G., Park, Y.J. & Chang, S.H. (2002). Symmetric redox supercapacitor with conducting polyaniline electrodes. *Journal of Power Sources*. 103 (2). p.pp. 305–309.
- Sadasivuni, K.K., Kafy, A., Zhai, L., Ko, H.U., Mun, S. & Kim, J. (2015). Transparent and flexible cellulose nanocrystal/reduced graphene oxide film for proximity sensing. *Small*. 11 (8). p.pp. 994–1002.
- Sahoo, N.G., Rana, S., Cho, J.W., Li, L. & Chan, S.H. (2010). Polymer nanocomposites based on functionalized carbon nanotubes. *Progress in Polymer Science*. 35 (7). p.pp. 837–867.
- Santerre, J.P., Woodhouse, K., Laroche, G. & Labow, R.S. (2005). Understanding the biodegradation of polyurethanes: from classical implants to tissue engineering materials. *Biomaterials*. 26 (35). p.pp. 7457–7470.
- Sarapuu, A., Vaik, K., Schiffriin, D.J. & Tammeveski, K. (2003). Electrochemical reduction of oxygen on anthraquinone-modified glassy carbon electrodes in alkaline solution. *Journal of Electroanalytical Chemistry*. 541. p.pp. 23–29.
- Sasso, C., Zeno, E., Petit-Conil, M., Chaussy, D., Belgacem, M.N., Tapin-Lingua, S. & Beneventi, D. (2010). Highly Conducting Polypyrrole/Cellulose Nanocomposite Films with Enhanced Mechanical Properties. *Macromolecular Materials and Engineering*. 295 (10). p.pp. 934–941.
- Shang, L., Bian, T., Zhang, B., Zhang, D., Wu, L.-Z., Tung, C.-H., Yin, Y. & Zhang, T. (2014).

Graphene-supported ultrafine metal nanoparticles encapsulated by mesoporous silica: robust catalysts for oxidation and reduction reactions. *Angewandte Chemie (International ed. in English)*. 53 (1). p.pp. 250–254.

Shao, Y., Sui, J., Yin, G. & Gao, Y. (2008). Nitrogen-doped carbon nanostructures and their composites as catalytic materials for proton exchange membrane fuel cell. *Applied Catalysis B: Environmental*. 79 (1) p.pp. 89–99.

Sharifi, T., Hu, G., Jia, X. & Wågberg, T. (2012). Formation of active sites for oxygen reduction reactions by transformation of nitrogen functionalities in nitrogen-doped carbon nanotubes. *ACS Nano*. 6 (10). p.pp. 8904–8912.

Sharma, P. & Bhatti, T.S. (2010). A review on electrochemical double-layer capacitors. *Energy Conversion and Management*. 51 (12). p.pp. 2901–2912.

Shin, Y., Bae, I.T., Arey, B.W. & Exarhos, G.J. (2008). Facile stabilization of gold-silver alloy nanoparticles on cellulose nanocrystal. *Journal of Physical Chemistry C*. 112 (13). p.pp. 4844–4848.

Shin, Y., Bae, I.T., Arey, B.W. & Exarhos, G.J. (2007a). Simple preparation and stabilization of nickel nanocrystals on cellulose nanocrystal. *Materials Letters*. 61 (14–15). p.pp. 3215–3217.

Shin, Y., Blackwood, J.M., Bae, I.T., Arey, B.W. & Exarhos, G.J. (2007b). Synthesis and stabilization of selenium nanoparticles on cellulose nanocrystal. *Materials Letters*. 61 (21). p.pp. 4297–4300.

Shopowitz, K.E., Hamad, W.Y. & MacLachlan, M.J. (2011). Chiral nematic mesoporous carbon derived from nanocrystalline cellulose. *Angewandte Chemie International Edition*. 50 (46). p.pp. 10991–10995.

Shopowitz, K.E., Hamad, W.Y. & MacLachlan, M.J. (2012a). Flexible and iridescent chiral nematic mesoporous organosilica films. *Journal of the American Chemical Society*. 134 (2). p.pp. 867–870.

Shopowitz, K.E., Qi, H., Hamad, W.Y. & MacLachlan, M.J. (2010). Free-standing mesoporous silica films with tunable chiral nematic structures. *Nature*. 468 (7322). p.pp. 422–425.

Shopowitz, K.E., Stahl, A., Hamad, W.Y. & MacLachlan, M.J. (2012b). Hard Templating of Nanocrystalline Titanium Dioxide with Chiral Nematic Ordering. *Angewandte Chemie International Edition*. 51 (28). p.pp. 6886–6890.

Shrestha, S. & Mustain, W.E. (2010). Properties of Nitrogen-Functionalized Ordered Mesoporous Carbon Prepared Using Polypyrrole Precursor. *Journal of The Electrochemical Society*. 157 (11). p.pp. B1665–B1672.

Siaueira, G., Bras, J. & Dufresne, A. (2009). Cellulose whiskers versus microfibrils: Influence of

- the nature of the nanoparticle and its surface functionalization on the thermal and mechanical properties of nanocomposites. *Biomacromolecules*. 10 (2). p.pp. 425–432.
- Silva, R., Voiry, D., Chhowalla, M. & Asefa, T. (2013). Efficient metal-free electrocatalysts for oxygen reduction: Polyaniline-derived N- and O-doped mesoporous carbons. *Journal of the American Chemical Society*. 135 (21). p.pp. 7823–7826.
- Simonsen, J. (n.d.). <http://people.forestry.oregonstate.edu/john-simonsen/research-areas>.
- Singh, A.K. & Prakash, R. (2008). Conduction mechanism in electronic polymers: Effect of morphology. *Advanced Optoelectronic Materials and Devices, 2008. AOMD 2008. 2nd National Workshop on, Varanasi*. p.pp. 65–74.
- Siqueira, G., Bras, J. & Dufresne, A. (2010). New process of chemical grafting of cellulose nanoparticles with a long chain isocyanate. *Langmuir*. 26 (1). p.pp. 402–411.
- Sivakkumar, S.R. & Kim, D.-W. (2007). Polyaniline/carbon nanotube composite cathode for rechargeable lithium polymer batteries assembled with gel polymer electrolyte. *Journal of The Electrochemical Society*. 154 (2). p.pp. A134–A139.
- Sivakkumar, S.R., MacFarlane, D.R., Forsyth, M. & Kim, D.-W. (2007). Ionic Liquid-Based Rechargeable Lithium Metal-Polymer Cells Assembled with Polyaniline/Carbon Nanotube Composite Cathode. *Journal of The Electrochemical Society*. 154 (9). p.pp. A834–A838.
- Smart, R., McIntyre, S. & Bello, I. (2011). X - ray Photoelectron Spectroscopy. *Surface Science*. 6 (3). p.p. 86.
- Smits, F.M. (1958). Measurements of Sheet Resistivity with the Four-Point Probe. *Bell Syst Tech J*. 37 (3) p.pp. 711–718.
- Snethlage, R. & Wendler, E. (1999). Ullmann's Encyclopedia of Industrial Chemistry. *Petroleum science and technology*. 17 p.p. 445.
- Snook, G.A., Kao, P. & Best, A.S. (2011). Conducting-polymer-based supercapacitor devices and electrodes. *Journal of Power Sources*. 196 (1). p.pp. 1–12.
- Snook, G.A., Peng, C., Fray, D.J. & Chen, G.Z. (2007). Achieving high electrode specific capacitance with materials of low mass specific capacitance: Potentiostatically grown thick micro-nanoporous PEDOT films. *Electrochemistry Communications*. 9 (1). p.pp. 83–88.
- Stein, A., Wang, Z. & Fierke, M.A. (2009). Functionalization of porous carbon materials with designed pore architecture. *Advanced Materials*. 21 (3). p.pp. 265–293.
- Stoller, M.D., Park, S., Zhu, Y., An, J. & Ruoff, R.S. (2008). Graphene-based ultracapacitors. *Nano Lett*. 8 (10). p.pp. 3498–3502.
- Stoller, M.D. & Ruoff, R.S. (2010). Best practice methods for determining an electrode material's

- performance for ultracapacitors. *Energy & Environmental Science*. 3 (9) p.pp. 1294–1301.
- Su, C. & Loh, K.P. (2013). Carbocatalysts: Graphene oxide and its derivatives. *Accounts of Chemical Research*. 46 (10). p.pp. 2275–2285.
- Su, C., Zhang, C., Lu, G. & Ma, C. (2010). Nonenzymatic electrochemical glucose sensor based on Pt nanoparticles/mesoporous carbon matrix. *Electroanalysis*. 22 (16). p.pp. 1901–1905.
- Su, D.S., Perathoner, S. & Centi, G. (2013). Nanocarbons for the development of advanced catalysts. *Chemical Reviews*. 113 (8) p.pp. 5782–5816.
- Sun, Y., Li, C. & Shi, G. (2012). Nanoporous nitrogen doped carbon modified graphene as electrocatalyst for oxygen reduction reaction. *Journal of Materials Chemistry*. 22 (25). p.pp. 12810–12816.
- Tan, Y., Xu, C., Chen, G., Liu, Z., Ma, M., Xie, Q., Zheng, N. & Yao, S. (2013). Synthesis of ultrathin nitrogen-doped graphitic carbon nanocages as advanced electrode materials for supercapacitor. *ACS Applied Materials and Interfaces*. 5 (6). p.pp. 2241–2248.
- Tian, B. & Zerbi, G. (1990). Lattice dynamics and vibrational spectra of pristine and doped polypyrrole: Effective conjugation coordinate. *The Journal of Chemical Physics*. 92 (6). p.pp. 3892–3898.
- Tiwari, J.N., Nath, K., Kumar, S., Tiwari, R.N., Kemp, K.C., Le, N.H., Youn, D.H., Lee, J.S. & Kim, K.S. (2013). Stable platinum nanoclusters on genomic DNA-graphene oxide with a high oxygen reduction reaction activity. *Nature communications*. 4. p.p. 2221.
- Tripathi, P.K., Liu, M., Zhao, Y., Ma, X., Gan, L., Noonan, O. & Yu, C. (2014). Enlargement of uniform micropores in hierarchically ordered micro-mesoporous carbon for high level decontamination of bisphenol A. *Journal of Materials Chemistry A*. 2 (22). p.pp. 8534–8544.
- Turbak, A.F., Snyder, F.W. & Sandberg, K.R. (1983). Microfibrillated cellulose, a new cellulose product: properties, uses, and commercial potential. In: *J. Appl. Polym. Sci.: Appl. Polym. Symp.*; (United States). 1983, ITT Rayonier Inc., Shelton, WA.
- Valentini, L., Bittolo Bon, S., Fortunati, E. & Kenny, J.M. (2014). Preparation of transparent and conductive cellulose nanocrystals/graphene nanoplatelets films. *Journal of Materials Science*. 49 (3). p.pp. 1009–1013.
- Valentini, L., Cardinali, M., Fortunati, E., Torre, L. & Kenny, J.M. (2013). A novel method to prepare conductive nanocrystalline cellulose/graphene oxide composite films. *Materials Letters*. 105. p.pp. 4–7.
- Vikkisk, M., Kruusenberg, I., Joost, U., Shulga, E. & Tammeveski, K. (2013). Electrocatalysis of oxygen reduction on nitrogen-containing multi-walled carbon nanotube modified glassy carbon electrodes. *Electrochimica Acta*. 87. p.pp. 709–716.

- De Volder, M.F.L., Tawfick, S.H., Baughman, R.H. & Hart, a J. (2013). Carbon nanotubes: present and future commercial applications. *Science (New York, N.Y.)*. 339 (6119). p.pp. 535–539.
- Walcarius, A. (2008). Electroanalytical applications of microporous zeolites and mesoporous (organo) silicas: recent trends. *Electroanalysis*. 20 (7). p.pp. 711–738.
- Walcarius, A. (2013). Mesoporous materials and electrochemistry. *Chemical Society Reviews*. 42 (9). p.pp. 4098–4140.
- Walcarius, A. (2015). Mesoporous Materials-Based Electrochemical Sensors. *Electroanalysis*. 27 (6). p.pp. 1303–1340.
- Wang, C., Guo, S., Pan, X., Chen, W. & Bao, X. (2008a). Tailored cutting of carbon nanotubes and controlled dispersion of metal nanoparticles inside their channels. *Journal of Materials Chemistry*. 18 (47). p.pp. 5782–5786.
- Wang, C., Zhou, Y., Sun, L., Wan, P., Zhang, X. & Qiu, J. (2013a). Sustainable synthesis of phosphorus- and nitrogen-co-doped porous carbons with tunable surface properties for supercapacitors. *Journal of Power Sources*. 239. p.pp. 81–88.
- Wang, D.W., Li, F., Chen, Z.G., Lu, G.Q. & Cheng, H.M. (2008b). Synthesis and electrochemical property of boron-doped mesoporous carbon in supercapacitor. *Chemistry of Materials*. 20 (22). p.pp. 7195–7200.
- Wang, D.W., Li, F., Liu, M., Lu, G.Q. & Cheng, H.M. (2008c). 3D aperiodic hierarchical porous graphitic carbon material for high-rate electrochemical capacitive energy storage. *Angewandte Chemie - International Edition*. 47 (2). p.pp. 373–376.
- Wang, D.W., Li, F., Yin, L.C., Lu, X., Chen, Z.G., Gentle, I.R., Lu, G.Q. & Cheng, H.M. (2012a). Nitrogen-doped carbon monolith for alkaline supercapacitors and understanding nitrogen-induced redox transitions. *Chemistry - A European Journal*. 18 (17). p.pp. 5345–5351.
- Wang, D.W., Li, F., Zhao, J., Ren, W., Chen, Z.G., Tan, J., Wu, Z.S., Gentle, I., Lu, G.Q. & Cheng, H.M. (2009a). Fabrication of graphene/polyaniline composite paper via in situ anodic electropolymerization for high-performance flexible electrode. *ACS Nano*. 3 (7). p.pp. 1745–1752.
- Wang, G., Zhang, L. & Zhang, J. (2012b). A review of electrode materials for electrochemical supercapacitors. *Chemical Society Reviews*. 41 p.pp. 797–828.
- Wang, H., Bian, L., Zhou, P., Tang, J. & Tang, W. (2013b). Core-sheath structured bacterial cellulose/polypyrrole nanocomposites with excellent conductivity as supercapacitors. *Journal of Materials Chemistry A*. 1 (3). p.pp. 578–584.
- Wang, H., Gao, Q. & Hu, J. (2009b). High hydrogen storage capacity of porous carbons prepared by using activated carbon. *Journal of the American Chemical Society*. 131 (20). p.pp. 7016–

- Wang, H. & Roman, M. (2011). Formation and properties of chitosan– cellulose nanocrystal polyelectrolyte– macroion complexes for drug delivery applications. *Biomacromolecules*. 12 (5). p.pp. 1585–1593.
- Wang, H.W., Hu, Z.A., Chang, Y.Q., Chen, Y.L., Lei, Z.Q., Zhang, Z.Y. & Yang, Y.Y. (2010a). Facile solvothermal synthesis of a graphene nanosheet-bismuth oxide composite and its electrochemical characteristics. *Electrochimica Acta*. 55 (28). p.pp. 8974–8980.
- Wang, J. (1991). Modified electrodes for electrochemical sensors. *Electroanalysis*. 3 (4-5). p.pp. 255–259.
- Wang, J., Thomas, D.F. & Chen, A. (2008d). Nonenzymatic electrochemical glucose sensor based on nanoporous PtPb networks. *Analytical Chemistry*. 80 (4). p.pp. 997–1004.
- Wang, J., Xu, Y.L., Chen, X. & Sun, X.F. (2007). Capacitance properties of single wall carbon nanotube/polypyrrole composite films. *Composites Science and Technology*. 67 (14). p.pp. 2981–2985.
- Wang, L., Bo, X., Bai, J., Zhu, L. & Guo, L. (2010b). Gold Nanoparticles Electrodeposited on Ordered Mesoporous Carbon as an Enhanced Material for Nonenzymatic Hydrogen Peroxide Sensor. *Electroanalysis*. 22 (21). p.pp. 2536–2542.
- Wang, M.X., Wang, C.Y., Chen, M.M., Wang, Y.S., Shi, Z.Q., Du, X., Li, T.Q. & Hu, Z.J. (2010c). Preparation of high-performance activated carbons for electric double layer capacitors by KOH activation of mesophase pitches. *Xinxing Tan Cailiao/New Carbon Materials*. 25 (4). p.pp. 285–290.
- Wang, Q., Jia, W., Liu, B., Dong, A., Gong, X., Li, C., Jing, P., Li, Y., Xu, G. & Zhang, J. (2013c). Hierarchical structure based on Pd(Au) nanoparticles grafted onto magnetite cores and double layered shells: enhanced activity for catalytic applications. *Journal of Materials Chemistry A*. 1 (41). p.pp. 12732–12741.
- Wang, R., Higgins, D.C., Hoque, M.A., Lee, D., Hassan, F. & Chen, Z. (2013d). Controlled growth of platinum nanowire arrays on sulfur doped graphene as high performance electrocatalyst. *Scientific reports*. 3. p.p. 2431.
- Wang, S., Iyyamperumal, E., Roy, A., Xue, Y., Yu, D. & Dai, L. (2011). Vertically aligned BCN nanotubes as efficient metal-free electrocatalysts for the oxygen reduction reaction: A synergistic effect by co-doping with boron and nitrogen. *Angewandte Chemie - International Edition*. 50 (49). p.pp. 11756–11760.
- Wang, X., Lee, J.S., Zhu, Q., Liu, J., Wang, Y. & Dai, S. (2010d). Ammonia-Treated Ordered Mesoporous Carbons as Catalytic Materials for Oxygen Reduction Reaction. *Chemistry of Materials*. 22 (7). p.pp. 2178–2180.

- Wang, Y., Chang, C. & Zhang, L. (2010e). Effects of Freezing/Thawing Cycles and Cellulose Nanowhiskers on Structure and Properties of Biocompatible Starch/PVA Sponges. *Macromolecular Materials and Engineering*. 295 (2). p.pp. 137–145.
- Way, A.E., Hsu, L., Shanmuganathan, K., Weder, C. & Rowan, S.J. (2012). pH-Responsive Cellulose Nanocrystal Gels and Nanocomposites. *ACS Macro Letters*. 1 (8). p.pp. 1001–1006.
- Wei, L., Sevilla, M., Fuertes, A.B., Mokaya, R. & Yushin, G. (2011). Hydrothermal carbonization of abundant renewable natural organic chemicals for high-performance supercapacitor electrodes. *Advanced Energy Materials*. 1 (3). p.pp. 356–361.
- Wei, L., Sevilla, M., Fuertes, A.B., Mokaya, R. & Yushin, G. (2012). Polypyrrole-derived activated carbons for high-performance electrical double-layer capacitors with ionic liquid electrolyte. *Advanced Functional Materials*. 22 (4). p.pp. 827–834.
- Wen, Z., Wang, X., Mao, S., Bo, Z., Kim, H., Cui, S., Lu, G., Feng, X. & Chen, J. (2012). Crumpled nitrogen-doped graphene nanosheets with ultrahigh pore volume for high-performance supercapacitor. *Advanced Materials*. 24 (41). p.pp. 5610–5616.
- White, R.J., Luque, R., Budarin, V.L., Clark, J.H. & Macquarrie, D.J. (2009). Supported metal nanoparticles on porous materials. Methods and applications. *Chemical Society reviews*. 38 (2). p.pp. 481–494.
- Wong, W.Y., Daud, W.R.W., Mohamad, A.B., Kadhum, A.A.H., Loh, K.S. & Majlan, E.H. (2013). Recent progress in nitrogen-doped carbon and its composites as electrocatalysts for fuel cell applications. *International Journal of Hydrogen Energy*. 38 (22). p.pp. 9370–9386.
- Woo, Y.-T. & Lai, D.Y. (2001). Aromatic Amino and Nitro–Amino Compounds and Their Halogenated Derivatives. In: *Patty's Toxicology*.
- Wu, G.H., Song, X.H., Wu, Y.F., Chen, X.M., Luo, F. & Chen, X. (2013a). Non-enzymatic electrochemical glucose sensor based on platinum nanoflowers supported on graphene oxide. *Talanta*. 105. p.pp. 379–385.
- Wu, T.M., Chang, H.L. & Lin, Y.W. (2009). Synthesis and characterization of conductive polypyrrole/multi-walled carbon nanotubes composites with improved solubility and conductivity. *Composites Science and Technology*. 69 (5). p.pp. 639–644.
- Wu, X., Chabot, V.L., Kim, B.K., Yu, A., Berry, R.M. & Tam, K.C. (2014). Cost-effective and Scalable Chemical Synthesis of Conductive Cellulose Nanocrystals for High-performance Supercapacitors. *Electrochimica Acta*. 138. p.pp. 139–147.
- Wu, X., Lu, C., Zhang, W., Yuan, G., Xiong, R. & Zhang, X. (2013b). A novel reagentless approach for synthesizing cellulose nanocrystal-supported palladium nanoparticles with enhanced catalytic performance. *Journal of Materials Chemistry A*. 1 (30). p.p. 8645.

- Wu, X.L., Wen, T., Guo, H.L., Yang, S., Wang, X. & Xu, A.W. (2013c). Biomass-derived sponge-like carbonaceous hydrogels and aerogels for supercapacitors. *ACS Nano*. 7 (4). p.pp. 3589–3597.
- Wu, Y., Li, Y., Qin, L., Yang, F. & Wu, D. (2013d). Monodispersed or narrow-dispersed melamine-formaldehyde resin polymer colloidal spheres: preparation, size-control, modification, bioconjugation and particle formation mechanism. *Journal of Materials Chemistry B*. 1 (2). p.pp. 204–212.
- Wu, Z.S., Wang, D.W., Ren, W., Zhao, J., Zhou, G., Li, F. & Cheng, H.M. (2010). Anchoring hydrous RuO₂ on graphene sheets for high-performance electrochemical capacitors. *Advanced Functional Materials*. 20 (20). p.pp. 3595–3602.
- Wunder, S., Polzer, F., Lu, Y., Mei, Y. & Ballauff, M. (2010). Kinetic analysis of catalytic reduction of 4-nitrophenol by metallic nanoparticles immobilized in spherical polyelectrolyte brushes. *Journal of Physical Chemistry C*. 114 (19). p.pp. 8814–8820.
- X. Kong, Z. Sun, M.Chen, C.C. and Q.C. (2013). Metal-free Catalytic Reduction of 4-Nitrophenol to 4-Aminophenol by N-Doped Graphene. *Energy and Environmental Science*. 6 (11). p.pp. 3260–3266.
- Xia, Y. & Mokaya, R. (2005). Generalized and facile synthesis approach to N-doped highly graphitic mesoporous carbon materials. *Chemistry of Materials*. 17 (6). p.pp. 1553–1560.
- Xiao, X., Beechem, T.E., Brumbach, M.T., Lambert, T.N., Davis, D.J., Michael, J.R., Washburn, C.M., Wang, J., Brozik, S.M., Wheeler, D.R., Burckel, D.B. & Polsky, R. (2012). Lithographically defined three-dimensional graphene structures. *ACS Nano*. 6 (4). p.pp. 3573–3579.
- Xie, X., Long, J., Xu, J., Chen, L., Wang, Y., Zhang, Z. & Wang, X. (2012). Nitrogen-doped graphene stabilized gold nanoparticles for aerobic selective oxidation of benzylic alcohols. *Rsc Advances*. 2 (32). p.pp. 12438–12446.
- Xu, B., Wu, F., Su, Y., Cao, G., Chen, S., Zhou, Z. & Yang, Y. (2008). Competitive effect of KOH activation on the electrochemical performances of carbon nanotubes for EDLC: Balance between porosity and conductivity. *Electrochimica Acta*. 53 (26). p.pp. 7730–7735.
- Xu, J., Zhu, L., Bai, Z., Liang, G., Liu, L., Fang, D. & Xu, W. (2013a). Conductive polypyrrole-bacterial cellulose nanocomposite membranes as flexible supercapacitor electrode. *Organic Electronics*. 14 (12). p.pp. 3331–3338.
- Xu, Y., Wu, M., Liu, Y., Feng, X.-Z., Yin, X.-B., He, X.-W. & Zhang, Y.-K. (2013b). Nitrogen-doped carbon dots: a facile and general preparation method, photoluminescence investigation, and imaging applications. *Chemistry - A European Journal*. 19 (7). p.pp. 2276–2283.
- Xue, Y., Yu, D., Dai, L., Wang, R., Li, D., Roy, A., Lu, F., Chen, H., Liu, Y. & Qu, J. (2013).

- Three-dimensional B,N-doped graphene foam as a metal-free catalyst for oxygen reduction reaction. *Physical chemistry chemical physics : PCCP*. 15 (29). p.pp. 12220–12226.
- Yan, J., Wei, T., Shao, B., Fan, Z., Qian, W., Zhang, M. & Wei, F. (2010). Preparation of a graphene nanosheet/polyaniline composite with high specific capacitance. *Carbon*. 48 (2). p.pp. 487–493.
- Yang, C.M., Weidenthaler, C., Spliethoff, B., Mayanna, M. & Schüth, F. (2005). Facile template synthesis of ordered mesoporous carbon with polypyrrole as carbon precursor. *Chemistry of Materials*. 17 (2). p.pp. 355–358.
- Yang, X., Cheng, C., Wang, Y., Qiu, L. & Li, D. (2013). Liquid-mediated dense integration of graphene materials for compact capacitive energy storage. *Science (New York, N.Y.)*. 341 (6145). p.pp. 534–537.
- Yang, X., Shi, K., Zhitomirsky, I. & Cranston, E.D. (2015). Cellulose Nanocrystal Aerogels as Universal 3D Lightweight Substrates for Supercapacitor Materials. *Advanced Materials*. 27 (40). p.pp. 6104–6109.
- Yang, Y., Chiang, K. & Burke, N. (2011). Porous carbon-supported catalysts for energy and environmental applications: A short review. *Catalysis Today*. 178 (1) p.pp. 197–205.
- Yoon, H., Ko, S. & Jang, J. (2007). Nitrogen-doped magnetic carbon nanoparticles as catalyst supports for efficient recovery and recycling. *Chemical communications (Cambridge, England)*. (14). p.pp. 1468–1470.
- Yu, A., Chabot, V. & Zhang, J. (2013). *electrochmical supercapacitors for energy storage and delivery:Fundamentals and Applications*. CRS Press.
- Yu, A.P., Roes, I., Davies, A. & Chen, Z.W. (2010). Ultrathin, transparent, and flexible graphene films for supercapacitor application. *Applied Physics Letters*. 96 (25). p.p. 253105.
- Yu, A.P., Sy, A. & Davies, A. (2011). Graphene nanoplatelets supported MnO₂ nanoparticles for electrochemical supercapacitor. *Synthetic Metals*. 161 (17-18). p.pp. 2049–2054.
- Yu, Y., Ouyang, C., Gao, Y., Si, Z., Chen, W., Wang, Z. & Xue, G. (2005). Synthesis and characterization of carbon nanotube/polypyrrole core–shell nanocomposites via in situ inverse microemulsion. *Journal of Polymer Science Part A: Polymer Chemistry*. 43 (23). p.pp. 6105–6115.
- Yu, Z., Tetard, L., Zhai, L. & Thomas, J. (2015). Supercapacitor electrode materials: nanostructures from 0 to 3 dimensions. *Energy Environ. Sci.* 8 (3). p.pp. 702–730.
- Yuan, H., Nishiyama, Y., Wada, M. & Kuga, S. (2006). Surface acylation of cellulose whiskers by drying aqueous emulsion. *Biomacromolecules*. 7. p.pp. 696–700.

- Yuan, J., Wang, K. & Xia, X. (2005). Highly ordered platinum-nanotubule arrays for amperometric glucose sensing. *Advanced Functional Materials.* 15 (5). p.pp. 803–809.
- Zaman, M., Xiao, H., Chibante, F. & Ni, Y. (2012). Synthesis and characterization of cationically modified nanocrystalline cellulose. *Carbohydrate Polymers.* 89 (1). p.pp. 163–170.
- Zhai, Y., Dou, Y., Zhao, D., Fulvio, P.F., Mayes, R.T. & Dai, S. (2011). Carbon materials for chemical capacitive energy storage. *Advanced materials (Deerfield Beach, Fla.).* 23 (42). p.pp. 4828–4850.
- Zhang, B., Xu, Y., Zheng, Y., Dai, L., Zhang, M., Yang, J., Chen, Y., Chen, X. & Zhou, J. (2011). A facile synthesis of polypyrrole/carbon nanotube composites with ultrathin, uniform and thickness-tunable polypyrrole shells. *Nanoscale Res Lett.* 6 (431). p.pp. 1–9.
- Zhang, C., Xu, L., Shan, N., Sun, T., Chen, J. & Yan, Y. (2014a). Enhanced electrocatalytic activity and durability of Pt particles supported on ordered mesoporous carbon spheres. *ACS Catalysis.* 4 (6) p.pp. 1926–1930.
- Zhang, J. & Dai, L. (2015). Heteroatom-Doped Graphitic Carbon Catalysts for Efficient Electrocatalysis of Oxygen Reduction Reaction. *ACS Catalysis.* 5 (12) p.pp. 7244–7253.
- Zhang, J., Kong, L.-B., Wang, B., Luo, Y.-C. & Kang, L. (2009a). In-situ electrochemical polymerization of multi-walled carbon nanotube/polyaniline composite films for electrochemical supercapacitors. *Synthetic metals.* 159 (3). p.pp. 260–266.
- Zhang, J. & Zhao, X.S. (2012). Conducting Polymers Directly Coated on Reduced Graphene Oxide Sheets as High-Performance Supercapacitor Electrodes. *The Journal of Physical Chemistry C.* 116 (9). p.pp. 5420–5426.
- Zhang, J., Zhao, Z., Xia, Z. & Dai, L. (2015). A metal-free bifunctional electrocatalyst for oxygen reduction and oxygen evolution reactions. *Nature Nanotechnology.* 10 (5). p.pp. 444–452.
- Zhang, L., Zheng, N., Gao, A., Zhu, C., Wang, Z., Wang, Y., Shi, Z. & Liu, Y. (2012a). A robust fuel cell cathode catalyst assembled with nitrogen-doped carbon nanohorn and platinum nanoclusters. *Journal of Power Sources.* 220. p.pp. 449–454.
- Zhang, S., Kang, P., Ubnoske, S., Brennaman, M.K., Song, N., House, R.L., Glass, J.T. & Meyer, T.J. (2014b). Polyethylenimine-Enhanced Electrocatalytic Reduction of CO₂ to Formate at Nitrogen-Doped Carbon Nanomaterials. *Journal of the American Chemical Society.* 136 (22). p.pp. 7845–7848.
- Zhang, X. & Bai (2003). Surface Electric Properties of Polypyrrole in Aqueous Solutions. *Langmuir.* 19 (26). p.pp. 10703–10709.
- Zhang, X., Zhang, J. & Liu, Z. (2005). Tubular composite of doped polyaniline with multi-walled carbon nanotubes. *Applied Physics A.* 80 (8). p.pp. 1813–1817.

- Zhang, X., Zhang, J., Wang, R., Zhu, T. & Liu, Z. (2004). Surfactant-Directed Polypyrrole/CNT Nanocables: Synthesis, Characterization, and Enhanced Electrical Properties. *ChemPhysChem.* 5 (7). p.pp. 998–1002.
- Zhang, Y., Fugane, K., Mori, T., Niu, L. & Ye, J. (2012b). Wet chemical synthesis of nitrogen-doped graphene towards oxygen reduction electrocatalysts without high-temperature pyrolysis. *Journal of Materials Chemistry*. 22 (14). p.pp. 6575–6580.
- Zhang, Y., Li, H., Pan, L., Lu, T. & Sun, Z. (2009b). Capacitive behavior of graphene-ZnO composite film for supercapacitors. *Journal of Electroanalytical Chemistry*. 634 (1). p.pp. 68–71.
- Zhang, Y., Sun, X., Pan, L., Li, H., Sun, Z., Sun, C. & Tay, B.K. (2009c). Carbon nanotube-ZnO nanocomposite electrodes for supercapacitors. *Solid State Ionics*. 180 (32-35). p.pp. 1525–1528.
- Zhang, Z. & Wan, M. (2003). Nanostructures of polyaniline composites containing nano-magnet. *Synthetic metals*. 132 (2). p.pp. 205–212.
- Zhao, J., Lai, H., Lyu, Z., Jiang, Y., Xie, K., Wang, X., Wu, Q., Yang, L., Jin, Z., Ma, Y., Liu, J. & Hu, Z. (2015a). Hydrophilic Hierarchical Nitrogen-Doped Carbon Nanocages for Ultrahigh Supercapacitive Performance. *Advanced materials (Deerfield Beach, Fla.)*. 27 (23). p.pp. 3541–3545.
- Zhao, L., Fan, L.Z., Zhou, M.Q., Guan, H., Qiao, S., Antonietti, M. & Titirici, M.M. (2010). Nitrogen-containing hydrothermal carbons with superior performance in supercapacitors. *Advanced Materials*. 22 (45). p.pp. 5202–5206.
- Zhao, P., Feng, X., Huang, D., Yang, G. & Astruc, D. (2015b). Basic concepts and recent advances in nitrophenol reduction by gold-and other transition metal nanoparticles. *Coordination Chemistry Reviews*. 287. p.pp. 114–136.
- Zhao, X., Chu, B.T.T., Ballesteros, B., Wang, W., Johnston, C., Sykes, J.M. & Grant, P.S. (2009). Spray deposition of steam treated and functionalized single-walled and multi-walled carbon nanotube films for supercapacitors. *Nanotechnology*. 20 (6). p.p. 065605.
- Zhao, Y., Liu, B., Pan, L. & Yu, G. (2013a). 3D nanostructured conductive polymer hydrogels for high-performance electrochemical devices. *Energy Environ. Sci.* 6 (10). p.pp. 2856–2870.
- Zhao, Y., Liu, M., Deng, X., Miao, L., Tripathi, P.K., Ma, X., Zhu, D., Xu, Z., Hao, Z. & Gan, L. (2015c). Nitrogen-functionalized microporous carbon nanoparticles for high performance supercapacitor electrode. *Electrochimica Acta*. 153. p.pp. 448–455.
- Zhao, Y., Nakamura, R., Kamiya, K., Nakanishi, S. & Hashimoto, K. (2013b). Nitrogen-doped carbon nanomaterials as non-metal electrocatalysts for water oxidation. *Nature Communications*. 4. p.pp. 1–7.

- Zhao, Z., Hao, S., Hao, P., Sang, Y., Manivannan, A., Wu, N. & Liu, H. (2015d). Lignosulphonate-cellulose derived porous activated carbon for supercapacitor electrode. *Journal of Materials Chemistry A*. 3 (29). p.pp. 15049–15056.
- Zheng, D., Ye, J., Zhou, L., Zhang, Y. & Yu, C. (2009). Simultaneous determination of dopamine, ascorbic acid and uric acid on ordered mesoporous carbon/Nafion composite film. *Journal of Electroanalytical Chemistry*. 625 (1). p.pp. 82–87.
- Zhou, M., Shang, L., Li, B., Huang, L. & Dong, S. (2008). The characteristics of highly ordered mesoporous carbons as electrode material for electrochemical sensing as compared with carbon nanotubes. *Electrochemistry Communications*. 10 (6). p.pp. 859–863.
- Zhou, W. & Wang, Z.L. (2007). *Scanning microscopy for nanotechnology: Techniques and applications*.
- Zhou, X., Bai, Z., Wu, M., Qiao, J. & Chen, Z. (2015). 3-Dimensional porous N-doped graphene foam as a non-precious catalyst for the oxygen reduction reaction. *Journal of Materials Chemistry A*. 3 (7). p.pp. 3343–3350.
- Zhou, X., Xu, W., Liu, G., Panda, D. & Chen, P. (2010a). Size-Dependent Catalytic Activity and Dynamics of Gold Nanoparticles at the Single-Molecule Level. *Journal of the American Chemical Society*. 132 (1). p.pp. 138–146.
- Zhou, X., Zheng, X., Lv, R., Kong, D. & Li, Q. (2013). Electrodeposition of platinum on poly(glutamic acid) modified glassy carbon electrode for non-enzymatic amperometric glucose detection. *Electrochimica Acta*. 107. p.pp. 164–169.
- Zhou, Y., Ding, E.-Y. & Li, W.-D. (2007). Synthesis of TiO₂ nanocubes induced by cellulose nanocrystal (CNC) at low temperature. *Materials Letters*. 61 (28). p.pp. 5050–5052.
- Zhou, Y., Neyerlin, K., Olson, T.S., Pylypenko, S., Bult, J., Dinh, H.N., Gennett, T., Shao, Z. & O’Hayre, R. (2010b). Enhancement of Pt and Pt-alloy fuel cell catalyst activity and durability via nitrogen-modified carbon supports. *Energy & Environmental Science*. 3 (10). p.pp. 1437–1446.
- Zhou, Y., Qin, Z.-Y., Li, L., Zhang, Y., Wei, Y.-L., Wang, L.-F. & Zhu, M.-F. (2010c). Polyaniline/multi-walled carbon nanotube composites with core–shell structures as supercapacitor electrode materials. *Electrochimica Acta*. 55 (12). p.pp. 3904–3908.
- Zhu, C., Li, H., Fu, S., Du, D. & Lin, Y. (2016). Highly efficient nonprecious metal catalysts towards oxygen reduction reaction based on three-dimensional porous carbon nanostructures. *Chemical Society Reviews*. 45. p.pp. 517–531.
- Zhu, D., Wang, Y., Gan, L., Liu, M., Cheng, K., Zhao, Y., Deng, X. & Sun, D. (2015). Nitrogen-containing carbon microspheres for supercapacitor electrodes. *Electrochimica Acta*. 158. p.pp. 166–174.

- Zhu, J., Jia, Y., Li, M., Lu, M. & Zhu, J. (2013). Carbon nanofibers grown on anatase washcoated cordierite monolith and its supported palladium catalyst for cinnamaldehyde hydrogenation. *Industrial and Engineering Chemistry Research*. 52 (3). p.pp. 1224–1233.
- Zhu, L., Tian, C., Zhu, D. & Yang, R. (2008). Ordered mesoporous carbon paste electrodes for electrochemical sensing and biosensing. *Electroanalysis*. 20 (10). p.pp. 1128–1134.
- Zhu, S., Chen, Z., Li, B., Higgins, D., Wang, H., Li, H. & Chen, Z. (2011a). Nitrogen-doped carbon nanotubes as air cathode catalysts in zinc-air battery. *Electrochimica Acta*. 56 (14). p.pp. 5080–5084.
- Zhu, Y., Murali, S., Stoller, M.D., Ganesh, K.J., Cai, W., Ferreira, P.J., Pirkle, A., Wallace, R.M., Cychosz, K.A., Thommes, M., Su, D., Stach, E.A. & Ruoff, R.S. (2011b). Carbon-based supercapacitors produced by activation of graphene. *Science (New York, N.Y.)*. 332 (6037). p.pp. 1537–1541.
- Zoppe, J.O., Peresin, M.S., Habibi, Y., Venditti, R.A. & Rojas, O.J. (2009). Reinforcing Poly(ϵ -caprolactone) Nanofibers with Cellulose Nanocrystals. *ACS Applied Materials & Interfaces*. 1 (9). p.pp. 1996–2004.
- Zurutuza, A. & Marinelli, C. (2014). Challenges and opportunities in graphene commercialization. *Nature nanotechnology*. 9. p.pp. 730–734.